Measuring microvessel structure and function in the brain using magnetic resonance imaging

A thesis submitted to the University of Manchester for the degree of Doctor of Philosophy in the Faculty of Biology, Medicine and Health

2021

Lauren A Scott

School of Biological Sciences

MANCHESTER 1824
The University of Manchester

Contents

List of Figures . . . 7
List of Tables . . . 15
Abbreviations . . . 18
Symbols . . . 20
Abstract . . . 22
Declaration . . . 23
Copyright statement . . . 24
Acknowledgments . . . 25
Publications . . . 26
Conference abstracts . . . 27
1 Introduction . . . 28
1.1 Motivation . . . 28
1.2 Thesis Overview . . . 30
2 Evidence for microvascular changes and impact on neuronal function . . . 32
2.1 Structure and function of the cerebrovascular network . . . 32
2.2 Alteration in disease . . . 33
2.2.1 MRI measures of cerebrovascular pathology . . . 35
2.2.2 Small vessel disease and vascular dementia . . . 39
2.2.2.1 Measurable clinical manifestations . . . 39
2.2.2.2 Age related cSVD . . . 41
2.2.3 Alzheimer's disease . . . 42
2.3 Modifiable risk factors associated with microvascular changes . . . 45
2.3.1 Hypertension . . . 45
2.3.2 Diabetes . . . 46
2.3.3 Environmental factors . . . 47
2.4 Impact of altered vascular network on neuronal function . . . 47
3 Diffusion-weighted MRI methods to probe microvessel structure . . . 49
3.1 MRI . . . 49
3.1.1 Nuclear magnetic resonance . . . 49
3.1.2 Generating a signal . . . 50
3.1.3 Spatial localisation . . . 53
3.2 Diffusion-weighted MRI . . . 56
3.2.1 Pulse gradient spin echo . . . 56
3.2.2 Flow-compensation . . . 59
3.3 Modelling the DW-MRI signal . . . 60
3.3.1 b-value spectrum . . . 61
3.3.2 Monoexponential model . . . 63
3.3.3 Biexponential extravascular model . . . 64
3.3.4 Non-Gaussian extravascular models . . . 64
3.3.4.1 Signal representations . . . 64
3.3.4.2 Compartmentalised models . . . 64
3.3.5 Intravascular models: IVIM . . . 65
3.3.5.1 Biexponential IVIM model . . . 65
3.3.5.2 Triexponential IVIM models . . . 69

3.3.5.3 Higher order IVIM models 70
3.3.5.4 Diffusion-time dependent models 71
3.3.5.5 Flow-compensation in IVIM 72
3.3.5.6 Alternative IVIM models 74
3.4 Alternative theories and models 75
3.5 Summary 75
4 Characterisation of microvessel blood velocity and segment length in the brain using multi-diffusion-time diffusion-weighted MRI 78
4.1 Contribution of authors 78
4.2 Abstract 78
4.3 Introduction 79
4.4 Theory 80
4.4.1 Intravoxel Incoherent Motion 81
4.4.1.1 Method 1. IVIM (ballistic regime) 82
4.4.1.2 Method 2. Velocity Autocorrelation model . . . 82
4.4.1.3 Method 3. Velocity Autocorrelation model (ballistic regime) 82
4.5 Methods 83
4.5.1 MRI acquisitions 83
4.5.2 Extraction of regional MRI signals 84
4.5.3 Model fitting 85
4.5.3.1 Estimation of D and f 85
4.5.3.2 Estimation of intravascular parameters 85
4.5.3.3 Evaluating the validity of model approximations 86
4.5.4 Corrosion casting 86
4.5.5 Micro-CT of casts and analysis 88
4.5.6 Statistical Analysis 89
4.5.6.1 Comparison of MR with micro-CT estimates of capillary segment length 89
4.5.6.2 Assessment of scan-rescan repeatability 89
4.5.6.3 Comparison of MR estimates of velocity, v, and capillary segment length, l between rat strains . 90
4.5.6.4 Comparison of voxel-wise SNR between diffusion-times 90
4.6 Results 90
4.6.1 Comparison of MR and CT estimates of capillary segment length 90
4.6.2 Assessment of scan-rescan repeatability 91
4.6.3 Comparison of VA and VA ballistic MR estimates of velocity, v, and capillary segment length, l between rat strains . . . 91
4.6.4 Assessment of model validity 94
4.6.5 Signal to noise ratio 94
4.7 Discussion 96
4.8 Conclusion 99
4.9 Acknowledgements 99
4.10 Funding 99

4.11 Supplementary materials . . . 100
4.11.1 Animal breeding, housing, and husbandry . . . 100
4.11.2 Figures . . . 100
4.11.3 Tables . . . 104
5 Modelling the diffusion-time dependence of intravoxel incoherent motion in the brain: accounting for blood velocity, vessel length and water exchange . 108
5.1 Contribution of authors . . . 108
5.2 Moving from preclinical work to model development in clinical data 108
5.3 Abstract . . . 109
5.4 Introduction . . . 109
5.5 Theory . . . 111
5.5.1 Two compartment model . . . 111
5.5.1.1 Velocity-autocorrelation model . . . 111
5.5.2 Accounting for finite blood-brain barrier water exchange . 112
5.6 Methods . . . 112
5.6.1 MRI acquisitions . . . 113
5.6.2 Extraction of regional MRI signals . . . 114
5.6.3 Model fitting . . . 114
5.6.3.1 Estimation of D and f . . . 114
5.6.3.2 Estimation of k as a function of Δ . . . 114
5.6.3.3 Estimation of blood velocity, v, correlation time, T_0, vessel segment length, l, and exchange time, τ 115
5.6.4 Statistical analysis . . . 115
5.6.4.1 Assessing diffusion-time dependence . . . 115
5.6.4.2 Assessing model fit . . . 115
5.6.4.3 Assessment of intra-scan repeatability . . . 116
5.7 Results . . . 117
5.7.1 Velocity-autocorrelation model accounting for finite blood-brain barrier water-exchange . . . 117
5.7.2 Diffusion-time dependence of f, D and k . . . 117
5.7.3 Model comparison using Akaike information criterion . . . 120
5.7.4 Parameter estimates from the VA and VAX models . . . 121
5.7.5 Assessment of intra-scan repeatability . . . 121
5.8 Discussion . . . 123
5.9 Conclusion . . . 127
5.10 Acknowledgements . . . 127
5.11 Funding . . . 127
5.12 Supplementary materials . . . 127
5.12.1 Effects of BBB water-exchange on the intravascular signal attenuation coefficient, k . . . 127
5.12.2 Figures and tables . . . 129
6 Hypercapnia induced changes in multi-diffusion-time intravoxel incoherent motion imaging in the brain . . . 134
6.1 Contribution of authors . . . 134
6.2 Moving from model development to validation in clinical data . . . 134
6.3 Abstract . . . 135

6.4 Introduction . . . 136
6.5 Methods . . . 137
6.5.1 Data acquisition . . . 137
6.5.1.1 MRI acquisition . . . 137
6.5.1.2 Hypercapnic intervention . . . 138
6.5.2 Extraction of regional MRI data . . . 140
6.5.3 Extracting DW-MRI metrics . . . 140
6.5.3.1 Diffusive IVIM model . . . 140
6.5.3.2 Velocity autocorrelation model . . . 141
6.5.3.3 Extracting D and f . . . 141
6.5.3.4 Extracting D^*, v, T_0 and l . . . 141
6.5.4 Statistical analysis . . . 142
6.5.4.1 Assessing model fit . . . 142
6.5.4.2 Assessing effects of hypercapnia on DWI and ASL derived parameters . . . 143
6.6 Results . . . 143
6.6.1 Model comparison using Akaike information criterion . . . 143
6.6.2 Diffusion-time dependence of f, D and k . . . 143
6.6.3 Effects of hypercapnia . . . 144
6.6.3.1 End-tidal carbon dioxide . . . 144
6.6.3.2 The effect of hypercapnia on DW-MRI and ASL-derived parameters . . . 144
6.7 Discussion . . . 150
6.8 Conclusion . . . 155
6.9 Acknowledgements . . . 156
6.10 Funding . . . 156
6.11 Supplementary materials . . . 156
6.11.1 Velocity autocorrelation model corrected for blood-brain-barrier water exchange . . . 156
6.11.2 Sensitivity of ASL acquisition to ATT . . . 157
6.11.3 Figures . . . 159
7 Microvascular dysfunction in the elderly assessed using intra-voxel incoherent motion (IVIM) diffusion-weighted magnetic resonance imaging (DW-MRI): links to markers of cerebrovascular health, amyloid-β PET, and cognition . 168
7.1 Contribution of authors . . . 168
7.2 Implementing the model in a patient cohort . . . 169
7.3 Abstract . . . 169
7.4 Introduction . . . 170
7.5 Methods . . . 171
7.5.1 Subjects . . . 171
7.5.2 PET-MRI acquisitions . . . 173
7.5.3 PET data processing and amyloid status . . . 174
7.5.4 Extraction of regional MRI signals . . . 174
7.5.5 Extraction of white matter lesions volume . . . 175
7.5.6 Extraction of diffusion-weighted metrics . . . 175
7.5.6.1 IVIM . . . 175

7.5.6.2 Velocity autocorrelation model 175
7.5.6.3 Estimation of the extravascular diffusion coefficient, D, and perfusion fraction, f 176
7.5.6.4 Estimation of the pseudo-diffusion coefficient, D^*, blood velocity, v, and vessel segment length, l 177
7.5.7 Statistical analyses 177
7.5.7.1 Between-group differences in subject demographics 177
7.5.7.2 Assessment of scan-rescan repeatability 177
7.5.7.3 Relationship between vascular and tissue DW-MRI metrics and markers of cerebrovascular health 178
7.5.7.4 Value of vascular and tissue DW-MRI metrics and amyloid status for predicting cognition . . . 178
7.6 Results 179
7.6.1 Subject demographics 179
7.7 Assessment of scan-rescan repeatability 179
7.7.1 Relationship between vascular and tissue DW-MRI metrics and markers of vascular health 179
7.7.1.1 QRISK and WML 179
7.7.1.2 Intravascular measures, QRISK and WML . . . 180
7.7.1.3 Extravascular measures, QRISK and WML . . . 180
7.7.2 Value of vascular and tissue DW-MRI metrics and amyloid status for predicting cognition 180
7.7.2.1 Perfusion fraction and MoCA 182
7.8 Discussion 182
7.9 Conclusion 186
7.10 Acknowledgements 187
7.11 Funding 187
7.12 Supplementary materials 187
7.12.1 Figures 187
8 General discussion 192
8.1 Motivation and aims 192
8.2 DW-MRI models 193
8.3 Imaging studies 195
8.4 Limitations 201
8.5 Further work 209
8.6 Concluding remarks 211

A **212**
1 Determining bias and precision with simulation 212
1.1 Methods 212
1.2 Results 214
1.2.1 Signal to noise ratio in grey and white matter 214
1.2.2 Effect of b-value threshold on parameter estimates 215
1.2.3 Effect of two-step fitting method on diffusion-time dependence in f and D 219

1.2.4 Effects of fitting methods on parameter estimates (two-step versus one-step, and c) 219
1.2.5 Comparing in-vivo data for the one-step and two-step fits . 223
1.3 Discussion 224

Bibliography **228**

Word count: 58381

List of Figures

1.1 Vascular changes have been associated with neuronal dysfunction and neurodegenerative disease. Vascular risk factors such as hypertension and diabetes have been associated with changes in CBF and BBB permeability. Structural changes to the vasculature have also been measured. These changes can lead to hypoxia/ischaemia, impaired clearance of toxins and amyloid. Structural changes may be associated with impaired glucose and oxygen transport, as well as microbleeds. These changes can lead to neuronal damage and impaired cellular metabolism, possibly resulting in cell death and cognitive decline. Amyloid build up may cause further vascular damage (or can initiate vascular damage if one considers the amyloid-cascade hypothesis). Vascular changes and pathological processes overlap heavily. [1–6]. 29

2.1 Structure of cerebral capillaries. The lumen is surrounded by endothelial cells, which are joined together by tight junctions (not shown). The basement membrane and pericytes surround the endothelial cells. Astrocytic end feet surround the vessel. The endothelial cells contain mitochondria. Image from [1]. 33

2.2 **(a)** - early regional vascular dysfunction, including CBF disruption (reductions and dysregulation) and/or BBB breakdown (increased permeability and transporter dysfunction), which is commonly seen in several neurodegenerative diseases. In AD, early vascular changes are seen in the hippocampus and cortical regions. **(b)** - Sweeney et al. [3] update the hypothetical Jack model of AD biomarkers to include vascular dysfunction. The x axis represents disease progression over time. The y axis represents biomarker abnormality. Cognitive function is shown in blue. AD, Alzheimer's disease; PD, Parkinson's disease; HD, Huntington's disease; ALS, amyotrophic lateral sclerosis; MS, multiple sclerosis; CBF, cerebral blood flow; BBB, blood-brain-barrier; NCI, no cognitive impairment; MCI, mild cognitive impairment. Images from Sweeney et al. [3]. 34

2.3 Progression of characteristic cerebral small vessel disease (cSVD) pathology, visible using MRI, through time (left to right). Acute pathology such as infarcts and microbleeds can occur at any time. Infarcts, microbleeds and white matter hyperintensities can lead to cortical thinning and atrophy, which worsen through time, and eventually cause neurodegeneration and cognitive issues. BBB dysfunction may lead to oedema and inflammation. Image from Wardlaw et al. [7]. 39

2.4 Changes in microvascular structure. White backgrounds include healthy vessels, grey include changes in disease. Image from [5]. 44

3.1 The net magnetisation (blue arrow) parallel to B_0 due to an excess of protons in the spin-up state. Image sourced from [8]. 51

3.2 The NMR process; the longitudinal magnetisation precesses around the direction of the applied magnetic field; the application of a RF pulse along the x axis to force the magnetisation into the transverse plane; the transverse magnetisation starts to decay due to spin-spin interactions (dephasing) whilst the longitudinal magnetisation recovers due to spin-lattice interactions. Image sourced from [9]. 52

3.3 A spin echo pulse sequence (a). (b-g) are shown in the frame of reference of the spins. Spins are initially in phase after the 90 RF pulse (b), they dephase before application of the 180 RF pulse (c), the 180 Rf pulse is applied, reversing the phase (d), after which the spins dephase in what appears to be the opposite direction (e), which restores the net magnetisation, forming an echo (f), after which they dephase again (g). Image sourced from [8]. . . 54

3.4 A spin-echo MR sequence with localisation gradients. 55

3.5 A pulsed gradient spin-echo MR sequence. Two diffusion sensitising magnetic field gradients are applied for duration δ, amplitude G with time between them equal to Δ. Image sourced from [10]. 57

3.6 Diffusion-weighted MR images with increasing b-value. b= 10, 30, 50, 100, 200, 300, 500, 750 and 1000 smm^{-2} from left to right, moving down each row. 58

3.7 Flow-compensated (FC) and non-compensated (NC) spin echo (SE) sequences. G is the magnetic field gradient. ϕ is the phase. For static spins for both FC and NC, the phase is increased and decreased by equal amounts resulting in zero net phase shift. For spins with constant velocity, FC gradients result in a zero net phase shift. Note the quadratic dependence of phase on time. NC gradients do not null the signal from spins with constant velocity. Note spins that move and do not have constant velocity will result in a phase change for both FC and NC gradients. 59

3.8 Natural logarithm of the MR signal versus b-value. Three regions are shown corresponding to tissue properties accessible at the indicated b-values. At low b-values, information on the vasculature can be obtained. The vascular model most commonly used is the IVIM model. At mid b-values, information on cellularity can be obtained. Extravascular diffusion is considered Gaussian, and is modelled by a monoexponential model. At high b-values, information on tissue microstructures can be obtained since diffusion is non-Gaussian here. The b-values shown on the x-axis are typical values in the brain. However, they can vary depending on the tissue. Image sourced from [11]. . 62

3.9 A diffusion-weighted MR image (a) and its associated ADC map (b). The asterisks ($*$) represent an area affected by ischaemic stroke which is bright in the DWI and low in the ADC map compared to surrounding tissue, indicating decreased diffusion. Image sourced from Drake-Peréz et al. [12], under terms of Creative Commons license (http://creativecommons.org/licenses/by/4.0/.) 63

3.10 (A) If all spins in a voxel were to move coherently, there would be no phase dispersion and thus no effect on echo amplitude. This would result in a constant signal with b-value. (B) pure incoherent motions due to Brownian motion cause phase dispersion and a reduction in echo amplitude which increases with b-value. (C) in the microvasculature, a mixture of incoherent and coherent flow results in strong phase dispersion and a larger effect on echo amplitude. Again, this reduction increases with b-value. Image sourced from [13]. 66

4.1 Blood flow in a capillary network with capillary segment length, l, and average blood velocity, v: incoherent motion in the diffusive regime with long diffusion-times in (a) and in the ballistic regime with short diffusion-times (b). This image was adapted from Le Bihan et al. [14]. 81

4.2 Axial mid-brain slice DW-MR image across two b-values and one diffusion-time (a), region-of-interest (ROI) map, from the Schwarz et. al [15] rat atlas, overlaid on an axial mid-brain slice DW-MR image (b). Region 0: motor cortex; 1: parietal cortex; 2: hippocampus; 3: hypothalamus; 4: thalamus; 5: striatum; 6: corpus callosum; 7: temporal cortex; 8: entorhinal cortex; 9: cingulate cortex; 10: frontal cortex. 84

4.3 (a) A corrosion cast of a WKY rat – the circle of Willis is evident in blue. (b) and (c) show the volume render of reconstructed low resolution and high resolution μCT scans of the cast in (a) respectively. (d) shows the histogram of the capillary segment length l from the hippocampus and thalamus high resolution μCT scans. The median of each histogram is displayed in μm. The thalamus has a higher number of lower capillary segment lengths than the hippocampus- reflected in its lower median length of 13.5 μm compared to 17.0 μm 87

4.4 Regional average WKY MRI estimates of l ($\pm$ standard error of the mean) versus the median of the μCT estimates. Estimates are shown from three methods of velocity (v) estimation which then uses $D^* = vl/6$ to estimate l: the VA model (a), the VA ballistic (VAB) model (b) and the IVIM ballistic (IVIMB) model (c). The line of identity is displayed (blue), as is the regression line for each method (dashed black). Estimates for the striatum (S), thalamus (T), hypothalamus (HT) and hippocampus (H) are shown. . . 92

4.5 Regional averages ($\pm$ standard error of the mean) of velocity (v) and capillary segment length (l) for the two rat strains (F344 and WKY) for two different methods of parameter estimation: (a) and (c) for the VA model; and (b) and (d) for the VA ballistic model. Pearson's correlation coefficient, ρ is shown as well as the p-value which tests the hypothesis that there is no relationship between the observed parameters. Each point represents a different region. 93

4.6 (a) and (c) show F344 rat and region average (± standard error of the mean) for estimates of the velocity, v, and capillary segment length, l, for the velocity autocorrelation model (VA) and the VA ballistic model. l is calculated using the pseudo-diffusion coefficient (D^*) estimated using Δ=50 ms. (b) and (d) show the same for the WKY rat strain. The points are joined to show the relative values for each model more clearly. The values for the VA model are flat since all diffusion-times are used in parameter estimation. 95

4.7 The volume render (a), segmentation (b) and skeletonisation (c) of the reconstructed high resolution scan of the hippocampus. 101

4.8 The volume render and segmentation of the reconstructed high resolution scan of the hippocampus (a and b) and the thalamus (c and d). 102

4.9 Histograms of vessel diameter from the hippocampus (a), the thalamus (b), the hypothalamus (c) and the striatum (d). Median values: hippocampus – 2.93 μm, thalamus – 3.25 μm, hypothalamus – 3.97 μm, striatum – 3.58 μm. 103

5.1 The velocity-autocorrelation model when accounting for effects of trans-BBB-water-exchange (VAX) as a function of diffusion-time, Δ. The diffusion coefficient, D, was set to 7×10^{-4} mm^{2}s^{-1}; the velocity, v, was set to 1.3 mms^{-1}; the correlation time, T_0, was set to 19 ms; and the pulse gradient width, δ, set to 10 ms. The exchange time, τ, for each curve increases moving up the figure, indicating lower rates of exchange. 117

5.2 The grey matter (GM) and white matter (WM) parameter mean with standard error, for the perfusion fraction, f, in (a) and (d); the diffusion coefficient, D, in (b) and (e); and, the perfusion coefficient, k, in (c) and (f). Repeated-measures one-way analysis of variance (ANOVA) p-values are shown for each parameter. 119

5.3 Boxplots of the difference in AIC_c of the VAX and VA models for grey matter (GM) and white matter (WM). Paired sample t-tests between VAX and VA AIC_c values give p =0.29 and p =0.0028 for GM and WM respectively. 120

5.4 Parameter estimates of velocity (v), correlation time (T_0), capillary segment length (l) and the exchange time (τ) for two models (VA and VAX) for grey matter (GM) and white matter (WM). Plots for T_0 and l are close-up images with outliers for GM VA removed at T_0 = 0.819 s and l = 1567 μm. Red points show outliers, and blue lines, the mean. 122

5.5 (a) Table of minimum residual sum of squares (RSS) and associated τ values from the VAX model fits with stepped τ (0.005 step size) ranging from 0 to 1 s. The estimate of free τ for the VAX model is also shown. GM is grey matter and WM is white matter. (b) shows the plot of RSS versus stepped τ values for GM for 033. (c) shows the plot of RSS versus stepped τ value for WM for 023. 130

5.6 Mid-axial slices of diffusion-weighted (DW) MR images for three subjects (007, 008 and 023) with increasing b-value. b= 10, 30, 50, 100, 200, 300, 500, 750 and 1000 smm^{-2} moving from left to right. 131

5.7 Subject average normalised diffusion-weighted MRI signal (S/S_0) for white matter (WM) versus b-value for ten values of diffusion-time (Δ in ms). (a) shows the full b-value range, (b) shows the signal at low b-values and (c) shows the signal at high b-values. 132

5.8 Isolated perfusion signal (S/S_0–$(1-f)e^{-bD})/f$ versus diffusion-time (Δ) (data) and, VA (blue) and VAX (cyan) model fits. Multiple points at each diffusion-time represent the changing b-value. (a) and (b) show grey matter (GM) and white matter (WM) data respectively for subject 007, (c) and (d) show GM and WM data respectively for subject 008 and, (e) and (f) show GM and WM data for subject 023. 133

6.1 Hypercapnia acquisition. The MPRAGE was collected for regional segmentation. Arterial spin labelling (ASL) MRI was collected whilst subjects breathed normal air and CO_2 rich air to determine changes in cerebral blood flow and arterial transit time. Diffusion-weighted MRI (DWI) was collected for nine diffusion-times whilst subjects breathed normal air and CO_2 rich air to determine changes in IVIM parameters. There was an approximately 3 minute period between the baseline and hypercapnia acquisitions to reach a steady end-tidal CO_2 level. 139

6.2 Variation (%) in ASL and DW-MRI derived parameters from baseline (air) to hypercapnia (CO_2) scans. (a) shows cerebral blood flow (CBF) and (b) shows transit time (ATT). (c-e) show diffusive IVIM parameters. (c) shows the perfusion fraction (f), (d) shows the diffusion coefficient (D) and (e) shows the pseudo-diffusion coefficient (D^*). (f-g) show multi-diffusion-time IVIM parameters derived using the VA model. (f) shows the velocity (v) and (g) the correlation time (T_0). (h-i) show estimates of length derived using $l = 2vT_0$ ($l(T_0)$) in (h) and $l = 6D^*/v$ ($l(D^*)$) in (i). Black points show percentage variation for each subject (n=7), blue points show the mean and red points show outliers which lie outside of three median absolute deviations of the median. The plots for T_0 and both estimates of l are close ups and outliers are not shown at values of: T_0 GM:1390 % and WM:2090 % $l(D^*)$ GM:276 % and WM:363 % $l(T_0)$ GM:355 % and WM:610 %. . . . 147

6.3 Change in magnetisation ($\Delta M/M_0$) between control and labelled ASL images versus post labelling delay (PLD), for arterial transit time (ATT) 1.0-1.5 s (a and c) and 1.6-2.0 s (b and d) where (a) and (b) have varying labelling duration (LD) to approximately equalise the ASL signal at each PLD, and (c) and (d) have constant LD. 158

6.4 Mid-axial slices of diffusion-weighted (DW) MR images for subject 007 for baseline (first column) and hypercapnia (second column) scans. The third column shows the difference images between the two scans. Three different b-values are shown, moving down the rows, b= 10, 300 and 1000 smm^{-2}. . . 159

6.5 Subject average normalised diffusion-weighted MRI signal (S/S_0) for grey matter (GM) versus b-value for nine values of diffusion-time (Δ in ms). (a) shows the full b-value range, (b) shows the signal at low b-values and (c) shows the signal at high b-values. 160

6.6 Isolated perfusion signal $(S/S_0–(1-f)e^{-bD})/f$ versus diffusion-time (Δ) (data) and, VA (blue) and VAX (cyan) model fits. Multiple points at each diffusion-time represent the changing b-value. (a) and (b) show baseline and hypercapnia data for grey matter (GM) respectively for subject 006, (c) and (d) show baseline and hypercapnia data for GM respectively for subject 007. 161

6.7 Axial slices of cerebral blood flow (a) and arterial transit time (b) maps for subject 007 (left to right) for the baseline scan (top row) and hypercapnic scan (bottom row). 162

6.8 Boxplots of the difference in AIC_c of the VAX and VA models of baseline and hypercapnia DW-MRI data for (a) grey matter (GM) and (b) white matter (WM). Paired sample t-tests between VAX and VA AIC_c values give p=2.2e-05 and p=0.29 for baseline and hypercapnia data in GM respectively, and p=0.38 and p=0.20 for baseline and hypercapnia data in WM respectively. 163

6.9 The grey matter (GM) and white matter (WM) parameter means with standard error for baseline (blue) and hypercapnia (grey) data. Graphs show the perfusion fraction, f, in (a) and (d); the diffusion coefficient, D, in (b) and (e); and, the perfusion coefficient, k, in (c) and (f). The top row represents GM and the bottom, WM. Outliers removed outside of three median absolute deviations of the median for each diffusion-time. 164

6.10 165

6.10 Carbon dioxide (CO_2) levels (%) during the data acquisition for the seven subjects. The first approximately 30-35 minutes were with subjects breathing normal room air, followed by a 30 minutes period of subjects breathing CO_2. 166

6.11 Parameters with end-tidal CO_2 levels in grey (GM) and white (WM) matter, blue and orange respectively. (a) shows cerebral blood flow (CBF), (b) arterial arrival time (ATT), (c) perfusion fraction (f), (d) diffusion coefficient (D), (e) pseudo-diffusion coefficient (D^*), (f) average blood velocity (v), (g) correlation time (T_0), (h) and (i) show vessel segment lengths $l(T_0)$ and $l(D^*)$ which use $l = 2vT_0$ and $l = 6D^*/v$) respectively. 167

7.1 Regression plots of DW-MRI parameters against cardiovascular risk score (QRISK) and white matter lesion (WML) volume. Regions of interest were cortical grey matter (GM) and the hippocampus. Abbreviations: f, perfusion fraction; D, apparent diffusion coefficient of the extravascular space; D^*, pseudo-diffusion coefficient of the intravascular space; v, average blood velocity; and l, average vessel segment length. $^{**}p$ <0.05, $^{***}p$ <0.01, not corrected for multiple comparisons. 181

7.2 Perfusion fraction (f) correlated with Montreal Cognitive Assessment score (MoCA) for cortical grey matter (a) and the hippocampus (b). p=0.0066 and p=0.0052 respectively. 183

7.3 Mid-axial slices of diffusion-weighted (DW) MR images for four subjects for b= 10, 300 and 1000 smm^{-2} moving from left to right. Diffusion-time (Δ) is 49.89 ms. The top two rows show images for subjects diagnosed with mild cognitive impairment (005 and 006) and the bottom two rows for healthy subjects (009 and 010). 188

7.4 Subject average normalised diffusion-weighted MRI signal (S/S_0) for grey matter (GM) versus b-value for six values of diffusion-time (Δ in ms). (a) shows the full b-value range, (b) shows the signal at low b-values and (c) shows the signal at high b-values. 189

7.5 Isolated perfusion signal (S/S_0–$(1-f)e^{-bD})/f$ versus diffusion-time (Δ) (data) and, VA (blue) and VAX (cyan) model fits. Multiple points at each diffusion-time represent the changing b-value. (a) and (b) show grey matter (GM) data for subjects diagnosed with mild cognitive impairment (005 and 006) and, (c) and (d) show GM data for healthy subjects (009 and 010). . . 190

7.6 Regression plot of cardiovascular risk score (QRISK) with white matter lesion (WML) volume. p=0.013. 191

7.7 (a) average vessel segment length (l) for cortical grey matter estimated using $l = 6D^*/v$ and $l = 2vT_0$ ($l(T_0)$). (b) shows the point in (a) minus outliers (4 data points). 191

8.1 Estimating vessel segment length (l) using IVIM models. A biexponential model characterises extravascular diffusion (D, diffusion coefficient) and perfusion ($H(x)$). The perfusion fraction (f) quantifies the ratio of signal attenuation in each compartment. The diffusion-times (Δ) dictate which model is most appropriate. At short diffusion-times ($\Delta < T_0$), perfusion is characterised by ballistic flow, and ballistic models can be used to extract velocity (v). At long diffusion-times ($\Delta > T_0$), microvascular perfusion is characterised diffusive flow, and the diffusive IVIM model can be used to extract the pseudo-diffusion coefficient (D^*). The VA model can be fit across all diffusion-times to extract v and the correlation time (T_0). S is the DW-MRI signal, and S_0 is the signal with zero diffusion-weighting (b=0); b-value, describes diffusion sensitisation; k, perfusion attenuation coefficient. 194

A1 Mean parameter estimates ± standard deviation derived from 100 iterations of the diffusive IVIM signal with random noise at SNR levels between 20 and 1000. Parameter estimates are divided by true values, with exception of c which was set to zero in simulated signals. (a) shows the perfusion fraction (f), (b) the diffusion coefficient (D), (c) the pseudo-diffusion coefficient (D^*), (d) the parameter for improved fitting (c). Estimates for three b-value thresholds are shown: b=100 smm^{-2} (blue), b=200 smm^{-2} (orange) and b=300 smm^{-2} (yellow). Note that we use b=300 smm^{-2} in our data. 216

A2 Mean parameter estimates ± standard deviation derived from 100 iterations of the VA model signal with random noise at SNR levels between 20 and 1000. Parameter estimates are divided by true values, with exception of c which was set to zero in simulated signals. (a) shows the average blood velocity (v), (b) the average correlation time (T_0), (c) the parameter for improved fitting (c). Estimates for three b-value thresholds are shown: b=100 smm^{-2} (blue), b=200 smm^{-2} (orange) and b=300 smm^{-2} (yellow). Note that we use b=300 smm^{-2} in our data. 217

A3 Mean parameter estimates ± standard deviation over subjects versus b-value threshold. (a) shows the perfusion fraction (f), (b) the diffusion coefficient (D), (c) the pseudo-diffusion coefficient (D^*), (d) the average blood velocity (v), and (e) the average correlation time (T_0). 218
A4 Mean parameter estimates (± standard deviation) versus diffusion-time, derived from 100 random noise iterations, shown at SNR levels 500, 750 and 1000. Parameter estimates are divided by true values. (a) shows the perfusion fraction (f) and (b) the diffusion-coefficient (D). Estimates for the b=300 smm^{-2} threshold are shown. 219
A5 Mean parameter estimates ± standard deviation derived from 100 noise iterations of the diffusive IVIM model signal with random noise at SNR levels between 20 and 1000. Parameter estimates are divided by true values, with exception of c which was set to zero in simulated signals. (a) shows the perfusion fraction (f), (b) the diffusion coefficient (D), (c) the pseudo-diffusion coefficient (D^*), (d) the parameter for improved fitting (c). (e-h) are close-ups of parameter estimates at SNR 800-1000. Estimates for four methods of parameter estimation are shown: two-step fit with c (blue), two-step fit without c (orange), one-step fit with c (yellow) and one-step fit without c (purple). Plots for f and D for only show one two-step fit since c is in the intravascular term, thus does not affect these parameters. Note that we use the two-step fit with c in our data. 220
A6 Mean parameter estimates ± standard deviation derived from 100 iterations of the diffusive IVIM model signal with random noise at SNR levels between 20 and 1000. Parameter estimates are divided by true values, with exception of c which was set to zero in simulated signals. (a) shows the average blood velocity (v), (b) the average correlation time (T_0), (c) the additional parameter for improved fitting (c). Estimates for four methods of parameter estimation are shown: two-step fit with c (blue), two-step fit without c (orange), one-step fit with c (yellow) and one-step fit without c (purple). Note that we use the two-step fit with c in our data. 222

List of Tables

2.1 Table of MRI techniques used to image cerebrovascular changes and dysfunction in disease. A brief description of the technique and the pathology measured is included. TR, time to repetition; TE, time to echo; CSF, cerebrospinal fluid; SE, spin-echo. 36

3.1 Summary of biophysical models described which include a vascular compartment or allow for extraction of vascular parameters. The model name, equation number in the text, parameters obtained, blood flow regime validity and reference are listed. f is the perfusion fraction, where subscript fast and slow indicate the fraction for the fast and slow vascular compartments respectively; D is the diffusion coefficient; D^* is the pseudo-diffusion coefficient, where subscript fast and slow indicate the fraction for the fast and slow vascular compartments respectively; v is the average blood flow velocity; T_0 is the correlation time; l is the average vessel segment length; $\bar{D}$ is the mean pseudo-diffusivity ; σ is the pseudo-diffusion dispersion; a is a constant with units s^{-1}; CBV is the cerebral blood volume; Q is the mean vessel density; VSI is the vessel size index. 77

4.1 Coefficient of variation (%) of parameter estimates calculated from repeat measures. Results from five of the F344 strain. f – perfusion fraction, D – diffusion coefficient, D^* - pseudo diffusion coefficient (all from the IVIM diffusive model fit), v – average blood velocity (from the VA and VA ballistic models), l – capillary segment length (from $D^* = vl/6$). 91

4.2 F344 rat averages of the perfusion fraction (f), diffusion coefficient (D), pseudo-diffusion coefficient (D^*), velocity (v) and capillary segment length (l) for two models (VA – velocity autocorrelation model; and VA ballistic) with standard error of the mean. l is calculated using the relationship $D^* = vl/6$. 104

4.3 WKY rat averages of the perfusion fraction (f), diffusion coefficient (D), pseudo-diffusion coefficient (D^*), velocity (v) and capillary segment length (l) for two models (VA – velocity autocorrelation model; and VA ballistic) with standard error of the mean. l is calculated using the relationship $D^* = vl/6$. 105

4.4 Percentage outliers removed over all regions for each parameter and strain. D^* is the pseudo-diffusion coefficient and v is average blood velocity, from the velocity autocorrelation (VA) and VA ballistic models. 106

4.5 Repeated-measures two-way analysis of variance (ANOVA) p-values for the pseudo-diffusion coefficient (D^*), average blood velocity (v) and the average capillary segment length (l) for the velocity autocorrelation (VA) and VA ballistic models. 106

4.6 Voxel-wise signal to noise ratio (SNR) for four diffusion-times at $b = 10$ smm^{-2}, averaged across F344 rats using the mean ($\pm$ standard error of the mean). 107

5.1 Diffusion-times, Δ, and pulse durations, δ, used in the DW imaging protocol for ten participants. 113

5.2 Group mean values of the velocity (v), correlation time (T_0), capillary segment length (l) and the exchange time (τ) for two models (VA and VAX) with standard error of the mean, for grey matter (GM) and white matter (WM). 121

5.3 Intra-scan coefficient of variation (%) calculated from repeat measures of seven volunteers for the pseudo-diffusion coefficient (D^*), average velocity (v), correlation time (T_0), average capillary segment length (l) and the blood water exchange time (τ) for two models (VA and VAX). 123

5.4 Percentage outliers removed for the pseudo-diffusion coefficient (D^*), average velocity (v), correlation time (T_0), average vessel segment length (l) and the exchange time (τ) for two models (VA and VAX). 129

6.1 Diffusion-times, Δ, pulse durations, δ, used in the DW-MRI protocol. Due to scanner issues, participant 004 did not have diffusion-times 30.07 and 59.86 ms. 138

6.2 End-tidal CO_2 (%) $\pm$ standard deviation at baseline and with hypercapnia for each subject, and change in CO_2 (%). 145

6.3 Single diffusion-time (f, D, D^*) and multi-diffusion-time (T_0, v, l) IVIM parameters, and ASL derived parameters (CBF and ATT) for cortical grey matter (GM) for all volunteers and gas types. f perfusion fraction; D, diffusion coefficient; D^*, pseudo-diffusion coefficient; T_0, correlation time; v, blood velocity; $l(T_0)$, vessel segment length estimated using $l = 2vT_0$; $l(D^*)$, vessel segment length estimated using $l = 6D^*/v$; CBF, cerebral blood flow; ATT, arterial transit time. Outliers have been removed for the mean which lay outside of three median absolute deviations of the median. Outliers are highlighted in bold. Mean values $\pm$ standard error are show at the bottom. 148

6.4 Single diffusion-time (f, D, D^*) and multi-diffusion-time (T_0, v, l) IVIM parameters, and ASL derived parameters (CBF and ATT) for cerebral white matter (WM) for all volunteers and gas types. f perfusion fraction; D, diffusion coefficient; D^*, pseudo-diffusion coefficient; T_0, correlation time; v, blood velocity; $l(T_0)$, vessel segment length estimated using $l = 2vT_0$; $l(D^*)$, vessel segment length estimated using $l = 6D^*/v$; CBF, cerebral blood flow; ATT, arterial transit time. Outliers have been removed for the mean which lay outside of three median absolute deviations of the median. Outliers are highlighted in bold. Mean values $\pm$ standard error are show at the bottom. 149

6.5 p-values from repeated measures ANOVAs with region (GM/WM) and gas (baseline/ hypercapnia) as within subject factors. End-tidal CO_2 is input as a covariate. 150

7.1 Subject demographics, including; sex, age, Montreal Cognitive Assessment (MoCA) score, education, QRISK2-2017 score, Geriatric Depression Scale (GDS). Note: one participant had no amyloid status due to issues with the PET tracer (male; age 67 years; MoCA 23; education 10 years; QRISK 13.7). 172

7.2 Diffusion-times, Δ, pulse durations, δ, and b-values used in the DW-MRI protocol. 174

7.3 Inter-scan coefficient of variation (%) calculated from repeat measures of fourteen subjects for the perfusion fraction, f; diffusion coefficient, D; pseudo-diffusion coefficient, D^*; average velocity, v; and average vessel segment length, l. Regions of interest are cortical grey matter (GM) and the hippocampus. 179
7.4 Linear regression model outputs for the hippocampus with MoCA as dependent variable, and perfusion fraction (f), diffusion coefficient (D) and amyloid status as independent predictors. Effect size: ***large; **medium. Intercept coefficient: 42 182
7.5 Linear regression model outputs for cortical GM with MoCA as dependent variable, and perfusion fraction (f), diffusion coefficient (D) and amyloid status as independent predictors. Effect size: ***large; **medium. Intercept coefficient: 51 182
8.1 b-values used in each study presented and a selection of IVIM studies with their respective number of b-values and range of b-values. 207

A1 Voxel-wise SNR (± standard deviation), number of voxels per region (± standard deviation) and regional SNR averaged across subjects for diffusion-time 27 ms. 214
A2 One-step and two-step parameter estimates in grey matter (mean ± standard deviation) from in-vivo data collected in Chapter 5. f is the perfusion fraction, D is the diffusion coefficient, v is the average blood velocity and T_0 is the correlation time. Parameters are shown for three models for the one-step fit. Model 1 assumes no diffusion-time (Δ) dependence in the extravascular compartment. Model 2 assumes a linear diffusion-time dependence in f. Model 3 assumes a linear diffusion-time dependence in f, and D=$D_{inf} + A/\Delta$, where D_{inf} is the diffusion coefficient with infinite diffusion-time and A is a structural parameter [16]. Where a diffusion-time dependence is considered, presented values for f and D are from the longest diffusion-time. Two-step fitting is performed as desribed in chapter 5. . . . 223

Abbreviations

AD	Alzheimer's disease
ADC	Apparent diffusion coefficient
AIC	Akaike information criterion
ALS	Amyotrophic lateral sclerosis
ANOVA	Analysis of variance
ARRIVE	Animal research: reporting in vivo experiments
ASL	Arterial spin labelling
ATT	Arterial transit time
BBB	Blood-brain-barrier
BOLD	Blood oxygen level dependent
CAA	Cerebral amyloid angiopathy
CBF	Cerebral blood flow
CBV	Cerebral blood volume
CHARMED	Composite hindered and restricted model of diffusion
CNS	Central nervous system
COPD	Chronic obstructive pulmonary disease
CoV	Coefficient of variation
CSF	Cerebrospinal fluid
cSVD	Cerebral small vessel disease
CT	Computerised tomography
CTRW	Continuous-time random walk
CTTH	Capillary transit time heterogeneity
DCE	Dynamic contrast enhanced
DKI	Diffusion-kurtosis imaging
DNA	Deoxyribonucleic acid
DTI	Diffusion tensor imaging
DSC	Dynamic susceptibility contrast
DWI	Diffusion-weighted imaging
DW-MRI	Diffusion-weighted magnetic resonance imaging
FC	Flow compensated
FLAIR	Fluid attenuation inversion recovery
FM	Fractional motion
fMRI	Functional MRI
FROC	Fractional order calculus
GDS	Geriatric depression scale
GM	Cortical grey matter
GPA	Gaussian phase approximation
GRE	Gradient echo
HbA1c	Glycated haemoglobin
HD	Huntington's disease
ITK	Insight toolkit
IVIM	Intravoxel incoherent motion
JDR	Join dementia research

MCI	Mild cognitive impairment
MoCA	Montreal cognitive assessment
MPRAGE	Magnetisation prepared rapid gradient echo
MRA	Magnetic resonance angiography
MRI	Magnetic resonance imaging
MS	Multiple sclerosis
MTI	Magnetisation transfer imaging
MTT	Mean transit time
NC	Non-flow compensation
NFT	Neurofibrillary tangle
NMR	Nuclear magnetic resonance
NO	Nitric oxide
NODDI	Neurite orientation dispersion imaging
PD	Proton density
PD	Parkinson's disease
PET	Positron emission tomography
PGSE	Pulsed gradient spin echo
PLD	Post-label delay
PROMO	Prospective motion correction
RARE	Rapid acquisition with relaxation enhancement
RBC	Red blood cells
RF	Radiofrequency
ROI	Region of interest
ROS	Reactive oxygen species
RSI	Restriction spectrum imaging
RSS	Residual sum of squares
SE	Spin echo
SNR	Signal-to-noise ratio
SSE	Sum of squared errors
SWI	Susceptibility weighted imaging
TE	Time to echo
TI	Inversion time
TR	Time to repetition
VA	Velocity autocorrelation
VAB	Ballistic velocity autocorrelation
VASO	Vascular space occupancy
VAX	Velocity autocorrelation with exchange
VCI	Vascular cognitive impairment
VERDICT	Vascular, hindered and restricted diffusion for cytometry in tumours
VSI	Vessel size index
WKY	Wistar-Kyoto rats
WM	Cerebral white matter
WMH	White matter hyperintensities
WML	White matter lesions

Symbols

$\mathbf{J}$	Spin angular momentum
I	Spin quantum number
μ	Magnetic moment
$\hbar$	Reduced Planck's constant
$\mathbf{B_0}$	Static magnetic field
$\mathbf{M}$	Net magnetisation
γ	Gyromagnetic ratio
ω_0	Larmor frequency
$\mathbf{M}$	Net magnetisation
$\mathbf{M}_{\parallel}$	Net longitudinal magnetisation
$\mathbf{M}_{\perp}$	Net transverse magnetisation
t_{RF}	Duration of RF pulse
α	Flip angle
t_{RF}	Duration of radiofrequency pulse
ΔE	Change in energy
$\mathbf{B_1}$	Oscillating field
$\mathbf{G_z}$	Gradient field strength
T_1	Time taken for $\mathbf{M}_{\parallel}$ to recover by 63%
T_2	Time taken for $\mathbf{M}_{\perp}$ to reach 37% of its initial value
R_1	Relaxation rate $1/T_1$
R_2	Relaxation rate $1/T_2$
f	Perfusion fraction
f_f	Fraction of signal attenuation due to fast moving extravascular protons
f_s	Fraction of signal attenuation due to slow moving extravascular protons
f_{fast}	Fraction of signal attenuation due to fast blood flow
f_{slow}	Fraction of signal attenuation due to slow blood flow
f_{ex}	Volume fraction of spins entering the extravascular compartment due to water exchange
D	Diffusion coefficient
D_f	Diffusion coefficient of fast moving extravascular protons
D_s	Diffusion coefficient of slow moving extravascular protons
D_b	Diffusion coefficient of water in blood
D^*	Pseudo-diffusion coefficient
D^*_{fast}	Pseudo-diffusion coefficient of fast flowing blood
D^*_{slow}	Pseudo-diffusion coefficient of slow flowing blood
$\bar{D}$	Mean pseudo-diffusivity
σ	Pseudo-diffusion dispersion
k	Perfusion attenuation coefficient
v	Mean blood flow velocity
T_0	Correlation time
l	Mean vessel segment length
τ	Residence time of spins exchanging across the blood-brain barrier
S	Diffusion-weighted MRI signal, usually as a function of b (and sometimes Δ)
S_0	Diffusion-weighted signal at b=0

H	Intravascular signal attenuation, usually as a function of b (and sometimes Δ)
b	b-value, or sensitisation to diffusion
G	Magnitude of magnetic field gradient
Δ	Diffusion-time
δ	Diffusion pulse application time
Φ	Phase shift
ϕ	Phase
T	Total diffusion encoding time
Q	Mean vessel density
c	Parameter for improved fitting
a	Fractal model constant with units one over time
m	Flow weighting factor
ρ	Pearson's correlation coefficient

Abstract

'Measuring microvessel structure and function in the brain using magnetic resonance imaging.' A thesis submitted to The University of Manchester for the degree of Doctor of Philosophy by Lauren A Scott (2021).

Evidence supporting a link between cerebrovascular pathology and neurodegeneration is ever increasing. In-vivo studies of vascular pathology generally focus on measuring cerebrovascular dysfunction whilst changes to microvascular structure are not considered - likely due to the lack of established and validated methods of measuring structure in-vivo. However, these measures could have lower inter- and intra-measurement variability than functional measures and could even precede them in the pathological process. The work reported in this thesis aims to use multi-diffusion-time diffusion weighted (DW) magnetic resonance imaging (MRI) and intra-voxel incoherent motion (IVIM) modelling to derive measures of microvascular structure in the rat and the human brain. We aim to validate structural measures and determine the diagnostic potential in neurodegenerative disease.

In the rat brain, we show measures of vessel structure derived using the multi-diffusion-time velocity autocorrelation (VA) model of IVIM and its ballistic approximation (VAB) (valid at short diffusion-times), combined with the diffusive IVIM model (valid at long diffusion-times), have high accuracy when compared to measures derived from micro-CT imaging of a vascular corrosion cast in four brain regions. The perfusion fraction, diffusion coefficient, pseudo-diffusion coefficient, and blood velocity are also estimated. These values are consistent with literature.

In healthy volunteers, we demonstrate the diffusion-time dependence of diffusive IVIM parameters, which is generally not considered in literature. The VA model is found to accurately characterise the diffusion-time dependence of the intravascular DW-MRI signal in grey matter, but not white matter. We adapt the VA model to account for blood-brain barrier water exchange and find that it improves data characterisation in white matter. Using these models, we estimate vessel segment length in human data which agrees with the range presented in literature.

To determine the biophysical origin of VA and diffusive IVIM model parameters, we use a hypercapnic gas challenge and arterial spin labelling (ASL) measures of cerebral blood flow (CBF) and arterial transit time (ATT). Functional parameters were expected to change with hypercapnia, but vessel segment length was not. ATT decreased with gas challenge. No significant changes were found in other functional parameters (or in vessel segment length) with gas challenge. CBF, ATT, and blood velocity were associated with end-tidal CO_2 levels, irrespective of inhaled gas. This suggests that gas challenge did not modify end-tidal CO_2 enough to provoke a detectable cerebrovascular response. Results from the study are unclear. Increasing the number of subjects would help clarify.

Finally, we implement techniques in an elderly cohort to investigate the sensitivity of parameters to vascular disease and cognitive impairment. Vessel segment length is not altered in these pathologies. However, the perfusion fraction was significantly higher with vascular disease and worse cognitive performance. Increasing the number of subjects would also help clarify results in this study.

This work improves our understanding of diffusion-time dependent intravascular DW-MRI, and shows diffusion-time dependent models can characterise data and potentially produce accurate estimates of microvessel structure.

Declaration

No portion of the work referred to in the thesis has been submitted in support of an application for another degree or qualification of this or any other university or other institute of learning.

Copyright statement

- The author of this thesis (including any appendices and/or schedules to this thesis) owns certain copyright or related rights in it (the 'Copyright') and she has given The University of Manchester certain rights to use such Copyright, including for administrative purposes.

- Copies of this thesis, either in full or in extracts and whether in hard or electronic copy, may be made only in accordance with the Copyright, Designs and Patents Act 1988 (as amended) and regulations issued under it or, where appropriate, in accordance with licensing agreements which the University has from time to time. This page must form part of any such copies made.

- The ownership of certain Copyright, patents, designs, trade marks and other intellectual property (the 'Intellectual Property') and any reproductions of copyright works in the thesis, for example graphs and tables ('Reproductions'), which may be described in this thesis, may not be owned by the author and may be owned by third parties. Such Intellectual Property and Reproductions cannot and must not be made available for use without the prior written permission of the owner(s) of the relevant Intellectual Property and/or Reproductions.

- Further information on the conditions under which disclosure, publication and commercialisation of this thesis, the Copyright and any Intellectual Property University IP Policy (see `http://documents.manchester.ac.uk /display.aspx?DocID=24420`), in any relevant Thesis restriction declarations deposited in the University library, The University library's regulations (see `//www.library.manchester.ac.uk /about /regulations/`) and in The University's policy on Presentation of Theses.

Acknowledgements

To my amazing supervisors, I really cannot thank you enough. You have been so kind and patient throughout my entire PhD, and lots of fun to work with. Your enthusiasm and dedication to your work really has been inspiring. You have taught me so much and have made me a much better scientist. You also (miraculously) forced me to get over my fear of public speaking, one **very** painful presentation at a time. I am so grateful for all of your time and help (and also for sending me to Paris and Montreal - still a little sad about Sydney).

To all of the lovely volunteers who spent so many hours being scanned, without you this work would not have been possible. I have loved working with you all. Thank you to all of the research nurses who worked so hard on recruitment for the SIDD study, and to the radiographers and medics who helped collect our data. Our scanning sessions were so much fun, although I think I've probably eaten enough biscuits and Haribo to last a lifetime.

To all my MRC and public engagement buddies, you are all fabulous humans. Thank you for the happy memories and for being there to share a good moan. Finally, thank you to my lovely friends and fam who have supported me through what's starting to feel like endless studying (only a few more years, I promise!). You have tolerated my complaining so amazingly for the final couple of months and have supplied much needed distractions and cake.

Publications

Chapters 4-7 are based on the following papers:

- Scott LA, Dickie BR, Rawson SD, Coutts G, Burnett TL, Allan SM, Parker GJM, Parkes LM. Characterisation of microvessel blood velocity and segment length in the brain using multi-diffusion-time diffusion-weighted MRI. Journal of Cerebral Blood Flow and Metabolism. Dec 2020.
- Scott LA, Priest AN, McFadden J, Parkes LM, Dickie BR. Modelling the diffusion-time dependence of intravoxel incoherent motion in the brain: accounting for blood velocity, vessel length and water exchange. Preparing for resubmission to Magnetic Resonance in Medicine.
- Scott LA, Corfield DR, Sparasci O, Priest AN, Dickie BR, Parkes LM. Hypercapnia induced changes in multi-diffusion-time intravoxel incoherent motion imaging in the brain. Under preparation.
- Scott LA, McFadden J, Priest AN, Handley J, Sparasci O, Kyrtata N, Ahmed S, Emsley H, Matthews J, Parker GJM, Herholz K, Dickie BR, Parkes LM. Detecting microvascular dysfunction in cognitive impairment and vascular disease using intravoxel incoherent motion (IVIM) diffusion-weighted magnetic resonance imaging (DW-MRI). Under preparation.

Additional co-author publication:

- McFadden J, Matthews J, Scott LA, Parker GJM, Lohezic M, Parkes LM. Optimisation of Quantitative Susceptibility Mapping for regional estimation of oxygen extraction fraction in the brain. Magnetic Resonance in Medicine, In Press, Feb 2021.

Conference abstracts

The following conference abstracts were submitted relating to work presented in this thesis:

- Scott LA, Dickie BR, Burnett TL, Parker GJM, Allan SM, Parkes LM. Multi-diffusion-time DW-MRI detects altered microvessel structure in hypertensive rats. Presented at the 3rd UK Dementia MRI Conference, Cambridge, UK, 2018. Awarded best poster presentation.
- Scott LA, Dickie BR, Burnett TL, Rawson S, Coutts G, Parker GJM, Allan SM, Parkes LM. Multi-diffusion-time DWI to detect altered microvessel structure in a rat model of hypertension. In Proceedings of the 27th Annual Meeting of ISMRM, Montreal, Canada, 2019. Awarded ISMRM Magna Cum Laude.
- Scott LA, Dickie BR, McHugh D, McFadden J, Priest AN, Parkes LM. Characterisation of microvascular blood velocity, exchange and structure using multi-diffusion-time DWI. In Proceedings of the 28th Annual Meeting of ISMRM, Virtual Conference and Exhibition, 2020.

1 Introduction

1.1 Motivation

Patients with neurological disorders, including neurodegenerative disease, often have vascular comorbidities such as cerebral small vessel disease (cSVD) [17]. Vascular injury may contribute to the progression or development of neurological disease [1, 18–21]. Vascular changes may be part of a 'two-hit' process [1] whereby vascular damage leads to neuronal dysfunction or damage and subsequently, cognitive decline. For example, endothelial cell atrophy and loss of tight junctions in the capillary inner wall could increase movement of toxins across the blood-brain-barrier (BBB) [22]. Alterations in capillary blood flow may limit the extraction efficacy of oxygen in tissue which may lead to local ischaemia on a microscopic level [23–25]. Iadecola et al. [18] describe the process in reverse in Alzheimer's disease (AD), whereby accumulation of amyloid-beta plaques may have an avalanche effect on the vascular system. Build up of plaques may weaken vessel walls and increase BBB permeability, or cause haemorrhage which could lead to ischaemia/hypoxia, resulting in further reduced amyloid-beta clearance and increased vessel deformation. Figure 1.1 shows these vascular changes and how they may eventually cause neurodegeneration.

To date, most research on the cerebrovasculature in neurodegenerative disease has concentrated on changes in cerebral blood flow (CBF) and blood-brain-barrier (BBB) permeability [1, 4, 18, 19] where reductions in CBF and increased BBB permeability (increased leakiness) have been measured [1]. However, alterations in microvessel structure have also been observed [5, 6, 26]. For example, thin vessels, abnormal branching and increased tortuosity have been documented in AD [1, 5, 6]. A lack of accurate and validated measures of microvessel structure in-vivo means the impact of structural abnormalities in the microvascular network remains unclear.

Magnetic resonance imaging (MRI) allows for measurement of vascular function and may give access to parameters describing microvessel structure. MRI methods used to determine vascular function are well established and have been used extensively to investigate vascular pathology. For example, measuring CBF using arterial spin labelling (ASL), or vascular permeability using dynamic contrast enhanced (DCE) MRI. However, CBF is dependent on environmental factors such as anxiety and caffeine intake [27], and measurements generally have large variability and poor repeatability [28]. DCE methods use contrast agents which are contraindicated in some patients and some contrast agents may build up in the brain [29]. Measurements of microvessel structure may be less susceptible to biological and environmental factors than measures of function, and may precede functional changes [23].

Diffusion-weighted (DW) MRI is a clinically valuable tool used to non-invasively image the diffusion environment of water in the body. Clinical uses include tractography in white

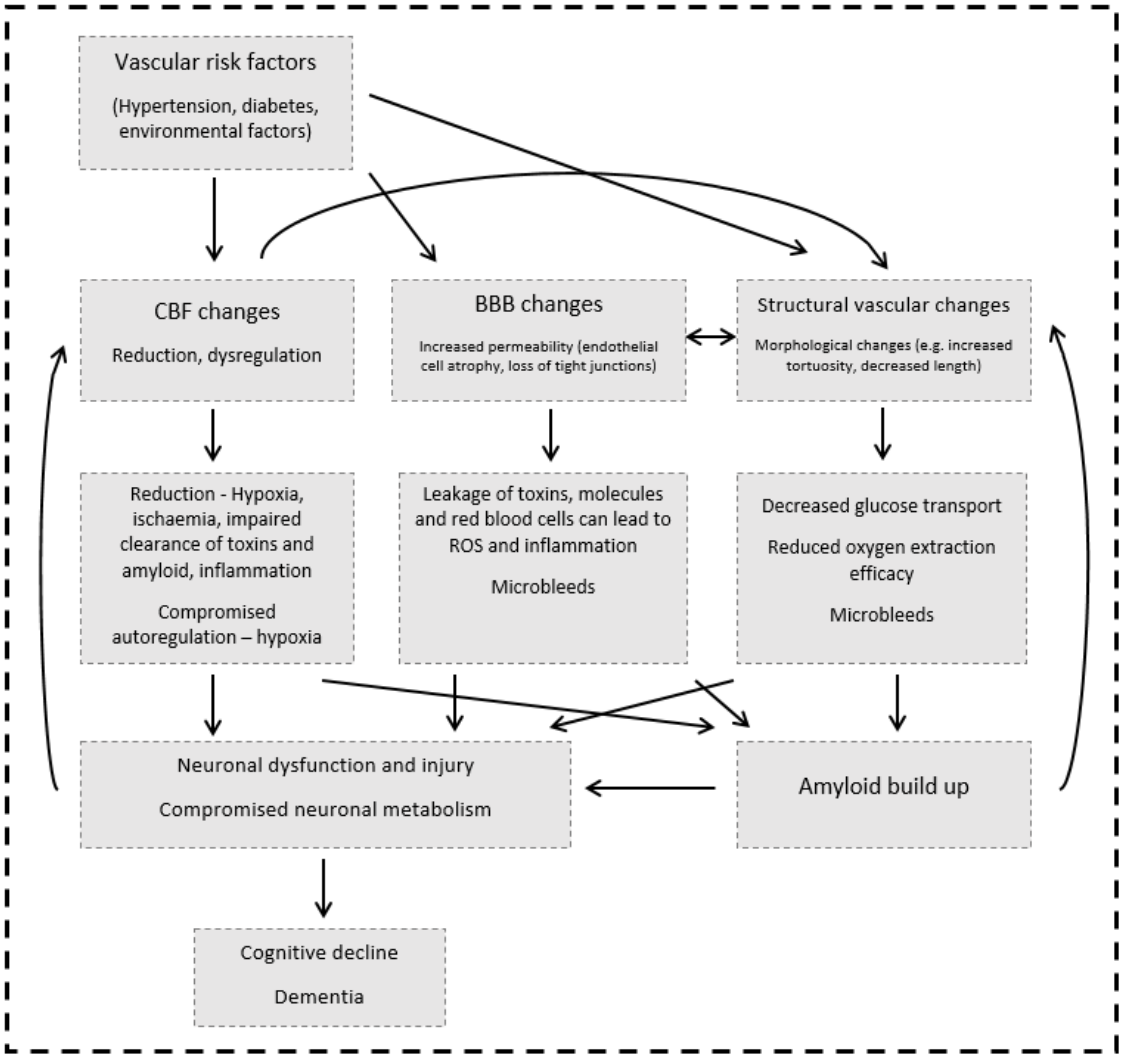

Figure 1.1: Vascular changes have been associated with neuronal dysfunction and neurodegenerative disease. Vascular risk factors such as hypertension and diabetes have been associated with changes in CBF and BBB permeability. Structural changes to the vasculature have also been measured. These changes can lead to hypoxia/ischaemia, impaired clearance of toxins and amyloid. Structural changes may be associated with impaired glucose and oxygen transport, as well as microbleeds. These changes can lead to neuronal damage and impaired cellular metabolism, possibly resulting in cell death and cognitive decline. Amyloid build up may cause further vascular damage (or can initiate vascular damage if one considers the amyloid-cascade hypothesis). Vascular changes and pathological processes overlap heavily. [1–6].

matter, tumour classification, and identification of infarction due to stroke [30–32]. In a typical DW-MRI acquisition, diffusion-sensitising gradients are applied which cause varying degrees of signal attenuation depending on the motion of water (i.e. direction and speed of motion). Attenuation of the DW-MRI signal is primarily thought to be a result of motion of water within the intravascular and extravascular compartments [14]. The rate of motion is higher in the intravascular compartment, meaning higher signal attenuation and more rapid decay of the DW-MRI signal with diffusion-weighting. Thus, the components can be isolated by varying diffusion sensitisation.

The DW-MRI signal can also be sensitised to water diffusion over different length scales by altering the diffusion-time over which the measurement is sensitive. Hence, information regarding tissue and vascular structure, such as fibre orientation, cell size, or vessel length could be extracted [16, 33, 34]. Whilst methods for investigating extravascular microstructure are fairly well established, current methods of measuring microvessel structure are scarce. The few that have been proposed have either not been validated [35] or have not been used in human subjects and rely on the use of contrast agents [36].

The work presented in this thesis seeks to develop and validate a non-invasive method of measuring microvessel structure. Preclinical studies were performed to enable validation of DW-MRI derived microvessel structure using micro-CT of corrosion casts. Measurements developed in the preclinical setting were translated onto clinical scanners and applied in healthy volunteers as part of further validation studies and model development. The measures were also assessed in aged patients with varying cognitive status (including healthy subjects, those with cognitive complaints, and those with mild cognitive impairment) and cardiovascular disease scores to investigate microvascular changes associated with dementia.

1.2 Thesis Overview

Chapter 2 and Chapter 3 provide background information and a review of current literature relevant to the project. Chapter 2 focuses on the biological concepts which motivate the work presented in this thesis. Vascular alterations in neurological and cerebrovascular disease are discussed, in particular in Alzheimer's disease, as well as those in vascular risk factors such as hypertension or diabetes. MRI methods of imaging the brain and perfusion are briefly reviewed. Chapter 3 focuses on the physical concepts and theory underlying the work presented in this thesis. The review discusses MRI and DW-MRI theory, and modelling of the DW-MRI signal to access vascular parameters.

Chapter 4 describes the initial use of DW-MRI models to extract parameters describing microvessel structure. DW-MRI data was collected in two rat strains with eight b-values and four diffusion-times. Standard and multi-diffusion-time IVIM models are fit to extract blood velocity and vessel segment length. The repeatability of parameters is assessed and

parameters are compared between rat strains. A vascular corrosion cast is produced from one rat from one strain, and the cast imaged using micro-CT. Vessel structure was assessed to validate MRI derived measures. Three models of extracting velocity and vessel segment length were compared and their accuracy and precision assessed.

To improve accuracy and precision of vascular parameter estimates, Chapter 5 focuses on model development. Specifically, this work investigates the diffusion-time dependence of the standard IVIM model parameters in detail and the effects of trans-BBB water exchange. Water exchange is considered negligible in IVIM studies in literature and, to the best of our knowledge, the effects on the IVIM signal have not been investigated. DW-MRI data was collected in ten healthy volunteers with ten b-values and ten diffusion-times. Multi-diffusion-time IVIM models are used to extract parameters quantifying vascular structure and parameter repeatability assessed for each model.

To further validate vascular parameters after model development in Chapter 5, Chapter 6 presents a hypercapnic gas challenge in human subjects. Changes in multi-diffusion-time DW-MRI derived vascular parameters are assessed in healthy subjects with two gases; normal air and carbon-dioxide rich air. ASL MRI is also used to determine changes in CBF and arterial transit time (ATT), to ensure changes with gas challenge were as predicted in literature (i.e increased CBF and decreased ATT). We hypothesised that parameters quantifying vascular structure would not alter, but those quantifying function would.

A key aim of this PhD is to investigate any changes to the cerebral microvascular network in neurodegenerative disease. Chapter 7 presents vascular parameters, extracted from multi-diffusion-time DW-MRI data using multi-diffusion-time and standard IVIM models, as well as amyloid-beta status and white matter lesion volume in an elderly cohort. Subjects were recruited with cognitive complaints, diagnoses of mild cognitive impairment (MCI) and no cognitive issues, as well as those with and without cardiovascular risk factors. A reduced protocol is used from that in Chapter 5, so repeatability of parameters is re-assessed. The correlation with cerebrovascular and cardiovascular health is assessed, and sensitivity to cognitive performance.

The thesis concludes with a discussion of findings, limitations and further work in Chapter 8. Ongoing work is presented in Appendix A.

The aims of this PhD are:

- To develop a non-invasive method of measuring microvessel structure in-vivo using diffusion-weighted magnetic resonance imaging.
- To comprehensively validate measures using vascular casts of the rat brain and hypercapnia challenge in humans.
- To investigate the link between microvascular structural measures and, vascular risk, amyloid and links to cognition, in the elderly population.

2 Evidence for microvascular changes and impact on neuronal function

2.1 Structure and function of the cerebrovascular network

Despite comprising around 2% of total body mass, the human brain is responsible for approximately 20% of the body's oxygen consumption and 25% of glucose consumption [2]. The supply of oxygen and nutrients, and removal of waste or toxins, is achieved through a vast network of blood vessels, reaching approximately 644 km in length [3], comprising arteries, arterioles, capillaries, venules and veins.

Blood is supplied to the brain via the carotid arteries. The largest vessels in the brain (cerebral arteries) branch out into smaller arteries and arterioles that sit on the surface of the brain (pial arteries). The pial arteries give rise to arterioles that enter the parenchyma. These penetrating vessels are separated from brain tissue by perivascular spaces filled with cerebrospinal fluid (CSF). The arteries and arterioles comprise endothelial and smooth muscle cells, amongst other cells, allowing for vasoconstriction and dilation. As we move deeper into the brain and vessels become progressively smaller, the perivascular space disappears, as do the smooth muscle cells. The vessels then come in to closer contact with tissue, separated by specialised layer of cells, and eventually become cerebral capillaries [37].

The nonfenestrated capillaries in the brain (and smaller arterioles/venules) have a series of properties which tightly regulate the movement of molecules, ions and cells between the vessel lumen and central nervous system (CNS). This is referred to as the blood-brain-barrier (BBB). The BBB protects the brain from toxins, pathogens, inflammation etc. [38]. The vessels comprise endothelial cells which surround the vessel lumen, these cells are further surrounded by pericytes and the basement membrane, followed by the basal lamina and astrocyte end feet. Figure 2.1 shows this structure. The endothelial cells are held together by tight junctions which have low permeability to large molecules [1, 38]. The density of capillaries within the brain is regionally heterogeneous and varies according to regional blood flow and metabolic demands [37]. After reaching the capillary bed, the vascular network becomes progressively larger. The capillaries branch out to venules which then become veins.

As well as delivering essential nutrients and oxygen, and removing waste, the vascular network also plays an important role in maintaining and regulating perfusion via neurovascular coupling, cerebral vasoreactivity and cerebral autoregulation [39]. Neurovascular coupling, or functional hyperaemia, is the mechanism by which adequate delivery of oxygen and nutrients is supplied to localised areas of neuronal activity [37]. Cerebral vasoreactivity is the mechanism by which blood flow alters in response to arterial CO_2 and O_2 levels [39].

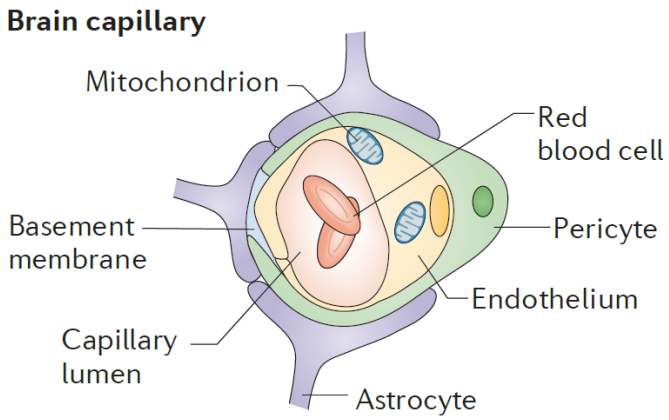

Figure 2.1: Structure of cerebral capillaries. The lumen is surrounded by endothelial cells, which are joined together by tight junctions (not shown). The basement membrane and pericytes surround the endothelial cells. Astrocytic end feet surround the vessel. The endothelial cells contain mitochondria. Image from [1].

For example, high CO_2 leads to vasodilation which increases cerebral blood flow. Cerebral autoregulation is the mechanism by which perfusion is regulated in response to changes in blood pressure that occur during normal day-to-day activities [39]. For example, postural changes can alter blood pressure and cerebral blood flow. This can be counteracted by vasoconstriction and dilation.

2.2 Alteration in disease

Disruption to cerebral blood flow (CBF) can cause cognitive dysfunction and cell death within minutes. The effects of ischaemic injury can continue for hours or even days after CBF disruption [40]. As such, it is unsurprising that an increasing number of studies evidence an association between vascular dysfunction and neurodegenerative disease.

Figure 2.2 shows the early involvement of vascular dysfunction (CBF and/or BBB disruption) in five neurodegenerative diseases. Subcortical regions are generally affected, with exception of AD, where large areas of the cortex have early vascular changes. The revised hypothetical model of AD progression is also shown, with vascular changes preceding characteristic AD biomarkers and brain atrophy [3].

There is great scope for further understanding the vascular mechanisms behind neurodegenerative disease, particularly with regards to microvascular structure. The following Chapter will review MR methods of imaging cerebrovascular pathology, vascular changes in cerebral small vessel disease (cSVD) and vascular dementia, as well as those in Alzheimer's disease, since it is thought to be the largest cause of dementia [1]. Vascular changes with modifiable risk factors are also discussed.

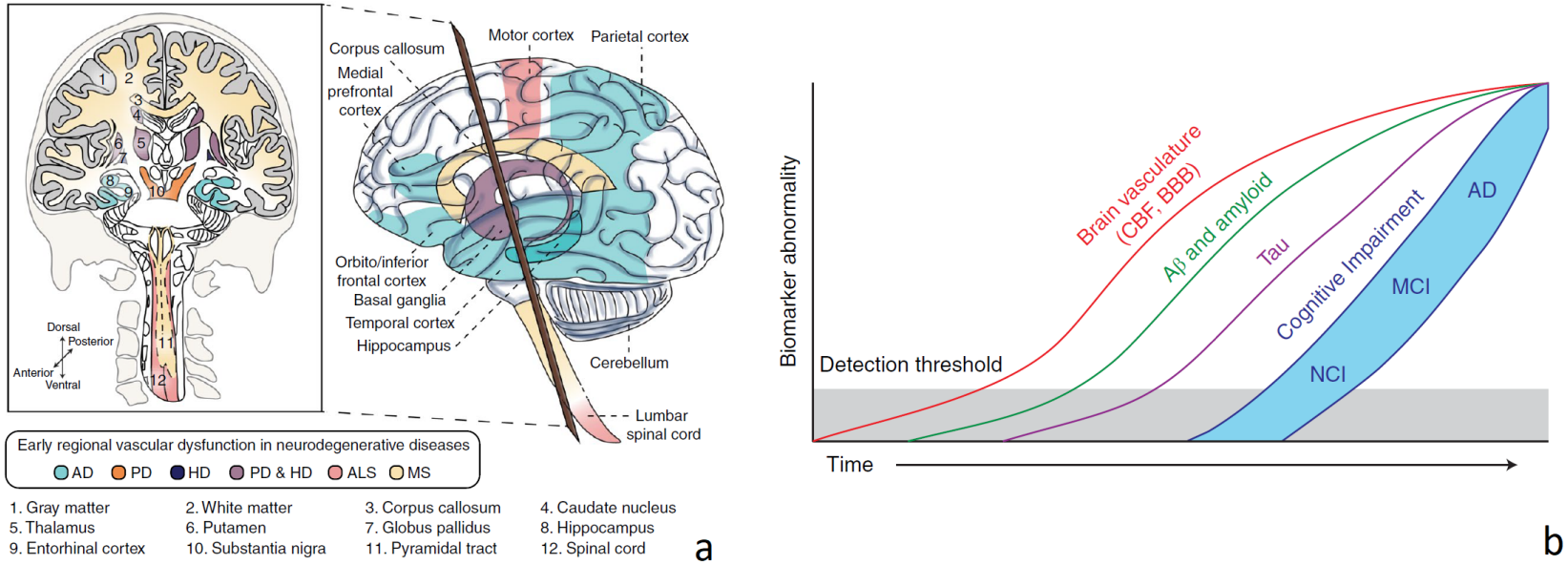

Figure 2.2: **(a)** - early regional vascular dysfunction, including CBF disruption (reductions and dysregulation) and/or BBB breakdown (increased permeability and transporter dysfunction), which is commonly seen in several neurodegenerative diseases. In AD, early vascular changes are seen in the hippocampus and cortical regions. **(b)** - Sweeney et al. [3] update the hypothetical Jack model of AD biomarkers to include vascular dysfunction. The x axis represents disease progression over time. The y axis represents biomarker abnormality. Cognitive function is shown in blue. AD, Alzheimer's disease; PD, Parkinson's disease; HD, Huntington's disease; ALS, amyotrophic lateral sclerosis; MS, multiple sclerosis; CBF, cerebral blood flow; BBB, blood-brain-barrier; NCI, no cognitive impairment; MCI, mild cognitive impairment. Images from Sweeney et al. [3].

2.2.1 MRI measures of cerebrovascular pathology

MR methods of imaging cerebrovascular pathology are listed in Table 2.1. Information is used from review papers by Wardlaw et al. [17], Blair et al. [41], Frantellizzi et al. [42] and Montagne et al. [43]. Information regarding imaging techniques is taken from books by McRobbie et al. [8] and Suetens [9].

Table 2.1: Table of MRI techniques used to image cerebrovascular changes and dysfunction in disease. A brief description of the technique and the pathology measured is included. TR, time to repetition; TE, time to echo; CSF, cerebrospinal fluid; SE, spin-echo.

Technique	**Acronym**	**Brief description**	**Pathology**
T_1-weighted		T_1 weighted MR images are structural or anatomical images. The short TR and TE mean fat has a high signal and CSF a low signal due to the different T_1 values (CSF has a longer T_1 than fat). White matter is brighter than grey matter.	Detection of atrophy and lacunes, white matter lesions (hypointense).
T_2-weighted		T_2 weighted MR images are structural or anatomical images. The long TR and TE mean CSF has a high signal and fat a lower signal, yet still bright, due to the different T_2 values (CSF has a longer T_2 than fat). Grey matter is brighter than white matter. The technique uses a SE readout sequence to remove effects of field inhomogeneities.	Detection of atrophy, white matter lesions (hyperintense), lacunes and infarcts.
T_2^* gradient echo	**T_2^*-GRE**	Similar to T_2-weighted images. However, since a GRE sequence is used, phase dispersion due to field inhomogeneities is present. The technique is useful for identifying bleeds due to the magnetic susceptibility of deoxyhaemoglobin and haemosiderin	Detection of haemorrhage and cerebral microbleeds.
Diffusion-weighted imaging	**DWI**	DWI uses additional bipolar magnetic field gradients to sensitise the MR signal to movement of water. The technique is particularly sensitive to necrosis or inflammation	Detection of acute ischaemic lesions and infarcts.

Fluid attenuation inversion recovery	**FLAIR**	FLAIR MRI nulls the signal from CSF, improving the ability to detect free water in the image. A 180° RF pulse is applied, before the initial 90° RF pulse, for a long enough time (TI; inversion time) such that the CSF signal is suppressed. Note if TI is short, fat is suppressed and the technique is referred to as STIR (short TI inversion recovery).	Detection of large subcortical infarcts and white matter lesions (hyperintense).
Magnetic resonance angiography	**MRA**	MRA images larger vessels and can be divided into dark and bright blood techniques. Dark blood techniques suppress the signal from flowing blood. Bright blood techniques are self-descriptive and can be achieved using contrast agents or the properties of the flowing blood itself.	Detection of stenosis and ischaemia.
Susceptibility weighted imaging	**SWI**	Similar to T_2^* weighted imaging, however the phase information is utilised which means blood products can be identified more easily. A 3D-GRE sequence is routinely used.	Detection of haemosiderin, a product of cerebral microbleeds, or superficial siderosis.
Dynamic contrast enhanced	**DCE**	DCE uses a contrast agent, most commonly gadolinium (Gd), to probe vascularity and perfusion of the brain. The technique first collects T_1-weighted images with varying flip-angle to compute the baseline T_1-weighted image, following which a series of T_1-weighted images are collected as the Gd bolus passes through the vasculature and accumulates in extracellular space. Gd is strongly paramagnetic and shortens T_1 resulting in increased signal where it accumulates.	Measurement of blood-brain barrier (BBB) permeability (K^{trans}).

Dynamic susceptibility contrast	**DSC**	DSC also uses a contrast agent, most commonly gadolinium (Gd), to probe vascularity and perfusion of the brain. The technique collects a series of T_2^*-weighted images as the Gd bolus passes through the vasculature only. Gd is strongly paramagnetic and decreases the T_2^* signal due susceptibility effects.	Measurement of cerebral blood volume (CBV), cerebral blood flow (CBF) and mean transit time (MTT) through vessels.
Arterial spin labelling	**ASL**	ASL uses endogenous water as a tracer, which is magnetically and proximally labelled with RF pulses. As these labelled protons perfuse, they saturate the tissue due to magnetisation exchange. This reduces the net longitudinal magnetisation and so the signal intensity in the labelled image relative to the non-labelled image. The reduction in signal intensity is proportional to perfusion.	Measurement of cerebral blood flow (CBF) and arterial transit time (ATT) of labelled blood to tissue.
Functional MRI	**fMRI**	fMRI measures dynamic signal change as a secondary effect to changes in neuronal activity. The primary fMRI method is BOLD-fMRI - blood oxygen level dependent. It uses the magnetic susceptibility of blood to measure changes in the T_2^* signal due to increase in perfusion to particular brain regions. An increase in blood flow alters the amount of oxy and deoxy-haemoglobin which are diamagnetic and paramagnetic respectively.	Measures blood flow response to stimuli.
Vascular space occupancy	**VASO**	VASO uses inversion recovery to null the blood signal, resulting in images of the extravascular tissue only. As blood flow increases in response to a stimulus, the signal decreases. A short TE is generally used to minimise BOLD effects. From the decrease in signal, the change in CBV can be derived.	Measures relative changes in CBV.

2.2.2 Small vessel disease and vascular dementia

Cerebral small vessel disease (cSVD) is an umbrella term for pathological processes of the small vessels in the brain [44]. It is the most common cause of vascular dementia, a contributor to dementia with mixed pathologies and the cause of approximately 20 % of strokes [4, 7, 17]. cSVD shares pathology and risk factors with AD, the most common cause of dementia [7, 17]. It can result in acute illness such as ischaemic stroke or can progressively lead to symptoms such as cognitive decline, depression, changes to gait, or loss of autonomy due to effects on parenchyma (Figure 2.3) [17, 45]. Patients may also be completely asymptomatic, and the disease isn't identified until neuroimaging examinations take place [17].

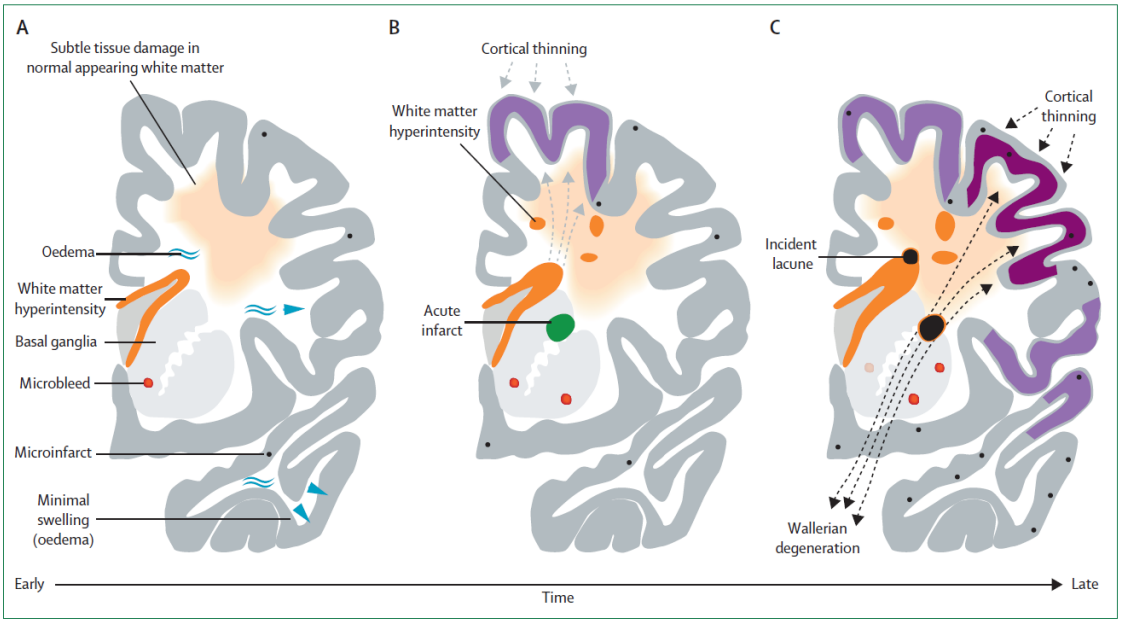

Figure 2.3: Progression of characteristic cerebral small vessel disease (cSVD) pathology, visible using MRI, through time (left to right). Acute pathology such as infarcts and microbleeds can occur at any time. Infarcts, microbleeds and white matter hyperintensities can lead to cortical thinning and atrophy, which worsen through time, and eventually cause neurodegeneration and cognitive issues. BBB dysfunction may lead to oedema and inflammation. Image from Wardlaw et al. [7].

2.2.2.1 Measurable clinical manifestations

Measured using MRI, clinical manifestations of cSVD include small subcortical infarcts, white matter hyperintensities (WMH), lacunes (of presumed vascular origin), enlarged perivascular spaces, cerebral microbleeds and atrophy [17]. These changes are shown in

Figure 2.3 [7] where pathology accumulates and worsens over time. Atrophy and Wallerian degeneration occur later in the cSVD timeline, after vascular pathology progresses. Acute pathology, such as infarcts and microbleeds, can occur at any time.

WMH (or leukoaraiosis) are white matter lesions with a hyperintense signal in T2-weighted or FLAIR MRI [17, 46, 47]. The pathogenesis of WMH is poorly understood [17], however some studies suggest they are ischaemic in origin as a result of vascular pathologies, for example arteriolosclerosis, vessel tortuosity or venous collagenosis. Others suggest induced cytotoxic and vasogenic oedema may be the cause, due to BBB leakage [47–50]. For more information regarding the mechanisms, see a review by Caunca et al. [49]. WMH are generally associated with demyelination and axonal loss, which can result in disruption of white matter networks [7, 47]. They were also shown to correlate with autoregulatory dysfunction and cognitive impairment [51].

Lacunes are small round, or ovoid, fluid filled cavities [17]. The cause of most lacunes is thought to be small subcortical infarcts [49]. However, some may be the result of small deep haemorrhages [52], lipohyalinosis or microatheroma [49]. Lacunes are often seen in elderly patients who are asymptomatic [17]. The FLAIR MRI signal will most commonly be hypointense with a surrounding rim of hyperintensity [17].

Small subcortical infarcts are recent infarctions in the region of a perforating arteriole [17]. They are thought to be associated with the occlusion of small arteries, although the mechanisms behind such occlusions are unclear [17]. Small subcortical infarcts have also been referred to as lacunar infarcts or infarctions, and lacunar strokes. However, not all small subcortical infarcts will become lacunes, so this terminology is not precise [17].

Perivascular spaces, also know as Virchow-Robin spaces [42, 49], are fluid filled cavities which follow the path of a vessel in either grey or white matter. They are thought to play a role in removing waste products from the brain, support interstitial fluid exchange and form part of the glymphatic system [7, 42]. Enlarged perivascular spaces indicate pathological changes. The cause of enlarged perivascular spaces is still under debate, however some research suggests they are a result of increased vascular permeability (impaired BBB function), obstruction of the glymphatic system or parenchymal atrophy [49, 53].

Cerebral microbleeds are self descriptive. In MRI, there is a signal void (approximately 2 to 10 mm in diameter) which is surrounded by a 'blooming' area that can be seen on methods sensitive to susceptibility [17]. MR visible lesions may correspond with haemosiderin-laden macrophages in perivascular tissue; evidence of blood cell leakage [17, 54]. Systemic inflammation is a proposed mechanism [49]. Lipofibrohyalinosis and cerebral amyloid angiopathy were strongly associated with cerebral microbleeds in a study by Shoamanesh et al. [54]. Østergaard et al. [55] discuss microstructural damage following the breakdown of haemogloblin after these microbleeds. Breakdown may result in the release of reactive oxygen species (ROS) which may deplete nitric oxide levels leading to vasoconstriction and

structural damage.

2.2.2.2 Age related cSVD

Older age is significantly associated with cSVD [50]. WMH are very common with older age [50] - it has been suggested that they are a 'neuroimaging correlate of age-associated disability' [45]. At age 75 years, patients with cSVD were twice as likely to develop dementia than those without [45]. Furthermore, age related cSVD is associated with cerebral amyloid angiopathy (CAA) [56] whose pathophysiology appears to interact with that of AD [57].

Changes in CBF and BBB permeability have been measured in the aged brain. Reductions in capillary density and CBF are prominent, as are string vessels (unused vessel remnants), in both animals and human brains with ageing [1, 4, 58–60], perhaps as a result of the reduction of brain volume and metabolic demand. Although, Chen et al. [59] find that 'regional effects of age on CBF differed from that of grey-matter atrophy', suggesting some other process is affecting CBF reductions. An increase in BBB permeability is described in review papers [1, 61]. Montagne et al. [62] demonstrate age dependent BBB breakdown in humans (i.e. increased permeability) in the hippocampus using DCE-MRI, a region associated with AD [3] (Figure 2.2). BBB integrity was maintained in other brain regions with ageing. Verheggen et al. [63] also use DCE-MRI to investigate BBB integrity in healthy middle to older age individuals. The authors demonstrate BBB leakage was significantly associated with older age in white and grey matter. Ohene et al. [64] also observe increased BBB permeability to water in older mice using ASL-MRI.

On a microvascular level, loop formations and increased tortuosity are found with increasing age [55, 58, 65]. A review by Brown et al. [58] discusses a decrease in in total capillary length with ageing, by up to 19%. A review by Farkas et al. [4] describes thickening of the basement membrane. Degradation of pericytes was also described [61, 66]. Kalaria et al. [67] also describe 'accumulation of extracellular matrix components' in the basement membrane, a decrease in density of mitochondria in endothelial cells (which could increase the number of string vessels [58]) and loosening of tight-junctions. Yang et al. [68] use histological techniques in mice to show that alteration of transport proteins in the BBB permitted passage of neurotoxic proteins to the parenchyma. The authors also demonstrate loss of pericyte coverage.

Effects of vessel wall degradation and impaired BBB function are likely to include microinfarcts, and impaired transport of nutrients and clearance of toxins. A dysfunctional endothelium also increases the likelihood of leukocyte adhesion. The accumulation of leukocytes may cause obstructions to blood flow and thus affect flow patterns or cause the release of ROS [69]. Disruption of the signalling between endothelial cells may reduce capillary control and as a result, blood flow may be redirected through the shortest

arteriolo-venular pathway (shunting), rather than perfusing tissue and providing nutrients [55]. Microvascular alterations may increase capillary transit time heterogeneity (CTTH), resulting in higher blood velocity in some capillaries meaning reduced oxygen extraction efficacy [69].

2.2.3 Alzheimer's disease

Alzheimer's disease (AD) is most commonly associated with two defining pathological features - the accumulation of amyloid-beta plaques and neurofibrillary tau tangles. The amyloid-cascade hypothesis was the dominant theory of cognitive decline in AD, whereby amyloid-beta accumulation lead to neuronal damage and cognitive deficit [70]. However, treatment to reduce amyloid-beta burden has been ineffective, in that it neither prevented cognitive decline nor reduced cognitive deficit [71, 72].

Despite AD being the major cause of dementia, post-mortem data suggests only 21% of patients have pure AD pathology [73]. Substantial evidence now links AD with cerebrovascular dysfunction, and vascular changes are increasingly recognised as a key AD pathology [1, 3, 6, 18, 19, 43, 70, 74, 75]. AD is also more prevalent in those with cardiovascular risk factors [76], further highlighting this link. The overlap between cerebrovascular dysfunction and neurodegenerative disease is complex, and the pathophysiology of the amyloid-vascular hypothesis is unclear.

There are two schools of thought pertaining to the hypothesis. Determining which factor comes first, whether vascular damage is a cause or result of AD is challenging [77]. Amyloid accumulation could have an avalanche effect on the vascular system, weakening the vessel walls and increasing the risk of leakage across the BBB. This could also lead to ischaemia or hypoxia which would further reduced amyloid clearance and increase vessel deformation [18]. Ni et al. [78] show that advanced cerebral amyloidosis in mice is associated with a decrease in cortical CBF. Amyloid accumulation could also have a damaging effect on the parenchyma, thus reducing the need for oxygen and other essential nutrients, reducing blood flow. Jiang et al. [79] find that patients with worse cognitive performance had lower oxygen extraction fraction (OEF), suggesting reduced metabolic need of parenchyma, which could lead to rarefaction of the vasculature.

Zlokovic et al. [1, 43] discuss the 'two-hit' hypothesis whereby AD onset is caused by primary damage to microcirculation ('hit one') leading to a cascade of pathological events including the accumulation of amyloid and eventually, neuronal dysfunction ('hit two'). Vascular risk factors cause vascular dysfunction and could contribute to 'hit one' of the two hit hypothesis [80]. Montagne et al. [43] discuss the contribution of an impaired BBB and inhibited CBF promoting amyloid and neurofibrillary hyperphosphorylated tau accumulation. The neurotoxic effects of these species could further impair vascular function

[43].

CBF reductions in AD are extensively described in literature [1, 3, 19, 81, 82]. Alterations in CBF may be a useful indicator of who will develop the disease [4, 77] or as a measure of severity of cognitive decline [83]. Hypoperfusion may occur in early pathology before any neuronal degradation [3, 19, 80, 84], particularly in areas with tau pathology [58], however not to the point where ischaemia occurs [76], indicating the reductions are not due to neuronal dysfunction. A study using the Alzheimer's disease neuroimaging initiative (ADNI) database [85] suggested CBF reductions occur before detectable changes in amyloid and tau. Leeuwis et al. [86] show that whilst a decrease in CBF (measured using ASL) was associated with worse cognitive performance in AD patients, it wasn't in patients with mild cognitive impairment (MCI) or those with subjective cognitive decline, perhaps suggesting pathological effects are limited by compensatory mechanisms early on.

Nielsen et al. [20] show patients with a diagnosis of MCI and amyloid accumulation (prodromal Alzheimer's disease) have widespread microvascular flow disturbances in addition to cortical hypoperfusion. The authors suggest the disturbances may be a result of capillary constriction, due to amyloid-beta effects on pericytes [87], or rarefaction. Using transcranial Doppler to measure CBF-velocity and a stand-sit manoeuvre to alter blood pressure, Abeelen et al. [88] measure impaired cerebrovascular autoregulation in patients with early AD compared to healthy controls. Impaired cerebral autoregulation has been associated with amyloid-beta deposition [70]. Neurovascular coupling may also be affected, a reduced CBF response was measured in hippocampal regions of AD patients during learning-related tasks [89].

BBB breakdown [62, 90, 91] is also featured prominently in literature. Montagne et al. [43, 62] demonstrate age dependent BBB breakdown in humans (i.e. increased permeability) in the hippocampus, which is more pronounced in patients with mild cognitive impairment. At a cellular level, Baloyannis and Baloyannis [6] found mitochondrial abnormalities in endothelial cells in the microvascular system. In vitro, pericytes have been shown to undergo degeneration when exposed to some amyloid-beta types [55]. BBB breakdown can lead to microbleeds, a manifestation of cSVD. The appearance of microbleeds is increased in AD [92] and appears to be associated with structural network alterations, as measured by diffusion-tensor MRI [93].

Functional changes (CBF and BBB) are generally the focus in literature with regards to vascular markers or mechanisms of AD. Less has been done on structural alterations in the microvasculature. Changes include rarefaction, a decrease in length and diameter, atrophic thin, string and fragmented vessels, glomerular loop formations, fusiform dilatations, abnormal branching, increased tortuosity and thickened basement membranes [4, 6, 18, 19, 84, 94]. Figure 2.4 shows some of these changes.

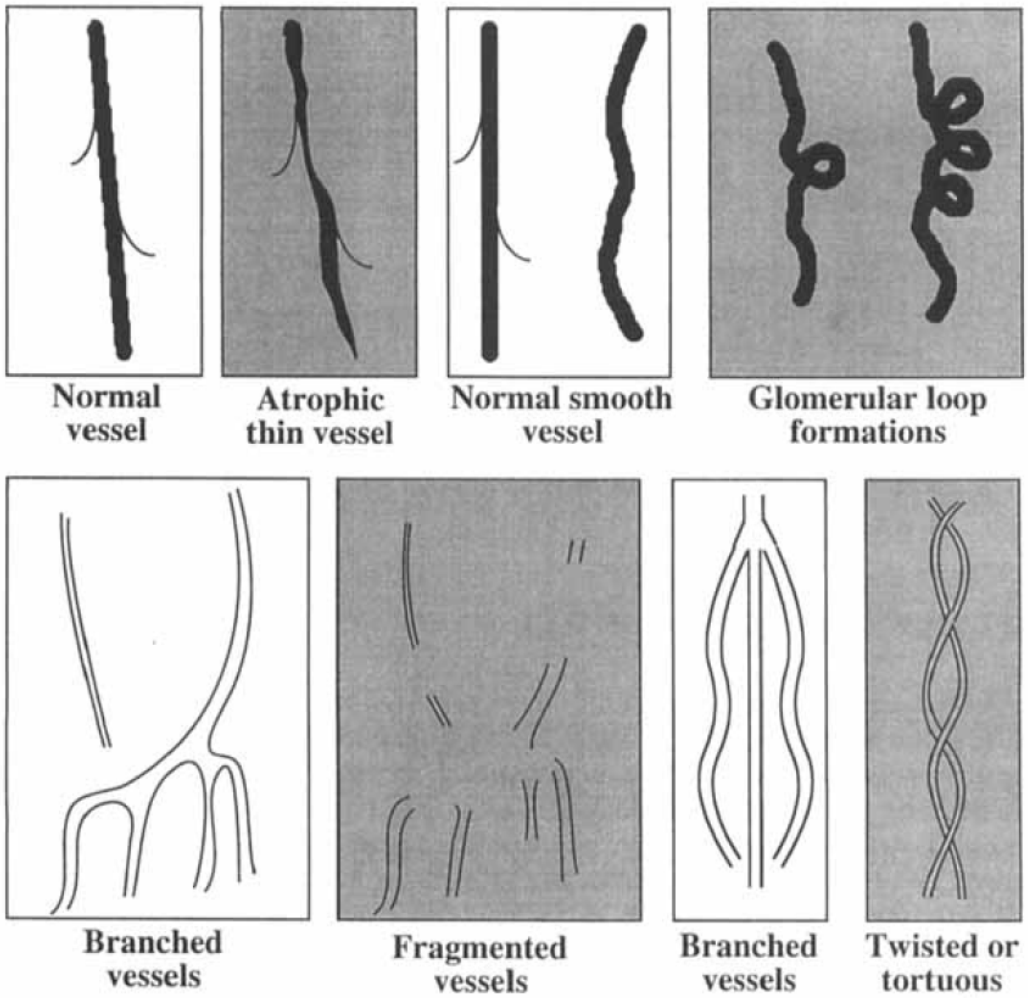

Figure 2.4: Changes in microvascular structure. White backgrounds include healthy vessels, grey include changes in disease. Image from [5].

2.3 Modifiable risk factors associated with microvascular changes

The following section discusses vascular risk factors and their effects on the cerebral vasculature. There are a multitude of risk factors, however the main contributors are age, hypertension and diabetes [95]. Effects of ageing were discussed in the cSVD section. Environmental factors are briefly discussed as, whilst they may cause hypertension and diabetes, they may also cause changes to the vascular network independently. Unfortunately, inherited conditions or genes may also cause vascular dysfunction (e.g. Fabry's disease which can cause deposits in vascular cells and the lumen [55]). These conditions result in similar vascular changes to the three main risk factors, albeit through different pathways [55]. These factors will not be discussed further.

2.3.1 Hypertension

'There is growing evidence that hypertension is the most important modifiable vascular risk factor for development and progression of both cognitive decline and dementia' [96]. Hypertension afflicts approximately 25% of the population. It is among the most common causes of small vessel pathology [69] and the major cause of stroke [97]. The impact of hypertension on cognitive function is well documented, it is associated with a range of cognitive deficits [98] - for example, impaired executive function, motor speed and attention [99]. It is a leading cause of vascular cognitive impairment (VCI) and can lead to vascular dementia, as well as being a risk factor for AD. There is evidence that those who have a history of hypertension around mid-life have a higher risk of developing dementia, AD in particular [98]. Atrophy, amyloid plaques and neurofibrillary tangles are increased in the brains of patients with a history of hypertension [97]. Additionally, hypertension may increase neurofibrillary tangles in the hippocampus of non-demented aged individuals [18].

Hypertension increases stress on artery walls [100]. Adaptive responses to hypertension in larger vessels aim to reduce stress on the vessel walls and to protect downstream vessels [97, 100]. Vessel remodelling can result in thicker walls and/or reduced lumen in arteries [101]. Vessel stiffening also occurs which decreases elasticity of the vessel walls. Without these adaptive mechanisms, alterations to the BBB [102], cerebral oedema and other pathologies can occur [97]. However, the alterations themselves can be damaging since they reduce the space through which blood can flow and increase resistance. The result is a greater susceptibility to vascular insufficiency, increased pulse pressure [101] and vessel occlusion, particularly since hypertension increases the risk for atherosclerotic plaques [97, 99]. Hypertension can also cause fibrinoid necrosis of arteries and arterioles supplying white matter, resulting in lacunes or haemorrhage [97].

Hypertension increases BBB permeability, this could be due to the mechanical stresses from increased pressure which result in cell damage [100]. Pires et al. [100] also suggest

that vascular remodelling may affect BBB integrity. For example, vessel wall thickening may require endothelial cell rearrangement and tight junction disruption. Additionally, ROS and inflammation could mediate BBB disruption [3].

Hypertension can impair functional hyperaemia [103] and resting CBF [99]. The normal increase in blood flow to regions of increased neuronal activity is attenuated in those with chronic hypertension. Furthermore, autoregulation is affected, with an increase in mean arterial pressure. This leads to ischaemia if blood pressure drops for any reason (e.g. postural hypotension) [40, 98]. Cerebrovascular reactivity may also decline with hypertension [7].

Effects on the microvasculature include increased vessel tortuosity [104] and rarefaction. As endothelial cells are damaged, the vessels become unperfused and eventually disappear [105] which can give rise to string vessels [58].

2.3.2 Diabetes

Both hypertension and diabetes are among the most common causes of small vessel pathology [69]. The incidence of both type 2 and type 1 diabetes are increasing [95]. The prevalence of cognitive dysfunction in patients is as high as 40% in those with poorly controlled or long-standing diabetes [95].

A review by Østergaard et al. [55] discusses changes in capillary morphology due to diabetes. The review mentions thickened basement membranes and pericyte loss [106]. Pericyte loss may be due to apoptosis caused by hyperglycaemic induced oxidative stress (i.e. excess of ROS). Pericytes are involved in several essential functions, such as regulation of angiogenesis, vessel maturation and remodelling, and maintenance of BBB integrity [107]. Hyperglycaemia may also result in endothelial dysfunction, causing a reduction in flow-mediated vasodilation and downstream effects of atherosclerosis [95]. The occlusion of small vessels can result in lacunar infarcts which are observed more frequently in diabetic patients than healthy controls [108]. The pericytes and endothelial cells form part of the BBB, damage to which can allow movement of molecules usually restricted from the brain.

Vascular disease in diabetes is associated with impaired autoregulation, determined from mean blood-flow velocity in the middle cerebral artery using a transcranial Doppler probe [95, 109]. Some studies demonstrated region-dependent CBF changes in type 1 diabetics [95]. Altered CBF was correlated with poor glycaemic control (indicated by elevated HbA1c, a marker of blood sugar control) [110]. Last et al. [111] show reduced grey and white matter volumes in type 2 diabetic patients as well as reduced baseline regional CBF and carbon dioxide reactivity. This was also associated with higher HbA1c. Increases in blood viscosity were also identified in patients with diabetes which was found to correlate with the degree of microvascular complications [25, 55].

2.3.3 Environmental factors

Lifestyle choices including smoking, nutrition and low levels of physical activity can result in vascular dysfunction. Consumption of a high cholesterol diet can cause hypercholesterolemia [112], which increases the risk of ischaemic stroke and may cause cSVD by impairing the vasodilatory response and causing inflammation [113]. A high salt diet is associated with hypertension [112]. The pathophysiological mechanism is debated in literature, however evidence indicates effects of water retention [114]. Saturated fat intake is associated with diabetes and its complications [112]. A high saturated fat diet has been positively correlated with brain lesion volume [115]. Exercise decreases blood pressure, blood coagulation, systemic inflammation, insulin resistance, and low-density-lipids (atherogenic cholesterol) [112, 116]. A lack of exercise thus increases risk and can lead to obesity. Studies in rats show obesity impairs functional hyperaemia by affecting endothelial cell function [117]. Evidence shows CBF is reduced in obese patients [118].

Although smoking is predominantly associated with lung cancer and respiratory disease, almost 50% of premature deaths from smoking are due to cardiovascular disease [112]. Smoking can increase blood viscosity, a risk factor for vascular dementia and stroke [116]. Smoking is associated with oxidative stress which could affect endothelial cells by affecting nitric oxide availability. ROS in cigarette smoke can cause direct damage to endothelial cells, further impairing vasodilation [119].

Air pollution has been linked to premature mortality due to cardiovascular disease [120]. Strong evidence suggests that chronic exposure to air pollution can increase the progression of atherosclerosis, affect endothelial function and cause hypertension. The mechanism through which these effects are caused are not clear, however it is suggested that exposure to air pollution induces oxidative stress and inflammation [112, 121].

2.4 Impact of altered vascular network on neuronal function

A review by Østergaard et al. [55] suggests that progressive microvessel dysfunction can lead to irreversible damage to parenchyma, caused by chronic effects of vascular risk factors. Vascular risk factors can damage the cerebral vasculature, resulting in impaired CBF and BBB permeability (Figure 1.1) [3]. This can lead to downstream effects such as mitochondrial deficiency, oxidative stress, protein degradation or amyloid accumulation [122].

BBB breakdown is linked to pathological substance entry to the brain and impaired amyloid clearance [19]. Zlokovic et al. [1] examine the literature regarding BBB dysfunction in neurodegenerative disease, and describe the loss of pericytes which impairs BBB function and leads to accumulation of molecules usually restricted from the brain. For example, the release of red blood cells into the parenchyma can cause the release of ROS [1]. An excess

of ROS can lead to oxidative damage and neuron death [123]. The release of albumin across the BBB can lead to oedema which can contribute to hypoxia by restricting blood supply to the tissue [1]. Neurotoxic proteins may also enter the brain. The BBB comprises many components, impairment or damage to which could affect neuronal function. For example, reduced expression of glucose transporters could impair glucose delivery and affect cellular respiration [124].

De la Torre et al. [94] describe a critical threshold for CBF, below which the microvasculature is damaged and regulation of nitric oxide is impaired. Reduced nitric oxide levels can damage endothelial cells by restricting changes in cell shape, meaning nutrient delivery is compromised resulting in a 'dysfunction metabolic cascade' which affects the aerobic respiration pathway. Reduced CBF can result in ischaemia/hypoxia, an obvious effect of which is reduced availability of oxygen for cellular respiration. An additional downstream effect may also include inflammation, which can stimulate the formation of amyloid-beta plaques and neurofibrillary tangles in AD [69, 76]. As discussed previously, hypoxia can also cause release of ROS from the mitochondria, creating an excess (oxidative stress), which can damage endothelial cells [125] and neurons of high metabolic activity. This is via damage to the mitochondrial nucleus or apoptosis [126]. Capillary rarefaction or damage could increase the distance between vessels and cells meaning oxygen, glucose etc. have further to travel and might not reach cells [127, 128].

Østergaard et al. [76] show correlation between increased capillary transit time heterogeneity (CTTH), and cortical thinning and reduced glucose metabolism. Patients with elevated CTTH and lower tissue oxygen tension (local oxygen availability for metabolic demands) [22, 23] are associated with worse cognitive function.

3 Diffusion-weighted MRI methods to probe microvessel structure

Evidence linking vascular changes to neurodegenerative disease is substantial and consistent. Most effort in-vivo has focused on measuring vascular function (i.e. CBF and BBB permeability) rather than structure, likely due to the lack of validated methods of measuring microvascular structure in-vivo. Structural and organisational changes have been measured in disease histologically. By measuring structural changes in-vivo, as well as functional changes, there is potential to identify additional biomarkers and gain a greater understanding of the mechanisms of disease onset and progression. Non-invasive techniques (e.g. MRI) allowing for microvascular characterisation, in particular structural and organisational aspects, are needed.

Diffusion-weighted (DW) MRI non-invasively images the movement of protons in water in the body. The DW-MRI signal can be sensitised to movement over different length scales. Information regarding tissue and microvascular structure, such as fibre orientation, cell size, or vessel length, can be extracted [16, 33, 34]. Complex modelling of the signal attenuation with diffusion-weighting is required to extract structural parameters due to limited spatial resolution.

This Chapter will give a brief overview of MRI theory, DW-MRI theory and the biophysical models describing the DW-MRI signal, some of which allow derivation of parameters quantifying vessel structure.

3.1 MRI

MRI had its beginnings in the 1970s, and has since become a powerful imaging technique, integral to modern day clinical care. The technique is sensitive to protons in the body which can be excited and detected by magnetic fields. Three types of magnetic field are used: the main static field which creates a net magnetisation; the gradient fields which are used for spatial localisation; and the oscillating radiofrequency field [8]. When radiofrequency energy is applied via a transmitter coil, protons are excited and precess in phase, the subsequent dephasing is measured by a receiver coil. The following section will discuss the theory in more detail and the process of producing an image.

The MRI theory in the following section is sourced from McRobbie et al. [8], Suetens et al. [9] and Buxton et al. [129].

3.1.1 Nuclear magnetic resonance

The atomic nucleus comprises protons and neutrons (nucleons) which have an intrinsic quantum mechanical property named spin angular momentum, $\mathbf{J}$. The spin angular

momentum can be described in terms of the spin quantum number, I. For protons and neutrons, $I = 1/2$. Atomic nuclei with an odd number of nucleons, or an even number comprising both odd numbers of protons and neutrons, have non-zero spin. These nuclei may experience nuclear magnetic resonance (NMR). Primarily, MRI focuses on the hydrogen nucleus (^{1}H) with $I = 1/2$, due to its abundance in organic tissue. Associated with the spin angular momentum is the magnetic moment, $\boldsymbol{\mu}$. The magnetic moment is related to J and I by: $\boldsymbol{\mu} = \gamma \mathbf{J} = \gamma\hbar\sqrt{I(I+1)}$, where γ is the gyromagnetic ratio, a constant which varies for different nuclei, and $\hbar$ is the reduced Planck's constant ($h/2\pi$).

The net magnetisation ($\mathbf{M}$) of a tissue is the sum of magnetic moments, $\mathbf{M} = \sum_{i=1}^{N} \boldsymbol{\mu_i}$ where N is the number of nuclei. In the absence of an external magnetic field, the nuclei in a tissue sample have random orientation, and $\mathbf{M} = 0$. In the presence of an externally applied magnetic field, $\mathbf{B_0}$, the spin angular momentum of the nuclei is quantised, giving $2I + 1$ eigenstates. If one considers the hydrogen nucleus, only two eigenstates are created; a spin-up and spin-down state. This process is known as the Zeeman effect.

The spin-up state is lower energy and lies parallel to $\mathbf{B_0}$, whereas the higher energy spin-down state is anti-parallel to $\mathbf{B_0}$. The magnetic moments of the protons precess around the axis of $\mathbf{B_0}$ due to torque produced by the applied field. The frequency of precession depends on the chemical environment and $\mathbf{B_0}$, and is known as the Larmor frequency (ω_0):

$$\omega_0 = \gamma \mathbf{B_0}. \tag{3.1}$$

The Boltzmann distribution shows that, statistically, there is a slightly higher probability of a proton being in the spin-up state at room temperature (293 K). The excess of spin-up states causes a small net longitudinal magnetisation ($\mathbf{M}_{\parallel}$) parallel to $\mathbf{B_0}$ (Figure 3.1). The difference in energy, ΔE, between the two eigenstates is proportional to the applied field ($\mathbf{B_0}$), and is thus also proportional to the Larmor frequency: $\Delta E = \hbar\omega_0$.

3.1.2 Generating a signal

To detect the net magnetisation, it needs to be tipped into a plane where it is measurable. To achieve this, a second weaker magnetic field is applied perpendicular to $\mathbf{B_0}$. An oscillating field ($\mathbf{B_1}$) is applied using a radiofrequency (RF) pulse with Larmor frequency ω_0. The RF pulse provides the energy required for the protons to change quantum state, increasing the likelihood that a proton is in the spin-down state (higher energy state). This effectively tips the net magnetisation towards the transverse plane (Figure 3.2). The protons precess around the axis of B_1 and the net magnetisation oscillates around B_0. The angle by which the magnetisation will change is called the flip angle, α. This reduces the component of M parallel to B_0 ($\mathbf{M}_{\parallel}$) by a factor $\cos\alpha$. The flip angle is dependent on the duration of the RF pulse (t_{RF}) and the B_1 field: $\alpha = \gamma t_{RF} B_1$. Most commonly, 90 degree

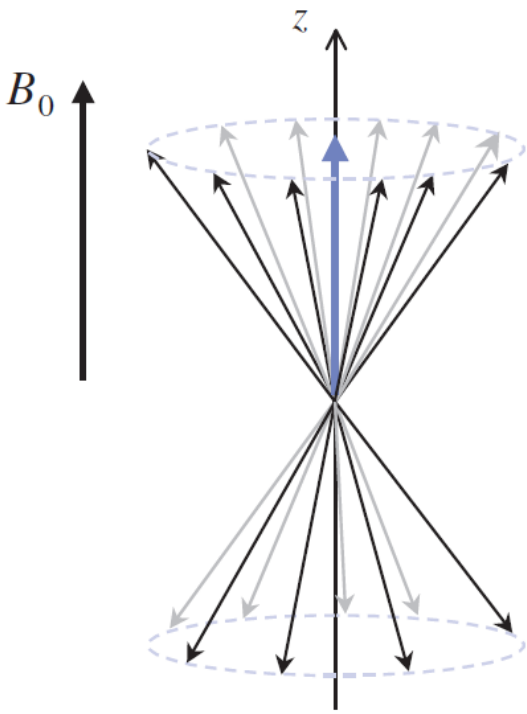

Figure 3.1: The net magnetisation (blue arrow) parallel to B_0 due to an excess of protons in the spin-up state. Image sourced from [8].

and 180 degree RF pulses are used.

The oscillation of the net magnetisation around B_0 means it can be detected, since it induces a current in receiver coils via electromagnetic induction as dictated by Faraday's law.

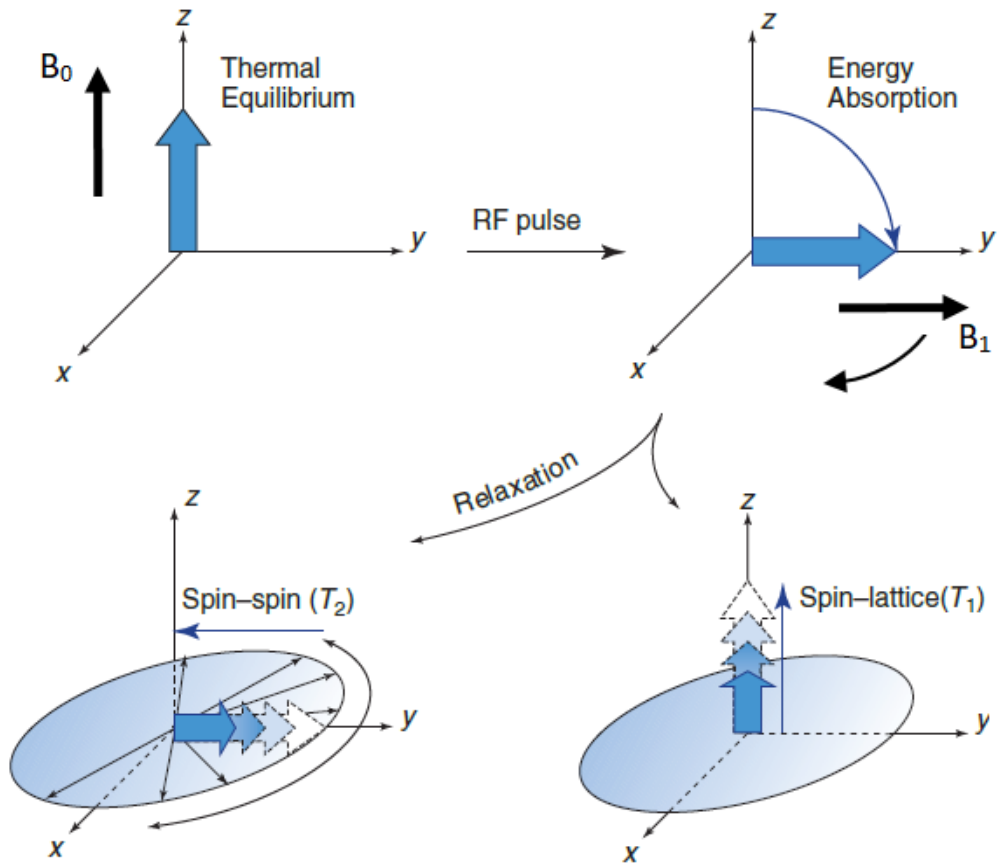

Figure 3.2: The NMR process; the longitudinal magnetisation precesses around the direction of the applied magnetic field; the application of a RF pulse along the x axis to force the magnetisation into the transverse plane; the transverse magnetisation starts to decay due to spin-spin interactions (dephasing) whilst the longitudinal magnetisation recovers due to spin-lattice interactions. Image sourced from [9].

When the application of the RF pulse ends, the protons dephase in the transverse plane and decay in the longitudinal plane (Figure 3.2). The dephasing causes a free induction decay of $\mathbf{M}_{\perp}$. The processes contributing to dephasing are: differing chemical environments and magnetic susceptibility of tissues producing magnetic field inhomogeneities, spin-spin interactions, and dephasing by magnetic field gradients. The rate of dephasing is governed by the time constant T_2. The protons do not lose energy whilst dephasing, they lose energy

in the decay back to alignment with $\mathbf{B_0}$. They do this via interaction with surrounding tissues (spin-lattice interactions), which can absorb energy and disperse it via blood flow.

The dephasing of the transverse magnetisation, $\mathbf{M}_\perp$, can be described by:

$$\mathbf{M}_\perp = \mathbf{M_0} e^{-i\omega t} e^{-t/T_2}, \tag{3.2}$$

where t is the time from the application of the RF pulse, and T_2 is the time for $\mathbf{M}_\perp$ to reach 37% of its initial value.

Inhomogeneities in the static field mean that the decay is faster than predicted if only intrinsic T_2 processes are considered. This is characterised by T_2^* and can be corrected for using spin-echo pulse sequences. For spin echo sequences, two RF pulses are used; 90 degree and 180 degree. The 90 degree RF pulse tips the net magnetisation into the axis of $\mathbf{B_1}$, perpendicular to $\mathbf{B_0}$. The 180 degree RF pulse tips the magnetisation anti-parallel to its original angle, producing a spin echo (Figure 3.3). The 180 RF pulse reverses dephasing caused by inhomogeneities, recovering T_2. Since the precession of the transverse magnetisation induces currents in the receiver coil, T_2 relaxation limits the time over which we have a measurable signal.

The recovery of $\mathbf{M}_\parallel$ grows exponentially and can be described by:

$$\mathbf{M}_\parallel = \mathbf{M_0}(1 - e^{-t/T_1}) \tag{3.3}$$

where T_1 is the time taken for $\mathbf{M}_\parallel$ to recover by 63%. T_1 relaxation needs to be considered when applying multiple RF pulses, since it will determine the availability of $\mathbf{M}_\parallel$ for the next excitation.

3.1.3 Spatial localisation

To form an MR image, the signal needs to be localised to individual voxels. Localisation is achieved in three orthogonal directions using a linear magnetic field gradient for each dimension. The data in this thesis is acquired through multiple two dimensional slices along a third dimension. This method will be discussed here, however it is worth noting that a three dimensional volume can be collected using slightly different localisation gradients.

Slice selection is first achieved using a magnetic field gradient along the z direction. Using the field gradient ($\mathbf{G_z}$) alters the Larmor frequency (Equation 3.1) such that it becomes a function of position along the z axis:

$$\omega_0(z) = \gamma(\mathbf{B_0} + z\mathbf{G_z}). \tag{3.4}$$

Using a bandwidth-limited RF pulse centred on the Larmor frequency of a small section of the gradient, a slice of protons can be excited. Only spins precessing at frequencies

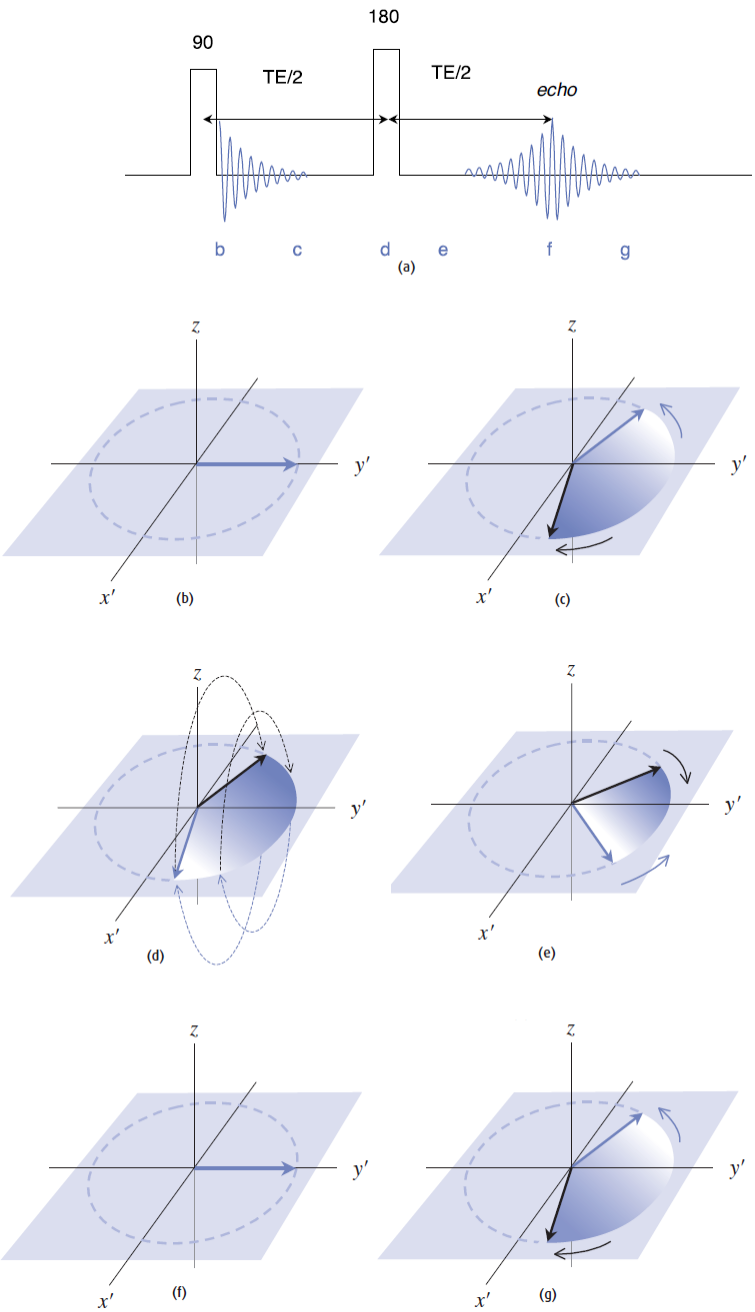

Figure 3.3: A spin echo pulse sequence (a). (b-g) are shown in the frame of reference of the spins. Spins are initially in phase after the 90 RF pulse (b), they dephase before application of the 180 RF pulse (c), the 180 Rf pulse is applied, reversing the phase (d), after which the spins dephase in what appears to be the opposite direction (e), which restores the net magnetisation, forming an echo (f), after which they dephase again (g). Image sourced from [8].

covered by the RF pulse bandwidth will be excited and contribute towards the transverse magnetisation. To reduce the slice width, the gradient ($\mathbf{G_z}$) can be increased or the RF bandwidth decreased.

Localisation in the two orthogonal planes to create the two dimensional slice is done via frequency and phase encoding using magnetic field gradients. Frequency encoding uses a magnetic field gradient to create different precessional frequencies along its principle direction during the entire readout stage of the pulse sequence. The detected signal comprises a range of frequencies whose contribution depends on the density and location of spins relative to the gradient null point. A Fourier transform is used to separate the signal for each frequency. Phase encoding uses a magnetic field gradient to create a position-dependent phase difference by altering precessional frequency momentarily. The spins return to precess at the frequency dictated by the frequency encoding gradient following removal of the phase encoding gradient. The phase encoding gradient is applied between the application of the RF pulse and T_E. Multiple phase encoding steps must be used for resolution in this plane (Figure 3.4).

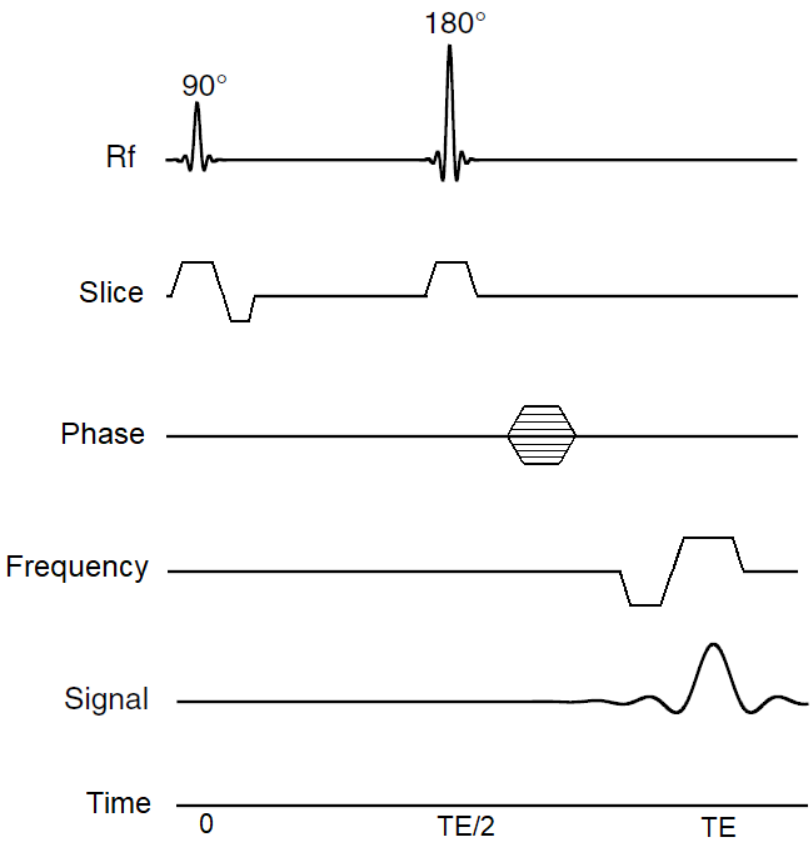

Figure 3.4: A spin-echo MR sequence with localisation gradients.

3.2 Diffusion-weighted MRI

Diffusion is the perpetual mixing of molecules caused by thermally driven Brownian motion [10], requiring no bulk motion of the substance. Diffusion-weighted MRI (DW-MRI) is sensitive to the phase dispersion of transverse magnetisation caused by diffusion of water during the application of magnetic field gradients. The movement produces a phase shift of the transverse magnetisation ($\mathbf{M}_\perp$) which reduces the signal in the direction of the applied gradient when compared to an MR image with zero diffusion-sensitising gradients. The reduction depends on the extent of diffusion. Usually, diffusion encoding is performed along at least three orthogonal directions and the results averaged.

The technique has been used clinically with great success in stroke and oncology [11]. However, most effort is focused on extracting parameters that describe the movement of extravascular spins. Protons flowing in the vasculature also cause dephasing under the influence of a diffusion-sensitising gradient. Methods to probe movement of blood were introduced around thirty years ago; Le Bihan et al. [14] provided a framework to model the signal in 1988. However, the intravascular compartment is generally much smaller than the extravascular, resulting in low sensitivity to parameters [13]. Technological advancements, resulting in higher field strengths and faster imaging, have made intravascular imaging more successful.

This section reviews the theory and methods behind DW-MRI, alongside the biophysical models that aim to describe the extra and intra-vascular compartments of tissue. The main focus is on intravascular models and how they can be used to characterise microvascular structure.

3.2.1 Pulse gradient spin echo

To characterise the effects of diffusion, additional gradients must be used to sensitise MRI signals to moving spins. This can be achieved using pairs of pulsed magnetic field gradients. The gradients must be bipolar in that they have equal and opposite magnitude, this ensures stationary protons are forced out of and back in to phase with no net effect. Moving spins, however, will travel across the gradient and will not be equally rephased. All MRI sequences, not only DW-MR images, are affected by movement of molecules. To distinguish the faster movement of water diffusion, a short pulse time is required and a high amplitude for the pulse gradient. This ensures substantial loss of phase coherence in the short sampling time and no or little contribution from bulk movements in the patient [130].

Pulsed gradient spin echo (PGSE) diffusion sensitising sequences were first described by Stejskal and Tanner [130] in 1965. The sequence is still very widely used today, and was used to collect all DW-MRI data in this thesis. The sequence is shown in Figure 3.5.

Note that since this spin-echo sequence has the 180 degree RF pulse to compensate for field inhomogeneities, the bipolar gradients must be in the same direction to create zero net phase shift in stationary spins. For readout, an echo planar imaging (EPI) sequence is used.

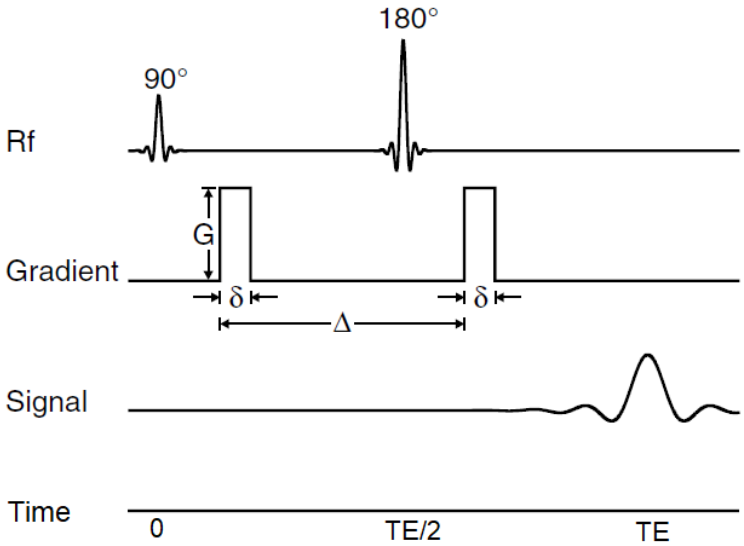

Figure 3.5: A pulsed gradient spin-echo MR sequence. Two diffusion sensitising magnetic field gradients are applied for duration δ, amplitude G with time between them equal to Δ. Image sourced from [10].

The imaging parameters shown in Figure 3.5 are combined into a single parameter that describes diffusion sensitisation. The parameter is known as the b-value and is defined by:

$$b = \gamma^2 \int_0^{TE} |x(t)|^2 \mathrm{d}t, \tag{3.5}$$

where γ is the gyromagnetic ratio, TE is the time to echo, and;

$$x(t) = \int_0^t G(t')\mathrm{d}t', \tag{3.6}$$

where G is the amplitude of the diffusion-sensitising magnetic field gradient pulses, and t is the time from the start of the sequence [131]. For a PGSE sequence, the b-value is equivalent to:

$$b = \gamma^2 G^2 \delta^2 \left(\Delta - \frac{\delta}{3}\right) \tag{3.7}$$

where δ is the length of the pulse and Δ is the time between the onset of each pulse [10, 32, 130]. As b-value increases, the sensitivity to diffusion increases as shown in Figure 3.6.

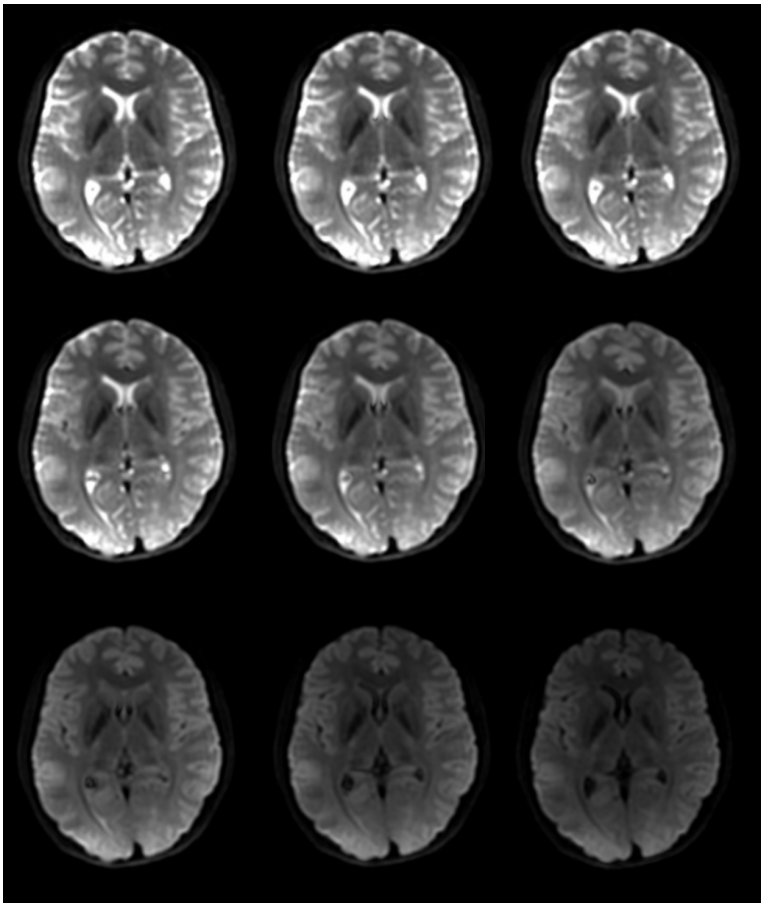

Figure 3.6: Diffusion-weighted MR images with increasing b-value. b= 10, 30, 50, 100, 200, 300, 500, 750 and 1000 smm^{-2} from left to right, moving down each row.

3.2.2 Flow-compensation

Some studies try to compensate for motion-induced phase shifts, for example, to remove artifacts due to flow or to simply null the signal in larger blood vessels. This can be achieved using an additional pair of gradient lobes prior to signal readout. The technique is called flow-compensation (FC) and to be effective, velocity should be constant.

The phase shift (Φ) experienced by a spin travelling along a path $x(t)$ with velocity $v(t)$ during the application of magnetic field gradient, $G(t)$, for time, T, can be described by [35]:

$$\Phi = \gamma \int_0^T x(t) \cdot g(t)\mathrm{d}t = \gamma \int_0^T v(t) \cdot \int_0^t g(t')\mathrm{d}t'\mathrm{d}t. \tag{3.8}$$

This gives;

$$\Phi \propto \frac{1}{2}\gamma G v T^2. \tag{3.9}$$

where γ is the gyromagnetic ratio as described previously.

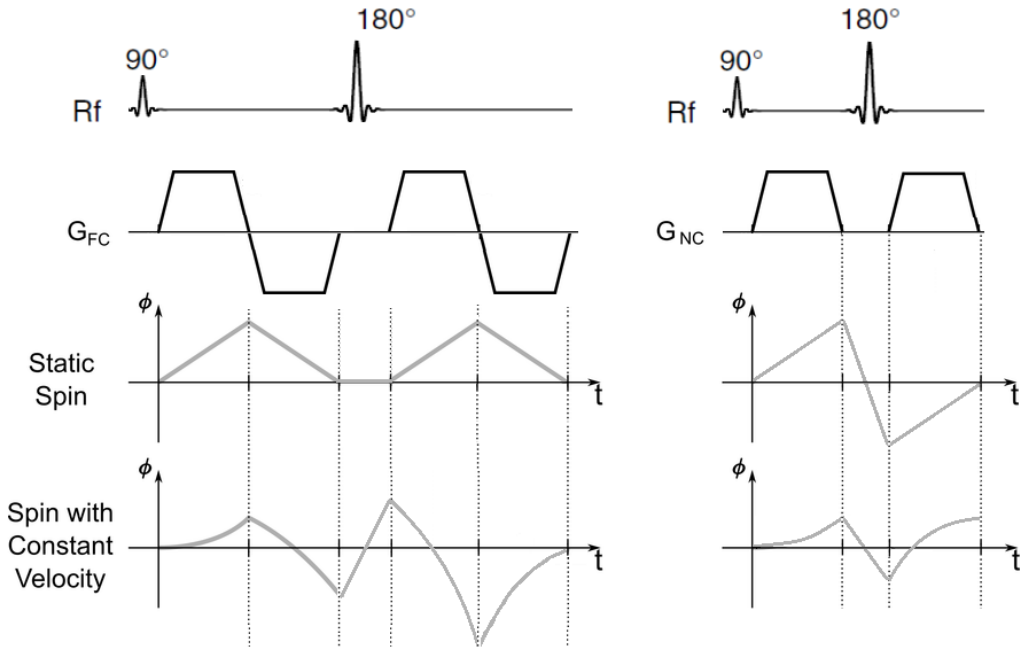

Figure 3.7: Flow-compensated (FC) and non-compensated (NC) spin echo (SE) sequences. G is the magnetic field gradient. ϕ is the phase. For static spins for both FC and NC, the phase is increased and decreased by equal amounts resulting in zero net phase shift. For spins with constant velocity, FC gradients result in a zero net phase shift. Note the quadratic dependence of phase on time. NC gradients do not null the signal from spins with constant velocity. Note spins that move and do not have constant velocity will result in a phase change for both FC and NC gradients.

The two pairs of bipolar FC gradients are set up with specific parameters to ensure spins with zero velocity and those with constant velocity have zero net phase gain at readout. The FC sequence affects spins with zero velocity in the same way that a PGSE sequence does, with equal dephasing and rephasing. For spins moving at constant velocity, it is slightly more complex as the phase gain increases with time squared, as demonstrated in Equation 3.9. The gradient strength or timing of each lobe within a bipolar pair are manipulated to ensure net phase gain is zero. For example, one lobe within a pair might have a higher gradient or longer application time, as shown in a study by Wetscherek et al. [35]. It is imperative that the total time and magnitude (but opposite polarity) of all gradients before and after the 180 pulse are equal, to ensue zero net phase gain in stationary spins.

Examples of basic FC and non-FC (NC) spin echo diffusion sensitising sequences are shown in Figure 3.7. The NC gradient pair will not allow for zero net phase gain in flowing spins. The FC pairs of gradients allow this by applying the negative lobe for each gradient pair in succession.

Introducing FC gradients in DW-MRI lengthens the TE and TR since an additional gradient pair must be used, this also increases the minimum diffusion-time. The technique also increases susceptibility to eddy currents which can affect image quality. However, they can be useful in reducing any affects of bulk motion and can isolate spins flowing with changing velocity which could be useful for imaging the microvasculature.

3.3 Modelling the DW-MRI signal

DW-MRI is incredibly useful to discern movement of water and structural information on scales much smaller than the image resolution. Mathematical modelling is required to extract useful quantitative parameters. Generally, the models can be described as a signal representation or a tissue model [132].

Signal representations describe the DW-MRI signal without making assumptions about the underlying tissue. They can be used in any tissue or pathology. The model parameters are often not specific and thus are not a true characterisation of the tissue [132]. An example of a signal representation is the diffusion kurtosis imaging (DKI) model [133], which is briefly discussed later. Tissue models make assumptions about the underlying tissue structure and geometry. The parameters are potentially more specific than those for signal representations, if the assumptions made about the tissue are correct. An example of a tissue model is neurite orientation dispersion and density imaging (NODDI) [34].

The imaging parameters used in collecting DW-MRI data dictate which models can be used and thus which parameters can be extracted. In particular, the b-value and diffusion-time (Δ) need to be considered when choosing a model. Varying the diffusion-time

(Δ), as well as the b-value, is well documented in the extravascular compartment [11, 31]. The technique can be used to determine structural properties of underlying tissue and pathology [11]. Varying the diffusion-time in the intravascular compartment is emerging as a potentially useful technique to determine parameters pertaining to blood flow and vascular structure. Models with b-value and diffusion-time dependence are reviewed in detail in the following sections.

3.3.1 b-value spectrum

The b-value is an imaging parameter quantifying the degree of diffusion sensitisation (Section 3.2.1). The DW-MRI signal always decreases with b-value, as shown in Figure 3.8. The rate of water movement, and thus phase dispersion, varies in different physiological environments. Intravascular protons move at a faster rate than extravascular protons, causing a greater degree of phase dispersion and a higher signal attenuation with increasing b-value. Since the intravascular signal decays so quickly, it is found only at low b-values ($b < 200$ on Figure 3.8). Intravascular effects are most commonly modelled using the diffusive intravoxel incoherent motion (IVIM) model [14]. At a certain b-value, or threshold, the intravascular signal is assumed to be negligible and phase dispersion due to Gaussian extravascular diffusion dominates. This is shown as $b = 200$ smm^{-2} on Figure 3.8, however this threshold can be as high as $b = 500$ smm^{-2} depending on the field strength used and tissue perfusion [131, 134, 135].

The signal attenuation in the Gaussian extravascular compartment is generally modelled as a monoexponential decay. At high b-values ($b > 1500$ on Figure 3.8), the diffusion-weighting becomes sensitive to non-Gaussian, or anisotropic, extravascular diffusion. This threshold can be as low as $b = 1000$ smm^{-2} [136], but can reach approximately 2000 smm^{-2} [11]. Studies investigating non-Gaussian extravascular diffusion might use very high b-values between 5000 and 10000 smm^{-2} [137, 138].

The selection of b-values needs careful consideration, as it will affect which compartments can be accessed and which model, or models, will be used. The selection will also depend on the tissue being studied. For example, in the brain, the intravascular fraction is lower than in other more highly perfused organs (e.g. liver), meaning lower b-values may be required to study the vascular signal [11]. Note, the b-value threshold must be chosen carefully, since parameters are dependent on the value [139, 140].

The b-values used throughout this thesis are between $b = 0$ and $b = 1000$ smm^{-2}, and all data is collected in the brain. Therefore we assume the impact of anisotropic diffusion is negligible.

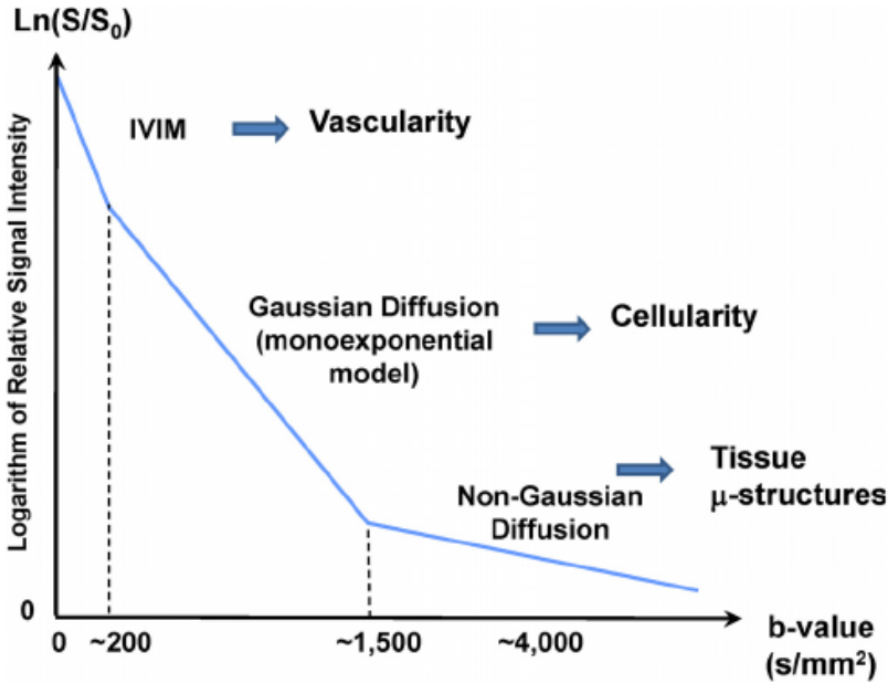

Figure 3.8: Natural logarithm of the MR signal versus b-value. Three regions are shown corresponding to tissue properties accessible at the indicated b-values. At low b-values, information on the vasculature can be obtained. The vascular model most commonly used is the IVIM model. At mid b-values, information on cellularity can be obtained. Extravascular diffusion is considered Gaussian, and is modelled by a monoexponential model. At high b-values, information on tissue microstructures can be obtained since diffusion is non-Gaussian here. The b-values shown on the x-axis are typical values in the brain. However, they can vary depending on the tissue. Image sourced from [11].

3.3.2 Monoexponential model

In a pure isotropic solution, thermally driven Brownian motion results in an exponential decay of the MR signal as a function of the b-value and the diffusion coefficient, D:

$$\frac{S}{S_0} = e^{-bD} \tag{3.10}$$

where S_0 is signal with no diffusion-sensitisation ($b = 0$). The diffusion coefficient is a measure of mobility of spins and can be described by: $D = lv/6$, where l is the mean path length, and v, the mean velocity during Brownian motion [13, 14].

In reality, biological structures and incoherent motions which aren't thermally driven (e.g. active transport across cell membranes) affect the DW-MRI signal [13]. In the extravascular compartment, an 'apparent diffusion coefficient' (ADC) is used in place of D to reflect this. A minimum of two b-values are required to measure the ADC for each voxel and produce an ADC map. Often, a b-value in the moderate limit is chosen (Figure 3.8), such as $b = 800$ smm^{-2}, and $b = 0$ smm^{-2}. Equation 3.10 is used extensively throughout literature [11] and ADC maps are useful for identifying early ischaemia and lesions in stroke [11]. An example is shown in Figure 3.9 where effects of ischaemic stroke are seen on the DW-MR image and ADC map.

Note that, in some literature and in this thesis, the ADC is still labelled D and is referred to as the diffusion coefficient. However, it is not to be confused with the diffusion coefficient of Brownian motion.

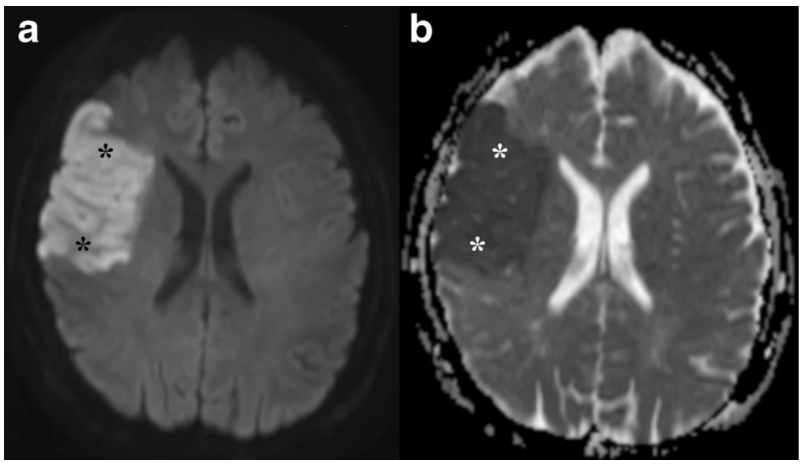

Figure 3.9: A diffusion-weighted MR image (a) and its associated ADC map (b). The asterisks ($*$) represent an area affected by ischaemic stroke which is bright in the DWI and low in the ADC map compared to surrounding tissue, indicating decreased diffusion. Image sourced from Drake-Peréz et al. [12], under terms of Creative Commons license (http://creativecommons.org/licenses/by/4.0/.)

3.3.3 Biexponential extravascular model

When DW-MRI data is collected at high b-values ($b \approx 1500$, Figure 3.8), the monoexponential model does not adequately describe the data. It is observed that the signal decays biexponentially above this threshold and can be described by:

$$\frac{S}{S_0} = f_f e^{-bD_f} + f_s e^{-bD_s} \tag{3.11}$$

where D_f corresponds to the diffusion coefficient of the mono-exponential decay described above; the fast compartment of extravascular diffusion. D_s corresponds to the diffusion coefficient of high b-value data; the slow compartment of extravascular diffusion. f_f and f_s are the fractions of the signal due to fast and slow extravascular diffusion respectively [11, 136].

It was originally hypothesised that these two components were intracellular and extracellular compartments. However, the two volume fractions obtained through model fitting do not correspond to histologically assessed data [137, 138, 141–144]. Fast and slow compartments have also been observed in the intracellular compartment alone [138]. It is currently unclear as to what these two compartments actually pertain.

3.3.4 Non-Gaussian extravascular models

The biexponential model of extravascular diffusion does not model anisotropy, however the model can be used in different directions to quantify anisotropy. Non-Gaussian diffusion models, such as compartmentalised models, signal representations or a combination of the two, can also be used. A brief list of non-Gaussian models will follow. For an in-depth review and summary of the methods described, refer to a review paper by Tang et al. [11].

3.3.4.1 Signal representations

One can introduce adaptations to the exponential models described without making assumptions of the underlying tissue physiology [11]. These are referred to as non-compartmentalised models, or signal representations, and include; diffusion kurtosis imaging (DKI) [145], the stretched exponential model [146], the fractional order calculus (FROC) model [147], the continuous-time random walk (CTRW) model [148] and fractional motion (FM) models [149].

3.3.4.2 Compartmentalised models

Compartmentalised models divide the signal in each voxel into multiple compartments dependent on tissue or diffusion properties. Compartmentalised models include [11]; neurite orientation dispersion and density imaging (NODDI) [34]; AxCaliber [150]; vascular,

extracellular and restricted diffusion for cytometry in tumours (VERDICT) [151]; composite hindered and restricted model of diffusion (CHARMED) [152] and; restriction spectrum imaging (RSI) [153].

Note that the VERDICT model does have a vascular compartment which is described as anisotropic pseudo-diffusion. The model was developed for use in tumours, so whilst mentioned, is not used to model tissue in the brain in this thesis.

3.3.5 Intravascular models: IVIM

At low b-values ($b < 200$ in Figure 3.8), the signal attenuation is caused by phase dispersion due to blood flow and Gaussian extravascular diffusion. The theory of intravoxel incoherent motion (IVIM) was introduced by Le Bihan et al. [14] in 1988, providing a framework for modelling the intravascular contribution to signal attenuation and separating it from the extravascular contribution.

IVIM refers to the microscopic movements that occur in each voxel which lead to a distribution in the position of spins causing phase dispersion and reduced echo amplitude. Conversely, coherent motion causes an identical translation of spins in a given direction, having no effect on phase dispersion and thus no effect on echo amplitude (Figure 3.10) [13]. The source of IVIM motions are thought to be predominantly due to extravascular diffusion and blood flow in capillaries [134], however larger vessels may contribute [35] and other sources may exist, such as CSF or the glymphatic system [134, 154].

Diffusion in an isotropic environment is inherently incoherent, i.e. Gaussian extravascular diffusion is incoherent. In the randomly and isotropically oriented microvasculature, at long diffusion-times blood flow can be considered as incoherent as spins change vessel segment, and so direction, many times. At shorter diffusion-times, some spins may not change direction, so the flow within a vessel may be coherent. There is most likely a mixture of incoherent and coherent motions. The isotropic distribution of the microvasculature means there is no net coherent flow in any direction however (Figure 3.10).

3.3.5.1 Biexponential IVIM model

A biexponential model of signal attenuation was proposed to separate the effects of microcirculatory flow and extravascular diffusion [14]:

$$\frac{S}{S_0} = (1 - f)e^{-bD} + fe^{-b(D_b + D^*)} \tag{3.12}$$

where f is the perfusion fraction, the fraction of the signal due to the microvascular contribution. $1 - f$ represents the extravascular contribution. D^* reflects dephasing due to perfusion in semi-randomly organised microvessels, D_b is the diffusion coefficient of water

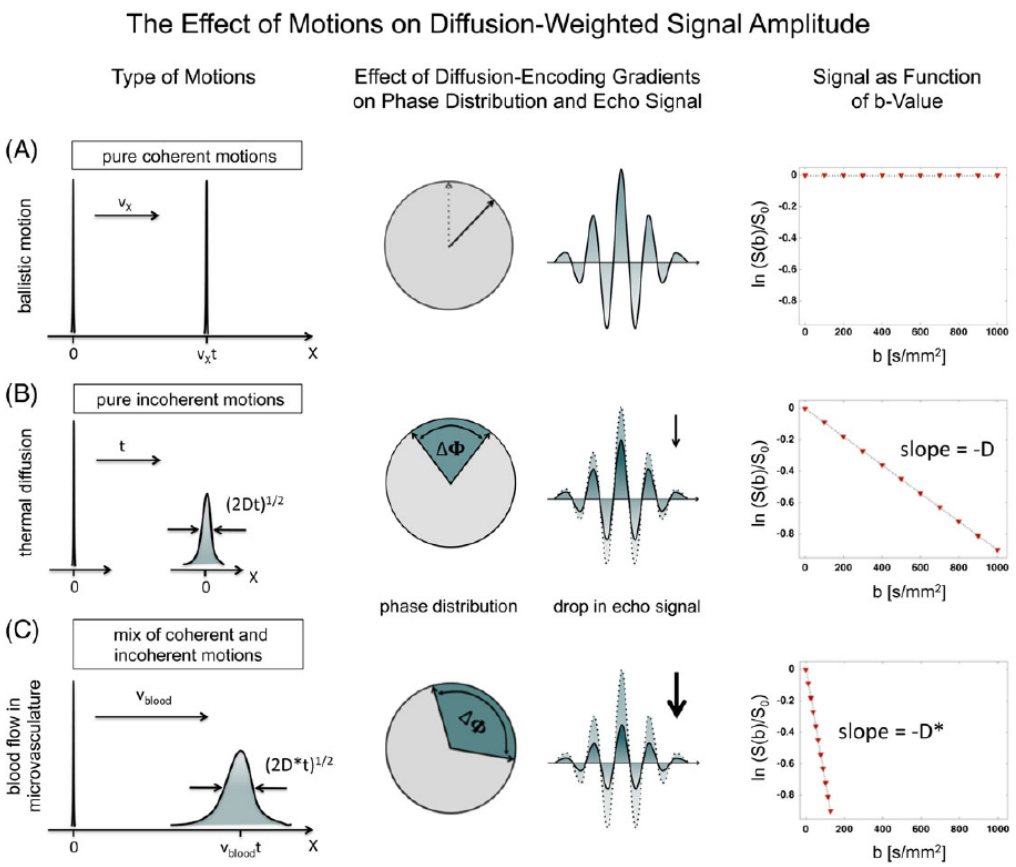

Figure 3.10: (A) If all spins in a voxel were to move coherently, there would be no phase dispersion and thus no effect on echo amplitude. This would result in a constant signal with b-value. (B) pure incoherent motions due to Brownian motion cause phase dispersion and a reduction in echo amplitude which increases with b-value. (C) in the microvasculature, a mixture of incoherent and coherent flow results in strong phase dispersion and a larger effect on echo amplitude. Again, this reduction increases with b-value. Image sourced from [13].

in blood, D is the diffusion coefficient of extravascular water [14, 155].

The capillary network is modelled as a network of straight segments with mean capillary length $\langle l \rangle$ and mean blood velocity $\langle v \rangle$. Thus, one can describe the pseudo-diffusion coefficient, D^*, as [14]:

$$D^* = \langle l \rangle \langle v \rangle / 6. \tag{3.13}$$

Blood flow is assumed to change vessel segment multiple times, mimicking diffusion, hence vascular phase dispersion being described by the pseudo-diffusion coefficient. This is often referred to as the 'diffusive regime' of blood flow. The number of times required for blood flow to change direction to ensure this regime is valid is debated in literature. Kennan et al. [33] use Monte Carlo simulations to determine that the number is around four or five. Le Bihan [134] states that this number is at least three. Simulations by Wetscherek et al. [35] using full phase information also show the number may be higher than three.

When authors refer to the IVIM model in literature, they most often mean Equation 3.12 [35, 156]. However, a second IVIM model exists which considers microcirculatory flow when the diffusion-time is not long enough for flow to change vessel segment. Blood flow in each segment is coherent and is referred to as being in the 'ballistic regime'. The signal due to blood flow is modelled by a sinc function, and is independent of vessel length:

$$\frac{S}{S_0} = (1-f)e^{-bD} + fe^{-bD_b}\mathrm{sinc}(mv). \tag{3.14}$$

v is the average blood flow velocity, and m is a flow weighting factor [131]:

$$m = \gamma \int_0^{TE} G(t)t dt, \tag{3.15}$$

where all symbols are as previously defined. For a PGSE sequence:

$$m = \Delta\sqrt{b/(\Delta - \delta/3)}. \tag{3.16}$$

An advantage of the IVIM sequence is short imaging time. The imaging sequence could be easily added on to clinical DW-MRI without a large time penalty. The method also differs from other perfusion MR methods and provides complementary information not otherwise available [13]. However, assumptions are made and there are inherent problems associated with the model.

Le Bihan reported in his original paper [14] that the IVIM method was particularly sensitive to motion and a high SNR was required to separate perfusion and extravascular diffusion [157]. The use of higher field strengths since its introduction mean that SNR requirements do not pose such a large problem. Averaging over multiple directions and acquiring repeat measurements is now commonplace. However, fitting the biexponential

model is still difficult [135] and parameter estimates can be spurious. A two or three-step approach to fitting the IVIM model is often used to avoid this, which brings its own problems such as introducing bias and the requirement for higher SNR still [158]. Some studies fit only the extravascular diffusion component of Equation 3.12 and estimate only f and D as a result of these difficulties [159, 160].

A concern with the ballistic IVIM model is that blood is assumed not to change vessel segment. However, blood is distributed throughout the length of the vessel, and as such, water molecules near the end of a vessel segment will undoubtedly change segment. In addition, the velocity profile is assumed to correspond to plug flow. Although this is an assumption made in some perfusion imaging [161–163], models which use a parabolic velocity profile may characterise the DW-MRI signal more accurately [33, 35, 164].

Although the diffusive IVIM model is the most commonly used, work by Wetscherek et al. [35] and Ahlgren et al. [164] have cast doubt on the validity of the diffusive regime. The authors suggest that blood flow may be in the ballistic regime at diffusion-times used in standard IVIM imaging. However, Fournet et al. [131] study a model of mixed regimes versus the diffusive IVIM model and find that the two models converge at diffusion-time of 34 ms, indicating that the diffusive regime is valid. This diffusion-time is lower than that used in other IVIM brain studies in literature (42ms [165, 166] and 60ms [167]). However, many studies do not mention diffusion-time [135, 158, 168–174], only b-value, hence it is difficult to say what a standard diffusion-time would be in IVIM imaging.

IVIM may be sensitive to all vessels in a voxel, not only capillaries. This could lead to biased parameter estimates, particularly at low diffusion-times where blood may remain in the voxel in the largest vessels during the imaging time. Using full phase information from all vasculature, Wetscherek et al. [35] measure blood flow velocities between that of capillaries and arterioles, suggesting larger vessels do affect estimates. However, this was done in the liver and pancreas where the vasculature will differ from that in the brain. Ahlgren et al. [164] measure velocities expected in capillaries in the brain using the Gaussian phase approximation. In addition to larger vessels contributing to signal decay, partial volume effects can result in a biexponential decay since the diffusion coefficient of CSF is larger than extravascular diffusion. Erroneous values from the biexponential fit must therefore be carefully considered and removed [13].

Lastly, all IVIM models assume that there is no trans-BBB water exchange between the intravascular and extravascular compartments. Le Bihan et al. [14] originally stated that this source of error is likely to be small as exchange flow is $< 0.1\%$ of capillary flow. However, if longer diffusion-times are used, water exchange may have a considerable effect since it is a freely diffusible tracer.

3.3.5.2 Triexponential IVIM models

In 1992, Neil and Ackerman [175] used a perfluorinated hydrocarbon tracer as a blood substitute to determine that the signal in the intravascular compartment may not decay monoexponentially. Recent work shows that a biexponential intravascular model, and thus a triexponential model when including extravascular effects, may provide a better fit to data [131, 176, 177].

Fournet et al. [131] describe a tri-exponential model reflecting two vascular flow regimes: slow flow in the smallest microvessels and faster flow in larger vessels. With a PGSE sequence, the DW-MRI signal $S(b)$ can be described by:

$$\frac{S(b)}{S_0} = (1-f)e^{-bD} + fe^{-bD_b}\left(f_{slow}e^{-bD^*_{slow}} + f_{fast}e^{-bD^*_{fast}}\right) \tag{3.17}$$

where D^*_{slow} and D^*_{fast} are the pseudo-diffusion coefficients in the slow and fast compartments respectively. f is the perfusion fraction where 'slow' and 'fast' represent the corresponding compartments, $f_{\text{slow}} + f_{\text{fast}} = 1$. All other parameters are as previously described.

The model was shown to provide a better fit to brain DW-MRI data at lower diffusion-times (14 and 24 ms), however, not at higher diffusion-times (34 ms) where the biexponential fit was comparable [131]. Despite providing a better fit at lower diffusion-times, the tri-exponential model gave high values for the perfusion fraction. However, this was perhaps due to the high b-value threshold chosen [139, 140]. Wurnig et al. [140] suggest that this can be explained by increasing noise with b-value. Less of the extravascular diffusion curve is used with increasing b-value threshold, which is more noisy. Additionally, the repetition time was shown to affect parameter estimates, including the perfusion fraction [131]. Larger f at shorter TR was attributed to inflow effects (flow related signal loss in spin echo sequences). Signal loss due to inflow effects is caused by high velocity flow, and with the 14 ms diffusion-time used (i.e. short time between the 90 and 180 pulses, during which the blood must change slice), some of the larger vessels in the brain must have been included in the segmentation of the cortex for this to occur.

The triexponential model has been used predominantly in abdominal organs [177–181]. Cercueil et al. [178] investigated the mono, bi and tri-exponential models to determine the most appropriate for liver DW-MRI data. They determine the tri-exponential provides the best fit, and state that the additional term is due to flowing spins in large vessels such as arterioles or venules that are randomly oriented. Chevalier et al. [177] compare bi and tri-exponential IVIM models in the liver, again finding the tri-exponential model provides the better fit. However, they hypothesise that the additional exponential comes from spins in interstitial space. In the kidneys, van der Bel et al. [181] state that there

may be contribution from tubular pre-urine spins and larger blood vessels.

Wu et al. [176] take a slightly different approach to modelling the tri-exponential. The authors use the IVIM ballistic model in place of the fast intravascular component:

$$\frac{S}{S_0} = (1-f)e^{-bD} + f_{\text{slow}}e^{-bD^*} + f_{\text{fast}}|sinc(mv)|e^{-bD_b}, \tag{3.18}$$

where $f_{\text{slow}} + f_{\text{fast}} = f$, and all other parameters are as previously defined. The model explicitly assumes a ballistic and diffusive flow regime, rather than two pseudo-diffusive regimes as in the Fournet model. Depending on the diffusion-times used, this could increase or decrease the accuracy of measures. The model does not include D_b as separate parameter to D^* in the study which could lead to overestimation of D^*.

3.3.5.3 Higher order IVIM models

Maki et al. [182] take the compartmental approach further and introduce a five compartment model comprising; static (extravascular), isotropic incoherent (pseudo-diffusive flow in the smallest vessels), isotropic coherent (ballistic flow in slightly larger vessels), anisotropic coherent flow (in larger vessels still, but smaller than the voxel size) and constant velocity flow (in the largest vessels, much larger than the voxel size). Including such a large number of terms is likely to improve the fit of the model, however the estimated parameters may lose precision and accuracy due to overfitting unless a very large amount of data is collected.

Arguing that it is difficult to determine the number of perfusion compartments, leading to bias in parameter estimates, Kuai et al. [183] propose a generalised IVIM model to replace multi-compartment perfusion IVIM effects. The authors introduce a continuous pseudo-diffusion coefficient, which appears to be a distribution of coefficients, to replace the coefficients in multi-exponential IVIM models. They also introduce a perfusion volume fraction density function to characterise the different blood flow compartments pertaining to each exponent of the model, this is set to a Gaussian distribution.

The model has the advantage of not requiring additional b-value collection whilst still reflecting flow in all dynamic flow regimes. It also does not require that the number of compartments be known prior to model fitting. However, the model uses exponential forms with a single coefficient describing flow for each compartment and assumes a Gaussian distribution for the perfusion volume fraction density function. Neither of these assumptions may be valid, and could thus affect parameter estimates. As with most IVIM methods, high SNR is required for tissues with low perfusion fraction such as the brain.

The authors compared the model parameters to IVIM diffusive model parameters, which were similar, when using FC gradients with diffusion-times of 70 and 100 ms (although it is unclear whether this is the total diffusion-sensitisation time, or the time between pulse applications). This could indicate that most of the flow is in the diffusive regime.

3.3.5.4 Diffusion-time dependent models

When focussing on the intravascular compartment, diffusion-time is generally not considered as a separate imaging parameter to the b-value. Most IVIM studies use the diffusive IVIM model without any consideration of diffusion-time, despite the ballistic IVIM model being introduced alongside it with discussions of diffusion-time dependence. Recent studies have demonstrated a diffusion-time dependence in IVIM parameters. Wu et al. [176] show the dependence in parameters of f, D and D^*. Kuai et al. [183] show diffusion-time dependence of f and D^*. Wetscherek et al. [35] also showed diffusion-time dependence in the signal attenuation at small b-values.

Kennan et al. [33] proposed a model of intravascular signal attenuation based on velocity autocorrelation (VA) theory. Autocorrelation is dependent on diffusion-time since directionality, and thus correlation, in blood flow depends on directional changes. Signal attenuation using a PGSE sequence is modelled as:

$$\frac{S}{S_0} = (1-f)e^{-bD} + fe^{-bD_b}\exp\left(-b\Omega\frac{T_0 v^2}{n\delta^2(\Delta-\delta/3)}\right) \tag{3.19}$$

$$\Omega = \delta^2\left(\Delta - \frac{\delta}{3}\right) - 2T_0^2\delta - T_0^3 q \tag{3.20}$$

$$q = 2\exp\left(-\frac{\Delta}{T_0}\right) + 2\exp\left(-\frac{\delta}{T_0}\right) - \exp\left(-\frac{\Delta+\delta}{T_0}\right) - \exp\left(-\frac{\Delta-\delta}{T_0}\right) - 2 \tag{3.21}$$

where n is the number of dimensions in the system, and T_0 is the correlation time (time for fluid to change direction appreciably). All other parameters are as described previously.

In the diffusive limit, the VA model reduces to the diffusive IVIM model (Equation 3.12). For ballistic flow the signal becomes:

$$\frac{S}{S_0} = (1-f)e^{-bD} + fe^{-b\left(D_b + \frac{1}{2n}\frac{\Delta^2 v^2}{\Delta-\delta/3}\right)}. \tag{3.22}$$

The model in the ballistic regime is independent of vessel structure and thus T_0. Again, this could be a source of error in the ballistic model since, even with very short diffusion-times, protons at the end of a vessel segment will likely change direction. The VA model assumes a Gaussian phase distribution since there is a distribution of vessels sizes and isotropic orientation. The velocity profile is assumed to be parabolic, however if velocity is defined as an absolute value then the model collapses to a sinc function as in the ballistic IVIM model (Equation 3.14).

The validity of the Gaussian phase approximation (GPA) was questioned by Wetscherek

et al. [35]. They argue that the distribution implies an isotropic medium which is not the case in biological tissue unless one is sampling with extremely short diffusion-times where the water molecules would not have opportunity to meet with barriers. They show the GPA does not model the IVIM signal sufficiently when FC-DWI gradients are used, and subsequently developed a model based on normalized phase distributions. The model used by Wetscherek [35] provides estimates of velocity that are higher than expected. It is unclear whether this is due to influence from larger vessels, or if the estimation is biased. When Ahlgren et al. [164] use FC gradients and the GPA, estimates of velocity agree well with literature values for the capillary bed.

Fournet et al. [131] develop a bi-exponential model and compare it to the mono-exponential IVIM and Kennan models, showing their developed model is superior at shorter diffusion-times. Akaike weights are calculated for the three models, for the Kennan model, it was found to be lower than that of the diffusive IVIM model, so is not considered as a good representation of the data by the authors. However, the Akaike weights were not significantly different. Additionally, the VA model was fit to each diffusion-time separately, hence the methods did not play to the models strengths. Simultaneous fitting to all diffusion-times and b-values, as permitted with the VA model, may allow for improved estimation of parameters.

Kennan et al. [33] suggest using the VA model to determine v, and the diffusive IVIM model to determine D^*, to estimate l using Equation 3.13. This could be a useful method when using the ballistic VA model. However, the VA model is dependent on vessel structure and, as such, allows for extraction of correlation time, T_0, as well as v. The authors determine the relationship between l, T_0 and v by first assuming the time, $t(x)$, within a segment is given by: $t(x) = (l - x)/v$, where x is the position from the start of the segment. Integrating over $t(x)$ for all possible values of x gives:

$$T_0 = \frac{1}{l}\int_0^l \frac{l-x}{v}\mathrm{d}x = \frac{l}{2v}. \tag{3.23}$$

Neither the VA model nor the IVIM models have been used to estimate vessel segment length. Two of the aims of this PhD are to develop and validate methods of measuring microvessel structure. The models proposed by Kennan et al. [33] will be tested in-vivo.

3.3.5.5 Flow-compensation in IVIM

Flow-compensation (FC) is used in IVIM studies to null the signal due to coherent flow. This is to either isolate pseudo-diffusive flow if there is a mixture of the two, or to completely null the vascular signal if there is only coherent flow. Full rephasing of the intravascular signal can only take place in a purely ballistic regime where blood flow does not change

direction [164].

Although not explicitly modelled for FC gradients, Ahlgren et al. [164] derive a model of signal attenuation due to blood flow in the ballistic regime which is used with FC and non-compensated (NC) gradients. The authors suggest using the two pulse sequences to extract more robust vascular parameters. The Gaussian phase approximation is used to derive the velocity dispersion model:

$$\frac{S}{S_0} = (1-f)e^{-bD} + fe^{-bD_b}e^{-m^2\frac{v^2}{2}}, \tag{3.24}$$

where m is equal to Equation 3.15 and all other parameters are as previously described. When using FC gradients, the signal from coherent blood flow is nulled and $m = 0$. In the study, FC gradients effectively nulled the intravascular signal indicating that blood flow was in the ballistic regime as expected. This is unsurprising since the total diffusion encoding time was low (15 ms). Note that double diffusion encoding gradients were used, and a diffusion-time of 7.5 ms used for each gradient pair. For a PGSE NC sequence, Equation 3.24 becomes:

$$\frac{S}{S_0} = (1-f)e^{-bD} + fe^{-b(D_b+\frac{1}{2}\frac{\Delta^2}{\Delta-\delta/3}v^2)}. \tag{3.25}$$

Using simulations, the authors suggest joint FC and NC analysis outperforms NC analysis for tissue with $f > 0.1$. The model is used in the brain and reasonable estimates for blood velocity in capillaries are extracted, despite using the Gaussian phase approximation. The model is almost equivalent to the ballistic approximation of the VA model derived by Kennan et al. [33] (Equation 3.22), with exception of n.

Jiang et al. [184] use the velocity dispersion model in the placenta. They use a diffusion-time of 15 ms which, with double diffusion encoding gradients, gives a total diffusion encoding time of 30 ms. The authors fit the velocity dispersion model and the diffusive IVIM model to the same data, stating that the signal would comprise diffusive and ballistic flow. However, the models should have been combined in this case to create a tri-exponential. Fitting the two models separately would undoubtedly create bias if both regimes were present. The vascular parameters correlated well with Doppler ultrasound results however.

Wetscherek et al. [35] propose an IVIM model which is not bound by the diffusive and ballistic limits. The authors use full phase information to derive a model allowing for extraction of parameters describing vascular structure and blood flow velocity. The phase distribution model proposed [35, 156] can be used with FC and NC diffusion-sensitisation gradients.

The model is used to extract the average correlation time, T_0 and the average blood flow

velocity, v. Estimates of velocity were between those of capillaries and arterioles/venules in the liver, suggesting larger vessels are contributing to signal attenuation, not only capillaries. Using FC gradients, Wetscherek et al. [35] showed diffusion-time dependence in the signal attenuation at small b-values, indicating the presence of flow which is not purely ballistic. The attenuation due to NC gradients was greater than that due to FC gradients, indicating that there is diffusive flow. The authors argue that these two results indicate that vascular flow is between the two IVIM limits (diffusive and ballistic). However, they also state that the diffusive IVIM model is likely suitable for NC imaging since all models provide a similar fit, although D^* may be underestimated.

Simulations by Wetscherek et al. [35] using the phase distribution model show, for a parabolic velocity profile, the GPA matches complete phase information at very low b-values, but breaks down after approximately 50 smm^{-2}. This would invalidate the models proposed by Ahlgren et al. [164] and Kennan et al. [33], however the simulations are for the liver or pancreas rather than the brain and use high values for parameters (v=4.25 mms^{-1} and T_0=180 ms which would give a vessel length of 1.53 mm). Smaller values, such as those corresponding to capillaries, would give increased phase dispersion for the total diffusion-encoding time of 70 ms.

Schneider et al. [185] compare the diffusive IVIM model and the phase-distribution model using a capillary flow phantom. The study found that at low flow rates, the IVIM model best described the data. The phase distribution model was best at higher flow rates. Regardless, estimates of particle speed from both models agreed well. Gurney-Champion et al. [156] show via simulations that the phase distribution model performs better at high perfusion fractions. The precision of parameters decreased with perfusion fraction substantially. Note, that the author tightly constrained parameter estimates during the fitting method, potentially introducing bias.

3.3.5.6 Alternative IVIM models

Henkelman et al. [186] discuss the flaws of the diffusive IVIM model. The authors point out inaccuracies in the intravascular signal could arise due to the assumption that the intravascular compartment reflects flow in the capillaries only and that the vasculature is isotropically distributed. The authors then suggest a fractal model based on hierarchical vascular geometry and a distribution of velocities.

To investigate only the vascular contribution to the DW-MRI signal, blood was replaced with a perfluorinated hydrocarbon tracer and ^{19}F NMR used. The tracer does not cross the BBB, reflecting the models assumption of zero water exchange. A diffusion-time of 20 ms was used which is unlikely to reflect the pseudo-diffusive flow described by the diffusive IVIM model that the authors wish to compare to. A greater proportion of the signal is

likely to come form ballistic flow here, and the Henkelman model should perhaps have been compared to the ballistic IVIM model or a range of diffusion-times investigated.

The authors state the model agrees well with collected data, as do IVIM models, however they neglect to describe if parameter estimates are reasonable. As such it is difficult to assess whether the model reflects reality. The model makes assumptions such as geometric self similarity and the isotropic orientation of blood vessels, despite including much larger vessels such as the carotid arteries and the sagittal sinus.

3.4 Alternative theories and models

Alternative MR methods of extracting parameters describing vascular structure have been proposed, however to the best of our knowledge, only one method exists which estimates microvascular segment length [36]. The first to develop such a method was Bosmotwi et al. [36] who use a superparamagnetic iron oxide contrast agent and measure changes in T_2 and T_2^* to derive microvessel segment length and radius. This method requires multiple MR techniques (including DWI), meaning longer acquisition times, and the use of contrast agents. The technique produces estimates consistent with ground truth measures derived using laser scanning confocal microscopy and reasonable estimates compared to literature, although they are on the lower side of the range presented (approximately 12-33 μm). The vessel size index (VSI) proposed by Tropres et al. [187] can be used to investigate vascular structure. The measurement extracts vessel diameter.

3.5 Summary

DW-MRI is a useful technique able to discern intravoxel vascular information with the use of biophysical modelling. Models of signal attenuation are numerous and largely dependent on the choice of imaging acquisition parameters. The models have sensitivity to different vascular properties. Table 3.1 summarises these models and the parameters which can be extracted from MRI data. The first ten models use DW-MRI, the last two require several MRI techniques including DW-MRI.

Using the VA or phase distribution models across multiple diffusion-times, the correlation time (T_0) and blood flow velocity (v) can be extracted, allowing estimation of vessel segment length (l) using the relationship $l = 2vT_0$ [33]. Using the pseudo-diffusion coefficient (D^*) of the diffusive IVIM model and blood flow velocity from one of the many models also allows determination of vessel structure using the relationship $D^* = vl/6$ [134]. It is unclear if the pseudo-diffusion coefficients in the tri-exponential models would be useful here, perhaps two groups of vessel sizes could be determined. Although using a single average velocity for both coefficients is perhaps nonsensical since velocity would vary in different sized vessels, hence the vessel lengths would not be accurate. The phase distribution model

allows estimation of l. However, the use of FC gradients lengthens imaging times and may increase risk of susceptibility artefacts. The model has also not been validated. Although the Bosomtwi model allows for direct estimation of l, the model requires parameter input from many MRI techniques, thus lengthening imaging time and requiring the use of contrast agents. The DW-MRI techniques may be more appropriate in determining l. The same argument can be used for the VSI measure.

It is unclear at what diffusion-times the 'diffusive' and 'ballistic' regimes are valid and hence if the models can be used to accurately characterise microvessel structure. The model also assumes larger vessels do not contribute to signal attenuation, that the signal attenuation is purely vascular in nature and that water exchange has no effect on the signal. These assumptions are not trivial and any estimates of structure derived using the models will require validation. Also unclear, is whether the VA model accurately characterises the diffusion-time dependence of the intravascular signal attenuation and if the GPA is valid.

There is potential for measuring microvessel structure (Aim 1) using multi-diffusion-time DW-MRI. However, each model has associated challenges. The following Chapters will explore and seek to validate (Aim 2) these ideas through preclinical and clinical imaging.

Table 3.1: Summary of biophysical models described which include a vascular compartment or allow for extraction of vascular parameters. The model name, equation number in the text, parameters obtained, blood flow regime validity and reference are listed. f is the perfusion fraction, where subscript fast and slow indicate the fraction for the fast and slow vascular compartments respectively; D is the diffusion coefficient; D^* is the pseudo-diffusion coefficient, where subscript fast and slow indicate the fraction for the fast and slow vascular compartments respectively; v is the average blood flow velocity; T_0 is the correlation time; l is the average vessel segment length; $\bar{D}$ is the mean pseudo-diffusivity ; σ is the pseudo-diffusion dispersion; a is a constant with units s^{-1}; CBV is the cerebral blood volume; Q is the mean vessel density; VSI is the vessel size index.

Model	**Equation**	**Parameters**	**Regime**	**Reference**
Diffusive IVIM	3.12	f, D, D^*	$\Delta > T_0$	[14]
Ballistic IVIM	3.14	f, D, v	$\Delta < T_0$	[14]
Tri IVIM; Fournet et al.	3.17	f, f_{fast}, f_{slow}, D, D^*_{fast}, D^*_{slow}	all regimes	[131]
Tri IVIM; Wu et al.	3.18	f, f_{fast}, f_{slow}, D, v, D^*	all regimes	[176]
Generalised	N/A	f, D, $\bar{D}$, σ	all regimes	[183]
VA	3.19	f, D, v, T_0	all regimes	[33]
Ballistic VA	3.22	f, D, v	$\Delta < T_0$	[33]
Velocity dispersion	3.24	f, D, v	$\Delta < T_0$	[164]
Phase distribution	N/A	f, D, v, T_0	all regimes	[35]
Fractal	N/A	f, D, a	all regimes	[186]
Bosomtwi	N/A	D, CBV, Q for l	N/A	[36]
VSI	N/A	VSI	N/A	[187]

4 Characterisation of microvessel blood velocity and segment length in the brain using multi-diffusion-time diffusion-weighted MRI

Lauren A Scott[1,2], Ben R Dickie[1,2], Shelley D Rawson[3], Graham Coutts[1,2], Timothy L Burnett[3], Stuart M Allan[1,2], Geoff JM Parker[4,5], Laura M Parkes[1,2].

1. Division of Neuroscience and Experimental Psychology, School of Biological Sciences, Faculty of Biology, Medicine and Health, University of Manchester, Manchester, UK
2. Geoffrey Jefferson Brain Research Centre, Manchester Academic Health Science Centre, Northern Care Alliance & University of Manchester, Manchester, UK
3. The Henry Royce Institute, Department of Materials, The University of Manchester, Manchester, UK
4. Bioxydyn Limited, Manchester, UK
5. Centre for Medical Image Computing, Department of Computer Science and Department of Neuroinflammation, University College London, London, UK

4.1 Contribution of authors

LS performed data analysis. LS, BD and LP interpreted the data. BD collected MR data. SR and LS collected CT data. GC performed corrosion casting. BD, LP, TB and GP supervised the research. LS, BD, LP wrote the manuscript. SA, BD, LP, TB, GP contributed to experimental design.

4.2 Abstract

Multi-diffusion-time diffusion-weighted MRI can probe tissue microstructure, but the method has not been widely applied to the microvasculature. At long diffusion-times, blood flow in capillaries is in the diffusive regime, and signal attenuation is dependent on blood velocity (v) and capillary segment length (l). It is described by the pseudo-diffusion coefficient ($D^* = vl/6$) of intravoxel incoherent motion (IVIM). At shorter diffusion-times, blood flow is in the ballistic regime, and signal attenuation depends on v, and not l. In theory, l could be estimated using D^* and v. In this study, we compare the accuracy and repeatability of three approaches to estimating v, and therefore l: the IVIM ballistic model, the velocity autocorrelation model, and the ballistic approximation to the velocity autocorrelation model. Twenty-nine rat datasets from two strains were acquired at 7 T, with b-values between 0 and 1000 smm^{-2} and diffusion-times between 11.6 and 50 ms.

Five rats were scanned twice to assess scan-rescan repeatability. Measurements of l were validated using corrosion casting and micro-CT imaging. The ballistic approximation of the velocity autocorrelation model had lowest bias relative to corrosion cast estimates of l, and had highest repeatability.

4.3 Introduction

Damage to the cerebral microvasculature may contribute to the development and progression of several neurological disorders, including cerebral small vessel disease and Alzheimer's disease [1]. There is evidence for thin and fragmented vessels, reductions in capillary density, abnormal branching and increased vessel tortuosity in Alzheimer's disease and other dementias [1, 4, 6, 18, 19, 26]. Jespersen and Østergaard [23] suggest such morphological changes may alter capillary transit time heterogeneity which may limit the extraction efficacy of oxygen into tissue, impeding neural function. However, morphological changes may also be compensatory. For example, changes (e.g. angiogenesis) resulting in collateral flow [188] may tend to restore oxygen levels to normal. The nature and timing of these microvessel changes is unclear – questions remain as to whether changes precede or develop alongside neurodegeneration and whether they are detrimental or compensatory. Novel methods for non-invasively measuring microvessel structure in-vivo will help address these questions.

Varying the magnitude and timing of diffusion gradients in diffusion-weighted (DW) magnetic resonance imaging (MRI) allows access to, and isolation of, the extravascular and intravascular components of the DW-MRI signal. Most attention to date has focused on modelling the extravascular component of DW-MRI signals with the aim of estimating cell size, density, and membrane permeability [16]. The theory of intravoxel incoherent motion (IVIM) [14, 134, 157, 189] first modelled the capillary contribution to the DW signal in two flow regimes (Figure 4.1). In the diffusive regime (Figure 4.1a), blood flow is assumed to change direction numerous times during the diffusion-time. The signal attenuating effects of this motion are characterised by a pseudo-diffusion coefficient (D^*) where $D^* = vl/6$ (v is the average blood velocity and l is the average microvessel segment length). The ballistic regime (Figure 4.1b) describes the other limiting case, in which blood flow does not change direction during the diffusion-time. The signal attenuating effects are described by a sinc function which is dependent on v, but independent of l [14].

In theory, microvessel structure could be determined using the two IVIM flow regimes. Fitting the ballistic regime model to data acquired at low diffusion-times (estimating v), and the diffusive regime model to data acquired at longer diffusion-times (estimating D^*) allows l to be derived [14]. However, Le Bihan states that the sinc behaviour has never been reported experimentally [134] and some research suggests a higher order IVIM model

may be favourable [175–177, 179, 186], particularly at low diffusion-times [131]. Kennan et al. [33] introduced an alternative model of signal attenuation in microvessels based on velocity-autocorrelation (VA) theory. The VA model is diffusion-time dependent, so is valid between the two IVIM regimes, and reduces to the IVIM model in the diffusive regime. However, the model describes signal attenuation in the ballistic regime as a mono-exponential decay, rather than a sinc function.

Approaches to model the intravascular component are growing and recent efforts have focused on using flow-compensated gradients [35, 156, 164, 176] at a single or multiple diffusion-times. Flow-compensated gradients rephase signal loss from ballistic flow (i.e. that from spins undergoing zero direction changes in the diffusion-time), leaving only attenuation due to spins that change direction. Acquiring data at multiple diffusion-times enables estimation v and l [35]. However, flow-compensation doubles the minimum diffusion-time, limiting the ability to probe the smallest vessels, and lengthens the minimum echo time. Data acquired using non-flow compensated gradients (i.e. bipolar gradient) are also sensitive to v and l, and can be readily acquired on most commercial scanners.

In this paper, we show that accurate and precise estimates of v and l can be obtained using bipolar non-flow compensated gradients. The IVIM model is used to predict signal attenuation at long diffusion-times to estimate D^*, and three approaches for estimating v, and therefore l, are evaluated (ballistic IVIM model, velocity autocorrelation model (VA), ballistic approximation of the velocity autocorrelation model (VAB)). Accuracy of microvessel segment length estimates are assessed by comparison with micro-CT images of a microvascular corrosion cast. To assess agreement of measurements between two rat strains, expected to have similar regional variation, regional estimates are compared between two rat strains (Fischer 344 and Wistar-Kyoto). Scan-rescan reproducibility was assessed in a subset of F344 rats. We show the VAB model has the lowest bias relative to corrosion cast estimates, and the highest scan-rescan repeatability of the three methods tested.

4.4 Theory

In the presence of diffusion-sensitising gradients, attenuation of the MR signal can be described by a two-compartment model, describing the intra and extra-vascular contributions:

$$\frac{S(b)}{S_0} = fe^{-bD_b}H(b) + (1-f)e^{-bD} \tag{4.1}$$

where $b = \gamma^2\delta^2G^2(\Delta - \delta/3)$ when employing pulsed gradient spin echo (PGSE) sensitisation. γ is the proton gyromagnetic ratio; G, the magnitude of the diffusion gradient pulses; δ, the duration of each diffusion gradient pulse and; Δ, the diffusion-time, the time between the gradient pulses. $S(b)$ is the DW-MR signal as a function of b; $H(b)$, the attenuation due to

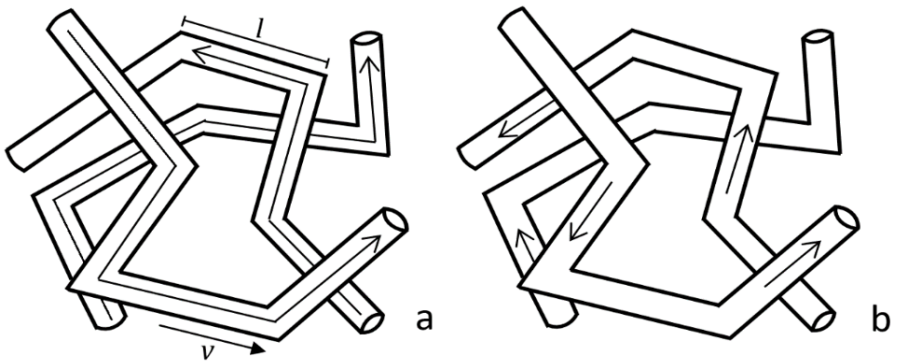

Figure 4.1: Blood flow in a capillary network with capillary segment length, l, and average blood velocity, v: incoherent motion in the diffusive regime with long diffusion-times in (a) and in the ballistic regime with short diffusion-times (b). This image was adapted from Le Bihan et al. [14].

flowing spins as a function of b-value; S_0, the signal at $b = 0$; D, the extravascular diffusion coefficient and; f, the perfusion fraction [10]. D_b is the apparent diffusion coefficient of water in blood [134]. The extra-vascular contribution is modelled as a monoexponential since the highest b-value used (b=1000 smm^{-2}) is below the threshold at which one sees biexponential signal attenuation due to fast and slow compartments [136].

4.4.1 Intravoxel Incoherent Motion

The IVIM model [134] has solutions for the diffusive and ballistic regime. In both regimes, IVIM assumes the pseudo-random orientation of capillaries. In the diffusive regime, blood in capillaries is assumed to change segment, and so direction, many times during the diffusion-time. Thus blood flow is described as pseudo-diffusion. The time between directional changes of blood flow (T_0, also termed correlation time) is assumed to be much shorter than the diffusion-time ($T_0 < \Delta$). The intravascular signal is described by the exponent of a fixed parameter, independent of Δ, which is termed the pseudo-diffusion coefficient, D^*:

$$H = e^{-bD^*} = e^{-b(vl)/6} \tag{4.2}$$

where v is the average blood velocity and l is the average vessel segment length. In theory, l could be estimated using Equation 4.2 and estimates for D^* and v. We consider three methods to estimate v, and therefore l:

4.4.1.1 Method 1. IVIM (ballistic regime)

In the ballistic regime ($\Delta < T_0$), blood is assumed not to change direction during the diffusion-time. The signal attenuation is then only dependent on v, not l, and is modelled by a sinc function [14]:

$$H = \mathrm{sinc}(mv) \tag{4.3}$$

where:

$$m = \gamma\left(\int_0^{TE/2} -Gt\mathrm{d}t + \int_{TE/2}^{TE} Gt\mathrm{d}t\right) \tag{4.4}$$

which is equivalent to $m = \Delta(b/(\Delta - \delta/3))^{1/2}$ for the bipolar gradients used in this study.

4.4.1.2 Method 2. Velocity Autocorrelation model

At intermediate diffusion-times, where the diffusion-time may be of the order of T_0 ($\Delta \approx T_0$), the signal attenuation due to blood flow is diffusion-time dependent and H is given by the velocity autocorrelation model of Kennan et al. [33]:

$$H = \exp\left(-b\frac{\Omega v^2 T_0}{3\delta^2(\Delta - \delta/3)}\right) \tag{4.5}$$

where:

$$\Omega = \delta^2(\Delta - \delta/3) - 2T_0^2\delta - T_0^3 q, \tag{4.6}$$

$$q = 2\exp\left(\frac{-\Delta}{T_0}\right) + 2\exp\left(\frac{-\delta}{T_0}\right) - \exp\left(-\frac{\Delta+\delta}{T_0}\right) - \exp\left(-\frac{\Delta-\delta}{T_0}\right) - 2. \tag{4.7}$$

In this model, two parameters must be estimated (v and T_0), in contrast to the ballistic models where only v is estimated.

In the limit of the diffusive regime ($T_0 < \Delta$), H reduces to the IVIM model of pseudo-diffusion and is equal to Equation 4.2.

4.4.1.3 Method 3. Velocity Autocorrelation model (ballistic regime)

In the limit of the ballistic regime ($T_0 > \Delta$), the velocity autocorrelation model remains exponential with H:

$$H = \exp\left(-b\frac{v^2\Delta^2}{6(\Delta - \delta/3)}\right). \tag{4.8}$$

Neil and Ackerman showed in 1992 [175] that the intravascular compartment may not be a monoexponential decay. This theory is also discussed by Henkelman et al. [186] who describe the flaws associated with the common monoexponential IVIM model which assumes flow in capillaries is contributing to signal attenuation only. The authors suggest

a model which reflects the hierarchical structure of the vessel network, and thus includes contribution from larger vessels. More recently, a more general approach has been taken to characterise the contribution of larger vessels. Fournet et al. [131], Wu et al. [176] and others [177, 179] use a two compartment intravascular model representing 'fast' and 'slow' perfusing components of the signal rather than specifically describing veins and arteries as in Henkleman's model [186]. The slow compartment may correspond to pseudo-diffusive flow and the fast, ballistic flow, as described by Wu et al. [176]. Unfortunately, due to limitations regarding the number of b-values, it was not justified to investigate these models in this work. The model suggested by Henkelman et al. [186] presents an interesting alternative method of modelling the signal attenuation. However, since it does not allow for estimation of v, and thus l, which is the main aim of this work, it is not used here. Here, we introduce sensitivity to v through manipulation of the diffusion-time at fixed b-values.

4.5 Methods

Multi-diffusion-time DW-MR data is acquired in two strains of rat in order to estimate D^*, v, and l using Equations 4.2-4.8. To determine the optimal method for estimating v, and therefore l, the accuracy of estimates from each method are evaluated against measurements obtained from x-ray CT images of a vascular corrosion cast. The scan-rescan repeatability of estimates from the two most accurate methods are compared, in addition to a regional comparison of parameter estimates between the two rat strains.

4.5.1 MRI acquisitions

MRI scanning was performed on a Bruker Avance III console (Bruker BioSpec, Karlsruhe, Germany) interfaced with an Agilant 7 T 16 cm bore magnet. A Bruker transmit only resonator (T11070V3) was used for transmission and a Bruker rat brain surface coil (T11205V3) was used for reception. To demonstrate robustness of measurements across different strains, two rat strains were scanned: Fischer-344 (F344) (n=19, 8 male, 11 female) and Wistar-Kyoto (WKY) (n=10, all male) at 13 months. Five F344 rats were re-scanned within two weeks to investigate scan-rescan repeatability of measures. The animals were anaesthetised with 2% isoflurane and 100% O_2 for the duration of the scans. High resolution T2-weighted RARE images were acquired for regional segmentation purposes (see later). The following parameters were used: TR=3188 ms, TE=11 ms, voxel size $0.11 \times 0.1 \times 1$ mm^3, RARE factor 8, NSA = 2. DW-MR images (Figure 4.2a) were obtained for each rat along three orthogonal diffusion-encoding directions. The b-value was varied through eight values: 0, 10, 20, 50, 100, 200, 500 and 1000 smm^{-2}. For each b-value, the diffusion-time (Δ) was varied through four values: 11.6, 20, 40, 50 ms. The lowest diffusion-time chosen was the lowest possible given the scanner maximum gradient strength (Gmax = 375 mTm^{-1})

and slew rate (3375 $\mathrm{Tm^{-1}s^{-1}}$). To ensure the b-value remained fixed while changing diffusion-time, the amplitude of the diffusion gradient pulse, G, was altered while fixing the gradient duration, δ. Other sequence parameters were: TR=3000 ms; TE=66.86 ms; voxel size = $0.313 \times 0.313 \times 1$ mm^3; $\delta = 5.8$ ms. MRI data is available upon reasonable request to the corresponding author.

Animal experiments were reviewed and approved by the Animal and Welfare Ethical Review Board of the University of Manchester and performed under appropriate Home Office authority in line with the Animals (Scientific) Procedures Act 1986. This work is in compliance with ARRIVE guidelines (Animal Research: Reporting in Vivo Experiments). Breeding, housing, and husbandry details, conforming to the ARRIVE reporting guidelines [190] can be found in supplementary materials.

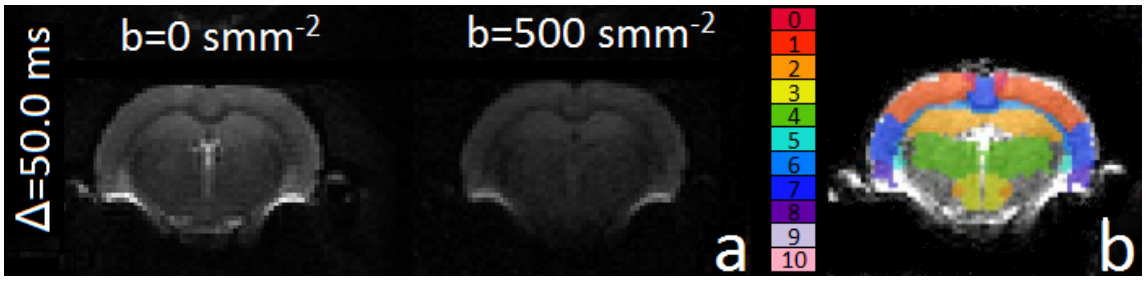

Figure 4.2: Axial mid-brain slice DW-MR image across two b-values and one diffusion-time (a), region-of-interest (ROI) map, from the Schwarz et. al [15] rat atlas, overlaid on an axial mid-brain slice DW-MR image (b). Region 0: motor cortex; 1: parietal cortex; 2: hippocampus; 3: hypothalamus; 4: thalamus; 5: striatum; 6: corpus callosum; 7: temporal cortex; 8: entorhinal cortex; 9: cingulate cortex; 10: frontal cortex.

4.5.2 Extraction of regional MRI signals

Segmentation of key brain regions was performed by registering the reference T2-weighted image from the Schwarz et al. [15] rat atlas (Figure 4.2b) to the acquired T2-RARE image using the Insight Toolkit (ITK) within the Advanced Normalisation Tools (ANTs) package (version 2) [191], and applying the estimated transform parameters to the label image. MRI signals from the following regions were extracted: striatum, temporal cortex, cingulate cortex, entorhinal cortex, frontal cortex, motor cortex, somatosensory cortex, hippocampus, hypothalamus and thalamus. Signal from each of the three orthogonal diffusion directions were averaged (using the mean). The voxel-wise signal to noise ratio (SNR) of normalised DW-MR data was estimated at $b = 10$ smm^{-2} using Equation A7 of Dietrich et al. [192] for each region using repeat F344 rat data. The various models were then fit to the average signal from each region, as described in the next section, in order to extract estimates for D^*, v and l for each rat. LS performed data processing and was blinded to rat strain.

4.5.3 Model fitting

4.5.3.1 Estimation of D and f

The extravascular component of the DW signal was estimated using high b-value data ($b = 500$ smm^{-2} and $b = 1000$ smm^{-2}) for which the contribution of the intravascular component is considered negligible ($\approx 0.2\%$ if $f \approx 0.08$, $D = 0.8 \times 10^{-4}$ mm^{2}s^{-1} and $D^* = 0.8 \times 10^{-3}$ mm^{2}s^{-1}). This 'two-step' method [158] is commonly used across IVIM studies [131, 134, 135, 168]. The extravascular diffusion coefficient, D, was estimated for each diffusion-time separately using Equation 4.9:

$$D = \frac{1}{b_1 - b_2} \ln\left(\frac{S_2}{S_1}\right). \tag{4.9}$$

The perfusion fraction, f, was then estimated for each diffusion-time using:

$$f = 1 - \frac{S}{S_0} e^{bD}. \tag{4.10}$$

4.5.3.2 Estimation of intravascular parameters

The extravascular component is subtracted from the total normalised DW signal and divided by f to isolate the intravascular component:

$$\frac{1}{f}\left(\frac{S}{S_0} - (1-f)e^{-bD}\right) = e^{-bD_b + c} H \tag{4.11}$$

where c is a parameter added to improve fitting. Theoretically c should be equal to zero. However, due to bias from the two-step method, non-zero values were observed. In log space, c is the intercept of the y-axis when b=0. For example, if $H = H(b) = e^{-bD^*}$, then the intravascular signal attenuation (I) would be defined by $I(b) = e^{-b(D_b + D^*) + c}$. In log space, $\ln(I(b)) = -b(D_b + D^*) + c$, allowing a linear fit with gradient $-(D_b + D^*)$ and intercept c. This intercept should be equal to zero since with zero diffusion-weighting ($b = 0$), there should be zero signal attenuation. However, when investigating the linear relationship, we found that it could not be accurately characterised since some points were above zero. Thus, an intercept term improved data characterisation.

Models of H independent of diffusion-time (Equations 4.2, 4.3 and 4.8) were substituted into Equation 4.11 and data fitted to each diffusion-time separately. The VA model (Equation 4.5) was fitted across all diffusion-times simultaneously. Data with $b < 500$ smm^{-2} was used and model fitting used 'lsqcurvefit' in Matlab (R2018a) with a trust-region-reflective algorithm. D_b was set to equal 1.75×10^{-3} mm^{2}s^{-1} [131].

At high diffusion-times (50 ms), Equation 4.2 is assumed to be valid, allowing for

estimation of D^*. Estimates from the IVIM ballistic and VA ballistic models were assumed to be valid at Δ=11.6 ms (assuming $l \approx 30$ μm [36] and $v \approx 2$ mms^{-1} [193], T_0 would be approximately 15 ms).

All models with exception of Equation 4.2 provide an estimate for v. Estimates of l were generated by combining estimates of v with those of D^* estimated using the IVIM diffusive model (Equation 4.2).

4.5.3.3 Evaluating the validity of model approximations

In theory, l, can be estimated from data sets acquired at only two diffusion-times – the first acquired in the diffusive regime to estimate D^* (Equation 4.2) and the second acquired in the ballistic regime to estimate v (Equations 4.3 or 4.8). While this approach is attractive as it promises short acquisition time, this method has not been tested in-vivo and it is not clear whether the conditions for diffusive and ballistic flow are met. A more general approach would be to fit the VA model (Equation 4.5), which could circumvent the need to approximate signals and possibly remove bias. Furthermore, data with intermediate Δ values could be included, potentially improving precision of parameter estimates. In order to determine the limit of validity, values for v and l were estimated for each diffusion-time for the VAB model, these values were then compared with those of the VA model. Since the VAB model is a simplification of the VA model, the two should converge where the VAB model is valid.

4.5.4 Corrosion casting

To validate MR measures, corrosion casting was used to capture the vascular morphology of a single WKY rat aged 13 months. The animal was anaesthetised using isofluorane and Mercox (Ladd Research, Williston, VT) agent injected via transcardial perfusion. The left ventricle was held with a pair of haemostats and a 21 g catheter was inserted into the apex of the heart and clamped. The right atrium was severed and a pump started, running at 20 mlmin^{-1} with 0.9% saline with heparin at 37 °C. 20 ml Mercox was prepared in a Leur lock syringe and slowly injected through the catheter into the heart. When perfusion was complete, the animal was stored overnight at 4 °C. The body was then removed, followed by a medial strip of the top of the skull. This was to maintain structural integrity of the cast during the dissolving of the tissue. Potassium hydroxide was used to dissolve tissue at 50 °C. The brain was rinsed numerous times with water and isopentane, then immersed in isopentane at -50 °C to freeze. A photographic image of the corrosion cast is shown in Figure 4.3a.

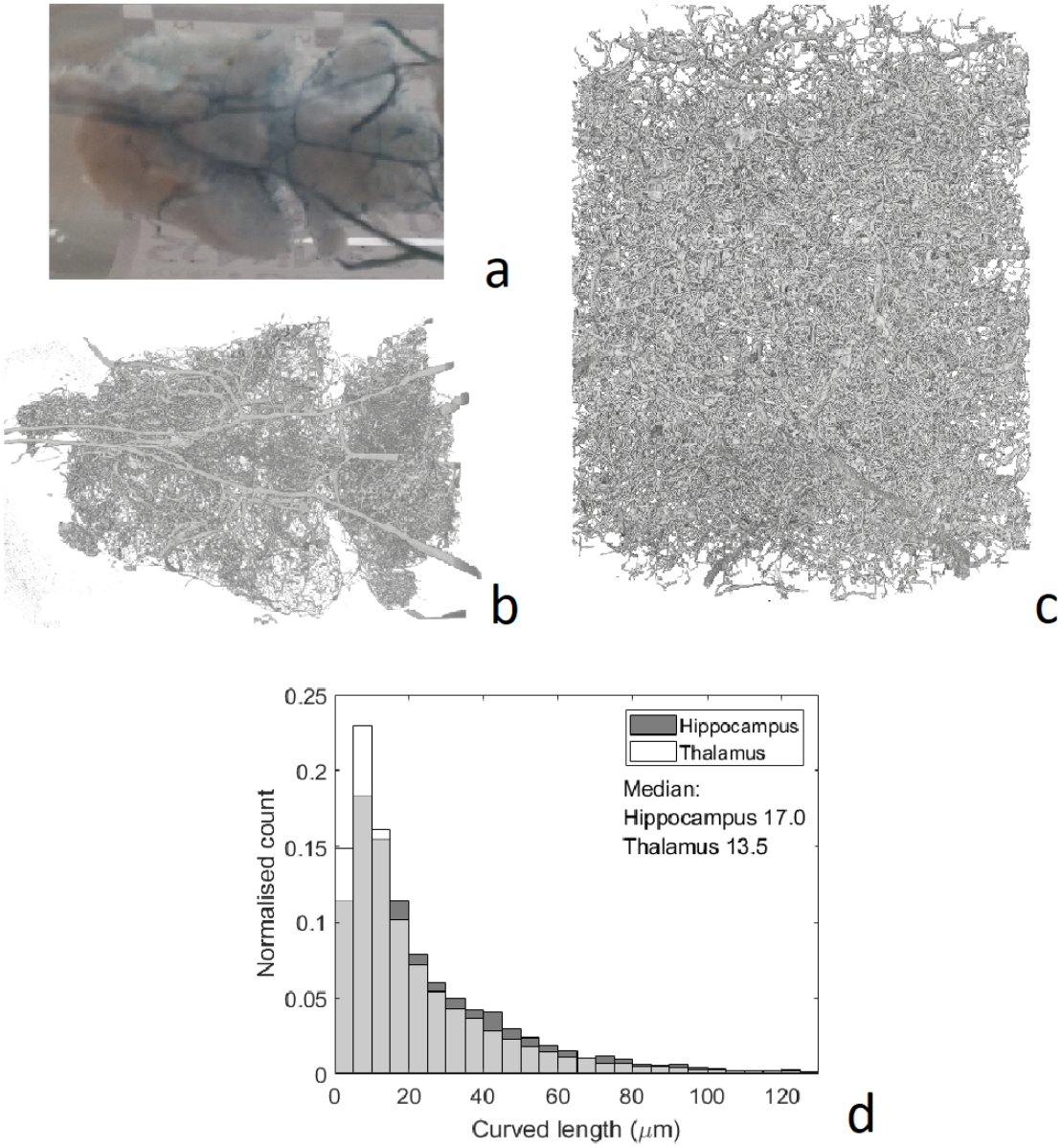

Figure 4.3: (a) A corrosion cast of a WKY rat – the circle of Willis is evident in blue. (b) and (c) show the volume render of reconstructed low resolution and high resolution μCT scans of the cast in (a) respectively. (d) shows the histogram of the capillary segment length l from the hippocampus and thalamus high resolution μCT scans. The median of each histogram is displayed in μm. The thalamus has a higher number of lower capillary segment lengths than the hippocampus- reflected in its lower median length of 13.5 μm compared to 17.0 μm

4.5.5 Micro-CT of casts and analysis

To capture the fine resolution of microvessels, μCT images were acquired of the corrosion cast. Large field of view (overview) scans were performed to facilitate positioning of higher spatial resolution ROI scans in the following brain regions: hippocampus, striatum, thalamus, and hypothalamus. Regions of interest were chosen by comparing the large vessel vascular architecture and structure of the reconstructed overview scan with the Paxinos structural rat atlas [194]. Scans were acquired using a Zeiss Xradia Versa 520 3D X-ray microscope (Zeiss, Oberkochen, Germany). Overview imaging, was performed using a magnification of $\times 0.39$, with a voltage of 70 kV and power of 6 W. Exposure time was set to 1 s, and 3201 projections were taken. The source-to-sample and sample-to-detector distances were 37.00 mm and 60.00 mm respectively. A binning of 2 was used, resulting in a cubic voxel of length 8.3 μm in the final reconstructed volume (Figure 4.3b). High resolution imaging used a magnification of $\times 4$, with a voltage of 80 kV and power of 7 W. Exposure time was set to 18 s, and 3201 projections were taken again. The source-to-sample and sample-to-detector distances were 25.01 mm and 87.65 mm respectively. A binning of 2 was used, resulting in a voxel size of 0.7499 μm^3 in the reconstructed volume (Figure 4.3c). The scanned volume for the high resolution image was 1.499 mm^3.

The original radiographs were reconstructed using filtered-back projection using the native Zeiss reconstructor software. A random subsample was selected from the high resolution dataset to allow practical data analysis. The subsample was chosen such that the largest vessels were avoided since these vessels were segmented less accurately than the smaller vessels. Approximately one quarter of the volume was chosen. The reconstructed 3D volume was segmented and skeletonised using Avizo software (Thermo Fisher Scientific, Waltham, Massachusetts, USA). The semi-automated segmentation was done using a user controlled threshold limit above which voxels were binarised to one, and below which voxels were binarised to zero. The threshold limit was chosen based on the structures highlighted in a preview window – the ideal threshold would separate corrosion cast and background completely. However, noise meant this was not possible and a threshold was chosen with as few background voxels binarised to one as possible whilst still highlighting vessels. The segmentation was corrected by hand where the intravascular space was incorrectly binarised as background.

For each region, microvessel segment lengths were determined from the skeletonised data using the 'auto skeleton' function (example histogram in Figure 4.3d). The 'auto skeleton' function computes a skeleton and a spatial graph, which consists of nodes and segments, from which segment length is automatically estimated. A 'spatial graph filter' is applied which removes nodes which have more than four adjoining nodes since this was deemed unphysiological and was likely a result of segmentation error.

An example of the processing pipeline is shown in Figure 4.7 (supplementary material) for the reconstructed high resolution scan of the hippocampus. Close up images of the volume render and segmentation of reconstructed high resolution scans of the hippocampus and thalamus are shown in Figure 4.8 (supplementary material). The volume render shows the smallest vessels were perfused and imaged, and these vessels were segmented correctly, as demonstrated by the distribution of diameters shown in Figure 4.9 (supplementary material) which are predominantly on the scale of capillary diameter [195–198]. However, we do see that the centre of some of the larger vessels were binarised as background (identified by non-solid planes cutting through the vessel), which were corrected for as discussed. We show that few larger vessels were present in subsamples of regions, as demonstrated by the distribution of diameters in Figure 4.9, which are assumed not to contribute to the IVIM signal [14].

4.5.6 Statistical Analysis

Before estimating summary statistics of parameter estimates, outliers were removed by excluding those outside three median absolute deviations of the median. This method was chosen rather than the standard deviation since it is not affected by large outliers [199]. Following outlier removal, the mean parameter estimate for each region for the two strains were calculated with standard error. The following analysis was performed to estimate the accuracy (bias) and repeatability (precision) in estimates from each model.

4.5.6.1 Comparison of MR with micro-CT estimates of capillary segment length

To assess accuracy and to validate the MR measurement of capillary segment length, the estimates were compared to those from the corrosion cast (ground truth) measure. The median vessel segment length of each region estimated from the μCT data was correlated against the rat average MR estimate obtained using the VA, IVIM ballistic and VAB models. Linear regression using 'polyfit' in Matlab (R2018a) was used to test the association between the μCT and MR estimates of l, returning the Pearson's correlation coefficient ρ, the associated p-value and the sum of squared errors (SSE).

4.5.6.2 Assessment of scan-rescan repeatability

A subset of five F344 rats underwent repeat measurements within two weeks of first measurement. The coefficient of variation (CoV) was calculated for each region to investigate repeatability of the measures and analysis methods:

$$CoV(\%) = 100\frac{\sigma}{\mu}, \tag{4.12}$$

where σ is the within subject standard deviation and μ the mean. σ is calculated using [200]:

$$\sigma = \sqrt{\frac{\Sigma(x_1 - x_2)^2}{2n}} \tag{4.13}$$

where n is the number of repeated measures, x_i is the parameter estimate for each subject at scan i. μ is found using:

$$\mu = \frac{\Sigma(x_1 + x_2)}{2n}. \tag{4.14}$$

4.5.6.3 Comparison of MR estimates of velocity, v, and capillary segment length, l between rat strains

To assess agreement of measures between two healthy rat strains, assumed to have similar regional variation, the regional averages of v and l were compared between F344 and WKY rats for the VA and VAB models. Pearson's correlation coefficient, ρ, and the associated p-value were estimated, as well as the regression equation. The Anderson-Darling test was used to assess normality – the 'adtest' function was used in Matlab (R2018a). Approximately 80% of data groups had a normal distribution, hence a repeated measures two-way ANOVA was performed for D^*, v and l to assess inter-strain and inter-regional differences. The test was performed for the VA and VAB models only using the 'ranova' function in Matlab (R2018a).

4.5.6.4 Comparison of voxel-wise SNR between diffusion-times

A repeated measures two-way ANOVA was also performed for voxel-wise SNR to assess inter-regional and inter-diffusion-time differences.

4.6 Results

4.6.1 Comparison of MR and CT estimates of capillary segment length

Figure 4.4 shows the μCT versus MR estimates for the VA, VAB and IVIM ballistic models in parts a, b and c respectively. The VAB model showed the greatest level of agreement with μCT estimates of capillary segment length (i.e. lowest bias indicated by the lowest sum of squared errors SSE = 70 and least negative y-intercept in the regression equation ($y(x = 0) = -16$)), although the VA model had similar levels of agreement (SSE = 77, $y(x = 0) = -19$). The IVIM ballistic model had substantially poorer agreement (SSE = 8800 and $y(x = 0) = -55$), with approximately 3.5-fold higher estimates of l than the VAB model. All models produced estimates of l that were highly correlated with μCT estimates ($\rho > 0.89$ for all models). The linear regression between μCT and MR estimates was significant only for the VAB and IVIM ballistic models, with $p = 0.017$ and $p = 0.014$

respectively. Evidence for a linear relationship between VA model estimates of l and μCT was low ($p = 0.11$). Since estimates using the IVIM ballistic model are inaccurate only the two VA models will be compared henceforth.

4.6.2 Assessment of scan-rescan repeatability

The CoV of parameters are shown in Table 4.1. The CoV of vascular parameters (f, D^*, v, l) was highest in the frontal cortex, and lowest in the striatum. Averaged across regions, scan re-scan CoVs were 32.0 % for f and 58.0 % for D^*. Extravascular D had a region-averaged CoV of 3.70 %, much lower than that of vascular parameters, likely due to the much higher signal fraction of extravascular water. The CoV for the VAB model was the lowest of the two methods, with average values of 22.4 % for v and 73.1 % for l. The CoV of the VA model had average values of 45.8 % for v and 109 % for l.

Table 4.1: Coefficient of variation (%) of parameter estimates calculated from repeat measures. Results from five of the F344 strain. f – perfusion fraction, D – diffusion coefficient, D^* - pseudo diffusion coefficient (all from the IVIM diffusive model fit), v – average blood velocity (from the VA and VA ballistic models), l – capillary segment length (from $D^* = vl/6$).

	IVIM diffusive			VA		VA ballistic	
Region	f	D	D^*	v	l	v	l
Striatum	10.2	1.84	13.0	39.3	79.1	16.8	32.2
Temporal Cortex	41.1	5.18	118	59.4	137	19.4	126
Cingulate Cortex	19.2	1.55	18.4	20.9	25.0	26.7	54.2
Entorhinal Cortex	33.2	3.40	70.2	36.2	147	22.4	85.6
Frontal Cortex	72.9	12.8	95.9	81.8	245	25.7	130
Motor Cortex	46.3	2.37	66.3	43.8	121	44.5	76.6
Parietal Cortex	11.6	0.508	27.4	50.8	70.0	27.3	28.2
Hippocampus	37.1	3.86	80.8	16.5	97.0	13.4	82.3
Hypothalamus	33.1	4.67	21.2	46.0	64.6	8.77	26.3
Thalamus	19.4	2.37	69.0	63.3	110	19.5	90.2
Mean	32.0	3.70	58.0	45.8	109	22.4	73.1

4.6.3 Comparison of VA and VA ballistic MR estimates of velocity, v, and capillary segment length, l between rat strains

Regional average values for v and l for the F344 and WKY rats are shown in Figure 4.5 for the VA and VAB models. Each point represents a different region of the brain (these values are also displayed in Tables 4.2 and 4.3 in the supplementary material, alongside estimates

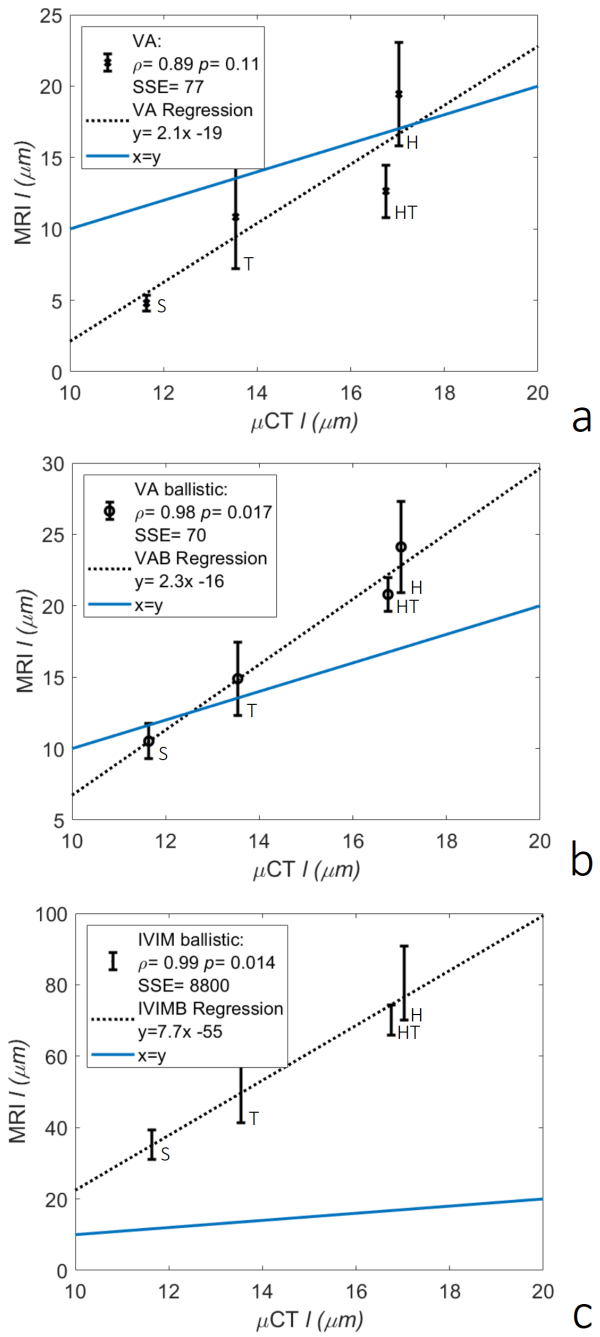

Figure 4.4: Regional average WKY MRI estimates of l ($\pm$ standard error of the mean) versus the median of the μCT estimates. Estimates are shown from three methods of velocity (v) estimation which then uses $D^* = vl/6$ to estimate l: the VA model (a), the VA ballistic (VAB) model (b) and the IVIM ballistic (IVIMB) model (c). The line of identity is displayed (blue), as is the regression line for each method (dashed black). Estimates for the striatum (S), thalamus (T), hypothalamus (HT) and hippocampus (H) are shown.

of the perfusion fraction, f, diffusion coefficient, D, and pseudo-diffusion coefficient, D^*). f and D are in good agreement with literature values [135, 168].

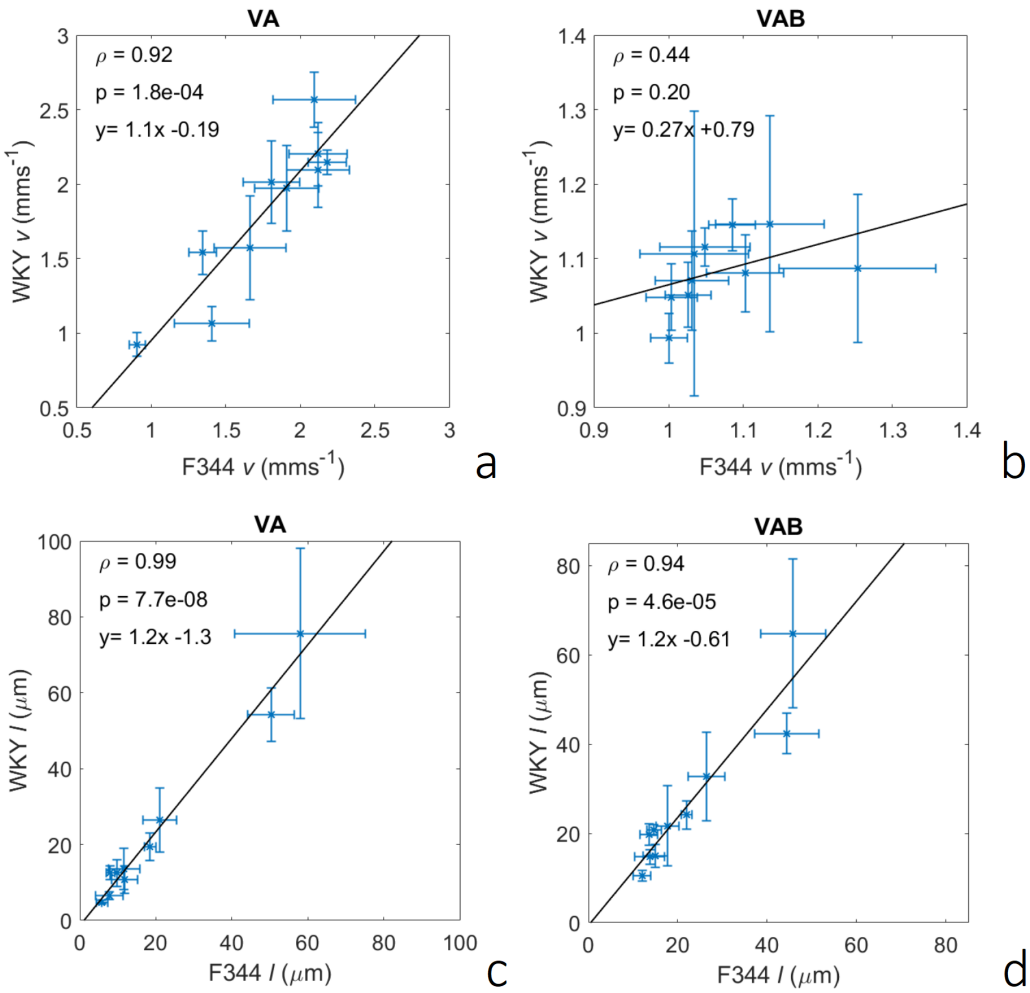

Figure 4.5: Regional averages (± standard error of the mean) of velocity (v) and capillary segment length (l) for the two rat strains (F344 and WKY) for two different methods of parameter estimation: (a) and (c) for the VA model; and (b) and (d) for the VA ballistic model. Pearson's correlation coefficient, ρ is shown as well as the p-value which tests the hypothesis that there is no relationship between the observed parameters. Each point represents a different region.

Generally, across both strains, v_{VA} was greater than v_{VAB} resulting in values for l that were slightly lower for the VA model, with exception of the cingulate cortex for both the F344 and WKY strains, and the frontal cortex for the WKY strain. l was lowest for the striatum across both methods of estimation and both rat strains. l was highest for the

frontal cortex. Variability of estimates between rats was also much larger in the frontal cortex than in other regions, as indicated by the generally larger standard error. This variability is likely due to poor measurement precision, as indicated by the poor scan-rescan repeatability in this region. Values for D^* were higher than other regional values for the frontal cortex which could explain large values for l. The mean values for v and l can be found in the supplementary material for each region, model and strain (Tables 4.2 and 4.3). Outlier removal for v and D^* are shown in Table 4.4.

Estimates of the blood velocity, v, were in good agreement between the strains - region average v_{VA} was equal to 1.77 mms^{-1} and 1.86 mms^{-1} , and v_{VAB} equal to 1.07 mms^{-1} and 1.08 mms^{-1}, for the F344 and WKY strains respectively. l varied between strains for the two models due to differing D^*. The correlation of parameter estimates between rat strains was highest for the VA model for both parameters ($\rho_v = 0.92$ and $\rho_l = 0.99$). The p-values of the linear regressions were also lowest for this model ($p_v = 1.8 \times 10^{-4}$ and $p_l = 7.7 \times 10^{-8}$), reflecting the ability of the VA model to estimate a wider dynamic range of parameters, particularly for v. The regression equations for v_{VA} and l_{VA} show low bias and excellent agreement between strains, as does the equation for l_{VAB}. The equation for v_{VAB} indicates less agreement between strains, although averages agree well, with a low gradient due to $v_{WKY} > v_{F344}$.

Two-way repeated measures ANOVA tests (Table 4.5) showed no significant effects of genotype on D^*, v or l for the VA and VAB models, reflecting the similar parameter values between rat strains. The effects of region were significant for the VA model only ($p_v = 0.029$ and $p_l = 1.8 \times 10^{-5}$), again reflecting the wider dynamic range of parameter estimates than those of the VAB model. The region and genotype interaction had no significant effects on any parameters.

4.6.4 Assessment of model validity

Since the VAB model is a simplification of the VA model, valid where $T_0 > \Delta$, estimates of v should converge to the VA estimate at lower diffusion-times. Figure 4.6a and b showed the beginning of this convergence, however, the estimates of v did not meet. This suggests the diffusion-time of 11.6 ms used in this study is not low enough for ballistic model validity (i.e. $T_0 > \Delta$ is not met) and v may be underestimated. The same trend occurred with l, although the estimates at 11.6 ms were much closer with only a small difference in l (Figure 4.6c and d).

4.6.5 Signal to noise ratio

The voxel-wise SNR for each region and diffusion-time at b=10 smm^{-2} are shown in Supplementary Table 4.6. The voxel-wise SNR does not exhibit large variation across

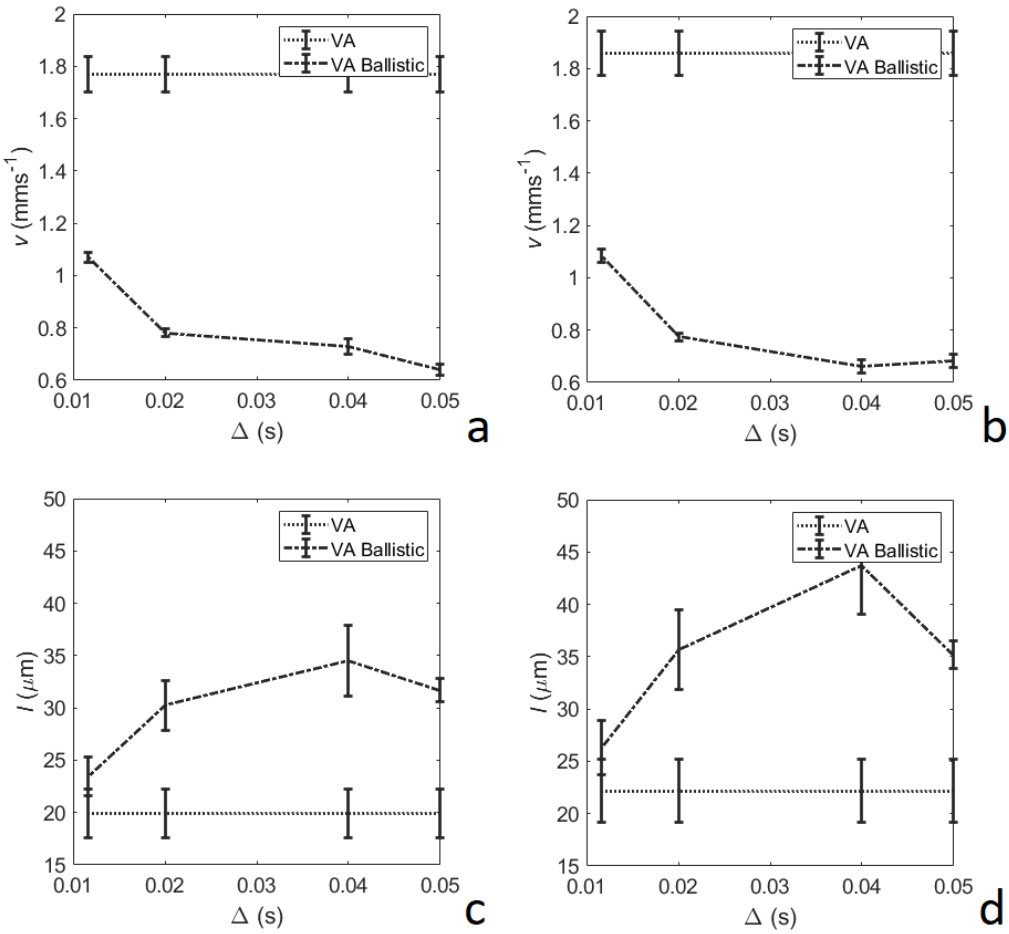

Figure 4.6: (a) and (c) show F344 rat and region average (± standard error of the mean) for estimates of the velocity, v, and capillary segment length, l, for the velocity autocorrelation model (VA) and the VA ballistic model. l is calculated using the pseudo-diffusion coefficient (D^*) estimated using Δ=50 ms. (b) and (d) show the same for the WKY rat strain. The points are joined to show the relative values for each model more clearly. The values for the VA model are flat since all diffusion-times are used in parameter estimation.

diffusion-times, however, the frontal cortex and motor cortex generally have lower SNR than other regions. This does not appear to have affected parameter estimates for the motor cortex, since the CoV and parameter estimates are comparable to other regions. However, parameter estimates and CoV in the frontal cortex are larger than those of other regions.

A two-way repeated measures ANOVA test showed a significant effect of region on SNR ($p = 9.48 \times 10^{-5}$), but no significant effect of diffusion-time ($p = 0.203$).

4.7 Discussion

In this study, we use multi-diffusion-time DW-MRI to compare models of vascular flow across different blood flow regimes (Figure 4.1) for estimating v and l. Through validating MR estimates against μCT measurements (Figure 4.3) and assessing scan-rescan repeatability and inter-strain comparisons, we show the VAB model has the highest accuracy (Figure 4.4) and precision (Table 4.1) in estimating l. While we are unable to ascertain the accuracy of v, we observe that the VAB model also provides high repeatability for this parameter. Results also highlight the potential of the VA model, with reasonable repeatability for v, high correlation between rat strains for both parameters and comparable accuracy to the VAB.

Comparing MR with μCT estimates (Figure 4.4) suggests that the VAB model produces the most accurate estimates of l. Although, as indicated by the low SSE, estimates made by the VA model also show low levels of bias. VAB estimates are generally higher than μCT estimates, whereas VA estimates are generally lower - the lowest being on the order of literature values for vessel diameter [193, 201, 202]. The IVIM ballistic model produced estimates approximately 3.5 times larger than μCT estimates.

Scan-rescan repeatability data (Table 4.1) suggests that the VAB model gives more precise estimates of v and l. These high levels of precision could be due to the inability of the VAB model to capture variability, as indicated by the low regional range in v_{VAB} (Figure 4.5). Although this is difficult to determine, since values for v in literature vary substantially and information regarding regional variation is scarce. We speculate that high values for CoV for the frontal cortex are due to inclusion of some non-brain voxels due to segmentation errors, but may also be due to susceptibility artefacts or the lower voxel-wise SNR in this region (Table 4.6 in supplementary material).

Values of v_{VA} and l_{VA} (Figure 4.5) had high correlation between the two rat strains, indicating the VA model may be more sensitive to regional variability – the VAB model generally produces estimates within a smaller range. ANOVA results confirm this, with region having a significant effect on v_{VA} but not v_{VAB}. The similar regional variation between the strains may indicate replicability of the methods since one might expect

similar parameter values between two healthy strains. However, the underlying microvessel structure differences/similarities between the two strains are not described in literature, so this data does not currently validate our methods. The strong correlation in l_{VAB} between the two strains could be driven by D^* - this would also explain why the pattern of results is similar between the VA and VAB methods (Figure 4.5c and d). Both methods produce a comparable number of spurious values (i.e. outliers, see Table 4.5).

Estimates of v in the literature vary substantially. Unekawa et al. [193, 198] used laser-scanning confocal microscopy with a high speed camera to measure a mean red blood cell (RBC) velocity in cortical capillaries of 2.05 ± 1.6 mms^{-1}. Masamoto et al. [197] measured mean RBC velocity in cortical microcirculation to be 1.5 ± 0.4 mms^{-1}. These values are in agreement with some of our regional values of v_{VA}. Unekawa et al. [198] also present results from previous studies, with a variety of methods, where the mean across studies is 0.86 ± 0.47 mms^{-1}, which is closer to estimates from the VAB model. The variation between studies possibly comes from differing definitions of capillaries, through which v is likely to vary – for example, depending on the study, capillaries have been defined previously as vessels with diameter $< 5\mu$m [195], $< 6\mu$m [196], $< 8\mu$m [197] and $< 10\mu$m [198]. Differing anaesthesia will also affect RBC velocity estimates – Masamoto et al. [197] show a mean velocity of 0.4 ± 0.4 mms^{-1} and 1.5 ± 0.4 mms^{-1} for α-chloralose and isoflurane respectively.

Although estimates of l herein agree with the range of results presented in literature [203–205], the estimates are generally lower than average values presented in the same papers. Bosomtwi et al. [36] present a method of measuring l in-vivo [187] in rats with embolic stroke. The paper estimates $l = 26.52 \pm 3.20$ μm in the contralateral region. An immunohistochemical approach presented by Morris et al. [206] estimate l in Wistar rats to be around 27μm. These estimates are comparable to our region average l_{VAB} , however a few regions, such as the striatum and motor cortex, have values of around half these estimates. Large estimates for length scale are presented by Mironov et al. [203] of 68.9 ± 4.5 μm in the superficial cortex of rats, which would agree with only the largest estimates of l_{VA} presented. Mirinov's result is the branch length obtained from corrosion casts, which differs greatly from both our MR and μCT estimates.

The VAB model is a simplification of the VA model and the two should converge where the ballistic regime ($T_0 > \Delta$) is valid. Figure 4.6 shows that this assumption is not necessarily met at the shortest diffusion-time of 11.6 ms with the VAB model underestimating v and overestimating l compared to the VA model. This could be due to blood flow changing direction when the model assumes no changes. Protons are distributed evenly across the length of the vessel segment at the onset of diffusion-sensitising gradients, so whilst all protons may travel the same distance, some will change segment and so direction during the pulse application time. This will result in a shorter apparent distance

travelled and so reduced estimated velocity. If diffusion-time could be lowered by using stronger diffusion gradients, the VAB model and VA model should in theory produce similar values for v. This would be difficult to achieve on a clinical scanner, unless oscillating gradients were used [176].

Studies using flow-compensated DWI have shown that the diffusive regime ($T_0 < \Delta$) is not met at diffusion-times similar to those used in this study (50 ms) [35, 164]. This may suggest that estimates of D^* are also biased. However, since values for l generally compare well with literature values and corrosion cast estimates, it appears that the effect of these biases are minor, or may cancel. Studies using flow-compensated DWI allow for extraction of v and, with the method proposed by Wetscherek et al. [35], T_0, therefore giving l. For our data set, T_0 was highly variable, had low repeatability and a large number of outliers, so was not used to estimate l (results not shown). This was likely due to the restricted number of diffusion-times. The flow-compensated method increases sensitivity to flow in capillaries by reducing signal contribution from larger vessels where blood does not change direction. However, estimates by Wetscherek et al. [35] in the liver and pancreas suggest v is higher than expected in capillaries, which would lead to overestimation of l. Ahlgren at al. [164] produce estimates of v closer to those expected in brain capillaries when using different assumptions about the phase distribution to Wetscherek. Increased imaging times and sensitivity to eddy currents mean that our proposed method may be more appropriate to clinically implement - although Gurney-Champion et al. [156] do show that a clinically feasible protocol is possible with flow-compensated gradients, but the protocol performs better in highly perfused tissues.

One general limitation of our method is the need to collect data at multiple b-values and diffusion-times leading to long acquisition times or relatively sparse sampling of the parameter space. In this study, this resulted in a small number of b-values in the intravascular range, meaning it was not possible to investigate the two-compartment intravascular models which have recently been proposed in IVIM studies. However, the monoexponential intravascular model fits well and the estimated length scales correlated well with ground truth measures from μCT of a corrosion cast, supporting the model. In addition, while biexponential modelling of the vascular signal may improve the accuracy of vessel segment length estimation, the precision of estimates may worsen. Regardless of the IVIM model used, assumptions made when developing biophysical models generally mean underlying biological processes are not fully characterised, which may result in inaccurate parameter estimates. For example, in the diffusive regime, D^* models blood flow in the microvasculature as Brownian motion. Additionally, all models of IVIM assume zero water exchange between compartments. In reality, both of these assumptions may break down.

In addition, the limited range of diffusion-times used could affect accuracy of parameter estimates – although, estimates of D^* and v were very reasonable when compared with the

literature. This, along with the μCT data, suggests estimates of l are also reasonable. While μCT imaging of corrosion casts provided a means to measure capillary segment length directly, it is important to note that a number of factors can lead to inaccuracies including: incomplete perfusion of the resin, potential change in shape of the cast during transit (although this was mitigated by the skull remaining intact when dissolving tissue and drying the cast) and possible cast damage when tissue is dissolved. Approximations made when reconstructing μCT data computationally may also introduce inaccuracies. Finally, we only had access to one corrosion cast from one rat strain (WKY) due to difficulties with the casting process. This clearly limits our ability to comprehensively validate the MRI measurements.

4.8 Conclusion

In this study, we determined that the ballistic approximation of the velocity autocorrelation (VAB) model applied in combination with the diffusive IVIM model to low and high diffusion-time data provides the most accurate and precise estimates of capillary segment length. The length scales estimated using these models correlated well with μCT measures of a vascular corrosion cast. Results from the VA model were encouraging, with good agreement with μCT estimates of l, however estimates were less repeatable according to CoV calculations. The ballistic IVIM model produced substantially biased estimates of l. We have shown that multi-diffusion-time DW-MRI is able to estimate capillary blood velocity and segment length with reasonable accuracy and precision.

4.9 Acknowledgements

Thanks to Damien McHugh for useful discussions regarding modelling DW-MR data, and to anonymous referees who provided useful comments whilst the paper was under review at JCBFM.

4.10 Funding

Medical Research Council for PhD funding. EPSRC (EP/M005909/1). The purchase, breeding, and maintenance of the F344 rat was jointly supported by the European Union's Seventh Framework Programme (FP7/2007-2013) under grant agreement number HEALTH-F2-2011-278850 (INMiND). The purchase of Wistar-Kyoto rat was supported by the Wellcome Trust Institutional Strategic Support Fund. The MRI facility is supported through an equipment grant from BBSRC UK (BB/F011350).

4.11 Supplementary materials

4.11.1 Animal breeding, housing, and husbandry

Fischer 344 rats were purchased from Terrence Town labs at the University of Southern California and then aged in-house. Wistar-Kyoto rats were purchased from Janvier Labs, France, and aged in-house. Throughout their lifetime, animals were housed in a conventional rodent facility in individually ventilated cages (between 3-4 animals per cage). The facility had a 12/12 hour dawn/dusk cycle, beginning at 7.30 am. Bedding was aspen woodchip and paper sizzle nest. Animals were given the following environmental enrichment: sizzle nest, play tunnels, aspen bricks (chew sticks) and aspen balls. Housing temperature and humidity were maintained at 19-23 °C and 45-65 % respectively, conforming to the Home Office code of practice for housing rodents. All animals were fed ad libitum on the BK001(E) diet (standard diet) and given free access to water. Animal health was checked daily and respiratory problems assessed prior to anaesthesia. After MRI, animals were recovered until they were able to take food and water, then returned to housing.

4.11.2 Figures

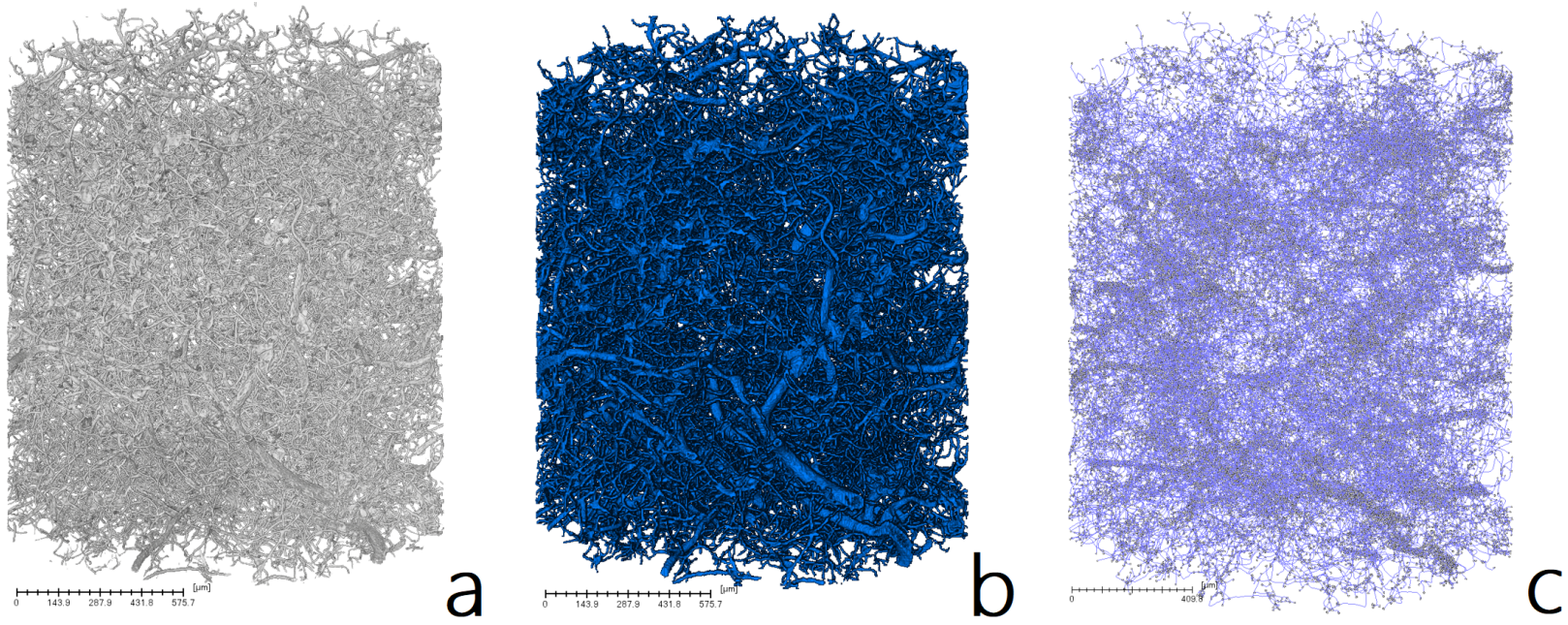

Figure 4.7: The volume render (a), segmentation (b) and skeletonisation (c) of the reconstructed high resolution scan of the hippocampus.

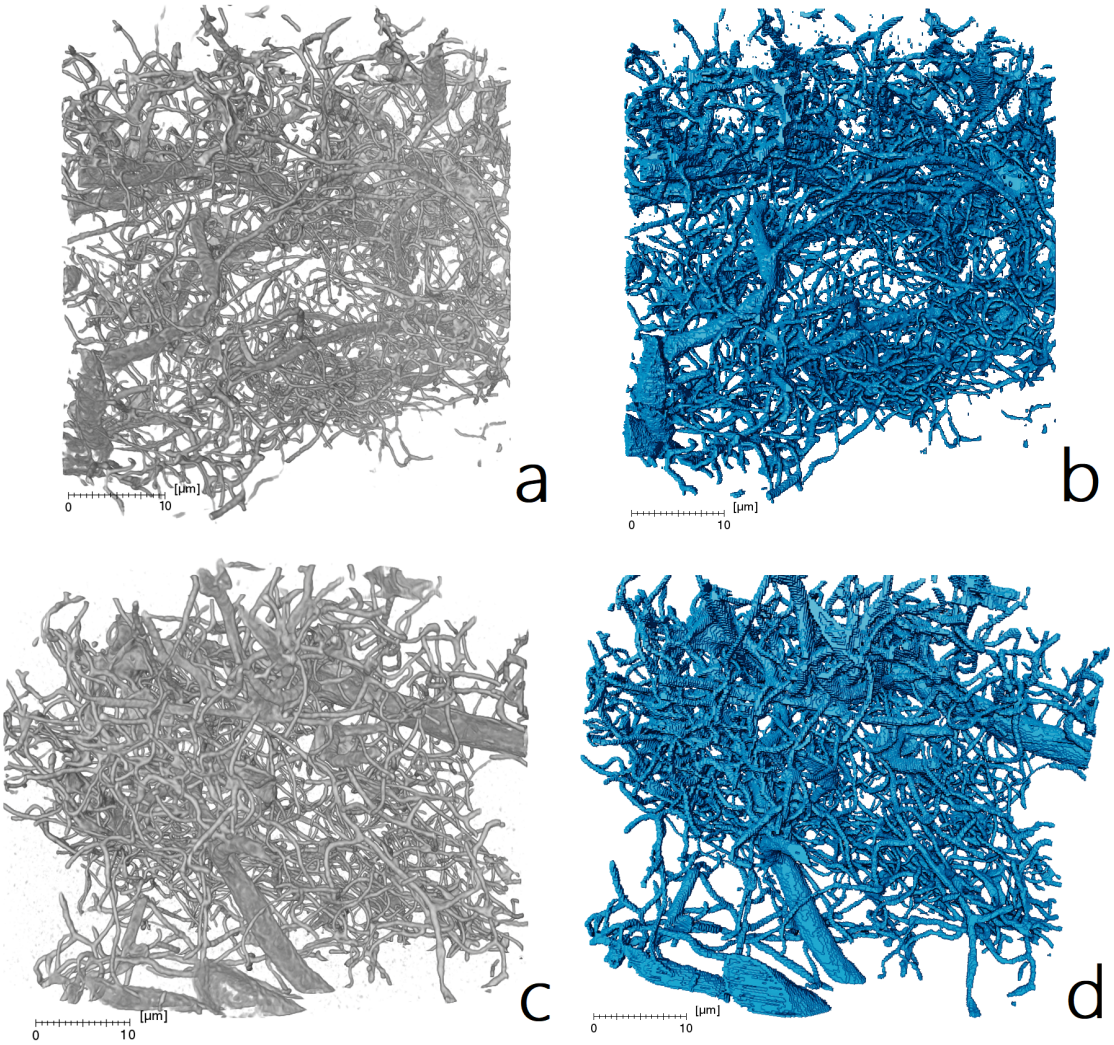

Figure 4.8: The volume render and segmentation of the reconstructed high resolution scan of the hippocampus (a and b) and the thalamus (c and d).

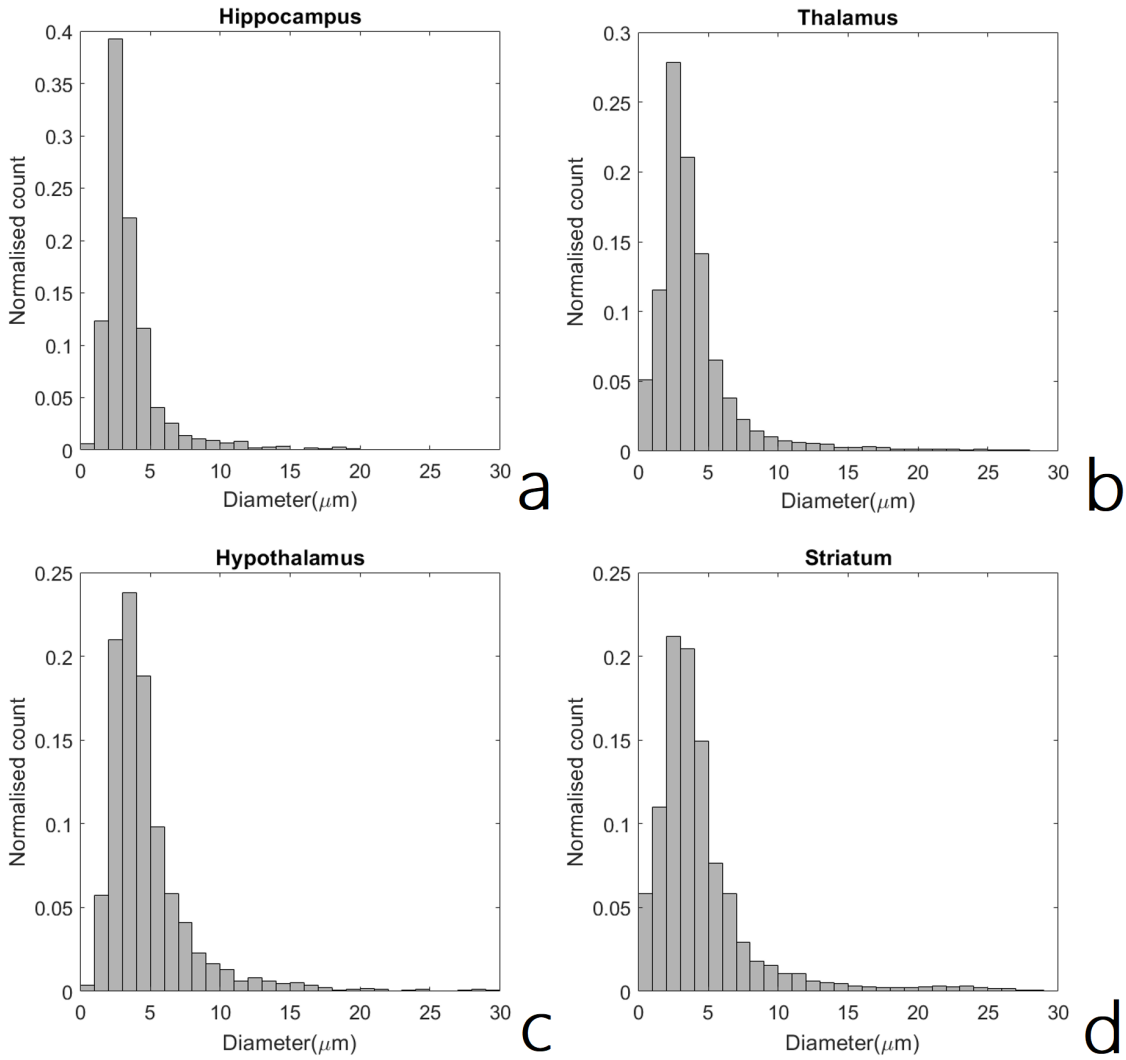

Figure 4.9: Histograms of vessel diameter from the hippocampus (a), the thalamus (b), the hypothalamus (c) and the striatum (d). Median values: hippocampus – 2.93 μm, thalamus – 3.25 μm, hypothalamus – 3.97 μm, striatum – 3.58 μm.

4.11.3 Tables

Table 4.2: F344 rat averages of the perfusion fraction (f), diffusion coefficient (D), pseudo-diffusion coefficient (D^*), velocity (v) and capillary segment length (l) for two models (VA – velocity autocorrelation model; and VA ballistic) with standard error of the mean. l is calculated using the relationship $D^* = vl/6$.

	IVIM diffusive			VA		VA ballistic	
Region	f	$D \times 10^{-4}$ (mm^2s^{-1})	$D^* \times 10^{-3}$ (mm^2s^{-1})	v (mms^{-1})	l (μm)	v (mms^{-1})	l (μm)
Striatum	0.0501 ± 0.0039	6.47 ± 0.046	1.90 ± 0.23	2.18 ± 0.13	5.83 ± 1.4	1.00 ± 0.025	12.0 ± 2.0
Temporal Cortex	0.0340 ± 0.012	6.73 ± 0.18	4.45 ± 0.73	1.66 ± 0.24	21.0 ± 4.4	1.03 ± 0.073	26.5 ± 4.1
Cingulate Cortex	0.0877 ± 0.0070	6.45 ± 0.064	6.65 ± 0.64	0.906 ± 0.054	50.3 ± 6.2	1.03 ± 0.049	44.4 ± 7.2
Entorhinal Cortex	0.0448 ± 0.0096	7.03 ± 0.14	2.82 ± 0.37	2.12 ± 0.21	11.7 ± 4.1	1.14 ± 0.073	17.6 ± 2.6
Frontal Cortex	0.0614 ± 0.018	7.05 ± 0.22	7.36 ± 1.1	1.41 ± 0.25	58.0 ± 17	1.25 ± 0.10	45.8 ± 7.2
Motor Cortex	0.0396 ± 0.0089	6.62 ± 0.045	1.9 ± 0.59	2.09 ± 0.28	7.76 ± 3.6	1.05 ± 0.060	13.7 ± 3.3
Parietal Cortex	0.0380 ± 0.0056	6.647 ± 0.065	2.38 ± 0.28	1.91 ± 0.21	9.74 ± 1.9	1.03 ± 0.031	13.5 ± 2.0
Hippo-campus	0.0612 ± 0.010	7.13 ± 0.16	3.64 ± 0.23	1.34 ± 0.094	18.5 ± 1.5	1.10 ± 0.052	21.9 ± 1.2
Hypo-thalamus	0.0793 ± 0.011	6.73 ± 0.097	2.51 ± 0.27	2.11 ± 0.20	8.02 ± 1.1	1.09 ± 0.031	14.7 ± 1.7
Thalamus	0.0587 ± 0.010	6.44 ± 0.13	2.46 ± 0.46	1.81 ± 0.19	11.8 ± 3.4	1.00 ± 0.034	15.0 ± 2.8
Mean ± std error	0.0522 ± 0.0020	6.75 ± 0.032	3.64 ± 0.24	1.77 ± 0.068	19.9 ± 2.3	1.07 ± 0.018	23.5 ± 1.9

Table 4.3: WKY rat averages of the perfusion fraction (f), diffusion coefficient (D), pseudo-diffusion coefficient (D^*), velocity (v) and capillary segment length (l) for two models (VA – velocity autocorrelation model; and VA ballistic) with standard error of the mean. l is calculated using the relationship $D^* = vl/6$.

	IVIM diffusive			VA		VA ballistic	
Region	f	$D \times 10^{-4}$ (mm^2s^{-1})	$D^* \times 10^{-3}$ (mm^2s^{-1})	v (mms^{-1})	l (μm)	v (mms^{-1})	l (μm)
Striatum	0.0559 ± 0.0041	6.40 ± 0.055	1.82 ± 0.19	2.15 ± 0.082	4.80 ± 0.55	0.994 ± 0.033	10.5 ± 1.2
Temporal Cortex	0.0568 ± 0.0070	6.68 ± 0.073	4.80 ± 1.2	1.57 ± 0.35	26.5 ± 8.5	1.11 ± 0.19	32.7 ± 9.9
Cingulate Cortex	0.108 ± 0.0051	6.38 ± 0.081	7.52 ± 0.68	0.924 ± 0.079	54.2 ± 7.0	1.07 ± 0.067	42.4 ± 4.5
Entorhinal Cortex	0.0524 ± 0.0066	6.86 ± 0.11	2.99 ± 0.74	2.09 ± 0.25	13.6 ± 5.4	1.15 ± 0.14	21.7 ± 9.0
Frontal Cortex	0.0727 ± 0.020	6.94 ± 0.34	10.1 ± 2.5	1.06 ± 0.12	75.6 ± 22	1.09 ± 0.099	64.8 ± 17
Motor Cortex	0.0539 ± 0.0045	6.70 ± 0.084	2.66 ± 0.33	2.57 ± 0.18	6.52 ± 0.94	1.12 ± 0.026	14.8 ± 1.6
Parietal Cortex	0.0483 ± 0.0032	6.60 ± 0.059	3.54 ± 0.21	1.97 ± 0.29	12.5 ± 3.5	1.05 ± 0.044	19.8 ± 2.4
Hippo-campus	0.0824 ± 0.0057	6.95 ± 0.055	4.31 ± 0.43	1.54 ± 0.15	19.4 ± 3.6	1.08 ± 0.051	24.1 ± 3.2
Hypo-thalamus	0.112 ± 0.0073	6.95 ± 0.10	3.97 ± 0.26	2.20 ± 0.21	12.6 ± 1.8	1.15 ± 0.035	20.8 ± 1.2
Thalamus	0.0645 ± 0.0047	6.40 ± 0.10	2.62 ± 0.35	2.01 ± 0.28	10.8 ± 3.6	1.05 ± 0.045	14.9 ± 2.6
Mean ± std error	0.0648 ± 0.00038	6.73 ± 0.029	4.48 ± 0.39	1.86 ± 0.068	22.2 ± 3.0	1.08 ± 0.027	26.3 ± 2.6

Table 4.4: Percentage outliers removed over all regions for each parameter and strain. D^* is the pseudo-diffusion coefficient and v is average blood velocity, from the velocity autocorrelation (VA) and VA ballistic models.

	F344			WKY		
	D^*	v		D^*	v	
Region	IVIM diffusive	VA	VA Ballistic	IVIM diffusive	VA	VA Ballistic
Striatum	13	16	5.9	20	10	0
Temporal Cortex	7.1	5.9	24	10	20	0
Cingulate Cortex	19	11	0	0	10	0
Entorhinal Cortex	23	0	0	0	0	0
Frontal Cortex	8.3	13	0	0	25	22
Motor Cortex	20	0	12	0	0	22
Parietal Cortex	12	0	12	30	0	11
Hippocampus	29	12	0	0	10	0
Hypothalamus	25	0	12	10	0	0
Thalamus	25	0	0	10	0	0
Mean	18	5.8	6.6	8	7.5	5.5

Table 4.5: Repeated-measures two-way analysis of variance (ANOVA) p-values for the pseudo-diffusion coefficient (D^*), average blood velocity (v) and the average capillary segment length (l) for the velocity autocorrelation (VA) and VA ballistic models.

	D^*	v		l	
Factors	IVIM diffusive	VA	VA ballistic	VA	VA ballistic
Genotype	0.073	0.51	0.98	0.21	0.055
Region	0.054	0.029	0.14	1.8×10^{-5}	0.11
Region*Genotype	0.65	0.48	0.38	0.056	0.96

Table 4.6: Voxel-wise signal to noise ratio (SNR) for four diffusion-times at $b = 10$ smm^{-2}, averaged across F344 rats using the mean ($\pm$ standard error of the mean).

	Diffusion-time, Δ (ms)			
Region	50	40	20	11.6
Striatum	13.8 ± 0.18	14.4 ± 0.11	14.6 ± 0.15	14.4 ± 0.24
Temporal cortex	12.3 ± 1.0	11.0 ± 1.3	12.3 ± 1.3	13.2 ± 1.4
Cingulate cortex	14.2 ± 0.31	17.7 ± 0.50	17.4 ± 0.30	17.3 ± 0.68
Entorhinal cortex	11.3 ± 0.73	11.0 ± 0.24	12.9 ± 0.45	11.7 ± 0.75
Frontal cortex	6.17 ± 0.92	7.46 ± 0.64	7.38 ± 0.92	7.73 ± 0.77
Motor cortex	2.80 ± 0.32	8.58 ± 0.29	8.08 ± 0.88	7.79 ± 0.93
Parietal cortex	9.50 ± 0.75	13.3 ± 0.98	11.6 ± 0.56	11.8 ± 0.97
Hippocampus	14.9 ± 0.34	14.2 ± 0.29	15.1 ± 0.32	15.7 ± 0.43
Hypothalamus	13.1 ± 0.28	13.3 ± 0.69	13.4 ± 0.73	14.4 ± 0.77
Thalamus	14.2 ± 0.34	14.0 ± 0.31	13.8 ± 0.19	14.3 ± 0.46

5 Modelling the diffusion-time dependence of intravoxel incoherent motion in the brain: accounting for blood velocity, vessel length and water exchange

Lauren A Scott[1,2], Andrew N Priest[3], John McFadden[1,2], Laura M Parkes[1,2], Ben R Dickie[1,2].

1. Division of Neuroscience and Experimental Psychology, School of Biological Sciences, Faculty of Biology, Medicine and Health, University of Manchester, Manchester, UK

2. Geoffrey Jefferson Brain Research Centre, Manchester Academic Health Science Centre, Northern Care Alliance & University of Manchester, Manchester, UK

3. Radiology, Cambridge University Hospitals NHS Foundation Trust, Cambridge Biomedical Campus, Hills Road, Cambridge, UK

5.1 Contribution of authors

LS performed data analysis and collected MR data. BD developed the exchange model. AP developed the pulse sequence for use on the GE PETMR scanner. JM performed ROI segmentation. LS, BD and LP interpreted the data. BD and LP supervised the research. LS wrote paper. LP and BD edited paper. LS, AP, LM, BD reviewed and approved the manuscript.

5.2 Moving from preclinical work to model development in clinical data

The upper and lower limitations on diffusion-time are driven by the choice of b-value and the gradient field strength in DW-MRI. We achieved diffusion-times as low as 11.6 ms in preclinical data, at which we assume that the ballistic regime is valid. However, this diffusion-time is not achievable on most clinical scanners since the gradient field strength is generally lower compared to preclinical systems. Thus, it may be difficult to use the VA ballistic model clinically. Due to this limitation, the next step of this PhD was to investigate the VA model further. There were several questions to answer regarding the VA model. The first, if increased number of diffusion-times would improve model fitting and parameter repeatability. The second, whether using T_0 to estimate l would produce reasonable estimates in agreement with preclinical data and literature. The last, whether water exchange affects the signal at long diffusion-times. Water exchange is considered negligible in IVIM studies. However, water may have more opportunity to cross the BBB with increasing diffusion-time. This Chapter aims to answer these questions.

5.3 Abstract

Purpose: To investigate and model the diffusion-time dependence of intravoxel incoherent motions (IVIM), including effects of blood-brain barrier (BBB) water-exchange, to estimate microvessel blood velocity (v), vessel segment length (l) and exchange time (τ) in the human brain.

Methods: Ten healthy volunteers underwent brain imaging at 3T using diffusion-weighted MRI, with ten b-values between 0 and 1000 smm^{-2} and ten diffusion-times between 27 and 60 ms. Seven volunteers were scanned twice with the same protocol during the same scan session to assess repeatability. The trace signal from grey and white matter ROIs were extracted. The standard IVIM model was fit at each diffusion-time to estimate the perfusion fraction (f), extravascular diffusion coefficient (D) and perfusion attenuation coefficient (k). The diffusion-time dependence of k was modelled using the velocity-autocorrelation model with (VAX) and without (VA) accounting for trans-BBB water-exchange, producing estimates of v, l and τ. The Akaike information criterion (AIC) was used to compare model fits.

Results: Diffusion-time dependence was observed in f and k. The VA model had lower AIC than VAX in grey matter, whereas VAX had lower AIC in white matter. Intra-scan repeatability was highest for VA parameters. Group mean values for v were between 1.07 and 1.33 mms^{-1}, for l, between 17.6 and 46.4 μm, and for τ, between 0.0622 and 0.125 s.

Conclusions: Diffusion-time affects IVIM parameters. The VA model can precisely estimate v and l. The VAX model fits better than the VA model in white matter, possibly reflecting higher BBB permeability to water.

5.4 Introduction

The effects of intravoxel incoherent motion (IVIM) on MRI signals were first described by Le Bihan et al. [207] in 1986. IVIM refers to the pseudo-random movement of protons within a voxel which causes rapid phase dispersion and decay of transverse magnetisation. The primary source of the translational motion is thought to be microcirculatory blood flow, which, together with diffusion of extravascular water, cause a decay of total transverse magnetisation with increasing diffusion weighting (b-value), which can be adequately modelled as a biexponential [14]. IVIM imaging has been applied across multiple organs and disease groups [134], for example in stroke [208] or oncology [139, 209, 210] where it has been used to determine microvascular heterogeneity and angiogenesis.

The biexponential 'IVIM model' [14] of signal attenuation is characterised by the extravascular diffusion coefficient, D, the pseudo-diffusion coefficient, D^* and the perfusion fraction, f. This model is valid at long diffusion-times (i.e. in the diffusive regime), in which blood changes vessel segment, and so direction, multiple times. Microcirculatory

flow thus mimics molecular diffusion and its signal attenuating effects can be described by a single fixed attenuation coefficient, D^*. At lower diffusion-times, blood may not change vessel segment within the diffusion-time (i.e. in the ballistic regime), or it may not change direction sufficiently such that microcirculatory flow can be considered pseudo-diffusive (i.e. in the intermediate regime). Under these conditions, the attenuating properties of microcirculatory flow are diffusion-time dependent. A number of models have been proposed to account for effects of diffusion-time under the ballistic and intermediate regimes [33, 35, 131, 134, 164, 176], however, in general, diffusion-time is still not considered in IVIM studies despite increasing literature showing a dependence in f, D and D^* [35, 131, 176].

By acquiring diffusion-weighted (DW) MRI data sensitised to multiple flow regimes, the average blood velocity (v) and vessel segment length (l) can be estimated. Wetscherek et al. [35] use flow-compensated gradients to estimate v and l, as do Ahlgren at al. [164] to estimate v. Flow compensated gradients re-phase spins that don't change direction during the diffusion-time, thus are sensitive only to diffusive flow. As the diffusion-time increases, the proportion of spins that encounter changes in direction increases, and so the fraction of spins re-phased by flow-compensated gradients reduces. Kennan et al. [33] proposed a general model to describe all flow regimes based on velocity-autocorrelation (VA) theory that is applicable to pulsed gradient spin echo sequences (PGSE). The model maps velocity-autocorrelation of spins undergoing microcirculatory flow to signal attenuation. The approach using flow-compensated gradients have longer imaging times and increase the risk of artefacts due to eddy currents, meaning the VA method may be more appropriate in a clinical setting.

In the presence of diffusion sensitising gradients, finite water-exchange across the blood-brain barrier (BBB) may also modify the attenuating properties of microcirculatory and extravascular spins, but is currently ignored in IVIM models. Alterations to the rate of BBB water-exchange could be early indicator of BBB dysfunction in neurodegenerative diseases and ageing, as demonstrated by our group [91] and others [211]. During the diffusion-time, water initially in blood may cross the BBB and experience the lower diffusion rate found in brain tissue. Similarly, spins in the extravascular space at the time of the first gradient lobe may exchange into blood by the time of the second, and experience the faster pseudo-diffusion of blood. For spins that exchange, the signal attenuation due to diffusion will be a mixture of both intravascular and extravascular environments. With longer diffusion-times, the number of spins crossing the BBB will increase, which may result in model inaccuracy when considering blood flow dynamics alone.

The aim of this study is to investigate and model the diffusion-time dependence of the DW-MRI signal using clinically feasible diffusion-times, to determine if the average blood velocity (v), capillary segment length (l) and BBB water-exchange time (τ) can be estimated in the human brain. We perform multi-diffusion-time DWI on ten healthy

volunteers, with intra-scan repeats on seven, across a range of b-values between 0 and 1000 smm^{-2}. We fit a diffusion-time dependent velocity-autocorrelation (VA) model and, to explore any effects of exchange on the intravascular signal, we extend the VA model to account for finite BBB water-exchange (VAX). We examine parameter estimates, assess residual sum of squares (RSS) and Akaike information criterion (AIC) values, and calculate the intra-scan coefficient of variation (CoV) to determine the most appropriate model for diffusion-time dependence of microcirculatory flow in grey and white matter.

5.5 Theory

5.5.1 Two compartment model

In the presence of diffusion-sensitising gradients, attenuation of the MR signal can be described by a two-compartmental model, describing the intra and extra-vascular contributions [14]. The total normalised signal is modelled as a sum of two exponentials:

$$\frac{S(b,\Delta)}{S_0} = fe^{-bD_b}H(b,\Delta) + (1-f)e^{-bD} \tag{5.1}$$

where $b = \gamma^2\delta^2G^2(\Delta - \delta/3)$ when employing pulsed gradient spin echo (PGSE) sensitisation. γ is the proton gyromagnetic ratio; G, the magnitude of the diffusion gradient pulses; δ, the duration of each diffusion gradient pulse and; Δ, the diffusion-time, the time between the gradient pulses. $S(b,\Delta)$ is the DW-MR signal as a function of b; S_0, the signal at b=0; D, the extravascular diffusion coefficient; and f, the perfusion fraction. D_b is the apparent diffusion coefficient of water in blood; and $H(b,\Delta)$ is the signal attenuation due to perfusion. The model assumes isotropic orientation of capillary segments and that they are distributed over 4π [176], the solid angle of a sphere.

5.5.1.1 Velocity-autocorrelation model

The velocity-autocorrelation (VA) model developed by Kennan et al. [33] models signal attenuation due to PGSE sequences under all dynamic flow regimes. The signal attenuation due to perfusion is modelled as a monoexponential:

$$H(b,\Delta) = e^{-bk(\Delta)} \tag{5.2}$$

where k is the perfusion attenuation coefficient due to microcirculatory flow in the presence of bipolar diffusion gradients:

$$k = \frac{\Omega v^2 T_0}{3\delta^2(\Delta - \delta/3)} \tag{5.3}$$

where v is the average blood velocity; T_0 is the average time that spins in the blood stay in a segment, and:

$$\Omega = \delta^2(\Delta - \delta/3) - 2T_0^2\delta - T_0^3 q \tag{5.4}$$

$$q = 2\exp\Big(-\frac{\Delta}{T_0}\Big) + 2\exp\Big(-\frac{\delta}{T_0}\Big) - \exp\Big(-\frac{\Delta+\delta}{T_0}\Big) - \exp\Big(-\frac{\Delta-\delta}{T_0}\Big) \tag{5.5}$$

This model assumes BBB water-exchange does not occur.

5.5.2 Accounting for finite blood-brain barrier water exchange

IVIM models currently ignore exchange of spins across the BBB, despite knowledge that water molecules exchange several times per second [211]. As diffusion-time increases, the fraction of spins initially present in the intravascular compartment that exchange into the extravascular compartment, and vice versa, increases. To model the effect of exchange on signal attenuation, we consider the replacement of intravascular water by extravascular water depending on the mean exchange time (also known as the residence time) of the spins in the intravascular compartment, τ. Assuming spins are well mixed in each compartment, the volume fraction of native intravascular spins entering the extravascular compartment after diffusion-time, Δ, is [211]:

$$f_{ex} = 1 - e^{-\Delta/\tau}. \tag{5.6}$$

The exponential term models the residue of intravascular spins that have not yet exchanged with the extravascular compartment after the diffusion-time, Δ. The effective (observed) perfusion attenuation coefficient in the presence of finite exchange is modelled as the mean of the perfusion and extravascular diffusion coefficients, weighted by the exchanged fraction f_{ex}:

$$k_{eff} = (1 - f_{ex})k + f_{ex}D \tag{5.7}$$

The derivation of Equation 5.7 is shown in the supplementary material.

5.6 Methods

Multi-diffusion-time DW-MRI data was acquired in ten healthy participants to investigate the diffusion-time dependence of microcirculatory flow. In order to estimate average blood velocity, v, and average vessel segment length, l, the velocity-autocorrelation (VA) model was applied. The effects of BBB water-exchange were also modelled using an adapted VA model (VAX). To determine the most appropriate model for parameter estimation, the Akaike information criterion (AIC_c) and intra-scan coefficient of variation (CoV) were assessed for both models in grey and white matter.

5.6.1 MRI acquisitions

Experiments were reviewed and approved by the University of Manchester Research Ethics Committee and written informed consent was obtained from all participants.

MRI was performed on a 3T GE Signa PET/MR scanner (GE Healthcare, Chicago, US) using a 32 multi-channel receiver head coil (Nova Medical Inc, Wilmington, US). Images were acquired for ten healthy participants (6 female, 4 male, mean age: 28 ± 5.8 years) – seven volunteers were scanned twice with the same protocol during the same scan session to assess intra-scan repeatability. Axial DW-MRI data (Figure 5.6 in supplementary material) was obtained over three orthogonal directions. The b-value was varied through ten values: 0, 10, 30, 50, 100, 200, 300, 500, 750 and 1000 smm^{-2}. For each b-value, the diffusion-time (Δ) was varied through ten values between 27 and 60 ms (subject average normalised signal versus b-value for each diffusion-time shown in Figure 5.7 in supplementary material). These acquisition parameters are shown in Table 5.1. The lowest diffusion-time was limited by the maximum gradient strength required to achieve high b-value data (b=1000 smm^{-2}). The magnitude of the diffusion gradient pulse (G) and gradient duration (δ) were altered to allow variation in the diffusion-time while maintaining the same b-value (Table 5.1). Other sequence parameters include: TR = 5525 ms, TE = 95 ms, voxel size $0.8125 \times 0.8125 \times 4$ mm^3. 3D IR-prepped FSPGR T1-weighted images were acquired for regional segmentation with the following parameters: TR = 6.9 ms, TE = 2.7 ms, TI = 400 ms, flip angle = 11°, isotropic voxel of length 1 mm.

Table 5.1: Diffusion-times, Δ, and pulse durations, δ, used in the DW imaging protocol for ten participants.

Δ (ms)	δ (ms)
27.73	20.36
30.07	19.09
33.02	17.83
35.98	16.80
39.95	15.70
42.93	15.00
45.92	14.40
49.89	13.70
54.87	12.96
59.86	12.34

5.6.2 Extraction of regional MRI signals

T1-weighted images requiring bias correction before segmentation were processed using FSL FAST [212]. Cortical reconstruction and volumetric segmentation was performed on all images with the Freesurfer image analysis suite (v6) [213], which is documented and freely available for download online (http://surfer.nmr.mgh.harvard.edu/). The Destrieux atlas [214] was used from available Freesurfer segmentation outputs.

SPM12 (http://www.fil.ion.ucl.ac.uk/spm) was used for re-slicing and co-registration of the T1-weighted images to the DW-MRI images. The DW-MRI signal from cortical grey matter (GM) and cerebral white matter (WM) regions were extracted. The trace of the signal across the three orthogonal diffusion directions was used. The models were then fit to the mean signal from each region, as described in the next section, in order to extract parameter estimates.

5.6.3 Model fitting

5.6.3.1 Estimation of D and f

Since the signal attenuation due to microcirculatory flow is of the order of 10-100 times larger than extravascular signal attenuation, the microcirculatory component is insignificant at b-values higher than 200-600 smm^{-2} (known as the b-value threshold) [131, 134, 139, 168] even in the presence of exchange (i.e. $fe^{-bD_b}H(b,\Delta) \rightarrow 0$). As such, we can separate the components using a two-step method, an approach commonly used in IVIM studies [131, 134, 139, 158, 168]. Model parameters describing the extravascular component were estimated using b-values 500, 750 and 1000 smm^{-2}. The extravascular diffusion coefficient, D, and perfusion fraction, f, were estimated for each diffusion-time separately by fitting the following model to the normalised data:

$$\frac{S}{S_0} = (1-f)e^{-bD} \tag{5.8}$$

The 'lsqcurvefit' function in Matlab (R2019b) was used (MathWorks, Natick, US) with a trust-region-reflective algorithm. All fitting described uses the same function.

5.6.3.2 Estimation of k as a function of Δ

To demonstrate the diffusion-time dependence of k, we first isolated the intravascular component of the signal by subtracting the extravascular component from the total normalised signal for each diffusion-time and dividing by f. The perfusion attenuation coefficient, k, was estimated by fitting the following exponential model to data with b <500

smm^{-2}:

$$\frac{1}{f}\left(\frac{S}{S_0} - (1-f)e^{-bD}\right) = e^{-bD_b+c}H(b,\Delta) \tag{5.9}$$

where $H(b,\Delta) = H(b) = e^{-bk}$, and c is a parameter added to improve fitting (see Chapter 4, Section 4.5.3.2). D_b was set to a fixed value of 1.75×10^{-3} mm^{2}s^{-1} [131].

5.6.3.3 Estimation of blood velocity, v, correlation time, T_0, vessel segment length, l, and exchange time, τ

To estimate T_0 and v, assuming no BBB water-exchange, Equation 5.9 was fit to all diffusion-times and b-values<500 smm^{-2} simultaneously, using Equation 5.2 for $H(b,\Delta)$ and Equation 5.3 for k. To estimate T_0, v and τ, assuming finite water-exchange, Equation 5.7 was used for k. Fitting of models to the isolated perfusion data for three subjects is shown in Figure 5.8 in supplementary material.

Estimates of vessel segment length, l, were generated for both no exchange, and finite exchange, using their respective estimates of v and T_0 [33]:

$$l = 2vT_0. \tag{5.10}$$

5.6.4 Statistical analysis

Prior to estimating summary statistics of parameter estimates, outliers were removed by excluding those outside three median absolute deviations of the median. This method was chosen rather than the standard deviation since it is not affected by large outliers [199]. Following outlier removal, the mean parameter estimate was calculated with standard error for each region.

5.6.4.1 Assessing diffusion-time dependence

To determine if any relationship exists between the estimated parameters f, D and k, and the diffusion-time, and to inform our analysis methods, one way repeated measures analysis of variance (ANOVA) tests were performed for GM and WM. The 'ranova' function was used in Matlab (R2019b).

5.6.4.2 Assessing model fit

To compare the VA and VAX models, the Akaike information criterion, corrected for small number of data points (AIC_c), was calculated for grey and white matter fits using [215]

$$AIC_c = N\ln\left(\frac{RSS}{N}\right) + 2m + \frac{2m(m+1)}{N-m-1} \tag{5.11}$$

where N is the number of data points used in the fit, m is the number of parameters in the model: an additional parameter must be included for the Gaussian noise hypothesis for the signal residuals [131]. RSS is the residual sum of squares from the 'resnorm' output of the 'lsqcurvefit' function in Matlab (2019b). Paired student's t-tests were performed between the AIC_c values for the VA and VAX models, for GM and WM, to determine if differences were statistically significant ($p<0.05$). The 'ttest' function in Matlab (R2019b) was used.

The additional parameter in the VAX model may increase model accuracy, however this likely comes at the cost of reduced precision due to increased freedom to fit to experimental noise. To investigate whether the VAX model can produce a well-defined minima, and thus robust parameter estimates, the value of τ was fixed in the fitting process through one thousand values from 0.005 to 5 s and the RSS calculated.

5.6.4.3 Assessment of intra-scan repeatability

Seven volunteers underwent repeat measurements within the same scan session. The coefficient of variation (CoV) was calculated to investigate repeatability of the measures and analysis methods:

$$\text{CoV}(\%) = 100\frac{\sigma}{\mu} \tag{5.12}$$

where σ is the within subject standard deviation and μ the mean. σ is calculated using [215]

$$\sigma = \sqrt{\frac{\Sigma_{i=1}^{n}(x_{i,1} - x_{i,2})^2}{2n}} \tag{5.13}$$

where n is the number of subjects, x_1 and x_2 are the parameter estimates for the first scan and repeat scan, respectively. μ is found using:

$$\mu = \frac{\Sigma_{i=1}^{n}(x_{i,1} + x_{i,2})}{2n}. \tag{5.14}$$

5.7 Results

5.7.1 Velocity-autocorrelation model accounting for finite blood-brain barrier water-exchange

Figure 5.1 shows the VAX model as a function of the diffusion-time (Δ), for $\tau = 0.05$ to 0.5 s; $D = 7{\times}10^{-4}$ mm^{2}s^{-1}; $v = 1.3$ mms^{-1}; $T_0 = 19$ ms; and, $\delta = 10$ ms. As τ decreases, indicating less time spent in the intravascular compartment, thus increasing exchange of spins, the peak of the curve decreases in magnitude and shifts to a lower diffusion-time.

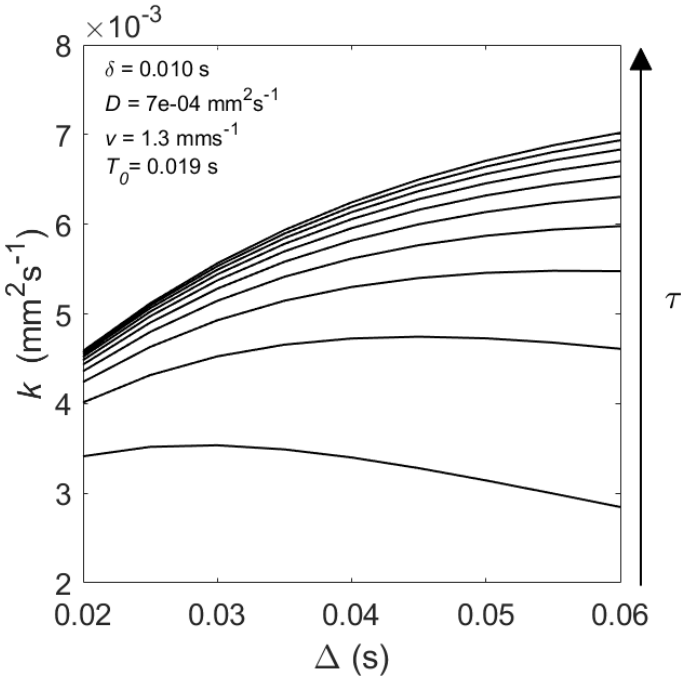

Figure 5.1: The velocity-autocorrelation model when accounting for effects of trans-BBB-water-exchange (VAX) as a function of diffusion-time, Δ. The diffusion coefficient, D, was set to $7{\times}10^{-4}$ mm^{2}s^{-1}; the velocity, v, was set to 1.3 mms^{-1}; the correlation time, T_0, was set to 19 ms; and the pulse gradient width, δ, set to 10 ms. The exchange time, τ, for each curve increases moving up the figure, indicating lower rates of exchange.

5.7.2 Diffusion-time dependence of f, D and k

Figure 5.2 shows the mean value ($\pm$ standard error) across participants for f, D, and k, as a function of the diffusion-time (Δ). The figure also shows p-values from one-way repeated measure ANOVA tests. f and k varied significantly with diffusion-time for both GM and WM, whereas D did not.

f shows a strong linear decrease with diffusion-time in both GM and WM. In GM, k

increases non-linearly with diffusion-time, at a faster rate at shorter diffusion-times. In WM, k increases slowly at shorter diffusion-times and decreases rapidly at higher diffusion-times – we hypothesize this reduction in k at high diffusion-time is caused by rapid BBB water-exchange in WM. Values for f and D are lower for WM than for GM. This is an expected result since WM is known to have a lower blood volume than GM [216], and there are increased barriers to diffusion in WM. Results for D and k agree well with literature values [165–168, 217]. Those for f sit within the range of values presented in literature for the brain [217], however one might expect them to be approximately half of their current value [216].

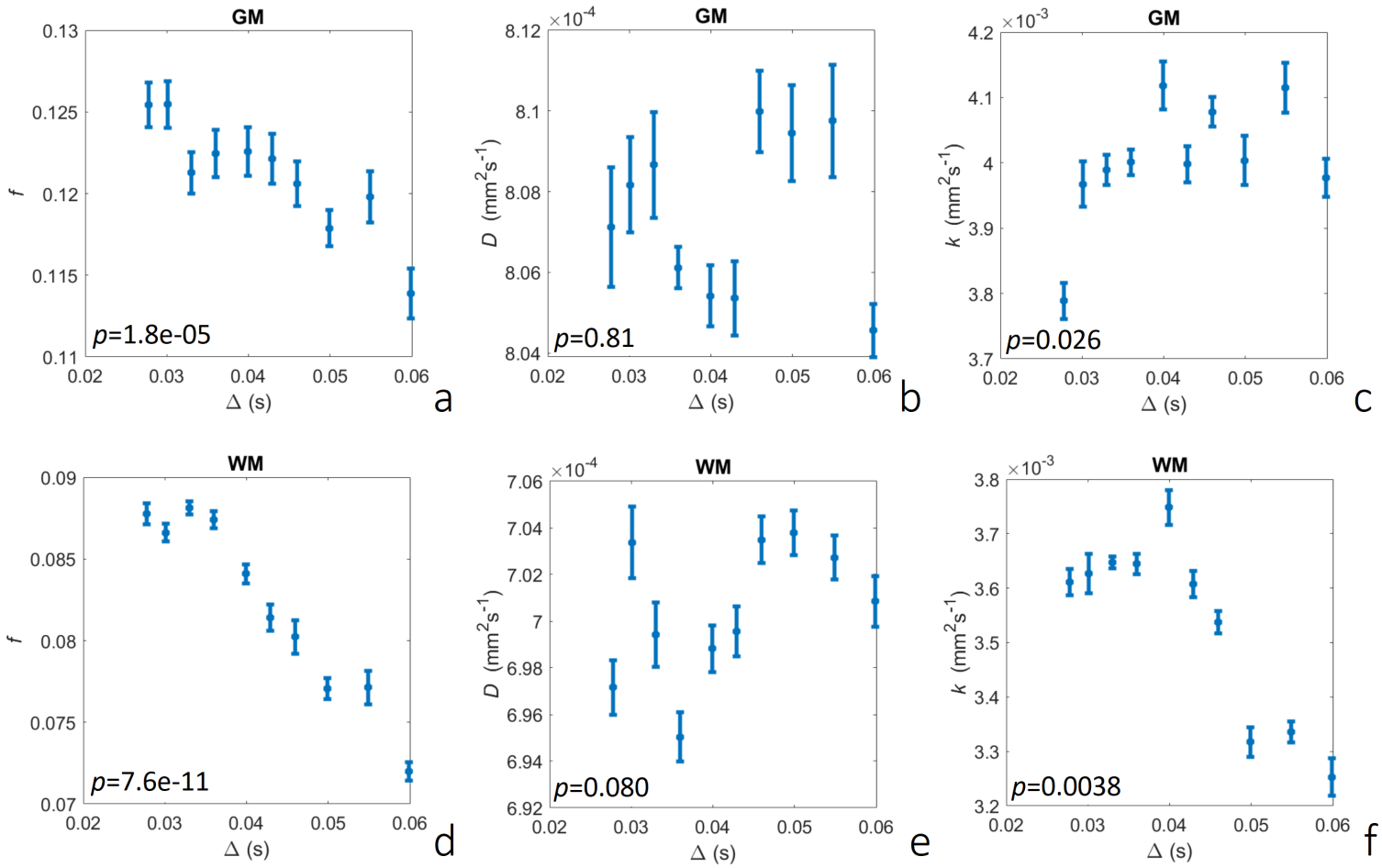

Figure 5.2: The grey matter (GM) and white matter (WM) parameter mean with standard error, for the perfusion fraction, f, in (a) and (d); the diffusion coefficient, D, in (b) and (e); and, the perfusion coefficient, k, in (c) and (f). Repeated-measures one-way analysis of variance (ANOVA) p-values are shown for each parameter.

5.7.3 Model comparison using Akaike information criterion

Figure 5.3 shows the difference in AIC_c between the VAX and VA models for GM and WM. Results show the VAX model is preferable for the majority of participants in WM ($p = 0.0028$) and the results were inconclusive for GM ($p = 0.29$). The spread of data is low for GM and close to zero, indicating the two models had a very similar fit which was consistent across all participants, although there is a slight skew towards the VA model. In WM, VAX produced better fits than the VA model. The difference in AIC_c between VA and VAX model in WM was more variable than for GM, perhaps indicating some heterogeneity in the degree of water-exchange between regions and participants.

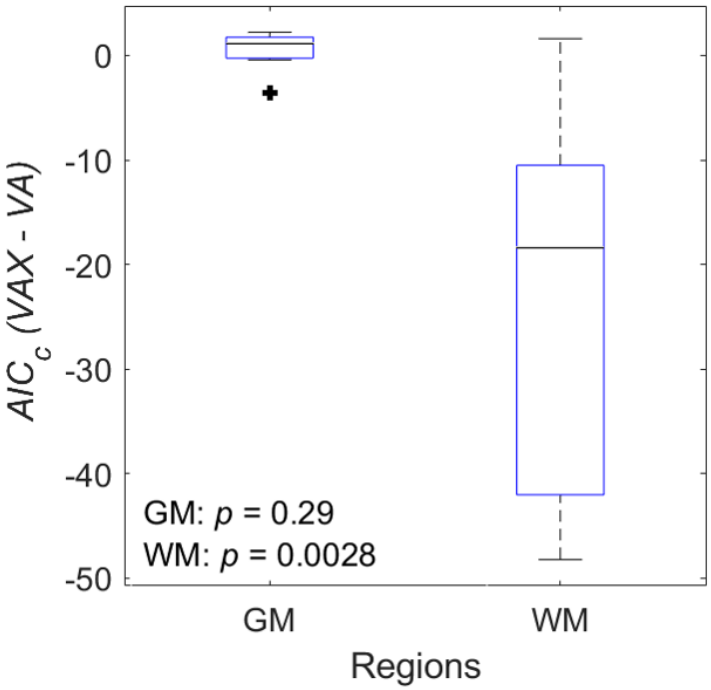

Figure 5.3: Boxplots of the difference in AIC_c of the VAX and VA models for grey matter (GM) and white matter (WM). Paired sample t-tests between VAX and VA AIC_c values give p =0.29 and p =0.0028 for GM and WM respectively.

Figure 5.5 (supplementary material) shows the minimum RSS and corresponding value of τ from the VAX model fit for each participant for GM and WM. The minimum RSS is well-defined in WM for all participants and for nine participants in GM, demonstrating that parameter estimates are robust.

5.7.4 Parameter estimates from the VA and VAX models

Group mean values for T_0, l and τ in GM and WM are shown in Table 5.2 for the VA and VAX models. Figure 5.4 shows individual estimates, with group average marked in blue. The participant average blood velocity, v, is higher for the VA model compared to the VAX model in both GM and WM. v in WM for the VA model is approximately 3-4 times higher than other estimates of v for all participants, closer to values one would expect in larger vessels [35]. Note that the plots of T_0 and l are close-ups due to the presence of outliers in GM for the VA model ($T_0 = 0.819$ s and $l = 1567$ μm). Estimates of l this high do not agree with literature values [218–220].

Table 5.2: Group mean values of the velocity (v), correlation time (T_0), capillary segment length (l) and the exchange time (τ) for two models (VA and VAX) with standard error of the mean, for grey matter (GM) and white matter (WM).

	GM		WM	
Parameter	VA	VAX	VA	VAX
v (mms^{-1})	1.33 ± 0.054	1.07 ± 0.024	4.44 ± 0.13	1.27 ± 0.060
T_0 (ms)	6.29 ± 1.2	16.1 ± 3.1	0.548 ± 0.35	18.6 ± 3.5
l (μm)	17.6 ± 2.4	36.2 ± 5.8	4.79 ± 0.17	46.4 ± 8.1
τ (s)	-	0.125 ± 0.022	-	0.0622 ± 0.0055

Participant average vessel segment length, l, is higher for the VAX model compared to the VA model. Estimates were more variable for the VAX model, due to high levels of variability in T_0. Estimates of l in WM obtained using the VA model were much lower than other estimates ($l_{VA,WM} = 4.79 \pm 0.17\,\mu$m), which is on the order of vessel diameter rather than length [221], and is a result of low estimated T_0. Estimates of l obtained using the VAX model were in better agreement with literature data [218–220].

The water-exchange time τ is lower for WM than GM, indicating that the BBB in WM has higher permeability to water. Outlier removal is shown in supplementary material (Table 5.4) and on individual point plots in Figure 5.4. Outlier removal is low for both models in WM, however there are higher levels in GM: 30% for v_{VA}, $T_{0,VAX}$ and l_{VAX}.

5.7.5 Assessment of intra-scan repeatability

Intra-scan CoV of parameters are shown in Table 5.3. CoV of all parameters are generally lower (more repeatable) in WM than GM for both models. CoV values are lower for the VA model than the VAX model in both GM and WM, with exception of v_{GM}. The CoV for the VA model in WM is low, likely reflecting the inability of the model to fit to data (as shown by AIC_c in Figure 5.3).

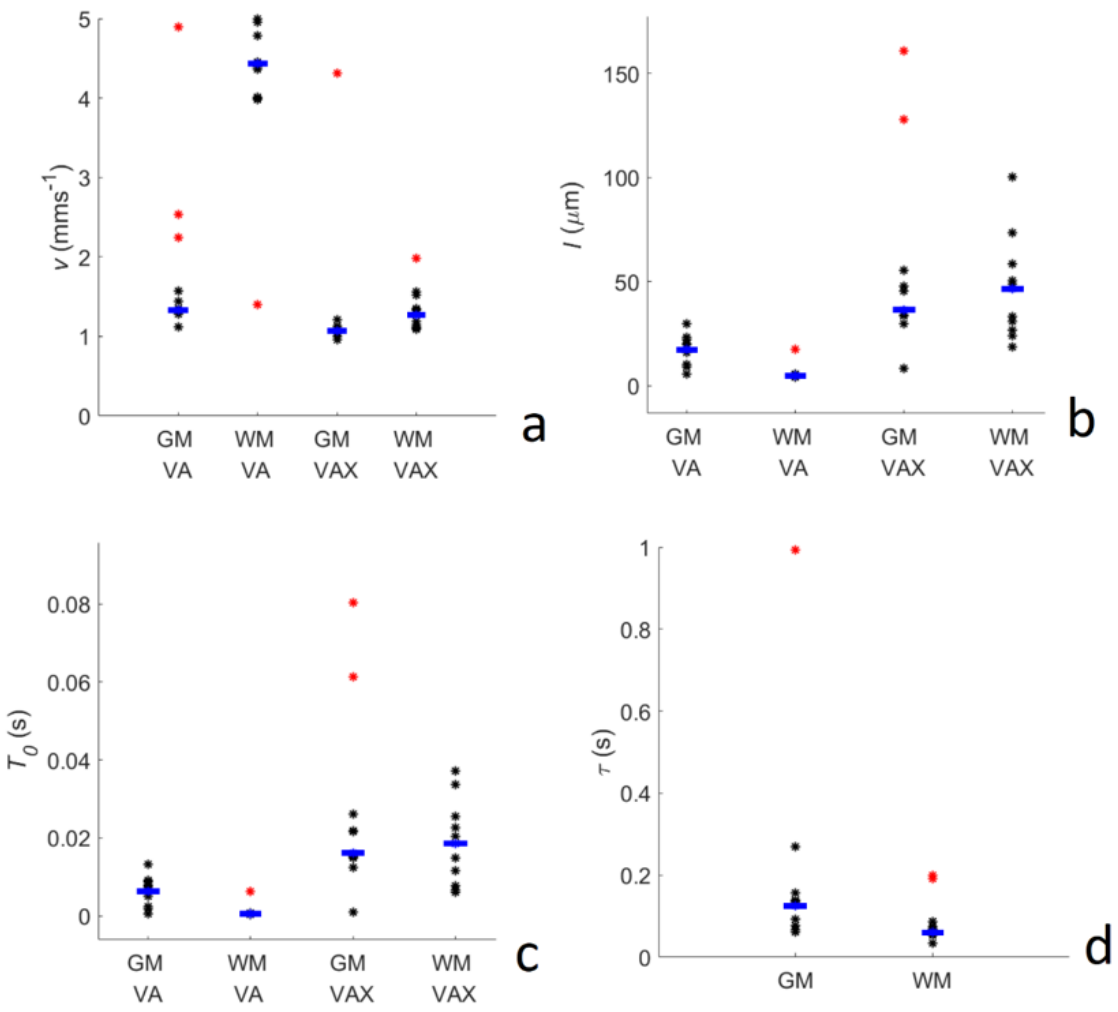

Figure 5.4: Parameter estimates of velocity (v), correlation time (T_0), capillary segment length (l) and the exchange time (τ) for two models (VA and VAX) for grey matter (GM) and white matter (WM). Plots for T_0 and l are close-up images with outliers for GM VA removed at $T_0 = 0.819$ s and $l = 1567$ μm. Red points show outliers, and blue lines, the mean.

In GM, the VAX model fit gives repeatable estimates of v, however repeatability for τ, T_0, and l is very poor with CoV>100%. In WM, the repeatability for T_0, l and τ are acceptable with values of 47.5%, 40.5% and 47.1% respectively.

Table 5.3: Intra-scan coefficient of variation (%) calculated from repeat measures of seven volunteers for the pseudo-diffusion coefficient (D^*), average velocity (v), correlation time (T_0), average capillary segment length (l) and the blood water exchange time (τ) for two models (VA and VAX).

	GM		WM	
Parameter	VA	VAX	VA	VAX
v	23.2	13.8	2.77	61.1
T_0	30.8	209	8.23	47.5
l	18.7	200	2.56	40.5
τ	-	123	-	47.1

5.8 Discussion

In this study, we investigate the diffusion-time dependence of the MR signal attenuation due to microcirculatory flow in the brain by modelling the effects of blood velocity, capillary segment length and blood-brain barrier water-exchange (Figure 5.1). Through estimating standard IVIM model parameters at ten diffusion-times, we determine that f and k have diffusion-time dependence (Figure 5.2). We show that model fitting is sensitive to the exchange time of exchanging blood water (Figure 5.5) and that the VAX model provides a better fit for WM data (Figure 5.3). Using the most appropriate model according to AIC_c, reasonable parameters estimates are produced for v, T_0, l and τ for both GM and WM (Table 5.2 and Figure 5.4). Intra-scan repeatability (Table 5.3) shows v and l can be estimated with high precision for the VA model in GM, and with reasonable precision for the VAX model in WM.

We observed a linear decrease in f with increasing diffusion-time, which is opposite to that observed in a study by Wu et al. [176]. This difference might be due to different pulse sequences or fitting methods used. We suspect the decrease in f is due to reduced contribution of larger vessels with increasing diffusion-time, since spins would have increased time to leave the voxel and thus not contribute to phase distribution. The absolute values of f are higher than expected (approximately double [217]), this is likely due to the high b-value threshold used. Evidence shows IVIM parameters are dependent on the b-value threshold [139, 140], perhaps due to non-negligible intravascular contribution which would increase as the threshold is lowered. Studies show f increases with b-value threshold and, D and D^* both decrease [139, 140].

The perfusion attenuation coefficient, k, also exhibited diffusion-time dependence. In GM, k increased with diffusion-time, and plateaued as predicted by the VA model [33]. This could be due to an increasing number of changes in direction in blood flow with increasing diffusion-time (i.e. blood flow moving from the ballistic to the diffusive regime [176]), thus increased dephasing and higher signal attenuation. The plateau likely occurs when the condition for pseudo-diffusive blood flow has been met. In WM, k peaked, then sharply decreased with diffusion-time. This behaviour is not compatible with the VA model, and we hypothesized this decrease in k could be due to exchange of water across the BBB (Figure 5.1). We proposed an adaptation to the VA model to account for finite water-exchange and were encouraged that the VAX provided a better fit to this data.

Adding complexity to models to improve accuracy must always be balanced against the ability to robustly estimate the parameters of interest. By examining the residual sum of squares with varying exchange time, τ, (Figure 5.5) we determined that fitting the VAX model was feasible. The VAX model was shown to be the better fit for WM (Figure 5.3) with lower AIC_c values, agreeing with predictions from Figure 5.2. For GM, results were inconclusive. AIC_c values for the two models were close, however there was insufficient evidence to indicate that the VAX model provided a better fit. These results are consistent with the observed diffusion-time dependency of k (Figure 5.2). The mean value for k decreases with diffusion-time for WM which may indicate a strong effect of water-exchange (Figure 5.1). In GM, k does not decrease which would indicate a weaker effect and thus difficulty characterising τ.

Estimates of v and l for the VA model in WM (Table 5.2 and Figure 5.4) are not characteristic of the microvasculature; with a mean of $4.79 \pm 0.17\mu$m, l is of the order of capillary diameter [220, 221], not segment length, and v of 4.4 mms^{-1} is too high for capillary flow [35]. Estimates of v converge on the upper bound of 5 mms^{-1} in a small number of cases, indicating either the model is failing to fit the data well, or the information content of the data is not sufficient to estimate v. The VAX model in WM produced estimates of v that are more consistent with the literature, indicating a more accurate model of the underlying physiology. We conclude therefore that the VA model may be an inaccurate model for characterising microvascular flow in WM, and that a model that incorporates BBB water-exchange may be more accurate. In GM, parameter estimates vary across the two models, but neither are inconsistent with literature, however CoV is lower for the VA model indicating this model may be preferable.

Estimates of v in human brain capillaries are scarce in literature. Smith at al. [218] used India ink injected human brain with confocal laser microscopy and simulations to estimate v in the temporal cortex of 1.48 ± 0.34 mms^{-1}. However, these simulations assumed all vessels had a diameter of 5 μm, hence this estimate of v may be low. Although, the same study also estimates v in rat brain to be 1.97 ± 0.43 mms^{-1}, which is similar to in-vivo

laser-scanning confocal microscopy studies [198], meaning the human estimate could be valid. Our estimate of v=1.33 mms^{-1} for the VA model in GM seems reasonable compared to this estimate. Although it is not possible to directly measure v in human brain capillaries due to the invasive nature of methods, red blood cell (RBC) velocity has been measured in the capillaries of the retina and skin. Wolf et al. [222] measure RBC velocity to be 2.87 mms^{-1} in the human retina and Ye et al. [223] and Hahn et al. [224] measure RBC velocity in the skin to be 1 mms^{-1} and 0.7 mms^{-1} respectively. Hence our estimates of 1.07 ± 0.024 and 1.27 ± 0.060 mms^{-1} using the VAX model in GM and WM respectively, and 1.33 $\pm$ 0.054 mms^{-1} using the VA in GM seem reasonable. Ahlgren et al. [164] use flow compensated MRI to measure velocity in frontal GM and WM to be 1.81 and 1.78 mms^{-1} respectively, whilst this measure is greater than ours, the results are very similar across regions and broadly agree with our findings.

Estimates of l, of $36.2 \pm 5.8\,\mu$m and $46.4 \pm 8.1\,\mu$m in GM and WM respectively, for the VAX model agree well with results in literature. For VA in GM, l is lower than literature values. Smith et al. [218] present a mean segment length in the human temporal cortex of $60.2 \pm 3.1\,\mu$m. Cassot et al. [219] use India ink injected human brain and confocal laser microscopy in the cortex to estimate a mean segment length of 56.6 μm and 62.2 μm in two brains. The peaks on the frequency distribution plots are skewed however and the mode appears to sit around 20 μm which agrees well with our GM-VA result of $17.6 \pm 2.4\,\mu$m. Lauwers et al. [220] also use India ink and confocal laser microscopy in the cortex to estimate a mean capillary length of $52.95 \pm 49.75\,\mu$m with a median of 36.07 μm. These results agree well with VAX estimates and the estimate for VA-GM sits within the standard deviation. Tata et al. [225] show that the measures of l vary depending on the histochemical method used which could make validation difficult. The minimum segment length is 10 μm larger for frozen India ink tissue than for celloidin standard perfusate tissue. The precise values of l and v obtained using DW-MRI and modelling methods such as those used in this study will likely depend on the b-values and diffusion-times used, and further work should determine the effects of acquisition parameters on parameter estimates.

Intra-scan repeatability data (Table 5.3) shows the VA model gives more precise estimates than the VAX model in GM. The VA model in WM is highly repeatable despite VAX having the better fit; although parameter values are not characteristic of microvascular velocity and length. We predict that this high repeatability comes from the inability of the model to capture variability (particularly the reduction of k with diffusion-time) in the data. Repeatability for VAX in WM is good for most parameters, with the exception of v. This may be due to the low SNR in WM due to smaller blood volume - although one might expect this to affect all parameters. It may also result from a lack of increasing k at lower diffusion-times for some participants, which is predicted by the VA model.

We found lower τ (higher exchange rate) in WM than GM. This is consistent with

other studies which have measured both GM and WM τ [211]. However, in comparison with other studies, our estimated values for τ are approximately 3.5-7 times lower. This is possibly due to the sensitivity of our method to exchange through capillaries, as opposed to methods that also include contributions from larger 'non-exchanging' vessels such as arterioles. Another explanation for the lower τ values could be inaccurate modelling of BBB water-exchange, or bias introduced from the two-step method. It is possible that vessels in WM require higher permeability to ensure the total amount of water entering and exiting the brain per unit time is maintained relative to GM, which has a higher blood volume.

A study using flow-compensated DW-MRI has shown that the Gaussian phase approximation of the VA model may be invalid when blood flow does not change microvessel segment more than three times [35]. Using FC gradients allows for extraction of v and, with the method proposed by Wetscherek et al. [35], T_0, therefore giving l. The FC method increases sensitivity to flow in capillaries by nulling signal contribution from larger vessels where blood does not change direction. However, estimates by Wetscherek et al. [35] in the liver and pancreas suggest v is higher than expected in capillaries, which would lead to overestimation of l. Ahlgren at al. [164] produce estimates of v closer to those expected in brain capillaries when using the Gaussian phase approximation. Increased imaging times and sensitivity to eddy currents of flow-compensated methods mean that our proposed method may be more appropriate for clinical use. Although, Gurney-Champion et al. [156] do show that a clinically feasible protocol is possible with flow-compensated gradients in strongly perfused organs.

One limitation of our data is the non-constant δ value (Table 5.1). Whilst effects are included in the VA model, they are not accounted for in the extravascular model. In the two-step method used, the extravascular signal is subtracted from the intravascular signal for each diffusion-time. This method accounts for the effects of diffusion-time on the extravascular signal attenuation, but does not account for δ. A small amount of literature exists describing the effect of the pulse gradient width on the extravascular DW-MRI signal. In the narrow pulse limit, the apparent diffusion coefficient (ADC) approaches the true diffusion coefficient [226], hence the smaller the pulse width, the more accurate the measure of the ADC. Zielinski and Sen [227] find a maximum error in the ADC of 20% when $\delta = \Delta$ in a highly restricted but open geometry (e.g. in rock). In an open but less restricted geometry, which is likely to be more characteristic of the brain, the maximum error is around 6% [227]. This maximum error is likely to be at shorter diffusion-times where the ratio of δ/Δ is higher (e.g. the highest ratio at $\Delta = 27.73$ ms, with $\delta = 20.36$ ms, was 0.73). These errors could have propagated through the analysis pipeline. The effect of δ is also not included in the model of exchange, however because $\delta < \Delta$ we expect these effects to be very small, particularly at long diffusion-times where exchange has the most impact.

A further limitation is the use of the entirety of cortical GM and cerebral WM as ROIs, rather than the use of sub-regions, thus assuming uniformity over the brain. Sub-region analysis may be more useful.

5.9 Conclusion

In this study, we show the diffusion-time dependence of the standard perfusion IVIM parameters in normal human brain. We use a velocity-autocorrelation model developed by Kennan et al. [33] to model the diffusion-time dependence of the intravascular component of the DW-MR signal. We investigated effects of BBB water-exchange and determined that the VA model is most appropriate for grey matter and the VA model with effects of exchange (VAX) for white matter. Parameter estimates agree well with literature values. The intra-scan coefficient of variation show that parameter estimates for the VA model in grey matter have good repeatability, in white matter the VAX model has reasonable repeatability. We have shown that multi-diffusion-time DW-MRI is able to estimate microvessel blood velocity and segment length in the human brain.

5.10 Acknowledgements

The authors wish to thank Damien McHugh for useful discussions regarding modelling DW-MR data. AP is financially supported by the Addenbrooke's Charitable Trust and the National Institute for Health Research [Cambridge Biomedical Research Centre at the Cambridge University Hospitals NHS Foundation Trust]. The views expressed are those of the authors and not necessarily those of the NHS, the NIHR or the Department of Health and Social Care

5.11 Funding

The authors wish to thank the Medical Research Council (MRC) for PhD funding, and the Engineering and Physical Sciences Research Council (EPSRC; grant EP/M005909/1) for funding data acquisition.

5.12 Supplementary materials

5.12.1 Effects of BBB water-exchange on the intravascular signal attenuation coefficient, k

BBB water-exchange is characterised by the mean exchange time, τ, which describes the mean time that spins stay in a compartment before moving to another. As time passes, water-exchange between compartments means that the fraction of spins originally present in a particular compartment decreases, i.e. in DW-MRI, the number of spins which were

present in the intravascular compartment at the onset of diffusion sensitisation gradients decreases. The same is true for spins originally present in the extravascular compartment. In this manuscript, the diffusion-time is varied to access different blood flow regimes, thus the amount of total water that exchanges between compartments will also vary, affecting signal attenuation.

The signal attenuation due to diffusion sensitisation gradients is defined as:

$$\frac{S}{S_0} = fe^{-bD_b}H(b,\Delta) + (1-f)e^{-bD} \tag{5.15}$$

where the first and second term represent the intravascular and extravascular compartments respectively, and $H(b,\Delta) = e^{-bk(\Delta)}$.

To model the effect of BBB water-exchange on signal attenuation, we assume:

1. that intravascular water is replaced by water from the extravascular space,
2. that spins are well mixed in each compartment,
3. that spins only exchange once during the diffusion-time, which may not be true for very fast exchange ($\tau < \Delta$),
4. contributions from blood flow are ignored.

The residue of intravascular spins left (non-exchanged spins) after diffusion-time Δ is given by $e^{-\Delta/\tau}$. These spins contribute the following attenuation to the total intravascular diffusion-related signal loss $e^{-\Delta/\tau}e^{-bk}$. The intravascular spins that have left the blood compartment (exchanged) are replaced with $(1-e^{-\Delta/\tau})$ spins from the extravascular compartment. These spins contribute the following attenuation to the total intravascular diffusion-related signal loss: $(1-e^{-\Delta/\tau})e^{-bD}$.

The total effect of exchange on the intravascular signal attenuation can thus be described as:

$$H(b,\Delta) = e^{-\Delta/\tau}e^{-bk(\Delta)} + (1-e^{-\Delta/\tau})e^{-bD} \tag{5.16}$$

where the volume fraction of spins entering the extravascular compartment from the intravascular compartment can be written as $f_{ex} = 1 - e^{-\Delta/\tau}$. The intravascular signal attenuation becomes:

$$H(b,\Delta) = (1-f_{ex})e^{-bk} + f_{ex}e^{-bD}. \tag{5.17}$$

The low number of small b-values ($b \leq 300$ smm^{-2}) used in this study mean it is not justified to fit a biexponential model. As such, we use first order approximations to produce a monoexponential model of the effects of BBB water-exchange on intravascular signal attenuation.

The first order Taylor expansion of $H(b, \Delta)$ gives:

$$H(b, \Delta) = 1 - b((1 - f_{ex})k + f_{ex}D). \tag{5.18}$$

This can be approximated to:

$$H(b, \Delta) = e^{-bk_{eff}} \tag{5.19}$$

where:

$$k_{eff} = (1 - f_{ex})k + f_{ex}D. \tag{5.20}$$

5.12.2 Figures and tables

Table 5.4: Percentage outliers removed for the pseudo-diffusion coefficient (D^*), average velocity (v), correlation time (T_0), average vessel segment length (l) and the exchange time (τ) for two models (VA and VAX).

	GM		WM	
Parameter	VA	VAX	VA	VAX
v (mms^{-1})	30	10	10	10
T_0 (ms)	0	30	10	0
l (μm)	0	30	10	0
τ (s)	-	10	-	20

Residual sum of squares (RSS) minimum and corresponding residence time (stepped τ) from VAX model fitting with stepped fixed values of τ (steps of 0.005), and estimates from routine fitting (free τ).

	GM			WM		
Participant ID	**Minimum RSS**	**Stepped τ**	**Free τ**	**Minimum RSS**	**Stepped τ**	**Free τ**
007	0.094	0.090	0.092	0.034	0.035	0.034
008	0.020	0.060	0.061	0.0094	0.20	0.20
023	0.20	0.13	0.13	0.12	0.055	0.054
026	0.016	0.075	0.077	0.019	0.065	0.065
029	0.031	0.065	0.066	0.031	0.060	0.058
031	0.027	0.15	0.16	0.021	0.060	0.058
032	0.024	0.14	0.13	0.027	0.075	0.075
033	0.045	0.14	0.14	0.040	0.070	0.069
034	0.030	0.25	0.27	0.021	0.085	0.086
035	0.047	1	0.99	0.031	0.19	0.19

a

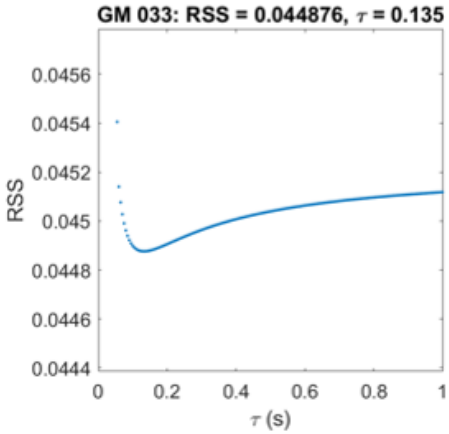

b

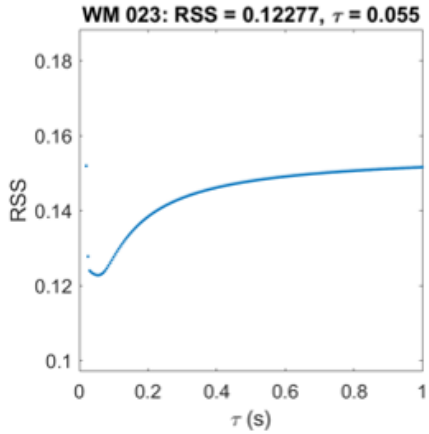

c

Figure 5.5: (a) Table of minimum residual sum of squares (RSS) and associated τ values from the VAX model fits with stepped τ (0.005 step size) ranging from 0 to 1 s. The estimate of free τ for the VAX model is also shown. GM is grey matter and WM is white matter. (b) shows the plot of RSS versus stepped τ values for GM for 033. (c) shows the plot of RSS versus stepped τ value for WM for 023.

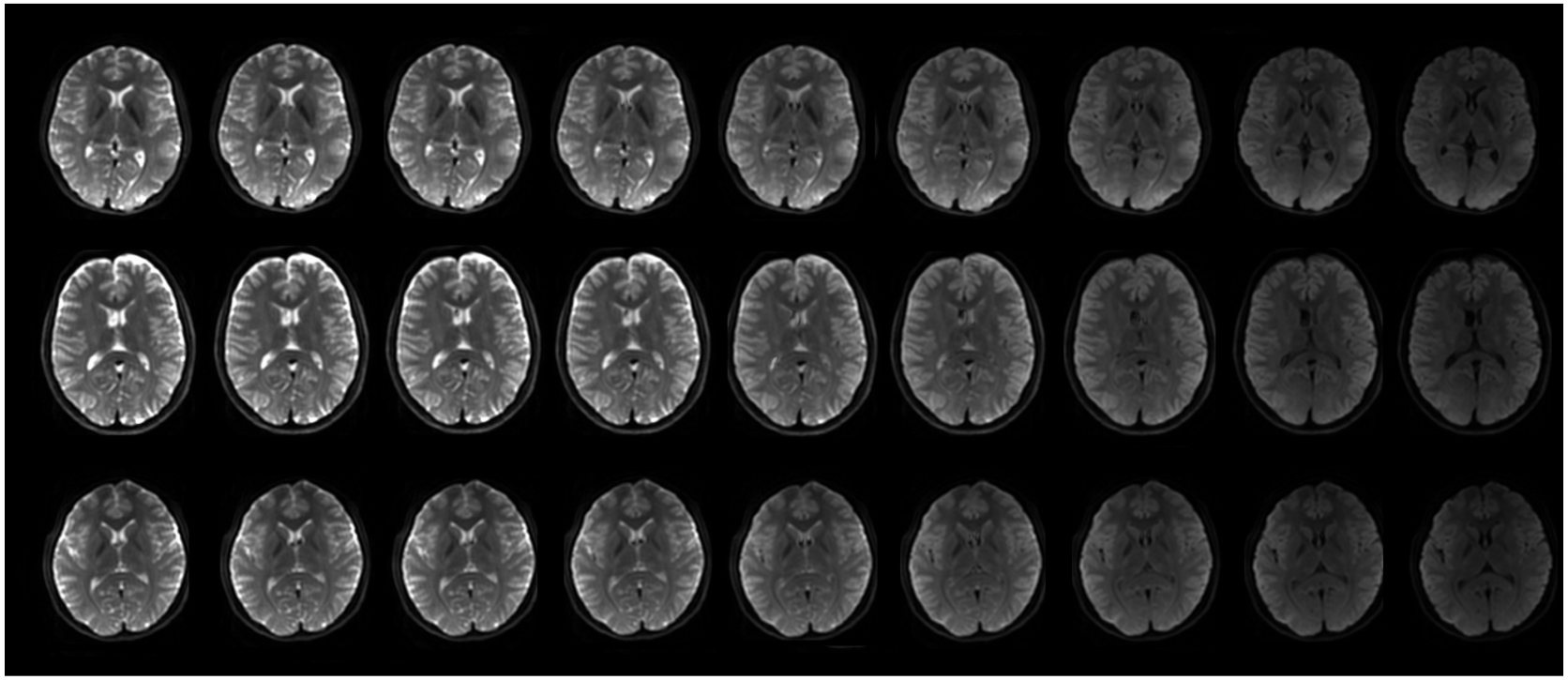

Figure 5.6: Mid-axial slices of diffusion-weighted (DW) MR images for three subjects (007, 008 and 023) with increasing b-value. b= 10, 30, 50, 100, 200, 300, 500, 750 and 1000 smm^{-2} moving from left to right.

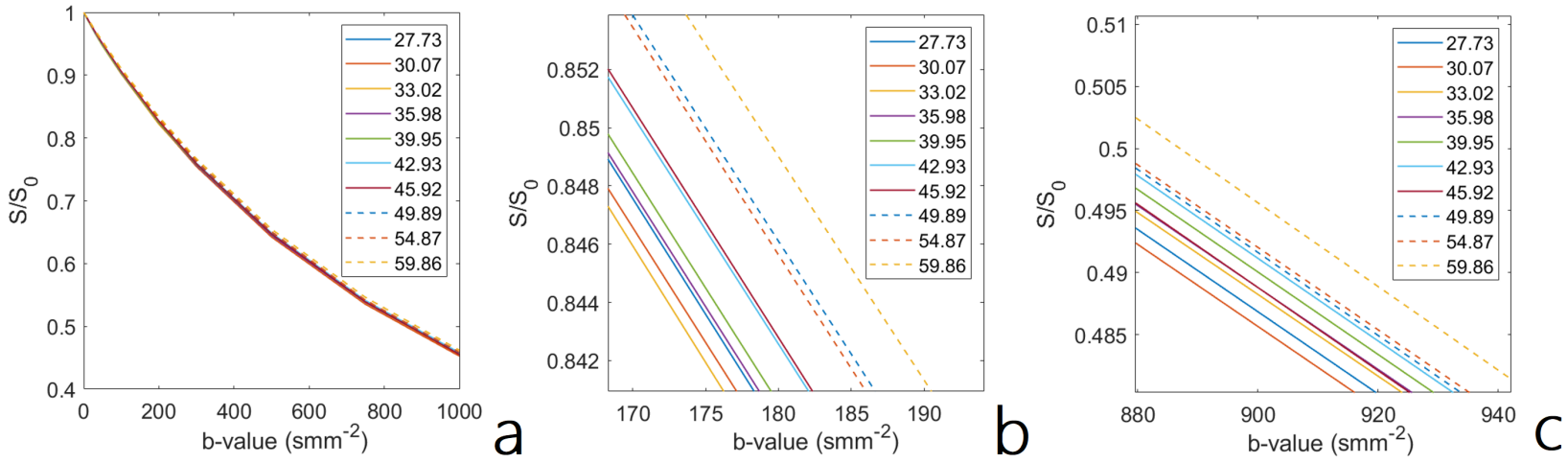

Figure 5.7: Subject average normalised diffusion-weighted MRI signal (S/S_0) for white matter (WM) versus b-value for ten values of diffusion-time (Δ in ms). (a) shows the full b-value range, (b) shows the signal at low b-values and (c) shows the signal at high b-values.

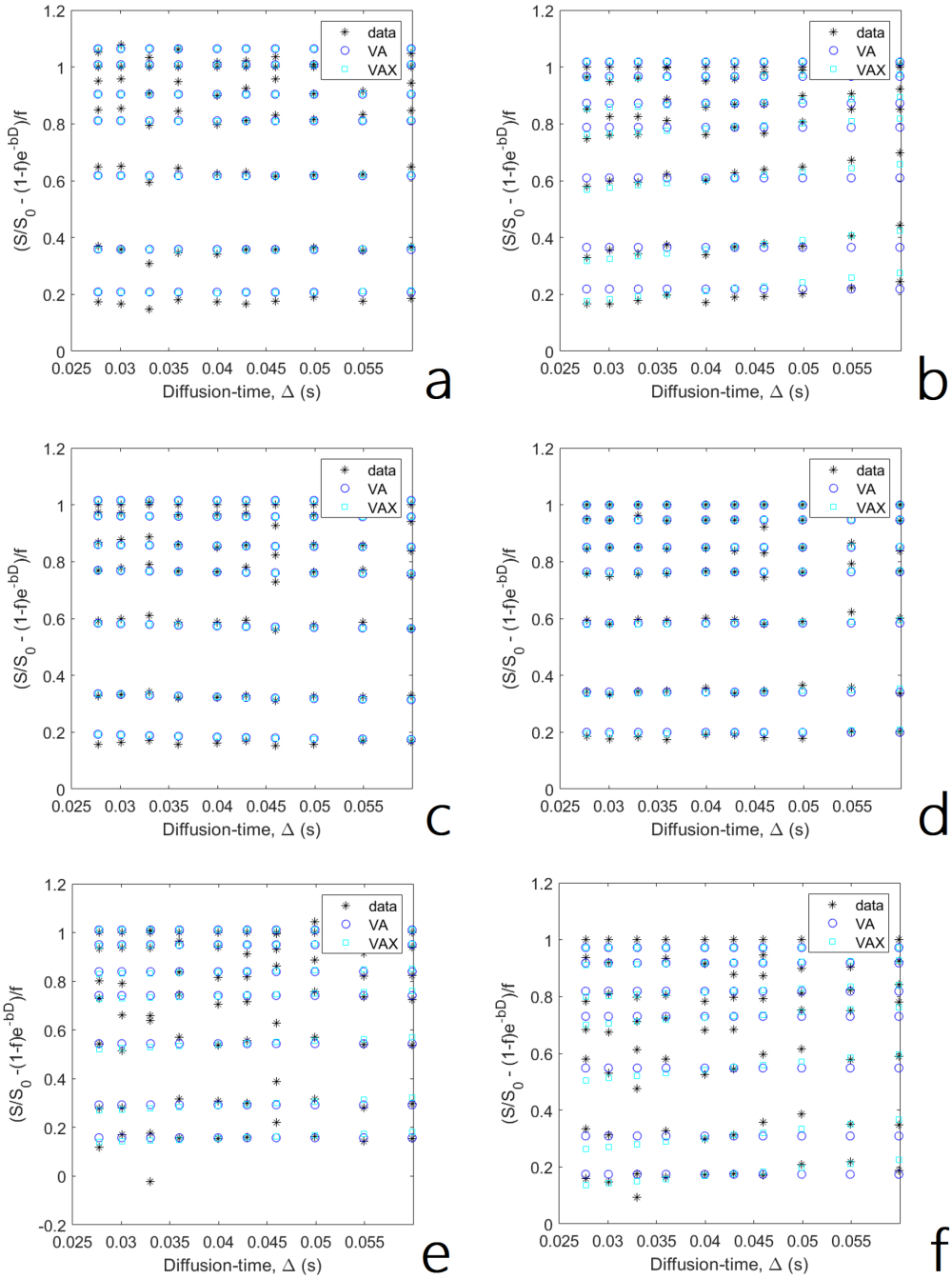

Figure 5.8: Isolated perfusion signal $(S/S_0–(1-f)e^{-bD})/f$ versus diffusion-time (Δ) (data) and, VA (blue) and VAX (cyan) model fits. Multiple points at each diffusion-time represent the changing b-value. (a) and (b) show grey matter (GM) and white matter (WM) data respectively for subject 007, (c) and (d) show GM and WM data respectively for subject 008 and, (e) and (f) show GM and WM data for subject 023.

6 Hypercapnia induced changes in multi-diffusion-time intravoxel incoherent motion imaging in the brain

Lauren A Scott[1,2], Douglas R Corfield[3], Oliver Sparasci[1,4], Andrew N Priest[5], Ben R Dickie[1,2], Laura M Parkes[1,2].

1. Division of Neuroscience and Experimental Psychology, School of Biological Sciences, Faculty of Biology, Medicine and Health, University of Manchester, Manchester, UK

2. Geoffrey Jefferson Brain Research Centre, Manchester Academic Health Science Centre, Northern Care Alliance & University of Manchester, Manchester, UK

3. Manchester Medical School, Faculty of Biology, Medicine and Health, The University of Manchester, Manchester, United Kingdom

4. Pennine Care NHS Foundation Trust, UK

5. Radiology, Cambridge University Hospitals NHS Foundation Trust, Cambridge Biomedical Campus, Hills Road, Cambridge, UK

6.1 Contribution of authors

LS collected MRI data, performed data analysis, interpreted data and wrote the manuscript. AP developed the pulse sequence for use on the GE PETMR scanner. DC provided expertise on the safety and implementation of the gas challenge. OS provided medical expertise during scanning and helped with MRI data collection. BD and LP supervised the research. LP and BD edited paper.

6.2 Moving from model development to validation in clinical data

Measures of vessel segment length, l, derived using $l = 6D^*/v$ (v from the VA model and D^* from the diffusive IVIM model) were validated against ground truth measures in the rat brain. After which, using data collected in the human brain, we developed the VA model and used $l = 2vT_0$ (v and T_0 from the VA model) to estimate vessel segment length. Limitations of the ground truth validation and the use of two different models to estimate l mean further work to validate the measure would be invaluable. The two methods of estimation of l need to be compared and the biophysical origin of parameters investigated. Parameters are based on biophysical modelling, therefore their relationship to the true underlying parameters they aim to describe is not clear, particularly in the case of v, T_0 and l.

Introducing a CO_2 challenge provides a well-known perturbation to cerebral blood flow, cerebral blood volume and blood velocity. It should not, however, alter vessel segment length. This therefore provides a means to check that the response in our estimated parameters are as expected: the perfusion fraction (f), pseudo-diffusion coefficient (D^*) and blood velocity (v) should increase, the correlation time (T_0) should decrease, and l should remain unchanged. The precision of estimates in terms of their sensitivity to change can also be assessed. ASL estimates of CBF and ATT are used to confirm the physiological response.

6.3 Abstract

Purpose: To determine the biophysical origin of diffusion-weighted (DW)-MRI derived parameters including blood velocity and vessel structure by assessing their sensitivity to hypercapnia induced cerebrovascular changes. Comparison with arterial spin labelling-derived changes in cerebral blood flow (CBF) and arterial transit time (ATT) are made.

Methods: Seven healthy volunteers underwent brain imaging at 3T using arterial spin labelling with multiple post-labelling delay times and diffusion-weighted (DW)-MRI. Diffusion-weighted MRI was collected at ten b-values between 0 and 1000 smm^{-2} and nine diffusion-times between 27 and 60 ms. ASL and DW-MRI were acquired while volunteers inhaled room air then carbon-dioxide rich air, each lasting approximately 30-35 minutes. Data from grey and white matter ROIs were extracted. The diffusive IVIM model (valid at long diffusion-times) was fit to DW-MRI data at each diffusion-time to estimate the perfusion fraction (f), extravascular diffusion coefficient (D) and perfusion attenuation coefficient (k, where $k = D^*$ at long diffusion-times). The diffusion-time dependence of k was modelled using the velocity-autocorrelation model producing estimates of blood velocity (v), correlation time (T_0) and vessel segment length (l). Vessel segment length was also estimated using IVIM estimates of D^* and VA estimates of v. CBF and ATT were estimated from ASL data. Differences in estimated parameters between baseline and hypercapnia scans were assessed using repeated measures ANOVAs.

Results: ATT decreased significantly with hypercapnia by a mean value of 6.6 ± 3.2 % and 5.0 ± 3.4 % in GM and WM respectively. There was a trend to higher CBF, perfusion fraction (f), and pseudo-diffusion coefficient (D^*), with hypercapnia, but no significant changes in these or any other parameters in GM or WM. End-tidal CO_2 was significantly associated with CBF, ATT and v, in both air and CO_2 groups.

Conclusion: Changes in ATT with hypercapnic gas challenge are consistent with literature. CBF, f and D^* showed a trend ($0.05 < p < 0.10$) towards an increase with hypercapnia, in line with literature. Furthermore, CBF, ATT and v are modulated by the level of CO_2, yet vessel segment length is not, in accordance with expectations. Increasing

the number of subjects and CO_2 supplied to subjects would clarify these results.

6.4 Introduction

Intravoxel incoherent motion was introduced in 1986 by Le Bihan et al. [207] as translational motions on a sub-voxel level which cause phase dispersion and the accelerated decay of the transverse MRI signal. The source is ascribed to molecular diffusion and microcirculatory blood flow, however other compartments might affect the signal, such as the glymphatic system [228]. The IVIM framework [14] allows for the separation and measurement of both diffusion and perfusion related parameters [135]. A two-compartment biexponential model of signal decay as a function of diffusion weighting (b-value) was originally proposed. The perfusion compartment is characterised by the pseudo-diffusion coefficient (D^*) and molecular diffusion by the diffusion coefficient (D). The perfusion fraction (f) quantifies the relative contribution of both compartments to signal attenuation. This model is the most commonly used IVIM model in research [35]. However, whether the assumptions of this model are met is often ignored [185].

The signal decay due to perfusion is dependent on the speed of blood flow and vessel architecture [14]; specifically, the length after which spins change direction due to vessel curvature or branching [185]. When blood flow changes direction multiple times during the diffusion-sensitisation time (diffusion-time), perfusion mimics molecular diffusion (diffusive regime) and the use of D^* is valid. However, when the diffusion-time is shortened, this diffusive regime may not be met [35, 131]. IVIM models have been proposed which characterise the signal across different diffusion-times and blood flow regimes [33, 35, 131, 164]. Kennan et al. [33] developed a diffusion-time dependent model of IVIM based on velocity autocorrelation (VA) theory which allows for estimation of the average blood velocity (v) and the average time between directional changes in blood flow (correlation time, T_0). These parameters can be used to estimate the average vessel segment length (l). Despite the development of these models, the additional parameters they give access to [33, 35], and increasing literature showing a diffusion-time dependence in f, D and D^* [35, 131, 176], the diffusion-time is still generally not considered in IVIM studies.

Recent work by our group (Chapter 4) applies the VA model and diffusive IVIM model in the rat brain where measures of l are validated using multiple rat strains and vascular corrosion casting. The VA model was then applied in healthy volunteers where diffusion-time dependence was investigated further and l estimated using the VA model (Chapter 5). Methods of estimating l using the VA model have not been validated in the human brain. Validation of structures on the micron level is challenging. In animals, direct and invasive methods of validation are often used, such as histology or corrosion casting [36]. In humans, gas challenges have been used to noninvasively validate parameters estimated

using the IVIM model in the diffusive regime [135]. Hypercapnia induces acidosis and affects chemoreceptor regulation of blood flow [229] resulting in cerebral vasodilation and increased blood flow velocity [195, 230] to increase cerebral blood flow (CBF) [231]. We hypothesise that l would remain unchanged in the brain under hypercapnia, whilst v, f and D^* would increase [135, 195, 230, 231] and T_0 would decrease.

The aim of this study is to determine the impact of hypercapnic gas challenge on multi-diffusion-time DW-MRI derived measures of velocity and vessel segment length in the human brain. We acquired multi-diffusion-time DWI in seven healthy volunteers using a range of b-values between 0 and 1000 smm^{-2} whilst subjects breathed room air and CO_2-enriched air (79%/21% CO_2/O_2 gas mixed with room air). Diffusive IVIM parameters (f, D, D^*) and multi-diffusion-time IVIM parameters (v, T_0, l) are extracted by fitting the VA and IVIM models to grey matter and white matter data. CBF is measured using arterial spin labelling (ASL) at multiple post-labelling delay times to ensure changes in blood flow occur as expected. Arterial transit time (ATT) is also extracted. Changes in parameters between the two gases are assessed.

6.5 Methods

Experiments were reviewed and approved by the University of Manchester Research Ethics Committee and written informed consent was obtained from all subjects. Seven healthy subjects were recruited for the study (mean age: 34 years [24 to 61 years], 4 female). Subjects had good general health with no history of neurological disease or breathing problems.

6.5.1 Data acquisition

6.5.1.1 MRI acquisition

MRI was performed on a 3T GE Signa PET/MR scanner (GE Healthcare, Chicago, US) using a 32 multi-channel receiver head coil (Nova Medical Inc, Wilmington, US). Axial DW-MRI data (Figure 6.4 in supplementary material) with whole brain coverage was obtained over three orthogonal directions. The b-value was varied through ten values: 0, 10, 30, 50, 100, 200, 300, 500, 750 and 1000 smm^{-2}. For each b-value, the diffusion-time (Δ) was varied through nine values between 27 and 60 ms (due to a scanner issue, one participant had only seven diffusion-times) (subject average normalised signal versus b-value for each diffusion-time shown in Figure 6.5 in supplementary material). These acquisition parameters are shown in Table 6.1. The lowest diffusion-time was limited by the maximum gradient strength required to achieve high b-value data (b=1000 smm^{-2}). The magnitude of the diffusion gradient pulse (G) and gradient duration (δ) were altered to allow variation in the diffusion-time while maintaining the same b-value (Table 6.1). Other sequence

parameters include: TR= 5525 ms, TE= 95 ms, voxel size 0.8125 × 0.8125 × 4 mm^3, FOV 256 × 256, number of slices 35. Acquisition time for each diffusion-time (with all b-values): 2 minutes 40 seconds. Total DW-MRI acquisition time: 24 minutes.

A 3D magnetisation prepared rapid gradient echo (MPRAGE) T1-weighted scan with prospective motion correction (PROMO) was collected for regional segmentations. Sequence parameters include: TR= 7.716 ms, TE= 3.044 ms, TI= 900 ms, flip angle= 8°, isotropic voxel size of 1 mm. Acquisition time: approximately 5 minutes.

Enhanced ASL data (using a GE prototype sequence) was collected with pCASL labelling, background suppression, vascular crushing, and a 3D spiral FSE read-out, with 6 spiral arms and 512 encoding points giving a resolution of 1.7 × 1.7 × 4 mm^3. Image parameters were TE = 10.7 ms, TR = 5992 ms and 3 post-label delay (PLD) times at 1000, 1573 and 2458 ms with labelling durations of 573, 885 and 2042 ms respectively. The label durations are set by the enhanced ASL sequence to approximately equalise the signal at each PLD; i.e. the longer PLDs have longer labelling durations (see supplementary material for analysis of sensitivity of the enhanced ASL data acquisition to ATT). In addition, a proton density image was collected for calibration purposes. Total ASL acquistion time: 4 minutes 20 seconds. CBF and ATT maps (Figure 6.7 in supplementary material) were calculated on the scanner console by the GE eASL research package using the recommended single blood compartment model [232] and voxel-wise correction for proton density.

Table 6.1: Diffusion-times, Δ, pulse durations, δ, used in the DW-MRI protocol. Due to scanner issues, participant 004 did not have diffusion-times 30.07 and 59.86 ms.

Δ (ms)	δ (ms)
27.73	20.36
30.07	19.09
33.02	17.83
35.98	16.80
39.95	15.70
42.93	15.00
45.92	14.40
49.89	13.70
59.86	12.34

6.5.1.2 Hypercapnic intervention

A non-rebreathing circuit was used to induce hypercapnia in subjects while in the MRI scanner. MRI acquisitions described above were collected with subjects breathing room air for a period of 35 minutes, following which hypercapnia was induced for a period

of 30 minutes, and the same scans performed (minus T1-weighted MRI). A period of approximately 3 minutes between baseline and hypercapnic scans ensured we reached a steady state of CO_2 output from the subject. The acquisition of all data is shown in Figure 6.1.

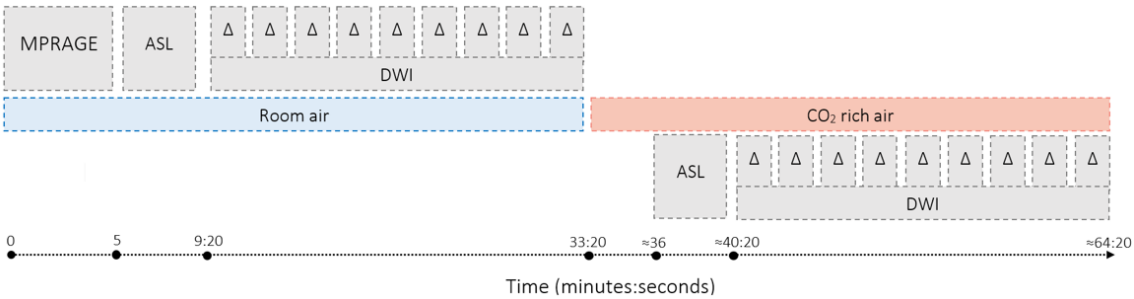

Figure 6.1: Hypercapnia acquisition. The MPRAGE was collected for regional segmentation. Arterial spin labelling (ASL) MRI was collected whilst subjects breathed normal air and CO_2 rich air to determine changes in cerebral blood flow and arterial transit time. Diffusion-weighted MRI (DWI) was collected for nine diffusion-times whilst subjects breathed normal air and CO_2 rich air to determine changes in IVIM parameters. There was an approximately 3 minute period between the baseline and hypercapnia acquisitions to reach a steady end-tidal CO_2 level.

A mixture of 79% CO_2/21% O_2 (BOC gases, UK) was delivered from the control room into the scanner room to induce hypercapnia [233, 234]. A rubber mouthpiece with gum guard (subjects also wore a nose clip) was connected to an antibacterial filter, which was connected to two-way valve. The valve was connected to wide corrugated open ended tubing which allowed normal air to flow in from the room. A medical air supply tube connected to the gas tank was placed inside the corrugated tubing, allowing a thin stream of CO_2 rich air to mix with normal room air. A thin sampling tube was connected to the mouthpiece to allow for monitoring of end-tidal CO_2 to determine the correct end-tidal increase of 1% was achieved, and for patient safety.

End-tidal CO_2 was monitored during baseline scans to determine normal levels using a Powerlab gas analyser and LabChart8 (ADI instruments, Colorado Springs, US). To achieve hypercapnia, the flow rate of the gas mixture was adjusted to achieve a target increase of approximately 1% above baseline CO_2 values. The rate of the gas mixture flow was limited to ensure that the maximum inspired CO_2 concentration did not exceed 5%. The composition of the gas mixture (containing 21% O_2) ensured that the level of inspired oxygen never fell below room level. Oxygen saturation and heart rate were also monitored for patient safety.

6.5.2 Extraction of regional MRI data

SPM12 (http://www.fil.ion.ucl.ac.uk/spm) was used for volumetric segmentation of T1-weighted images producing probability maps of grey matter (GM) and white matter (WM). The T1-weighted image and probability maps were then re-sliced and co-registered to the DW-MRI data and proton-density weighted images for ASL data. For DW-MRI data, the T1-weighted image was co-registered to each diffusion-time data separately to reduce any effects of subject motion. Mean CBF, ATT and DW-MRI signal at each b-value and diffusion-time were extracted from grey matter (GM) and cerebral white matter (WM) regions on an individual basis.

The trace of the DW-MRI signal across the three orthogonal diffusion directions was used. The models were then fit to the mean signal from each region in order to extract parameter estimates.

6.5.3 Extracting DW-MRI metrics

The diffusive IVIM model [14] and the velocity autocorrelation (VA) [33] model are used to extract DW-MRI metrics from baseline and hypercapnia data.

In the presence of diffusion-sensitising gradients, attenuation of the MR signal can be described by a two-compartmental model, describing the intra and extra-vascular contributions [14]. The total normalised signal is modelled as a sum of two exponentials:

$$\frac{S(b,\Delta)}{S_0} = fe^{-bD_b}H(b,\Delta) + (1-f)e^{-bD} \tag{6.1}$$

where $b = \gamma^2\delta^2G^2(\Delta - \delta/3)$ when employing pulsed gradient spin echo (PGSE) sensitisation. γ is the proton gyromagnetic ratio; G, the magnitude of the diffusion gradient pulses; δ, the duration of each diffusion gradient pulse and; Δ, the diffusion-time, the time between the gradient pulses. $S(b,\Delta)$ is the DW-MR signal as a function of b; S_0, the signal at b=0; D, the extravascular diffusion coefficient; and f, the perfusion fraction. D_b is the apparent diffusion coefficient of water in blood; and $H(b,\Delta)$ is the signal attenuation due to perfusion.

6.5.3.1 Diffusive IVIM model

When the diffusion-time is long enough that blood flow changes vessel segment multiple times, the signal attenuation due to perfusion can be described by the pseudo-diffusion coefficient (D^*):

$$H(b) = e^{-bD^*}. \tag{6.2}$$

This is commonly referred to as the IVIM model, or diffusive IVIM model.

6.5.3.2 Velocity autocorrelation model

The velocity-autocorrelation (VA) model [33] describes signal attenuation due to perfusion as function of both b-values and diffusion-time (Δ):

$$H(b, \Delta) = e^{-bk(\Delta)} \tag{6.3}$$

where k is the perfusion attenuation coefficient due to microcirculatory flow in the presence of bipolar diffusion gradients:

$$k = \frac{\Omega v^2 T_0}{3\delta^2(\Delta - \delta/3)} \tag{6.4}$$

where v is the average blood velocity; T_0 is the average time that spins in the blood stay in a segment, and:

$$\Omega = \delta^2(\Delta - \delta/3) - 2T_0^2\delta - T_0^3 q \tag{6.5}$$

$$q = 2\exp\Big(-\frac{\Delta}{T_0}\Big) + 2\exp\Big(-\frac{\delta}{T_0}\Big) - \exp\Big(-\frac{\Delta+\delta}{T_0}\Big) - \exp\Big(-\frac{\Delta-\delta}{T_0}\Big) \tag{6.6}$$

This model assumes BBB water-exchange does not occur. The VA model corrected for blood-brain-barrier water exchange (VAX) can be found in supplementary material.

6.5.3.3 Extracting D and f

The signal attenuation due to microcirculatory flow is higher than that of extravascular diffusion, thus the microcirculatory component is insignificant at b-values higher than 200-600 smm^{-2} [131, 134, 139, 168]. As such, the components can be separated using a two-step method, an approach commonly used in IVIM studies [131, 134, 139, 158, 168]. Model parameters describing the extravascular component were estimated using b-values 500, 750 and 1000 smm^{-2}. The extravascular diffusion coefficient, D, and perfusion fraction, f, were estimated for each diffusion-time separately by fitting the following model to the normalised data:

$$\frac{S}{S_0} = (1-f)e^{-bD} \tag{6.7}$$

The 'lsqcurvefit' function in Matlab (R2019b) was used (MathWorks, Natick, US). All fitting described here uses the same function.

6.5.3.4 Extracting D^*, v, T_0 and l

The extravascular component was subtracted from the total normalised signal for each diffusion-time and divided by f, to isolate the intravascular component of the signal:

$$\frac{1}{f}\left(\frac{S}{S_0} - (1-f)e^{-bD}\right) = e^{-bD_b+c}H(b, \Delta) \tag{6.8}$$

where c is a parameter added to improve fitting (see Chapter 4, Section 4.5.3.2). D_b was set to a fixed value of 1.75×10^{-3} mm^{2}s^{-1} [131].

To estimate D^*, Equation 6.8 was fit to the highest diffusion-time data (59.86 ms for all subjects except 004, where 49.89 ms was used as the highest available diffusion-time) and b-values<500 smm^{-2}, using Equation 6.2 for $H(b, \Delta)$. The diffusion-time is assumed to be long enough for perfusion to be in the diffusive limit. To estimate v and T_0, Equation 6.8 was jointly fit to all diffusion-times and b-values<500 smm^{-2}, using Equations 6.3 and 6.4 for $H(b, \Delta)$. Fitting of models to the isolated perfusion data for two subjects is shown in Figure 6.6 in supplementary material.

Estimates of vessel segment length, l, were generated using T_0 and v derived from the VA model [14, 33]:

$$l = 2vT_0 \tag{6.9}$$

and, using v from the VA model and D^* from the diffusive IVIM model:

$$l = \frac{6D^*}{v}. \tag{6.10}$$

6.5.4 Statistical analysis

Prior to calculating the mean of parameter estimates across subjects, outliers were removed by excluding those outside three median absolute deviations of the median. This method was chosen rather than thresholding based on the standard deviation since it is not affected by large outliers itself [199].

6.5.4.1 Assessing model fit

To determine if the VA or VAX model of the diffusion-time dependent intravascular IVIM compartment was most appropriate, the Akaike information criterion, corrected for small number of data points (AIC_c), was calculated for grey and white matter fits using [215]:

$$AIC_c = N\ln\Big(\frac{RSS}{N}\Big) + 2m + \frac{2m(m+1)}{N-m-1} \tag{6.11}$$

where N is the number of data points used in the fit, m is the number of parameters in the model: an additional parameter must be included for the Gaussian noise hypothesis for the signal residuals [131]. RSS is the residual sum of squares from the 'resnorm' output of the 'lsqcurvefit' function in Matlab (2019b). Paired student's t-tests were performed between the AIC_c values for the VA and VAX models, for GM and WM, to determine if differences were statistically significant (p<0.05). The 'ttest' function in Matlab (R2019b) was used.

6.5.4.2 Assessing effects of hypercapnia on DWI and ASL derived parameters

To determine if gas challenge had any effect on the diffusion-time dependence of f, D, or k, one-way repeated measures ANOVAs were performed for each brain region with within-subject factor (repeated measure) of diffusion-time. The difference between baseline and hypercapnia parameters was used as the dependent variable. The 'fitrm' and 'ranova' functions were used in Matlab (R2019b).

Two-way repeated measures analysis of variance (ANOVA) were performed for ASL and DW-MRI derived parameters with region (GM/WM) and gas (baseline/hypercapnia) as categorical within subject factors (repeated measures), and end-tidal CO_2 as a covariate. Analysis used the 'aov' function in R (version 1.2.1335). The correlation between parameters and end-tidal CO_2 was assessed using the 'corrcoef' function in Matlab (R2019b). The correlation coefficient (ρ) was extracted.

6.6 Results

6.6.1 Model comparison using Akaike information criterion

Figure 6.8 shows the difference in AIC_c between the VAX and VA models for baseline and hypercapnia DW-MRI data in GM and WM. Results show the VA model is most appropriate in GM for baseline data (p=2.2e-05). Results were inconclusive for GM hypercapnia data, although the data appears to be biased towards the VA model since the AIC_c difference is greater than zero with exception of one subject which was identified as an outlier.

Results are also inconclusive for both gases in WM. For baseline data, the median is close to zero which would indicate that SSE is smaller for VAX, but after correction for additional parameters, it does not describe any additional variability compared to the VA model. However, there are a few datasets where the VAX might be more appropriate if assessing the points individually. For hypercapnia data, there is a slight bias towards the VAX model with the median sitting below zero, potentially indicating increased water-exchange.

The spread of AIC_c(VAX-VA) is higher in WM than GM, indicating more variability in model fit across subjects.

Following these results, only parameters from the VA model were presented.

6.6.2 Diffusion-time dependence of f, D and k

Figure 6.9 shows the mean value ($\pm$ standard error) across participants for f, D, and k, as a function of the diffusion-time (Δ) derived from baseline and hypercapnia data. f does not appear to have a dependence on diffusion-time. D decreases with diffusion-time. This decrease appears to stop around 40 ms, following which the parameter seems to stabilise. In GM, k increases gradually for baseline data, with exception of the lowest

diffusion-times. k for hypercapnia data increases with diffusion-time with exception of the final data point which drops. In WM, k increases at shorter diffusion-times and decreases at longer diffusion-times for both curves, although the data is noisier for hypercapnia and some points are spurious. This shape is characteristic of the VAX model, although AIC_c data is inconclusive. Values for f, D and k are generally lower for WM than for GM. f in WM and k in GM are higher for most diffusion-times in hyerpcapnia compared to baseline. p-values show if the difference between parameters derived from baseline and hypercapnia data are associated with diffusion-time. Results are discussed in the following section.

6.6.3 Effects of hypercapnia

6.6.3.1 End-tidal carbon dioxide

Figure 6.10 shows the carbon dioxide levels (%) for subjects over the course of the MR imaging acquisition. The first approximately 35 minutes show CO_2 levels whilst subjects breathe normal air, the last approximately 30 minutes show CO_2 levels whilst subjects breathe CO_2 rich air. End-tidal CO_2 increases with the hypercapnic challenge. Subjects 001, 003 and 007 have low variability in end-tidal levels under hypercapnia (i.e. inspiratory and expiratory levels are consistent across the scan and few spurious peaks are detected), and subjects 002, 004, 005 and 006 show much more variable traces. Baseline levels are quite consistent across the acquisition for most subjects, for some it does begin to decrease (005 and 007).

Table 6.1 shows the mean end-tidal CO_2 level (%) for baseline and hypercapnia for each subject. The standard deviation shows baseline levels are fairly stable, with exception of subject 005 which has a standard deviation of almost 0.5%. Hypercapnia levels are much more variable with much higher values for standard deviation – over 1% for subjects 002 and 006. For subjects 003 and 007, the variability across hypercapnia is lower which agrees with the traces in Figure 6.10. We aimed for a mean change of 1% in end-tidal CO_2. This was not achieved for the subjects, with 001, 003, 004 and 007 <1% and 002, 005 and 006 >1%.

6.6.3.2 The effect of hypercapnia on DW-MRI and ASL-derived parameters

Tables 6.3 and 6.4 show parameter estimates for each subject from the diffusive IVIM model (f, D and k at the longest diffusion-time (i.e. $k \equiv D^*$)), VA model (v and T_0), structural estimates ($l(D^*)$ and $l(T_0)$) and ASL-derived parameters (CBF and ATT) in GM and WM for baseline (air) and hypercapnia (CO_2) scans. The percentage change for each of the parameters between the two gases are shown in Figure 6.2 for CBF, ATT, f, D, D^*, v, T_0 and l. Parameter variation with end-tidal CO_2 (and correlation coefficient, ρ)

Table 6.2: End-tidal CO_2 (%) ± standard deviation at baseline and with hypercapnia for each subject, and change in CO_2 (%).

Subject	Baseline	Hypercapnia	Change
001	6.78 ± 0.11	7.60 ± 0.32	0.82
002	6.27 ± 0.19	7.94 ± 1.1	1.67
003	6.49 ± 0.086	7.21 ± 0.15	0.72
004	6.49 ± 0.13	7.35 ± 0.90	0.86
005	5.01 ± 0.45	6.45 ± 0.59	1.44
006	6.53 ± 0.23	8.38 ± 1.4	1.85
007	6.06 ± 0.25	6.96 ± 0.14	0.90

are shown in Figure 6.11. p-values from repeated measures ANOVAs for each parameter are shown in Table 6.5.

CBF increases for each subject with hypercapnia in both regions with a mean increase of 26.3 ± 14% and 30.7 ± 20% for GM and WM respectively. CBF is trending towards significance with gas challenge (p=0.054). CBF significantly increases with end-tidal CO_2, with p=7.2e-05 and, ρ_{GM}=0.44 and ρ_{WM}=0.46. CBF varied significantly between regions with p=7.0e-04. GM had 39% higher CBF than WM in baseline data.

ATT decreases for six subjects in both regions with hypercapnia with a mean decrease of 6.6 ± 3.2% and 5.00 ± 3.4% for GM and WM respectively. For subject 002, the ATT increases in both regions – the change in GM is classed as an outlier. The effect of the gas challenge was significant with p=2.1e-06. ATT significantly decreases with end-tidal CO_2, with p=1.1e-06 and, ρ_{GM}=-0.50 and ρ_{WM}=-0.43. Effect of region was not significant.

f increases for six subjects in both regions with hypercapnia with a mean increase of 10.7 ± 16% and 10.4 ± 11% for GM and WM respectively. For subject 006, f decreases in both regions. The effect of the gas challenge on f was trending towards significance with p=0.067, as was the effect of end-tidal CO_2 with p=0.066 ($\rho_{GM} = 0.0093$ and ρ_{WM}=0.31). The effect of region was significant however with p=2.3e-09, with GM having 60% higher f than WM in baseline data.

D decreases for six subjects in each region with hypercapnia with a mean decrease of 1.34 ± 2.3% and 0.984 ± 0.92% for GM and WM respectively. For subject 006, D increases in GM, and for subject 004, D increases in WM. The effect of the gas challenge was not significant, but effect of end-tidal CO_2 was trending towards significance with p=0.094 ($\rho_{GM} = -0.26$ and $\rho_{WM} = -0.33$). Effect of region was significant, with p=7.4e-12, with GM having 12% higher D than WM in baseline data.

Changes in D^*, v and T_0 with gas change were not significant for any region. Although changes in D^* were trending towards significance with p=0.051 (mean increase of: 2.10 ±

20% and 10.4 ± 21% in GM and WM respectively). Increasing v was significantly associated with end-tidal CO_2 however, with p=0.038 (ρ_{GM}=0.22 and ρ_{WM}=0.34). Changes across subjects for each parameter were spread above and below zero. Subject variability for v and T_0 is quite large suggesting a lack of precision in estimates. D^* was 37% higher in GM than WM in baseline data (p=6.8e-06) and v was 119% higher in WM than GM in baseline data (p=0.012).

Changes in l with the gas challenge are spread above and below zero. The effect of the gas challenge is not significant. $l(D^*)$ was 124% higher in GM than WM in baseline data (p=9.5e-06). Mean values for the two methods of estimation appear to be fairly similar after outlier removal. GM values: $l(D^*)$=22.2 ± 1.1 μm and $l(T_0)$=24.6 ± 1.6 μm. WM values: $l(D^*)$= 9.93 ± 1.1 μm and $l(T_0)$= 8.42 ± 0.77 μm. The percentage decrease due to the gas challenge is also similar in GM; $l(D^*)$=25.5 ± 49% and $l(T_0)$=30.4 ± 58 %.

Repeated measures one-way ANOVAs show a significant association between diffusion-time and effects of the gas challenge on k. Although not significant, k and f are generally higher in WM with hypercapnia (Figure A1). There does not appear to be a visible difference in D.

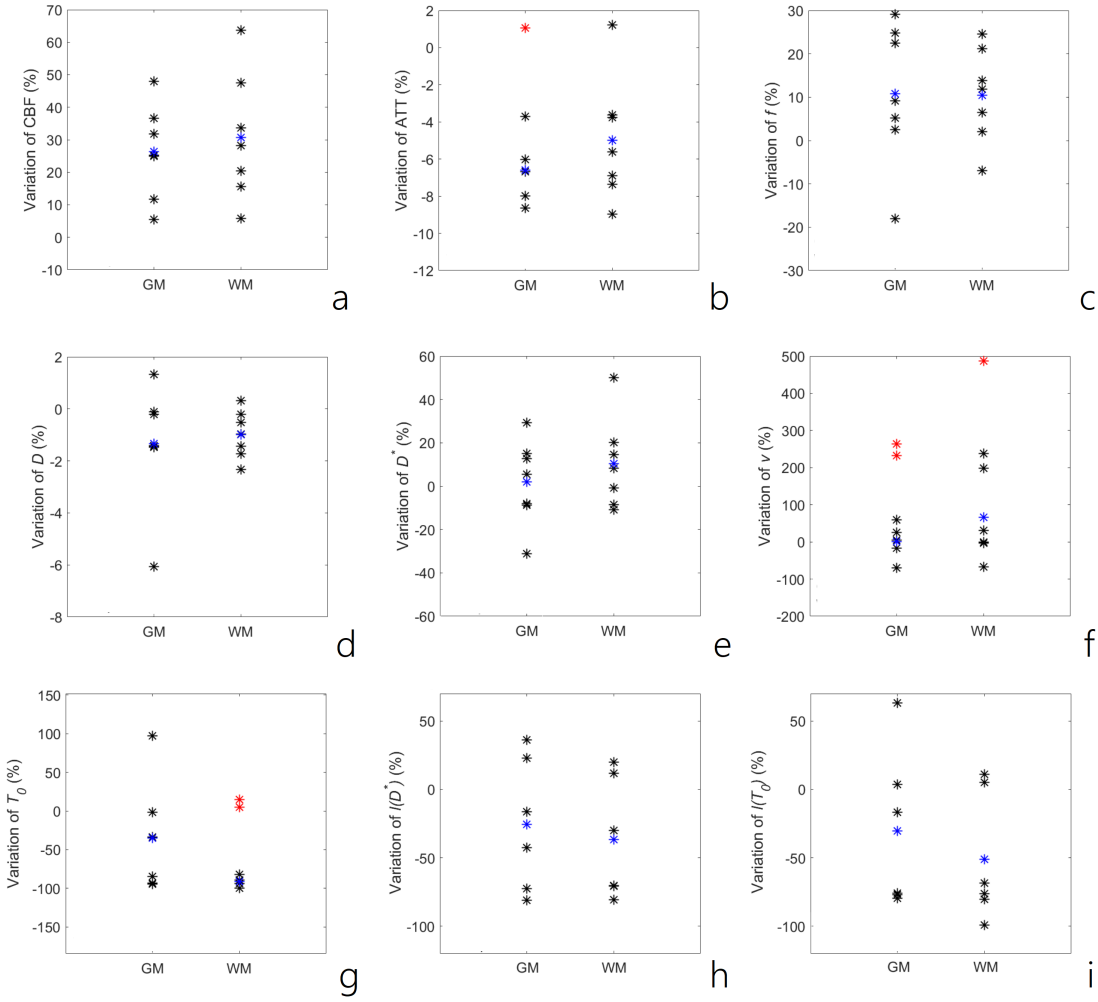

Figure 6.2: Variation (%) in ASL and DW-MRI derived parameters from baseline (air) to hypercapnia (CO_2) scans. (a) shows cerebral blood flow (CBF) and (b) shows transit time (ATT). (c-e) show diffusive IVIM parameters. (c) shows the perfusion fraction (f), (d) shows the diffusion coefficient (D) and (e) shows the pseudo-diffusion coefficient (D^*). (f-g) show multi-diffusion-time IVIM parameters derived using the VA model. (f) shows the velocity (v) and (g) the correlation time (T_0). (h-i) show estimates of length derived using $l = 2vT_0$ ($l(T_0)$) in (h) and $l = 6D^*/v$ ($l(D^*)$) in (i). Black points show percentage variation for each subject (n=7), blue points show the mean and red points show outliers which lie outside of three median absolute deviations of the median. The plots for T_0 and both estimates of l are close ups and outliers are not shown at values of:
T_0 GM:1390 % and WM:2090 %
$l(D^*)$ GM:276 % and WM:363 %
$l(T_0)$ GM:355 % and WM:610 %.

Table 6.3: Single diffusion-time (f, D, D^*) and multi-diffusion-time (T_0, v, l) IVIM parameters, and ASL derived parameters (CBF and ATT) for cortical grey matter (GM) for all volunteers and gas types. f perfusion fraction; D, diffusion coefficient; D^*, pseudo-diffusion coefficient; T_0, correlation time; v, blood velocity; $l(T_0)$, vessel segment length estimated using $l = 2vT_0$; $l(D^*)$, vessel segment length estimated using $l = 6D^*/v$; CBF, cerebral blood flow; ATT, arterial transit time. Outliers have been removed for the mean which lay outside of three median absolute deviations of the median. Outliers are highlighted in bold. Mean values ± standard error are show at the bottom.

Volunteer	Gas	f	$D \times 10^{-4}$ (mm^2s^{-1})	$D^* \times 10^{-4}$ (mm^2s^{-1})	T_0 (ms)	v (mms^{-1})	$l(T_0)$ (μm)	$l(D^*)$ (μm)	CBF (ml/100ml/min)	ATT (s)
001	Air	0.116	7.63	4.58	**60.6**	0.830	**101**	33.1	43.9	1.43
	CO_2	0.122	7.61	4.21	9.13	1.33	24.3	19.0	46.3	1.34
002	Air	0.137	7.72	4.58	5.95	1.57	18.7	17.5	37.0	1.45
	CO_2	0.154	7.61	4.83	3.94	1.98	15.6	14.6	41.3	1.47
003	Air	0.126	7.89	4.84	0.759	**4.41**	6.69	6.58	81.9	1.22
	CO_2	0.154	7.78	5.57	11.3	1.35	30.5	24.8	103	1.14
004	Air	**0.0855**	7.49	4.08	18.4	0.995	36.6	24.6	54.5	1.38
	CO_2	0.107	7.48	5.28	18.1	1.05	37.9	30.3	68.1	1.26
005	Air	0.116	7.90	5.39	14.1	1.13	31.8	28.7	24.3	1.61
	CO_2	0.150	7.42	3.72	0.793	**4.10**	6.50	5.44	35.9	1.51
006	Air	0.125	7.72	4.85	11.8	1.22	28.9	23.8	68.8	1.31
	CO_2	0.102	7.85	4.41	0.819	**4.06**	6.65	6.54	90.7	1.27
007	Air	0.131	7.87	4.83	9.3	1.35	25.1	21.4	65.3	1.35
	CO_2	0.134	7.76	5.44	18.3	1.11	41.0	29.2	89.2	1.24
Mean	Air	0.125 ± 0.0031	7.75 ± 0.054	4.74 ± 0.14	10.1 ± 2.3	1.18 ± 0.098	24.6 ± 4.0	22.2 ± 3.0	53.7 ± 7.0	1.39 ± 0.043
	CO_2	0.131 ± 0.0075	7.64 ± 0.020	4.78 ± 0.24	8.92 ± 2.6	1.36 ± 0.15	23.2 ± 4.9	18.6 ± 3.6	67.7 ± 9.4	1.32 ± 0.046

Table 6.4: Single diffusion-time (f, D, D^*) and multi-diffusion-time (T_0, v, l) IVIM parameters, and ASL derived parameters (CBF and ATT) for cerebral white matter (WM) for all volunteers and gas types. f perfusion fraction; D, diffusion coefficient; D^*, pseudo-diffusion coefficient; T_0, correlation time; v, blood velocity; $l(T_0)$, vessel segment length estimated using $l = 2vT_0$; $l(D^*)$, vessel segment length estimated using $l = 6D^*/v$; CBF, cerebral blood flow; ATT, arterial transit time. Outliers have been removed for the mean which lay outside of three median absolute deviations of the median. Outliers are highlighted in bold. Mean values ± standard error are show at the bottom.

Volunteer	Gas	f	$D \times 10^{-4}$ (mm^2s^{-1})	$D^* \times 10^{-4}$ (mm^2s^{-1})	T_0 (ms)	v (mms^{-1})	$l(T_0)$ (μm)	$l(D^*)$ (μm)	CBF (ml/100ml/min)	ATT (s)
001	Air	0.0789	6.92	3.43	**20.2**	0.926	**37.4**	22.2	31.8	1.43
	CO_2	0.0840	6.91	3.41	**1.19**	3.13	7.45	6.53	33.7	1.35
002	Air	0.0866	6.76	3.20	0.636	4.30	5.47	4.47	28.7	1.45
	CO_2	0.0986	6.72	3.85	0.667	4.31	5.74	5.36	33.2	1.47
003	Air	0.0812	6.99	3.40	0.531	4.92	5.22	4.15	58.4	1.21
	CO_2	0.101	6.92	3.69	0.607	4.77	5.80	4.63	74.8	1.13
004	Air	0.0698	6.95	3.83	**428**	0.688	**589**	**33.4**	38.4	1.34
	CO_2	0.0712	6.97	4.39	0.780	4.04	6.30	6.51	46.2	1.25
005	Air	0.0757	6.90	3.68	**5.28**	1.50	15.8	14.8	16.4	1.56
	CO_2	0.0918	6.74	3.28	0.563	4.46	5.02	4.41	26.9	1.50
006	Air	0.0840	6.86	3.94	1.35	2.99	8.06	7.91	49.5	1.31
	CO_2	0.0782	6.80	3.60	0.247	3.91	**1.93**	5.53	66.2	1.26
007	Air	0.0683	7.12	2.76	1.38	2.74	7.55	6.05	46.8	1.35
	CO_2	0.0764	7.00	4.14	**30.2**	**0.887**	**53.6**	**28.0**	69.1	1.24
Mean	Air	0.0778 ± 0.0024	6.93 ± 0.039	3.46 ± 0.14	0.974 ± 0.20	2.58 ± 0.57	8.42 ± 1.7	9.93 ± 2.7	38.6 ± 5.0	1.38 ± 0.039
	CO_2	0.0859 ± 0.0040	6.86 ± 0.040	3.76 ± 0.14	0.573 ± 0.080	4.10 ± 0.21	6.06 ± 0.36	5.50 ± 0.33	50.0 ± 6.9	1.31 ± 0.047

Table 6.5: p-values from repeated measures ANOVAs with region (GM/WM) and gas (baseline/ hypercapnia) as within subject factors. End-tidal CO_2 is input as a covariate.

Parameter	Region	Gas	End-tidal CO_2
f	2.3e-09	0.067	0.066
D	7.4e-13	0.63	0.094
D^*	6.8e-06	0.051	0.81
T_0	0.48	0.30	0.43
v	0.012	0.36	0.038
$l(T_0)$	0.57	0.32	0.41
$l(D^*)$	9.5e-03	0.52	0.13
CBF	1.3e-06	0.054	7.2e-05
ATT	0.21	2.1e-06	1.1e-06

6.7 Discussion

In this study, we aim to validate DW-MRI measures of microvessel function and structure in the brain by assessing parameter sensitivity to hypercapnia induced changes. We hypothesised that functional measures would change as a result of hypercapnia-induced vasodilation and associated increases in CBF, and structural measures would not. We collected multi-diffusion-time DW-MRI and ASL data in healthy subjects at baseline and during hypercapnia to extract cerebral blood flow (CBF), arterial transit time (ATT), perfusion fraction (f), diffusion coefficient (D), pseudo-diffusion coefficient (D^*), average blood velocity (v), correlation time (T_0) and vessel segment length (l) in grey (GM) and white matter (WM). We assessed model fits to determine the VA model was the most appropriate model of multi-diffusion-time data (Figure 6.8) and investigated the diffusion-time dependence of f, D and k (Figure 6.9). Multi-variate analyses show the hypercapnic gas challenge was associated with decreased ATT (Tables 6.3-6.5, Figure 6.2). However, whilst trends were observed in CBF, f and D^*, no other significant changes were measured with the gas challenge. Variation in CBF, ATT and v across subjects was associated with end-tidal CO_2 values. Using repeated measures ANOVAs, we determine the impact of gas challenge on k depends on the diffusion-time, with a stronger diffusion-time dependence seen in GM with hypercapnia in comparison to air.

We evaluated whether the velocity autocorrelation (VA) model or VA model corrected for blood-brain-barrier water exchange (VAX) (Chapter 5) was most appropriate in our data (Figure 6.8). The VA model is better in GM for baseline data, which differs from previous results where data was inconclusive (Chapter 5). This could be due to k generally increasing which is more representative of the VA model; in previous data we saw a slight

decline at the highest diffusion-time which can only be characterised by the VAX model. Results were inconclusive for hypercapnia in GM and both gases in WM. However, it is surprising that the VAX model is not more appropriate in WM since k appears to have a similar shape to the model (Figure 5.1 in Chapter 5). The hypercapnia data in both regions is likely affected by difficulties maintaining a steady end-tidal CO_2 across the thirty minute scan which would add different bias at each diffusion-time. The variation in end-tidal CO_2 can be seen on subjects 002, 004, 005 and 006 on Figure 6.10. This likely impacted the effect of diffusion-time on k with hypercapnia, and could be why this result is statistically significant.

The diffusion-time dependence of parameters (Figure 6.9) differed from previous work (Chapter 5), with no apparent diffusion-time dependence in f, a decrease in D with diffusion-time and a variation in curve shapes in k. The analysis pipeline for both datasets is identical, with exception of the segmentation software where Freesurfer was used in previous analysis and SPM12 here. Note that SPM12 was used due to time constraints and the limited expertise in the use of Freesurfer by the researchers involved. Small differences in the two automatic segmentation methods have been detected. For example, Palumbo et al. [235] and Dadar et al. [236] show SPM measured greater GM and lower WM volumes compared to FSL. Naess-Schmidt et al. [237] find Freesurfer and SPM estimates of fractional anisotropy differ significantly from those of manual segmentations in subcortical regions. The main effect in literature seems to be variable volume estimates, which shouldn't affect our results greatly since we are using averages over large regions. However, there could be different partial volume effects due to differently defined regions. The data collected for each study differed slightly – only seven subjects were imaged here compared to ten, and nine rather than ten diffusion-times were collected. Collecting one less diffusion-time should not have a large affect on diffusion-time dependence plots since the curves are quite well defined with nine values. Although a reduced number of subjects would increase the error on the mean across subjects, it would be surprising if it had such a large effect on diffusion-time dependence as seen here - particularly on f where the linear relationship was very strong in previous work (Chapter 5).

CBF estimates increased for all subjects with the gas challenge, in agreement with literature [195, 230, 231, 238–242]. However, effect of gas challenge was not significant (p=0.054). There was fairly large variability in the percentage change across subjects. This could be explained by the variation in end-tidal CO_2 levels (p=7.2e-05): increasing end-tidal CO_2 levels were associated with increasing CBF (in agreement with literature [242]). Although, variation in percentage change between subjects is in agreement with literature, as subjects can have very different vascular responses to hypercapnia [242–244]. Significant increases in CBF with end-tidal CO_2, but not with gas challenge, suggest the supply of CO_2 to subjects may have been too low to give consistent and sustained

vasodilation in all subjects. This meant differences in CO_2 between groups was too low compared to the intra-group variation in end-tidal CO_2. Low subject numbers could also be affecting our ability to measure a significant effect.

ATT estimates decreased for all but one subject with the gas challenge, also in agreement with literature [239, 244, 245]. ATT increased in GM and WM in subject 002. This could potentially be explained by the scan-rescan variability of the measure. Jain et al. [246] evaluate the coefficient of variation (CoV) of ATT in a paediatric cohort to be 5.52%, which is greater than the approximately 1.5% change in ATT for 002. The change in ATT with gas challenge was significant, as was inter-subject variability with end-tidal CO_2 (decreasing ATT was associated with increasing end-tidal CO_2). This suggests that changes in the velocity of arterial blood is a critical response of the brain to high CO_2 levels. The significance of ATT, but not CBF, with gas challenge may be due to higher repeatability of ATT. Cohen et al. [247] show ATT is more repeatable than CBF by a factor of approximately 3.

Increases in CBF have been attributed to increase in CBV and an increase in blood flow velocity [195, 230, 242, 245]. Theoretically, CBF is proportional to fD^* and CBV to f [189, 248]. fD^* has shown excellent agreement with DSC-MRI derived CBF in patients with acute ischaemic stroke [249]. DSC-MRI derived CBV was correlated with f [167] in healthy volunteers and in patients with high grade gliomas [250]. In meningiomas, f was in excellent agreement with histologically determined percentage vascular density [251]. Thus, with this evidence, it was expected that f and D^* would follow the results in CBF.

In f, there was a trend towards an increase with gas challenge (as shown in CBF) with exception of one subject for each region. The reduction in f for 006 could be partly be due to scan-rescan variability which was measured as 10% for GM in previous work (Chapter 7). Inter-subject variability in f was not significantly associated with end-tidal CO_2 level (p=0.066 (p=7.2e-05 for CBF)). In GM, there appears to be very little correlation between f and end-tidal CO_2.

The change in D^* with gas challenge was close to significance (p=0.051). The mean percentage change shows an increase, however points are spread above and below zero giving low confidence. The repeatability of D^* from previous work (Chapter 7) was 13% in GM which could explain some of the variability and negative percentage changes. End-tidal CO_2 did not explain inter-subject variability: the correlation seems to be negative for GM and positive for WM. This suggests that there may be another factor affecting this result. Increasing subject numbers would help clarify results in f and D^*.

Federau et al. [135] show significant increases in f (approximately 15% in GM and 5% in WM) and D^* (approximately 40% in GM and 15% in WM) using 5% CO_2. We measure a 10.7% and 10.4% increase in f, and a 2.1% and 10.4% increase in D^*, in GM and WM respectively. The authors do not measure end-tidal CO_2 levels and do not compare IVIM

results to other imaging techniques, so it is difficult to compare to our study. However, a review of gas challenge methods by Moreton et al. [252] states that a 5% supply of CO_2 raises CBF by 50% and delivery of a 6% CO_2 gas mixture results in an approximately 1.4% increase in end-tidal CO_2. Hence a 5% supply may be expected to raise end-tidal CO_2 by around 1.1-1.2% (if we assume a linear relationship). The average end-tidal CO_2 increase across our subjects was approximately 1.2%. Hence we would have expected to see a similar change to Federau et al. [135]. It's unclear why this isn't the case. Federau et al. [135] use a higher number of b-values in the intravascular range, perhaps giving them improved accuracy of D^*. They also use a lower b-value threshold, although this shouldn't have an effect on the percentage changes in parameters, only magnitude. It is not clear at which diffusion-time the authors collected data, but as shown in Figure 6.9, this can significantly affect the change in k with gas challenge.

Federau et al. [135] show no change in D with 5% CO_2 which agrees with our data. Grech-Sollars et al. [253] calculate the intra-volunteer CoV in WM in the cerebrum for D as 2.2% and previous data in GM shows a CoV of 1.6% (Chapter 7) which would explain most of the variability shown here. However, larger decreases could be due to vasodilation increasing pressure on tissue and compressing extravascular space, decreasing the space for diffusion and reducing the diffusion coefficient.

v and T_0 do not alter with gas challenge which disagrees with findings in literature. For example, Hutchinson et al. [244] measure an increase of 75 $\pm$ 114 % in RBC velocity in the capillaries of rats with 45 mmHg PCO_2. Hudetz et al. [195] measure a 46% change in RBC velocity in rats with a 5% CO_2 gas mixture. However, inter-subject variability in v was associated with end-tidal CO_2 (increasing v with increasing end-tidal CO_2) which agrees with the finding for CBF. The detected change in v, but not T_0, could be due to its higher CoV (23.2% for v and 30.8% for T_0 - Chapter 5). The lower CoV for these parameters compared to those of f and D (Chapters 5 and 7) could explain the higher inter-subject variability in percent parameter change. Although, in v, some of this variability is due to end-tidal CO_2. Some of the larger changes in both parameters might come from the variable end-tidal CO_2 through the protocol introducing bias across diffusion-time, resulting in poor fitting of the model to hypercapnia data.

Whilst functional parameters were expected to change, measures of l were not. Two methods of estimating l are used which are expected to give consistent results ($l = 6D^*/v$ and $l = 2vT_0$). Neither method shows significant changes in l with gas challenge or variability with end-tidal CO_2. However, given the variability in the results and small subject numbers it would be wrong to conclude that there is no change. Whilst no significant changes agrees in part with our hypothesis, the absence of changes in other parameters is of concern and thus we cannot say that our measures are validated. However, the two methods give similar values for l which gives confidence in models and means they could

potentially be used interchangeably depending on parameters available. The large outliers in each of the methods come from the largest values of v and T_0.

Parameter estimates are shown in Tables 6.3 and 6.4. CBF values and variation across subjects are generally in agreement with literature [238, 254–256]. Subject 003 has particularly high values of CBF compared to other subjects, however baseline measures are still in the range of values measured in literature [255]. Values of ATT are in excellent agreement with some studies [188, 246, 257], but not in others [254, 256] – perhaps due to different imaging parameters (e.g. distance between imaging and labelling slab [257]). The absolute values of f are higher than expected (approximately double [217]) and values of D^* slightly lower than expected. This is likely due to the high b-value threshold of b=500 smm^{-2}. Evidence shows IVIM parameters are dependent on the b-value threshold [139, 140], perhaps due to non-negligible intravascular contribution which would increase as the threshold is lowered, thus creating a seemingly larger extravascular compartment and reduced intravascular compartment. Studies show f increases with b-value threshold which confirms this, and D^* decreases [139, 140]. Additionally, the inclusion of D_b in the IVIM model would reduce estimated D^*. D_b is usually ignored, but since we estimate microvessel structure, the diffusion of water in blood needs to be separated. Values for D agree well with literature [166, 168, 217]. Estimates of v in human brain capillaries are scarce, however our estimates seem reasonable when compared to what is available (Chapter 5). Estimates of l agree with the range presented in literature, but are generally smaller (Chapter 5). In WM, values are of the order of vessel diameter [220, 221] which was found previously (Chapter 5), indicating that perhaps the VAX model should have been used for subjects with AIC_c in favour of the model (i.e. lower AIC_c(VAX-VA) in Figure 6.8). The VAX model gave estimates of l that were more consistent with literature in previous work (Chapter 5).

Multivariate analyses show region had a significant effect on CBF, f, D, D^*, v and $l(D^*)$. CBF is higher in GM, which is consistent with literature [238, 254–256] and due to higher metabolic need of its constituent cells [258]. f is higher in GM which is consistent with literature [165, 217] and known differences in CBV [256, 259] and helps to confirm the physiological origin of f. v is lower in GM which agrees with a study by Li et al. [56] who use two-photon microscopy to observe the speed of RBCs in the mouse brain. Although the velocity between regions only appears to vary by around 0.5 mms^{-1}. We suspect the larger difference could be due to the use of the VA model in WM which also gave higher values in previous data (Chapter 5). D^* is lower in WM which agrees with literature [165, 217], and is consistent with lower CBF. It potentially reflects different vessel lengths across the two regions or the different velocities, due to different vascular architecture. This would agree with different $l(D^*)$ across region. However, $l(T_0)$ does not alter significantly with region. Although this may be due to issues estimating T_0. Lastly, D is lower in WM, which is

well-known and can be explained by increased barriers to diffusion.

As discussed, the study is limited by difficulties in achieving and maintaining a 1% rise in end-tidal CO_2 for the duration of the hypercapnia scan. Multi-diffusion-time estimates (v and T_0) derived using the VA model would have been affected. Additionally, the ASL was collected at the beginning of the hypercapnia, so perhaps wasn't representative of the CBF through the rest of the scan. Furthermore, an unknown issue with the heat exchange cabinet of the scanner, resulting in a mid-scan shut-down, meant one participant (004) had fewer diffusion-times and uses a different diffusion-time for diffusive IVIM parameters. The percentage change could thus be affected as it was shown to be diffusion-time dependent. Only having seven participants limits our ability to detect changes in parameters. For example, using coefficient of variation (CoV) values presented for v and T_0 in (Chapter 5) for VA fits in GM (23.2% for v and 30.8% for T_0), power calculations show a number of 15 subjects is needed to detect a 25% increase in v from our mean in GM of 1.18 mms^{-1} and 16 subjects are needed to detect a 25% decrease in T_0 from our mean in GM of 10.1 ms. Although, we were able to reliably detect changes in ATT using ASL with the small numbers. It is clear that the method for estimating l requires refinement to improve sensitivity if it is to be useful.

Last, a further limitation of our data is the non-constant δ value (Table 6.1). Whilst effects are included in the VA model, they are not accounted for in the extravascular model. In the two-step method used, the extravascular signal is subtracted from the intravascular signal for each diffusion-time. This method accounts for the effects of diffusion-time on the extravascular signal attenuation, but does not account for δ. A small amount of literature exists describing the effect of the pulse gradient width on the extravascular DW-MRI signal. In the narrow pulse limit, the apparent diffusion coefficient (ADC) approaches the true diffusion coefficient [226], hence the smaller the pulse width, the more accurate the measure of the ADC. Zielinski and Sen [227] find a maximum error in the ADC of 20% when $\delta = \Delta$ in a highly restricted but open geometry (e.g. in rock). In an open but less restricted geometry, which is likely to be more characteristic of the brain, the maximum error is around 6% [227]. This maximum error is likely to be at shorter diffusion-times where the ratio of δ/Δ is higher (e.g. the highest ratio at $\Delta = 27.73$ ms, with $\delta = 20.36$ ms, was 0.73). These errors could have propagated through the analysis pipeline.

6.8 Conclusion

In conclusion, we find that only ATT alters significantly with hypercapnic gas challenge, although there was a trend towards an increase in CBF, f and D^*. CBF and v were positively correlated, and ATT negatively correlated, with end-tidal CO_2. Measures of l did not change significantly, as predicted, although we cannot reject the null hypothesis

of no difference in baseline and hypercapnia l due to high variability and no changes in functional parameters. Increasing the number of participants in the study would increase statistical power which might allow us to determine changes in IVIM parameters. Increasing CO_2 levels in the hypercapnic challenge would also be helpful in determining changes in parameters.

6.9 Acknowledgements

The authors wish to thank the Medical Research Council (MRC) for PhD funding. AP is financially supported by the Addenbrooke's Charitable Trust and the National Institute for Health Research [Cambridge Biomedical Research Centre at the Cambridge University Hospitals NHS Foundation Trust]. The views expressed are those of the authors and not necessarily those of the NHS, the NIHR or the Department of Health and Social Care

6.10 Funding

The authors wish to thank the Medical Research Council (MRC) for PhD funding.

6.11 Supplementary materials

6.11.1 Velocity autocorrelation model corrected for blood-brain-barrier water exchange

As diffusion-time increases, the fraction of spins initially present in the intravascular compartment that exchange into the extravascular compartment, and vice versa, increases. To model the effect of exchange on signal attenuation, we consider the replacement of intravascular water by extravascular water depending on the mean exchange time (also known as the residence time) of the spins in the intravascular compartment, τ. Assuming spins are well mixed in each compartment, the volume fraction of native intravascular spins entering the extravascular compartment after diffusion-time, Δ, is [211]:

$$f_{ex} = 1 - e^{-\frac{\Delta}{\tau}}. \tag{6.12}$$

The exponential term models the residue of intravascular spins that have not yet exchanged with the extravascular compartment after the diffusion-time, Δ. The effective (observed) perfusion attenuation coefficient in the presence of finite exchange is modelled as the mean of the perfusion (k) and extravascular diffusion (D) coefficients, weighted by the exchanged fraction f_{ex}:

$$k_{eff} = (1 - f_{ex})k + f_{ex}D. \tag{6.13}$$

6.11.2 Sensitivity of ASL acquisition to ATT

For a single compartment model, the change in magnetisation (ΔM) between control and labelled ASL images, normalised by the equilibrium magnetisation (M_0), is described by [260, 261]:

$$\frac{\Delta M}{M_0} = \frac{2fT_{1app}\alpha}{\lambda} e^{-\frac{ATT}{T_{1a}}} \left(1 - e^{-\frac{t-ATT}{T_{1app}}}\right) \text{ for } (ATT < t < LD + ATT) \tag{6.14}$$

$$\frac{\Delta M}{M_0} = \frac{2fT_{1app}\alpha}{\lambda} e^{-\frac{ATT}{T_{1a}}} \left(1 - e^{-\frac{LD}{T_{1app}}}\right) e^{-\frac{t-(ATT+LD)}{T_{1app}}} \text{ for } (LD + ATT < t) \tag{6.15}$$

where:

$$\frac{1}{T_{1app}} = \frac{1}{T_{1e}} + \frac{f}{\lambda}, \tag{6.16}$$

ATT is arterial transit time, LD is the duration of labelling, f is blood flow, T_{1e} is tissue relaxation time, T_{1a} is arterial blood water relaxation time, λ is tissue blood partition coefficient of water and α is the labelling efficiency.

For $t = LD + PLD$ and $T_{1app} = T_{1a}$, $\Delta M/M_0$ becomes [260, 261]:

$$\frac{\Delta M}{M_0} = \frac{2fT_{1a}\alpha}{\lambda} \left(e^{-\frac{ATT}{T_{1a}}} - e^{-\frac{LD+PLD}{T_{1a}}}\right) \text{ for } (ATT < LD + PLD < LD + ATT) \tag{6.17}$$

$$\frac{\Delta M}{M_0} = \frac{2fT_{1a}\alpha}{\lambda} \left(1 - e^{-\frac{LD}{T_{1a}}}\right) e^{-\frac{PLD}{T_{1a}}} \text{ for } (ATT < PLD). \tag{6.18}$$

To assess the sensitivity of the ASL imaging acquisition used in this study (with variable PLD and LD) to ATT, compared to an ASL acquisition which uses constant LD, we simulate $\Delta M/M_0$ with varying ATT for varying and constant LD. We assume α=0.85 for PCASL labelling, λ=0.9 mL/g, T_{1a}=1.65 s at 3T, and f=60 ml/min/100ml [232]. PLD = 1.0, 1.573 and 2.458 s, with LD of 0.573, 0.885 and 2.042 s, or LD=1.17 s (average of LD used in imaging acquisition). ATT is varied through 1.0-1.5 s and 1.6-2.0 s.

Figure 6.3 shows $\Delta M/M_0$ versus PLD for varying LD (a and b) and constant LD (c and d). The figure demonstrates that, regardless of the acquisition used, ΔM is sensitive to ATT. Hence, the standard methods of estimating CBF and ATT are used (i.e. using Equations 6.17 and 6.18).

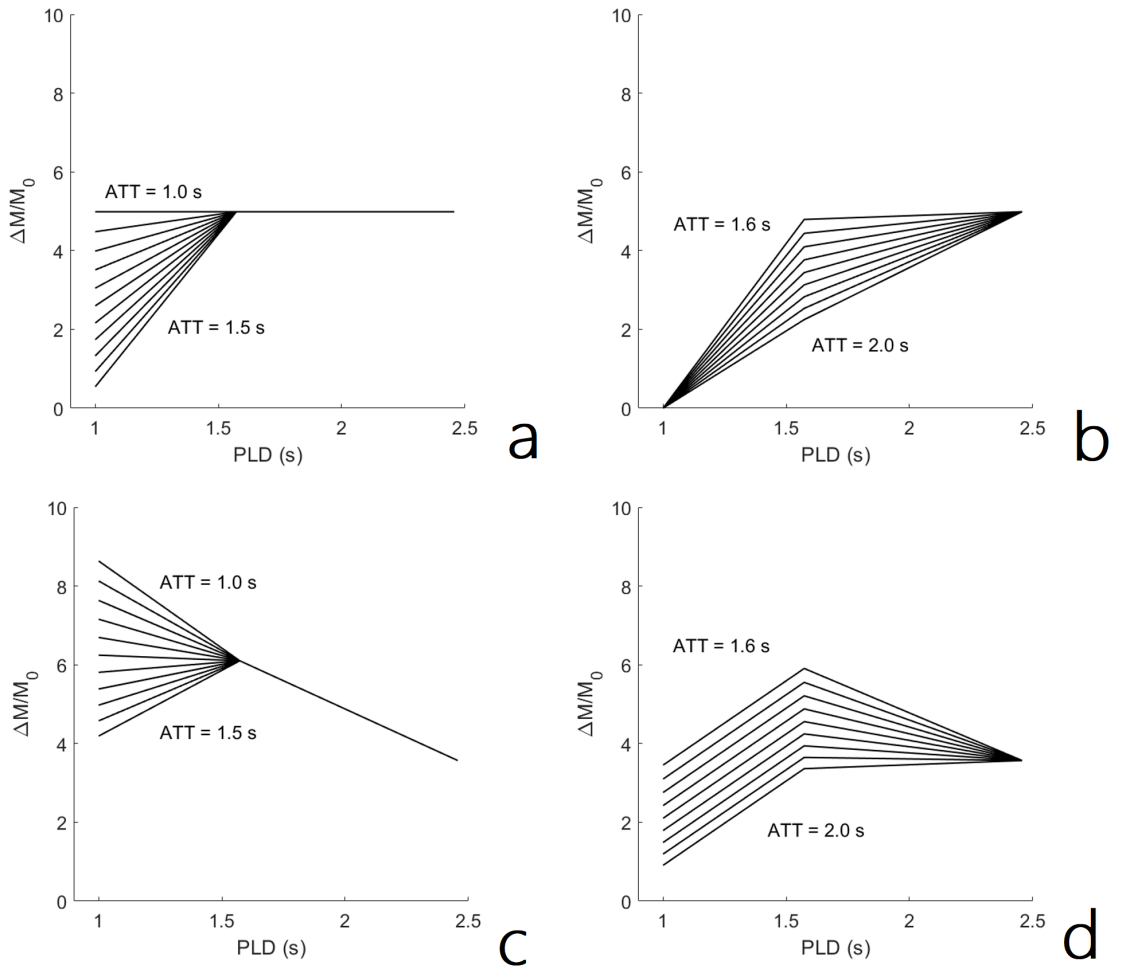

Figure 6.3: Change in magnetisation ($\Delta M/M_0$) between control and labelled ASL images versus post labelling delay (PLD), for arterial transit time (ATT) 1.0-1.5 s (a and c) and 1.6-2.0 s (b and d) where (a) and (b) have varying labelling duration (LD) to approximately equalise the ASL signal at each PLD, and (c) and (d) have constant LD.

6.11.3 Figures

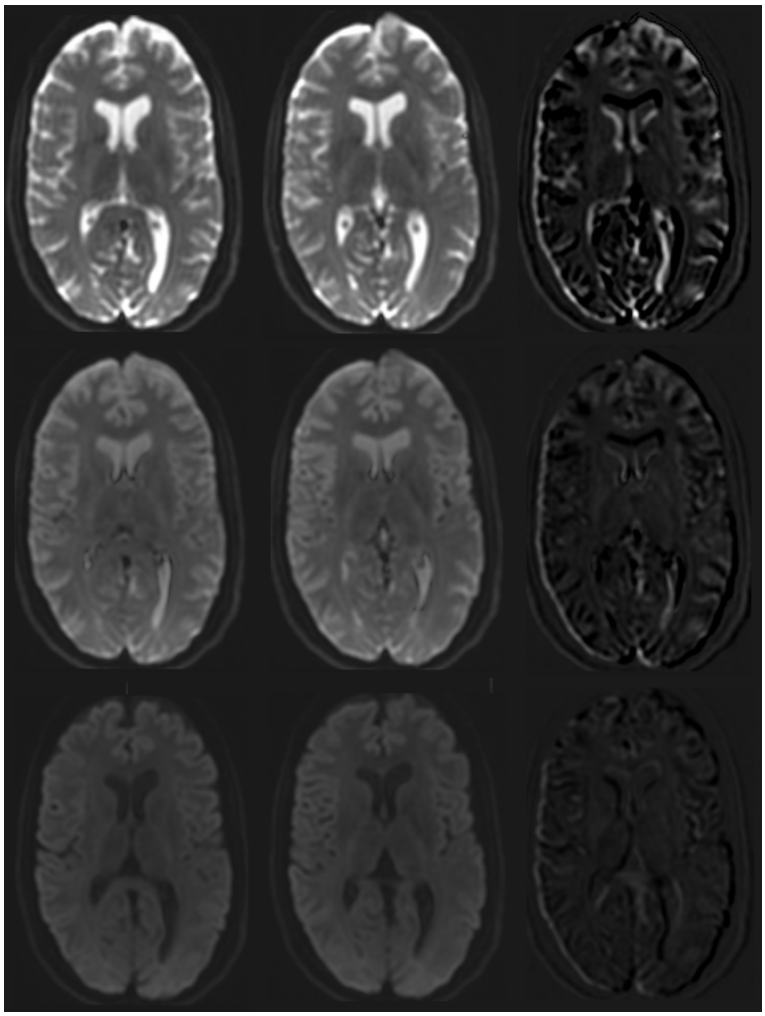

Figure 6.4: Mid-axial slices of diffusion-weighted (DW) MR images for subject 007 for baseline (first column) and hypercapnia (second column) scans. The third column shows the difference images between the two scans. Three different b-values are shown, moving down the rows, b= 10, 300 and 1000 smm^{-2}.

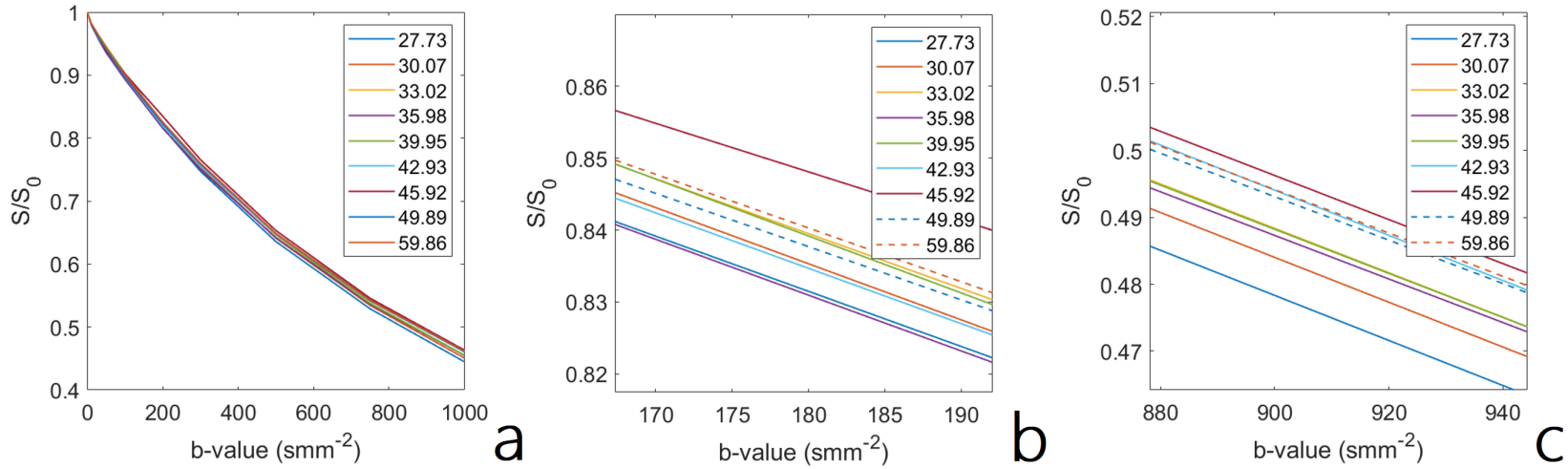

Figure 6.5: Subject average normalised diffusion-weighted MRI signal (S/S_0) for grey matter (GM) versus b-value for nine values of diffusion-time (Δ in ms). (a) shows the full b-value range, (b) shows the signal at low b-values and (c) shows the signal at high b-values.

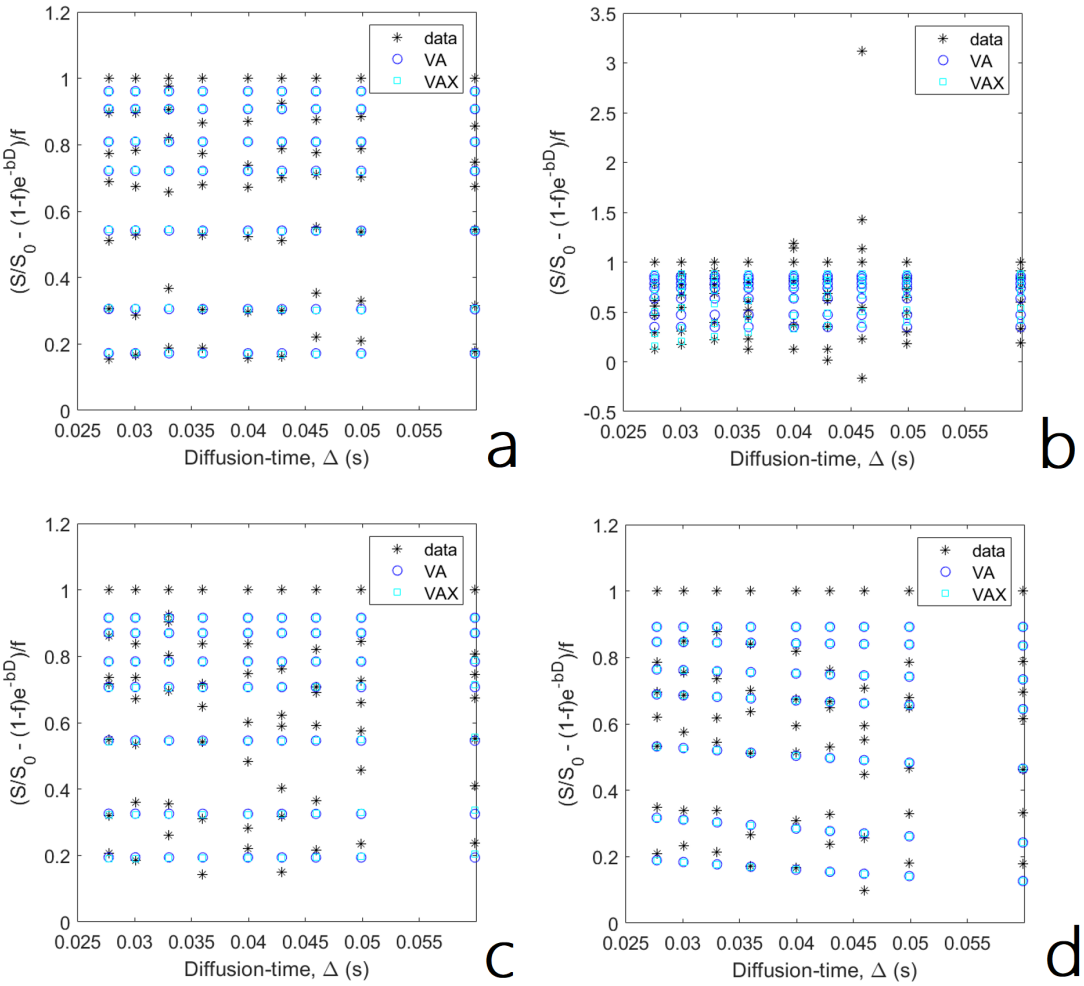

Figure 6.6: Isolated perfusion signal $(S/S_0–(1-f)e^{-bD})/f$ versus diffusion-time (Δ) (data) and, VA (blue) and VAX (cyan) model fits. Multiple points at each diffusion-time represent the changing b-value. (a) and (b) show baseline and hypercapnia data for grey matter (GM) respectively for subject 006, (c) and (d) show baseline and hypercapnia data for GM respectively for subject 007.

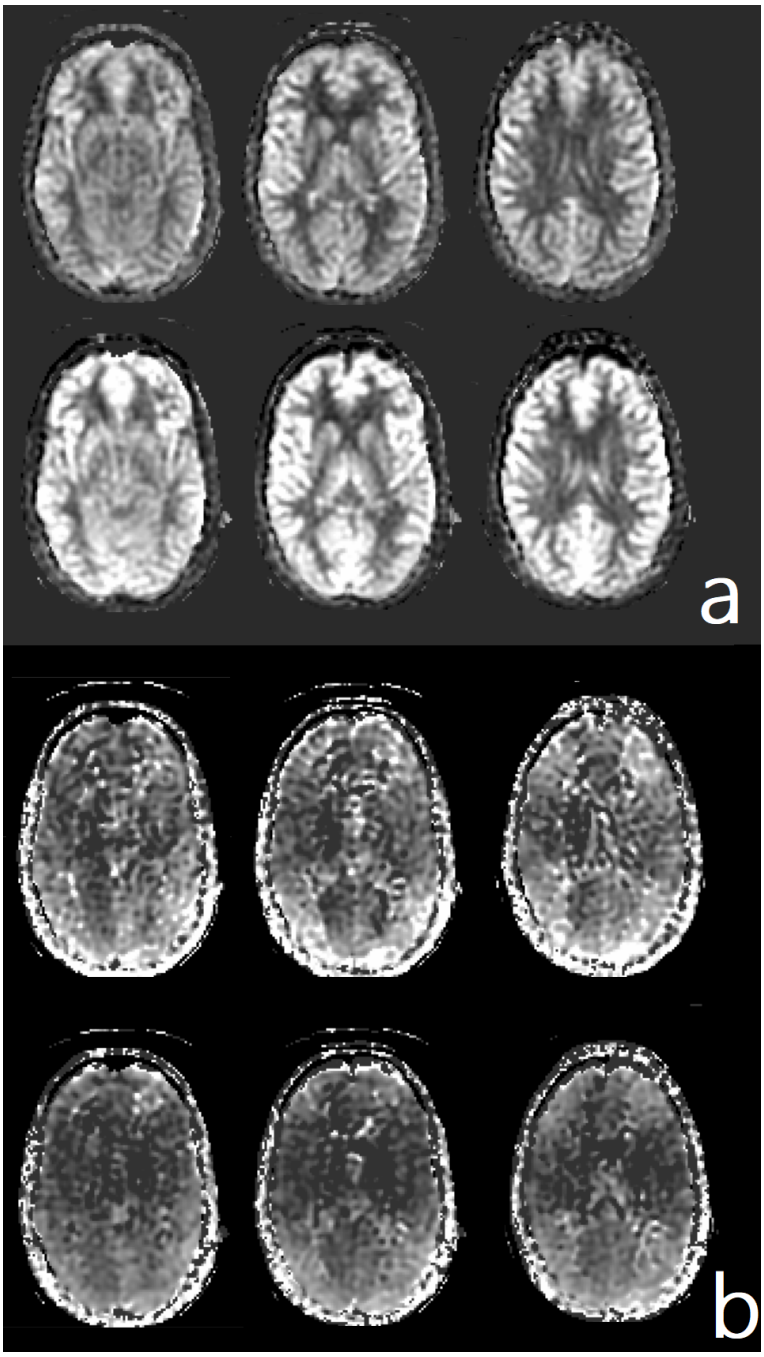

Figure 6.7: Axial slices of cerebral blood flow (a) and arterial transit time (b) maps for subject 007 (left to right) for the baseline scan (top row) and hypercapnic scan (bottom row).

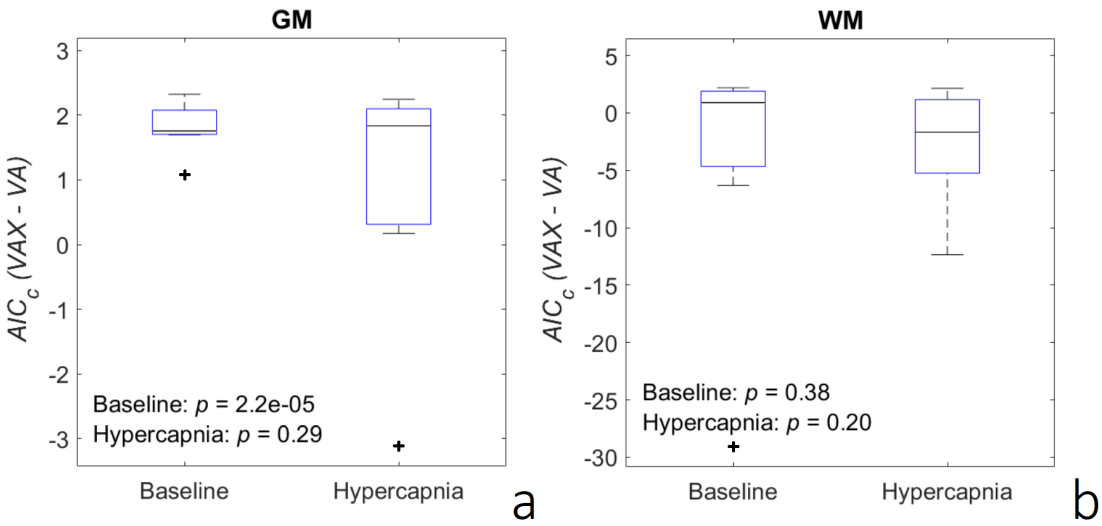

Figure 6.8: Boxplots of the difference in AIC_c of the VAX and VA models of baseline and hypercapnia DW-MRI data for (a) grey matter (GM) and (b) white matter (WM). Paired sample t-tests between VAX and VA AIC_c values give p=2.2e-05 and p=0.29 for baseline and hypercapnia data in GM respectively, and p=0.38 and p=0.20 for baseline and hypercapnia data in WM respectively.

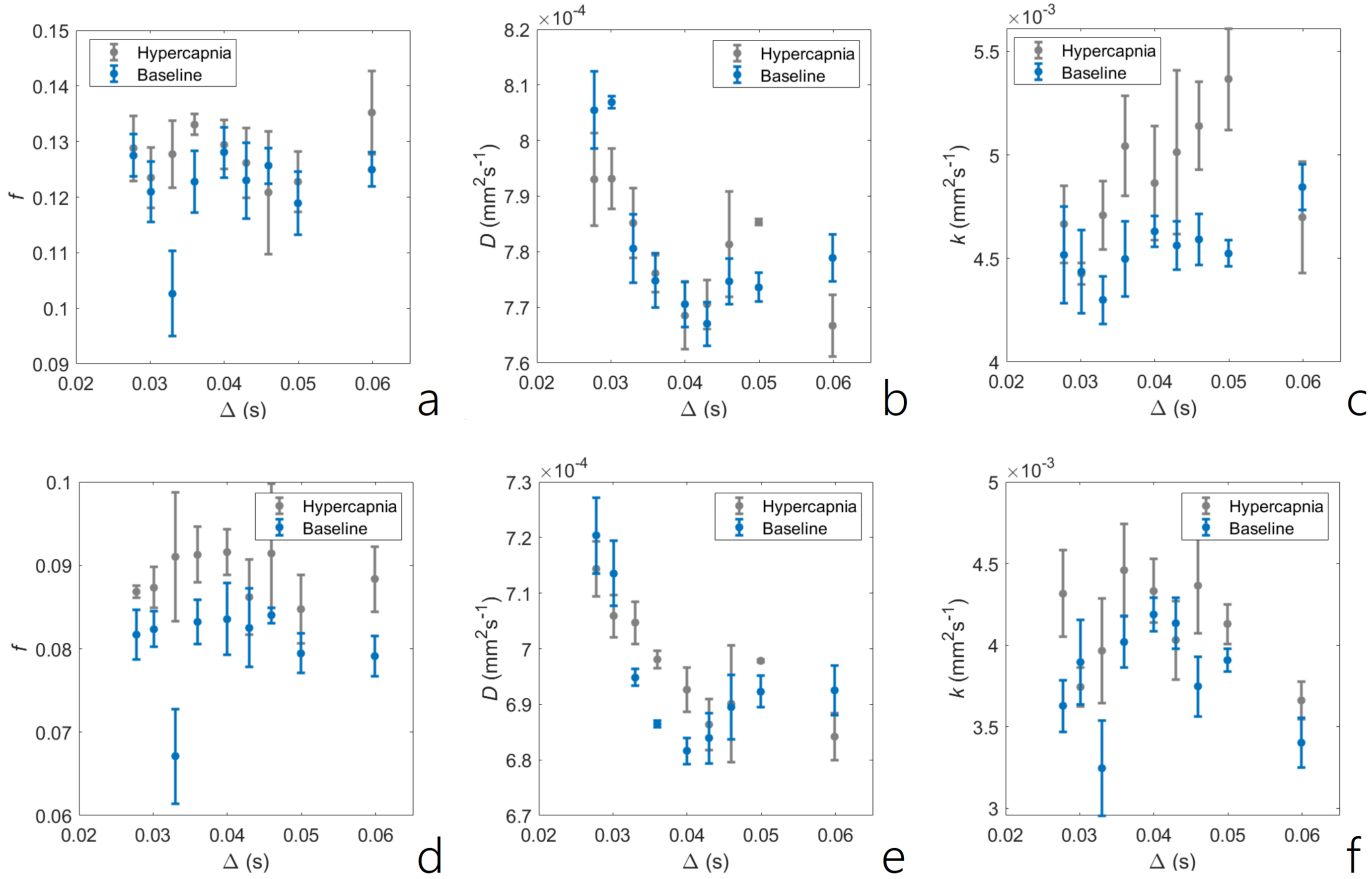

Figure 6.9: The grey matter (GM) and white matter (WM) parameter means with standard error for baseline (blue) and hypercapnia (grey) data. Graphs show the perfusion fraction, f, in (a) and (d); the diffusion coefficient, D, in (b) and (e); and, the perfusion coefficient, k, in (c) and (f). The top row represents GM and the bottom, WM. Outliers removed outside of three median absolute deviations of the median for each diffusion-time.

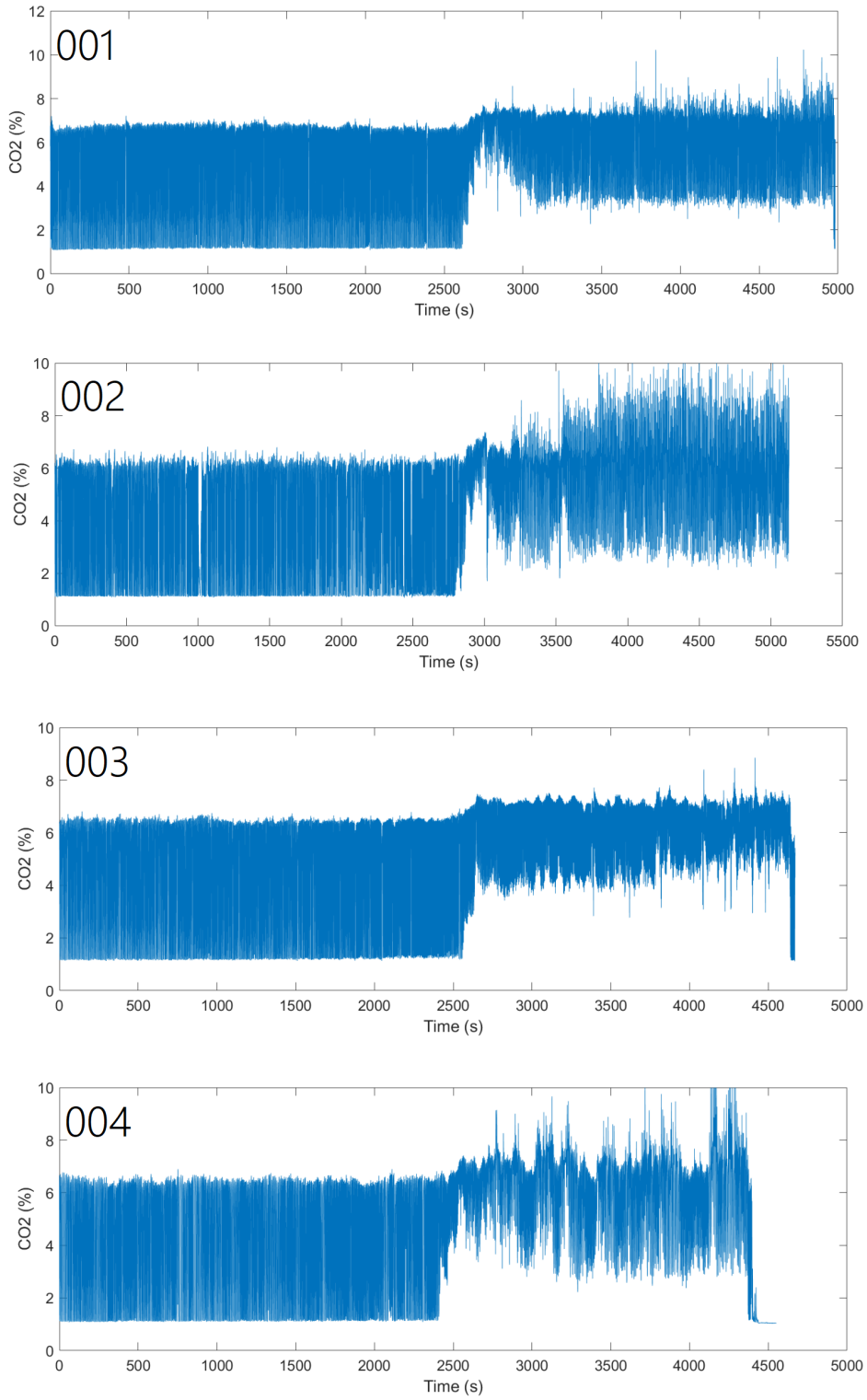

Figure 6.10

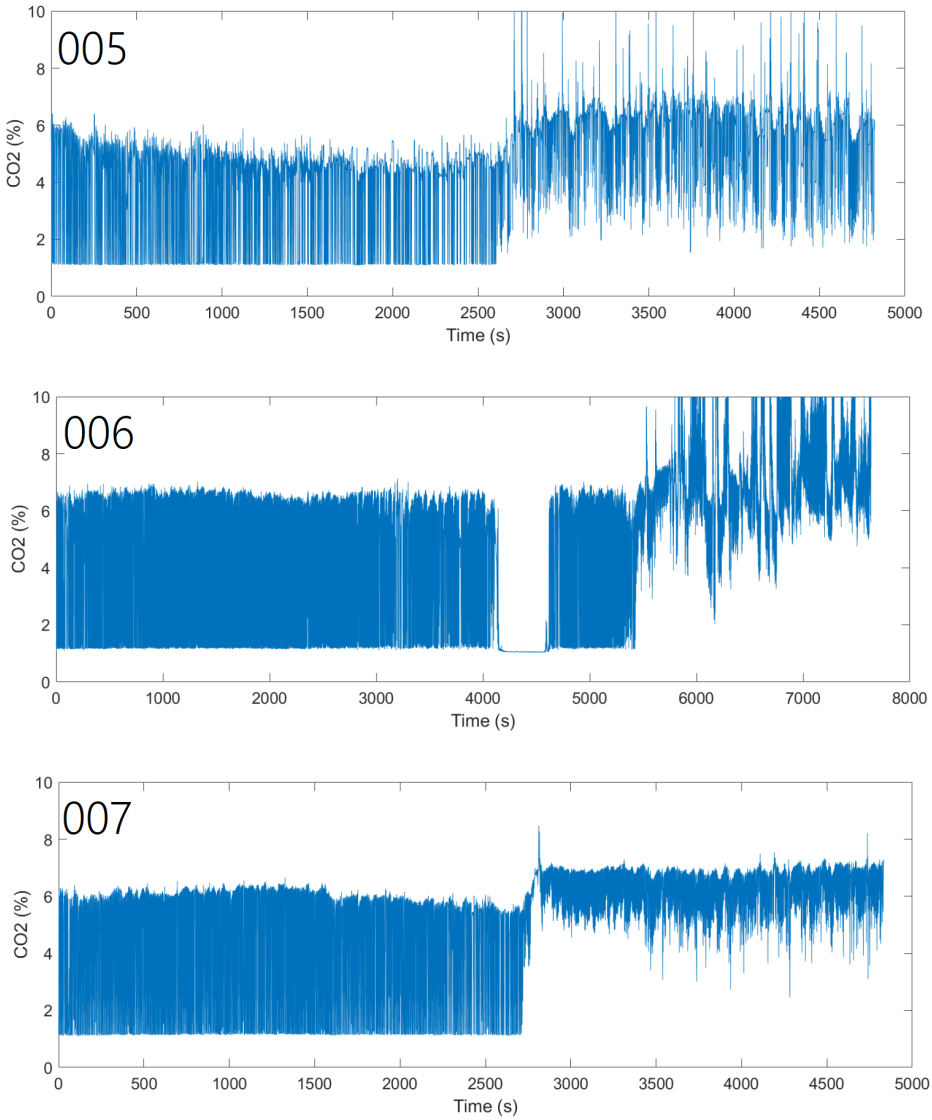

Figure 6.10: Carbon dioxide (CO_2) levels (%) during the data acquisition for the seven subjects. The first approximately 30-35 minutes were with subjects breathing normal room air, followed by a 30 minutes period of subjects breathing CO_2.

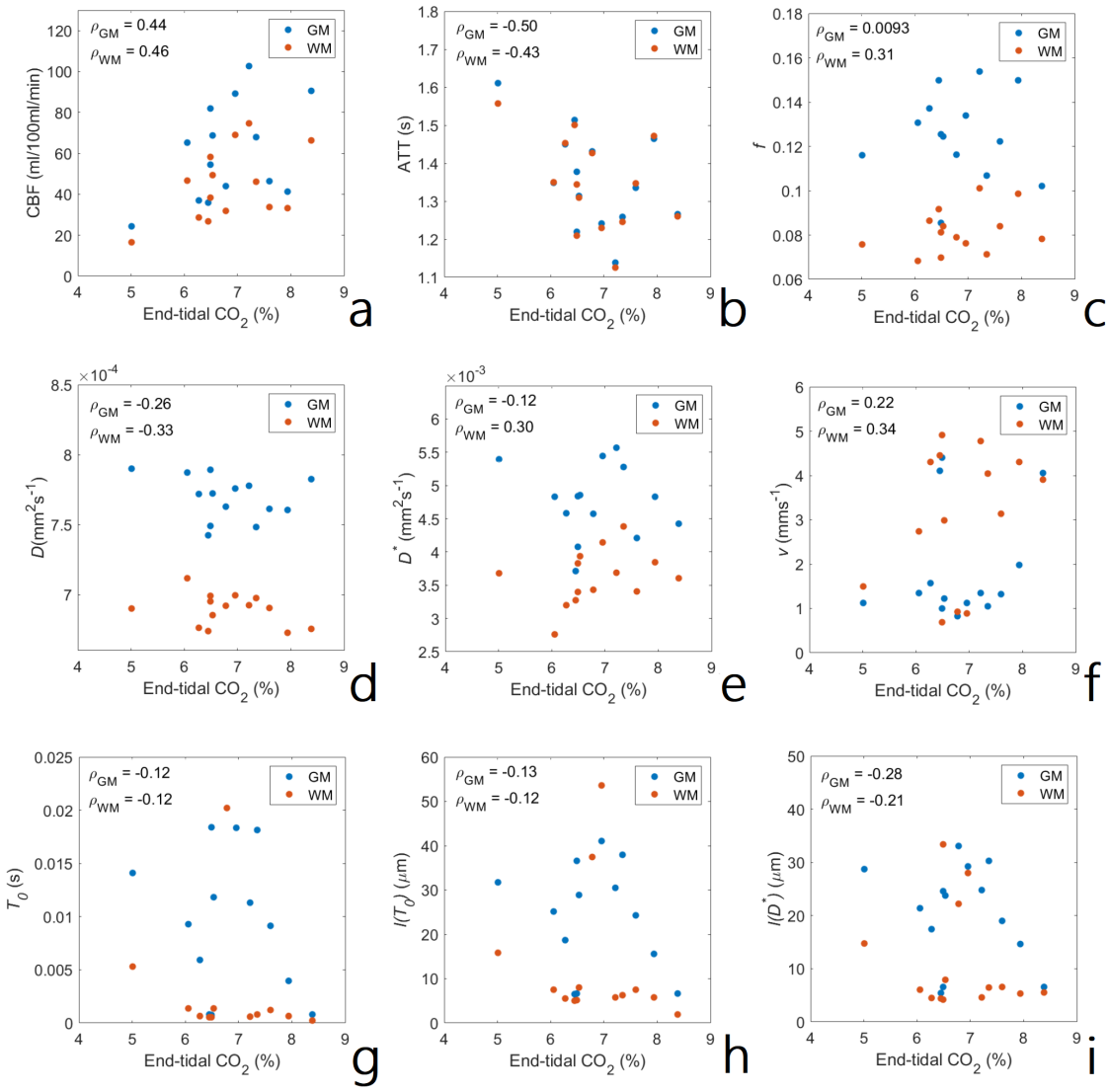

Figure 6.11: Parameters with end-tidal CO_2 levels in grey (GM) and white (WM) matter, blue and orange respectively. (a) shows cerebral blood flow (CBF), (b) arterial arrival time (ATT), (c) perfusion fraction (f), (d) diffusion coefficient (D), (e) pseudo-diffusion coefficient (D^*), (f) average blood velocity (v), (g) correlation time (T_0), (h) and (i) show vessel segment lengths $l(T_0)$ and $l(D^*)$ which use $l = 2vT_0$ and $l = 6D^*/v$) respectively.

7 Microvascular dysfunction in the elderly assessed using intra-voxel incoherent motion (IVIM) diffusion-weighted magnetic resonance imaging (DW-MRI): links to markers of cerebrovascular health, amyloid-β PET, and cognition

Lauren A Scott[1,2], John McFadden[1,2], Andrew N Priest[3], Joel Handley[6,9], Oliver Sparasci[7], Natalia Kyrtata[1,8], Saadat Ahmed[7], Hedley Emsley[1,9,10], Julian Matthews[1,2], Geoff JM Parker[4,5], Karl Herholz[1,2], Ben R Dickie[1,2], Laura M Parkes[1,2].

1. Division of Neuroscience and Experimental Psychology, School of Biological Sciences, Faculty of Biology, Medicine and Health, University of Manchester, Manchester, UK
2. Geoffrey Jefferson Brain Research Centre, Manchester Academic Health Science Centre, Northern Care Alliance & University of Manchester, Manchester, UK
3. Radiology, Cambridge University Hospitals NHS Foundation Trust, Cambridge Biomedical Campus, Hills Road, Cambridge, UK
4. Bioxydyn Limited, Manchester, UK
5. Centre for Medical Image Computing, Department of Computer Science and Department of Neuroinflammation, University College London, London, UK
6. Department of Neurology, Salford Royal Hospital, Salford, UK
7. Pennine Care NHS Foundation Trust, UK
8. University Hospital of Morecambe Bay NHS Foundation Trust, Lancaster, UK
9. Lancaster Medical School, Lancaster University, Lancaster, UK
10. Department of Neurology, Lancashire Teaching Hospitals NHS Foundation Trust, Preston, UK

7.1 Contribution of authors

LS performed DW-MRI data analysis, interpreted data, wrote paper, collected PET/MR data, and ran pre-scan visits and assessments. AP developed the pulse sequence for use on the GE PETMR scanner. JMF performed ROI and WML segmentation. KH performed PET analysis and estimated amyloid accumulation. JH, OS, NK, SA provided medical expertise during pre-scan visits and scanning sessions. HE, JM, GP, KH and LP designed PETMR study. LS, BD and LP interpreted the data. BD and LP edited paper and supervised the research.

7.2 Implementing the model in a patient cohort

We implemented the diffusive IVIM and VA models in the rat brain to extract measures of vessel segment length which agreed with measures from a vascular corrosion cast. Following this, we implemented the VA model in clinical data to extract measures of vessel segment length which agreed with the range presented in literature. We determined that measures are consistent regardless of the models used (i.e. VA alone, or VA and diffusive IVIM). The next step was to implement methods of estimating vessel segment length in a clinical cohort of aged patients, some of which had cardiovascular disease and/or cognitive impairment, to determine sensitivity to these pathologies. We also investigate changes in functional IVIM and VA parameters with disease.

7.3 Abstract

Introduction: Cerebrovascular dysfunction is now recognised as an emerging driver of cognitive dysfunction in the elderly. Cardiovascular disease increases the risk of developing AD and cerebral small vessel disease, and its effects on the brain may underlie, or contribute towards, cognitive decline in both conditions. We have recently developed and validated a non-invasive multi-diffusion-time diffusion-weighted (DW) MRI technique for measuring structural and functional aspects of the microvasculature. Here, we apply this method to study how cardiovascular risk factors and amyloid-β accumulation affect microvascular function and structure in the elderly, and to determine whether these measures are predictive of cognitive function.

Methods: Twenty-seven elderly subjects at risk of dementia between the ages of sixty and eighty underwent PET-MRI brain imaging, including structural MRI and multi-diffusion-time DW-MRI. Fourteen subjects were rescanned within one month to assess repeatability. White matter lesion (WML) volume was quantified from T2-weighted FLAIR MRI. Microvascular parameters (perfusion fraction (f), pseudo-diffusion coefficient (D^*), vessel segment length (l), and blood velocity (v)) were measured using multi-diffusion-time diffusion weighted MRI in cortical grey matter and the hippocampus. Cardiovascular risk was quantified using QRISK2-2017. Cognitive performance was quantified using the Montreal cognitive assessment (MoCA). Amyloid-status was determined from PET images by an experienced neurologist.

Results: Scan-rescan repeatability was high for f, D and D^* (coefficient of variation $< 25\%$). f was positively correlated with QRISK in both regions and with WML in the hippocampus. D was positively correlated with QRISK and WML in cortical GM. f was negatively correlated with MoCA score in both regions. Amyloid status did not significantly affect MoCA score.

Discussion: The IVIM perfusion fraction (f) was found to correlate significantly with

cardiovascular risk and cognitive impairment (higher f associated with higher risk and worse cognitive performance). Amyloid-status was not predictive of cognitive performance. Increased f may reflect increased blood volume as part of the auto-regulatory response to maintain CBF. This chronic dilation may mean the system is unable to respond well to further demand (e.g. demand due to increased neural activity) which could explain the negative correlation between f and MoCA score. Further work is needed to fully understand the cause of increased perfusion fraction, and its impact on brain function.

7.4 Introduction

Advancements in medicine resulting in increased longevity have caused an increase in the prevalence of cognitive dysfunction, since age is the primary risk factor for neurodegenerative disease. Approximately 50 million adults are living with dementia, with this number set to triple by 2050. Alzheimer's disease (AD) causes approximately 60 to 80 % of these cases [262], however many of these cases exhibit clear signs of mixed AD and cerebrovascular pathologies such as white matter lesions, microbleeds and capillary amyloid angiopathy [263]. Dementia arising from cerebral small vessel disease shares many of the same risk factors as AD [263], however, the impacts of these risk factors on the brains of AD patients have historically been overlooked [18, 185]. AD is characterised by the accumulation of amyloid-β plaques and neurofibrillary tangles (NFTs) [83]. However, it is unclear how these species are related to the neurodegenerative process and neuronal dysfunction in AD [18]. For example, some studies show that amyloid-beta levels do not have a large effect on cognitive status in AD patients [264] or healthy elderly [265], and therapeutic reductions in amyloid-beta do not substantially improve cognition [72], at least in the late stages of the disease.

Increasing evidence associates vascular dysfunction with AD [1, 4, 6, 19, 23, 43, 58, 67, 76, 77, 94]. Alterations in the cerebrovasculature ultimately reduce oxygen supply to tissue or impair blood-brain-barrier (BBB) function [62, 90, 266], which could result in ischaemic or hypoxic injury [1, 18, 55, 77], stimulate inflammation and possible build-up of amyloid and NFTs [19, 77, 83]. Nielsen et al. [83] discuss capillary rarefaction in AD and demonstrate that severity of cognitive symptoms is associated with reductions in cortical perfusion. BBB integrity has also been linked to cognitive function [90, 267]. Numerous studies have confirmed vascular alterations, as highlighted in review papers by Brown and Thore [58], Zlokovic et al. [1], Østergaard et al. [55], and Bell and Zlokovic [19]. Structural changes in capillaries have also been noted in AD for many years. In 1997, Buée et al. [5] documented fragmentation of vessels (particularly in the hippocampus), increased tortuosity, glomerular loop formations, thin vessels, and decreased length and branching. Baloyannis and Baloyannis [6] also found increased tortuosity in the capillaries of the

hippocampus and several cortical regions. It is currently unclear how these changes affect the brain, at what stage of disease they occur, and whether they contribute to cognitive impairment. Identifying and staging any vascular changes in pre-symptomatic patients could be important for early diagnosis and prevention trials [268].

Magnetic resonance imaging (MRI) enables microvascular function and structure to be measured non-invasively. Diffusion-weighted MRI has been used extensively to study changes in diffusion of water in tissue as a marker of cellular integrity and microstructure. Extravascular signal attenuation increases in the hippocampus of MCI and AD patients, compared to healthy controls [268–271] indicating changes such as cell degeneration. Bozzali et al. [272] show increased diffusivity in white matter regions likely due to fibre tract degradation associated with loss of cortical neurons. A similar approach can be used to sensitise MRI signals to movement of water in blood. Le Bihan et al. [14, 207] introduced intravoxel incoherent motion (IVIM) which models the signal attenuation caused by intravascular spins at low diffusion-weighting (b-value) and long diffusion-sensitisation times (diffusion-time) as a decay governed by a pseudo-diffusion coefficient (D^*). Recent studies have developed upon the standard IVIM approach by incorporating multi-diffusion-time to sensitise MRI signals to changes in blood velocity (v) and the length scale of microvessel segments (l) (Chapters 4 and 5). Standard IVIM parameters including the perfusion fraction (f), pseudo-diffusion coefficient (D^*), and extravascular diffusion coefficient (D) are also derived.

In this paper, we apply multi-diffusion-time DW-MRI to twenty-seven elderly subjects at risk of dementia and examine the relationships between the derived DW-MRI parameters and cardiovascular risk, amyloid-status, and cognitive function, with the aim of understanding the factors associated with cognitive impairment. We examine the correlation of parameters with white matter lesion volume and a measure of cardiovascular risk (QRISK-2017), and perform multivariate linear regression to determine the effect of MRI-derived microvascular parameters and amyloid status on the Montreal cognitive assessment (MoCA) score.

7.5 Methods

7.5.1 Subjects

The study was reviewed and approved by the University of Manchester Research Ethics Committee and written informed consent was obtained from all participants. Participants were recruited using a number of platforms; UK Join Dementia Research (JDR) platform (https://www.joindementiaresearch.nihr.ac.uk/), Greater Manchester Mental Health NHS Foundation Trust memory clinic (https://www.gmmh.nhs.uk/), word of mouth referrals and through advertisement at local University of the Third Age (U3A) groups. Subjects

with cognitive complaints, diagnoses of mild cognitive impairment (MCI) and no cognitive issues were recruited, as well as those with and without cardiovascular risk factors.

Key inclusion criteria were; age of 60 to 80 years and capacity to consent. Exclusion criteria included; a Geriatric Depression Scale (GDS-15) score >10; MRI or gadolinium contrast agent contraindications; renal insufficiency (eGFR <60); severe asthma or COPD; history of severe head trauma, brain tumours or brain infection; recurrent psychotic or neurodegenerative disorders; epilepsy; untreated B12 vitamin deficiency or thyroid disease; moderate stroke with a Modified Rankin Scale ≥2; history of drug abuse; alcohol consumption>35 units per week; or use of benzodiazepines, lithium carbonate, antipsychotics including atypical agents, high dose antidepressants or anticonvulsants.

Sociodemographic and clinical data were collected through an interview in an initial pre-scan visit. Participants completed the following forms: medical history, PET-MR safety screening forms and consent forms. Blood samples were taken for renal and lipid profiles, and HbA1c (shows average blood glucose levels over previous 2/3 months), to ensure sufficient renal function and calculate cardiovascular risk. Systolic and diastolic blood pressure was taken on each visit. The cardiovascular disease risk score was calculated using the QRISK2 2017 calculator (https://qrisk.org/2017/) which encompasses age, gender, ethnicity, cholesterol levels, blood pressure and treatment, diabetes, chronic kidney disease, atrial fibrillation, rheumatoid arthritis, body mass index and smoking status. QRISK2 is a validated algorithm which predicts the risk of an individual having a major vascular event (e.g. heart attack or stroke) in the next ten years. In this study, we use QRISK2 as a marker of cardiovascular health. The Montreal Cognitive Assessment (MoCA) and Geriatric Depression Scale (GDS-15) were also completed.

Subject demographics are detailed in Table 7.1.

Table 7.1: Subject demographics, including; sex, age, Montreal Cognitive Assessment (MoCA) score, education, QRISK2-2017 score, Geriatric Depression Scale (GDS). Note: one participant had no amyloid status due to issues with the PET tracer (male; age 67 years; MoCA 23; education 10 years; QRISK 13.7).

	Amyloid positive	Amyloid negative	*p*-value
Number	8	18	-
Sex, females, n (%)	5(62.5)	10(55.6)	0.74
Age, years, mean ± SD	71.6 ± 3.9	69.6 ± 5.6	0.29
MoCA, mean ± SD	24.3 ± 4.0	27.3 ± 3.0	0.077
Education, mean ± SD	16.8 ± 6.2	16.0 ± 3.9	0.76
QRISK, mean ± SD	22.0 ± 12	18.2 ± 10	0.45
GDS, mean ± SD	1.70 ± 1.8	0.778 ± 1.2	0.24

7.5.2 PET-MRI acquisitions

Simultaneous PET/MRI was performed on a 3T GE Signa PET/MR scanner (GE Healthcare, Chicago, Illinois, United States) using a 32 multi-channel receiver head coil (Nova Medical Inc, Wilmington, Massachusetts, United States). Participants were scanned dynamically for 30 minutes followed by a 40 minute break and a further 50 minute scan. Data were acquired in twenty-seven participants. One participant did not have PET imaging due to issues with scheduling the PET tracer.

Axial DW-MRI data was acquired across three orthogonal directions, with whole brain coverage (Figure 7.3 in supplementary material). The b-value was varied through values 0 and 1000 smm^{-2} (Table 7.2). The diffusion-time (Δ) was varied through six values between 16.54 and 49.89 ms (subject average normalised signal versus b-value for each diffusion-time shown in Figure 7.4 in supplementary material). The highest b-value was limited by the maximum gradient strength and diffusion-time, hence for shorter diffusion-times, we used a lower maximum b-value. The magnitude of the diffusion gradient pulse (G) and gradient application time (δ) were altered to vary the diffusion-time. Other sequence parameters include: TR=5525 ms, TE=95.3 ms, voxel size 0.8125 $\times$ 0.8125 $\times$ 4 mm^3, FOV 256 $\times$ 256, number of slices 35.

Participants underwent a 3D magnetisation prepared rapid gradient echo (MPRAGE) T1-weighted scan for regional segmentation, either with or without prospective motion correction (PROMO). Eight subjects had an MPRAGE T1-weighted scan without PROMO, and; TR=6.884 ms, TE=2.736 ms, TI=400 ms, flip angle = 11°, isotropic voxel of length 1 mm. Nineteen subjects had an MPRAGE T1-weighted scan with PROMO, and; TR=7.716 ms, TE=3.044 ms, TI=900 ms, flip angle = 9°, isotropic voxel length of 1 mm. The PROMO was introduced part way through the study to improve image quality.

Sagittal T2-weighted FLAIR images were acquired to determine white matter lesion (WML) volume. The following acquisition parameters were used: TR=6202 ms, TE=115 ms, TI=1760 ms, isotropic voxel size of 1 mm.

Dynamic PET data was acquired for 120 minutes following injection of 185 MBq of [18F]Flutemetamol through an antecubital vein. Data was not acquired between 30-70 minutes, during which time the subject was removed from the scanner room for a break. At 70 minutes participants were returned to the scanner bed, and a further 50 minutes of dynamic PET data acquired.

Fourteen participants were rescanned within one month to assess scan-rescan repeatability of DW-MRI measurements. PET imaging was not performed on the second visit.

Note that these data were acquired as part of a longer scan protocol which included arterial spin labelling (ASL), quantitative susceptibility mapping (QSM) and dynamic contrast enhanced (DCE) MRI.

Table 7.2: Diffusion-times, Δ, pulse durations, δ, and b-values used in the DW-MRI protocol.

Δ (ms)	δ (ms)	b-value (smm^{-2})
16.54	7.980	10, 30, 50, 100
18.39	10.93	10, 30, 50, 100, 200
23.14	15.60	10, 30, 50, 100, 200, 300, 500
30.96	18.68	10, 30, 50, 100, 200, 300, 500, 750, 1000
39.95	15.70	10, 30, 50, 100, 200, 300, 500, 750, 1000
49.89	13.70	10, 30, 50, 100, 200, 300, 500, 750, 1000

7.5.3 PET data processing and amyloid status

Amyloid-PET images were obtained by iterative reconstruction with corrections for attenuation and scatter, incorporating time-of-flight information (VPFX, 2.08 mm $\times$ 2.08 mm $\times$ 2.78 mm voxels, 4 iterations, 28 subsets, no resolution modelling, no post filtering). To assess amyloid-β status, a late-timepoint amyloid image was generated by co-registering PET frames acquired between 90-110 minutes post-injection to the 90 minute frame using in-house registration software written in Matlab (R2019b), and then taking the mean of these images. Amyloid-β status (positive/negative) was assessed via expert neurological examination (KH) of the averaged 90-110 minute image.

7.5.4 Extraction of regional MRI signals

T1-weighted images requiring bias correction before segmentation were processed using FSL FAST. Cortical reconstruction and volumetric segmentation was performed on all images with the Freesurfer image analysis suite [213] (version 6.0.0), which is documented and freely available for download online (http://surfer.nmr.mgh.harvard.edu/). The Destrieux atlas [214] was used from available Freesurfer segmentation outputs.

SPM12 (http://www.fil.ion.ucl.ac.uk/spm) was used for re-slicing and co-registration of the T1-weighted images (and associated segmentation) with DW-MRI images. The DW-MRI signal from cortical grey matter (GM) and the hippocampus were extracted. The trace of the signal across the three orthogonal diffusion directions was calculated for each b-value and diffusion-time. Mathematical models describing signal behaviour with b-value and diffusion-time were fit to the average signal from each region, as described later, in order to extract parameter estimates.

7.5.5 Extraction of white matter lesions volume

To extract white matter lesion (WML) volume, the SPM toolbox Lesion Segmentation Tool (LST) was implemented with a lesion growth algorithm [273], using the T1 and T2-FLAIR MR images.

7.5.6 Extraction of diffusion-weighted metrics

DW-MRI metrics were estimated using standard and multi-diffusion-time intravoxel incoherent motion modelling of the DWI signal attenuation. The standard IVIM model [14] and the velocity autocorrelation (VA) [33] model of multi-diffusion-time IVIM are described in the following section.

7.5.6.1 IVIM

In the presence of diffusion-sensitising gradients, attenuation of the MR signal can be described by a two-compartmental model, describing the intra and extra-vascular contributions [14]. The total normalised signal is modelled as a sum of two exponentials:

$$\frac{S(b,\Delta)}{S_0} = fe^{-bD_b}H(b,\Delta) + (1-f)e^{-bD} \tag{7.1}$$

where $b = \gamma^2\delta^2G^2(\Delta - \delta/3)$ when employing pulsed gradient spin echo (PGSE) sensitisation. γ is the proton gyromagnetic ratio; G, the magnitude of the diffusion gradient pulses; δ, the duration of each diffusion gradient pulse and; Δ, the diffusion-time, the time between the gradient pulses. $S(b,\Delta)$ is the DW-MR signal as a function of b; S_0, the signal at $b = 0$; D, the extravascular diffusion coefficient; and f, the perfusion fraction. D_b is the apparent diffusion coefficient of water in blood; and $H(b,\Delta)$ is the signal attenuation due to perfusion.

When the diffusion-time is long enough that blood flow changes vessel segment multiple times, the signal attenuation due to perfusion can be described by the pseudo-diffusion coefficient (D^*):

$$H(b) = e^{-bD^*} \tag{7.2}$$

This is commonly referred to as the IVIM model, or diffusive IVIM model.

7.5.6.2 Velocity autocorrelation model

The velocity-autocorrelation (VA) model [33] describes signal attenuation due to perfusion as a function of diffusion-time (Δ):

$$H(b,\Delta) = e^{-bk(\Delta)} \tag{7.3}$$

where k is the perfusion attenuation coefficient due to microcirculatory flow in the presence of bipolar diffusion gradients:

$$k = \frac{\Omega v^2 T_0}{3\delta^2(\Delta - \delta/3)} \tag{7.4}$$

where v is the average blood velocity; T_0 is the average time that spins in the blood stay in a segment (correlation time), and:

$$\Omega = \delta^2(\Delta - \delta/3) - 2T_0^2\delta - T_0^3 q, \tag{7.5}$$

$$q = 2\exp\Big(-\frac{\Delta}{T_0}\Big) + 2\exp\Big(-\frac{\delta}{T_0}\Big) - \exp\Big(-\frac{\Delta+\delta}{T_0}\Big) - \exp\Big(-\frac{\Delta-\delta}{T_0}\Big) - 2. \tag{7.6}$$

7.5.6.3 Estimation of the extravascular diffusion coefficient, D, and perfusion fraction, f

Since the signal attenuation due to microcirculatory flow is higher than extravascular signal attenuation, the microcirculatory component is insignificant at b-values higher than 200-600 smm^{-2} [131, 134, 139, 168]. As such, the components can be easily separated using a two-step method, an approach commonly used in IVIM studies [131, 134, 139, 158, 168]. In this study, the extravascular diffusion coefficient and perfusion fraction were estimated using b-value data between 500 and 1000 smm^{-2}. Since it was not possible to acquire data with such high b-values at the shortest diffusion-times (Table 7.2), D and f were calculated for the three highest diffusion-times only (30.96-49.89 ms) by fitting the following model to the normalised data:

$$\frac{S}{S_0} = (1-f)e^{-bD}. \tag{7.7}$$

For the three lowest diffusion-times (16.54-23.14 ms), D and f were inferred through linear extrapolation of f, and by taking the mean value of D. This agrees with previous clinical data which describes a linear relationship between f and Δ, and no relationship between D and Δ (Chapter 5).

The values for f and D presented in this study include only those calculated from the highest diffusion-time. However, the values inferred for f and D at shorter diffusion-times were used to estimate v and l (as described below).

The 'lsqcurvefit' function in Matlab (R2019b) was used (MathWorks, Natick, Massachusetts, USA) with a trust-region-reflective algorithm. All fitting described in this report uses the same function.

7.5.6.4 Estimation of the pseudo-diffusion coefficient, D^*, blood velocity, v, and vessel segment length, l

At low b-values, the signal is comprised of intravascular and extravascular contributions. To isolate the intravascular component, the extravascular component was subtracted from the total normalised signal for each diffusion-time and divided by f:

$$\frac{1}{f}\left(\frac{S}{S_0} - (1-f)e^{-bD}\right) = e^{-bD_b+c}H(b,\Delta) \tag{7.8}$$

c is a parameter added to improve fitting (Chapter 4, Section 4.5.3.2). D_b was set to equal 1.75×10^{-3} mm^{2}s^{-1} [131].

To estimate D^*, the right hand side of Equation 7.8 was fit to the normalised intravascular signal at the highest diffusion-time (49.89 ms) and b-values<500 smm^{-2}, using Equation 7.2 for $H(b,\Delta)$, since the diffusion-time is long enough for pseudo-diffusive flow.

To estimate v, the right hand side of Equation 7.8 was jointly fit to the normalised intravascular signal from all diffusion-times and b-values<500 smm^{-2}, using Equation 7.3 for $H(b,\Delta)$. Fitting of models to the isolated perfusion data for four subjects is shown in Figure 7.5 in supplementary material.

Estimates of vessel segment length, l, were generated using [14]:

$$D^* = \frac{vl}{6}. \tag{7.9}$$

7.5.7 Statistical analyses

7.5.7.1 Between-group differences in subject demographics

Patients were stratified into AD and non-AD groups based on amyloid-positivity. Differences in group characteristics were evaluated as follows. For continuous variables (age, MoCA, education, QRISK and GDS), independent two-sample Welch's t-tests were used ('ttest2' in Matlab). For categoric variables (sex), chi-squared tests were performed using the 'crosstab' function in Matlab.

7.5.7.2 Assessment of scan-rescan repeatability

To determine scan-rescan repeatability of DW-MRI measures, fourteen participants were scanned twice within one month. The coefficient of variation (CoV) was calculated to investigate repeatability:

$$\text{CoV}(\%) = 100\frac{\sigma}{\mu} \tag{7.10}$$

where σ is the within subject standard deviation and μ the mean. σ is calculated using [200]

$$\sigma = \sqrt{\frac{\Sigma_{i=1}^{n}(x_{i,1} - x_{i,2})^2}{2n}} \tag{7.11}$$

where n is the number of subjects, x_1 and x_2 are the parameter estimates for the first scan and repeat scan, respectively. μ is found using:

$$\mu = \frac{\Sigma_{i=1}^{n}(x_{i,1} + x_{i,2})}{2n}. \tag{7.12}$$

7.5.7.3 Relationship between vascular and tissue DW-MRI metrics and markers of cerebrovascular health

Univariate regression analysis was performed using the 'corrcoef' and 'regression' functions in Matlab (R2019b) to explore 1) the relationship between white matter lesion (WML) volume and QRISK, 2) relationships between intra- and extravascular DW-MRI parameters (f, v, l, D^*, and D), and QRISK score and WML volume. Separate analyses were performed for cortical grey matter and the hippocampus. Statistical analyses were not corrected for multiple comparisons due to the exploratory nature of this step of analysis. The DW-MRI parameters with statistically significant associations with WML volume and QRISK were included in multivariate analysis to predict cognition, as described below.

7.5.7.4 Value of vascular and tissue DW-MRI metrics and amyloid status for predicting cognition

Multivariate regression was performed using the 'lm' function in R studio (version 1.2.1335) to determine whether DW-MRI parameters can predict cognition, after adjustment for amyloid-status. Models were built using the perfusion fraction, f, and extravascular diffusion coefficient, D, as independent predictors due to their association with markers of cerebrovascular health as described above. Amyloid status (+ve/-ve) derived from PET was also included to adjust for any potential confounding effects of AD pathology on cognition. Separate regression models were built for cortical GM and the hippocampus to enable region-dependent effects to be investigated. p-values less than 0.025 were considered significant at the 5% level to correct for multiple-comparisons (one model built for each region). The statistical significance of the regression coefficients was determined using the 'anova' function. The effect size (η^2) and confidence intervals were determined using the 'effectsize' function. Effect size is considered large for $\eta^2 \geq 0.26$, medium for $0.26 > \eta^2 \geq 0.13$ and small for $0.13 > \eta^2 \geq 0.02$ [274].

7.6 Results

7.6.1 Subject demographics

Twenty-seven subjects are included in this study. All subjects received a PET-MRI scan, except for one subject who received only MRI. Of the twenty-six with both PET and MRI data, eight were amyloid positive and eighteen amyloid negative. Table 7.1 summarises subject demographics. The amyloid negative and positive groups are similar in sex, education and QRISK. The age and GDS are slightly lower for the negative group, and the MoCA score higher, however these differences are not significant.

7.7 Assessment of scan-rescan repeatability

Scan-rescan coefficient of variation (CoV) of parameters are shown in Table 7.3. The perfusion fraction, f, diffusion coefficient, D, and pseudo-diffusion coefficient, D^*, all have reasonably high repeatability (low CoV) for cortical GM and the hippocampus. CoV is slightly lower in cortical GM for D and D^*; an expected result considering the larger size of the region. Average blood velocity, v, and average vessel segment length, l, have higher CoV. The two regions have similar repeatability for v, l has lower CoV in cortical GM.

Table 7.3: Inter-scan coefficient of variation (%) calculated from repeat measures of fourteen subjects for the perfusion fraction, f; diffusion coefficient, D; pseudo-diffusion coefficient, D^*; average velocity, v; and average vessel segment length, l. Regions of interest are cortical grey matter (GM) and the hippocampus.

Region	f	D	D^*	v	l
Cortical GM	10	1.6	13	73	54
Hippocampus	11	4.3	25	72	61

7.7.1 Relationship between vascular and tissue DW-MRI metrics and markers of vascular health

7.7.1.1 QRISK and WML

Figure 7.6 (supplementary material) shows the relationship between white matter lesion (WML) volume versus QRISK. Elevated cardiovascular risk score (QRISK) was associated with increased WML volume (p=0.013).

7.7.1.2 Intravascular measures, QRISK and WML

Regression plots of the perfusion fraction (f), pseudo-diffusion coefficient (D^*), average blood velocity (v) and average vessel segment length (l) against QRISK and WML volume in cortical GM and the hippocampus are shown in Figure 7.1.

Elevated cardiovascular risk score (QRISK) was associated with increased perfusion fraction (f) in both cortical GM and the hippocampus (p <0.05 and p <0.01 respectively). Furthermore, increased f in the hippocampus (p <0.01) was associated with increased WML volume. The same trend was observed in grey matter but was not statistically significant. The pseudo-diffusion coefficient (D^*), average blood velocity (v) and average vessel segment length (l) were not correlated with either QRISK or WML in either region.

The hippocampus had higher absolute values for f and D^* than cortical grey matter ($p = 2.0 \times 10^{-5}$ and $p = 4.4 \times 10^{-6}$, respectively). Mean f across all subjects was 0.139 and 0.172 in GM and the hippocampus, respectively. Mean D^* was 4.07×10^{-3} and 8.65×10^{-3} mm^2s^{-1}. Values for l were also found to be higher in the hippocampus (p=0.0060) for some participants (mean: 17.8 versus 36.8 μm), although v is similar (p=0.18). The diffusion coefficient is also slightly higher for some participants in the hippocampus (p=0.0015). Mean D was 8.24×10^{-4} and 8.68×10^{-4} mm^2s^{-1}.

7.7.1.3 Extravascular measures, QRISK and WML

Regression plots of the diffusion coefficient (D) against QRISK and WML volume in cortical GM and the hippocampus are shown in Figure 7.1. Increased cardiovascular risk (QRISK) and WML volume were associated with increased extravascular diffusion (D) in cortical GM (p <0.01 and p <0.05 respectively). The same trend exists in the hippocampus, but is not significant.

7.7.2 Value of vascular and tissue DW-MRI metrics and amyloid status for predicting cognition

Tables 7.4 and 7.5 show the results of multivariate regression analyses for the hippocampus and cortical grey matter respectively. The perfusion fraction f and extravascular diffusion coefficient, D, were included since only these parameters had a significant correlation with markers of cerebrovascular disease in univariate analyses (Figure 7.1).

Results indicate that f in both cortical GM and the hippocampus has a large and significant effect on MoCA in both regions; p=0.0044 and η^2=0.31 (where η^2 is effect size) for the hippocampus, and p=0.011 and η^2=0.26 for cortical grey matter.

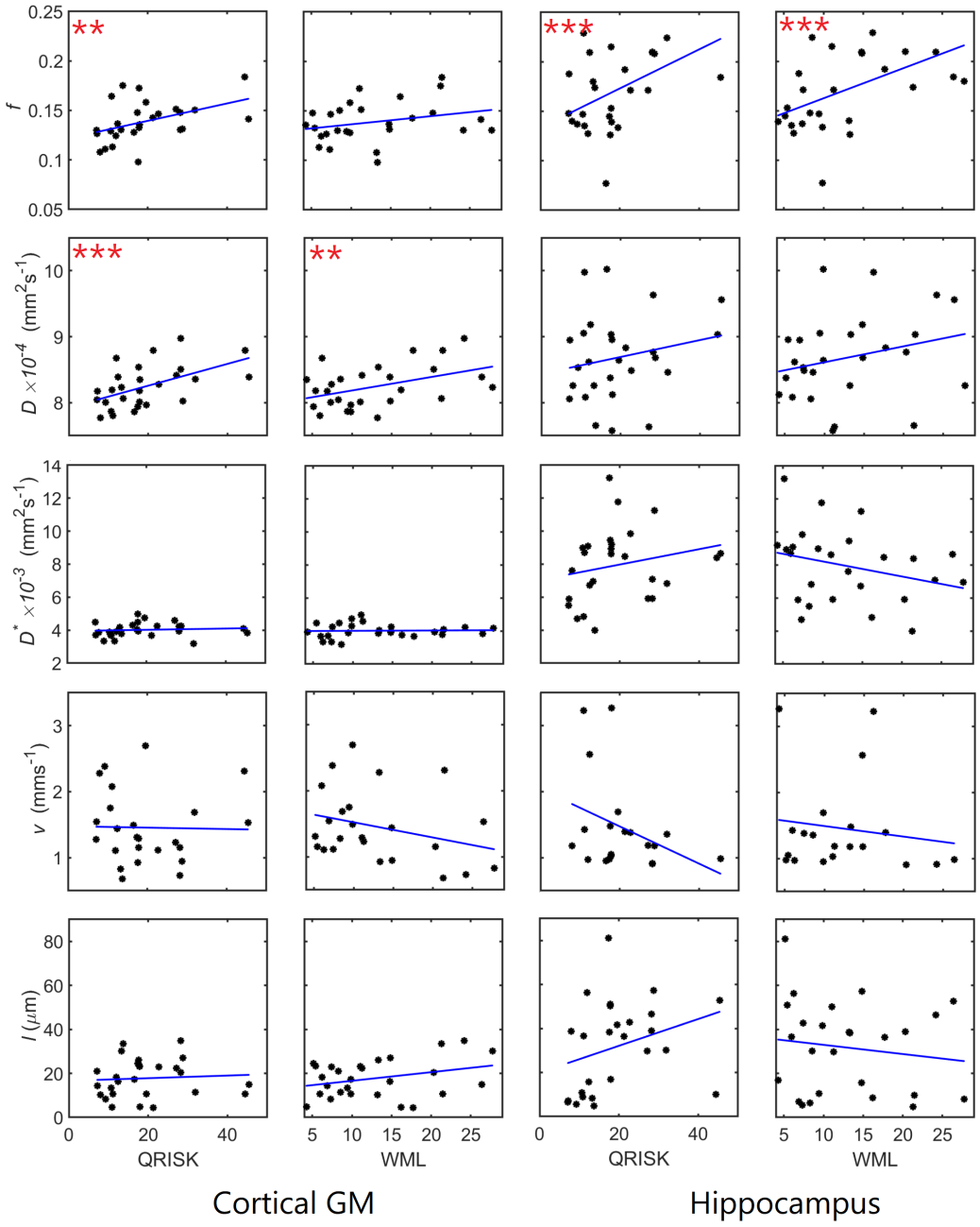

Figure 7.1: Regression plots of DW-MRI parameters against cardiovascular risk score (QRISK) and white matter lesion (WML) volume. Regions of interest were cortical grey matter (GM) and the hippocampus. Abbreviations: f, perfusion fraction; D, apparent diffusion coefficient of the extravascular space; D^*, pseudo-diffusion coefficient of the intravascular space; v, average blood velocity; and l, average vessel segment length. $^{**}p < 0.05$, $^{***}p < 0.01$, not corrected for multiple comparisons.

Table 7.4: Linear regression model outputs for the hippocampus with MoCA as dependent variable, and perfusion fraction (f), diffusion coefficient (D) and amyloid status as independent predictors. Effect size: ***large; **medium. Intercept coefficient: 42

Parameter	p-value	Coefficient	Effect size (partial η^2)	Confidence interval (90%)
f	0.0044	-39	0.31***	[0.07, 0.53]
D	0.20	-9100	0.07**	[0.00, 0.29]
Amyloid	0.16	-1.9	0.09**	[0.00, 0.31]

Table 7.5: Linear regression model outputs for cortical GM with MoCA as dependent variable, and perfusion fraction (f), diffusion coefficient (D) and amyloid status as independent predictors. Effect size: ***large; **medium. Intercept coefficient: 51

Parameter	p-value	Coefficient	Effect size (partial η^2)	Confidence interval (90%)
f	0.011	-69	0.26***	[0.04, 0.48]
D	0.17	-17000	0.08**	[0.00, 0.30]
Amyloid	0.26	-1.7	0.06**	[0.00, 0.27]

7.7.2.1 Perfusion fraction and MoCA

Figure 7.2 shows the perfusion fraction, f, versus MoCA for cortical GM (a) and the hippocampus (b). Cognitive dysfunction (lower MoCA) is associated with higher f for both regions (p=0.0066 and p=0.0052 respectively).

7.8 Discussion

In this study, we performed simultaneous diffusion-weighted MRI and amyloid-PET imaging to investigate the relationships between markers of cerebrovascular disease (QRISK, WML volume) in elderly subjects and, the functional and structural features of cortical and hippocampal vasculature, including the perfusion fraction (f), pseudo-diffusion coefficient (D^*), average blood velocity (v), vessel segment length (l) and extravascular diffusion coefficient (D), in cortical grey matter and the hippocampus. In univariate analyses, f and D were found to correlate with QRISK and WML volume (Figure 7.1). We then investigated the relative power of these parameters for predicting cognition, independent of amyloid-status, and found that f described a significant proportion of MoCA variability (Tables 7.4 and 7.5), whereas the extravascular diffusion coefficient and amyloid-status were not significant predictors. Results indicate that f could be an important biomarker for vascular and cognitive dysfunction, adding to growing literature highlighting the importance of vascular dysfunction in neurodegeneration.

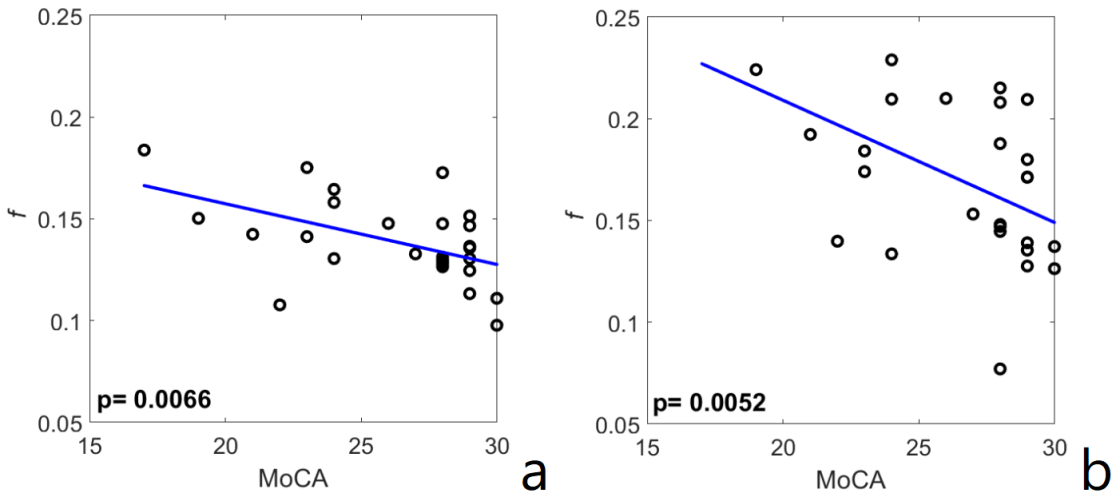

Figure 7.2: Perfusion fraction (f) correlated with Montreal Cognitive Assessment score (MoCA) for cortical grey matter (a) and the hippocampus (b). p=0.0066 and p=0.0052 respectively.

We evaluated the scan-rescan repeatability of DW-MRI measures. Table 7.3 shows f, D and D^* are highly repeatable. Our repeatability values for f and D agree with prior literature reports [174, 275]. However, D^* often has low reproducibility, which is generally attributed to the low vascular fraction in the brain and difficulty separating vascular and extravascular components [275–277], so is sometimes discarded [154]. We find the parameter has reasonably high repeatability, likely due to averaging of the DW-MRI signal across large regions and a 3T field strength giving higher SNR. This is evidenced by the decrease in repeatability between cortical GM and the hippocampus, the former of which is a much larger region, thus has higher SNR. Furthermore, the use of the two-step fitting in low perfused tissue, as used in this study, produces more repeatable parameters [158]. Parameters derived from multi-diffusion-time imaging have lower repeatability (v, l).

Previous work has shown higher repeatability for v and l using a more extensive imaging protocol with ten diffusion-times (Chapter 5). Hence, we suspect the lower repeatability presented here is partly due to reduced number of diffusion-times. Additionally, in previous work the correlation time (T_0) and v were used to estimate l (Chapter 5) using $l = 2vT_0$. Due to very low repeatability in T_0 in the hippocampus in this study (results not shown), we did not use this method. An alternate method was used, which was validated in preclinical data (Chapter 4), whereby l was estimated using D^* and v ($l = 6D^*/v$). It is worth noting, the value of l from these two methods are highly similar and strongly correlated in GM where T_0 was usable (Figure 7.7 in supplementary material).

The perfusion fraction correlated with QRISK in both cortical GM and the hippocampus,

and with WML volume in the hippocampus (Figure 7.1). It is unclear why the trend is not significant in cortical grey matter- it may reflect the pathological timeline of early stage AD where the hippocampus is first affected [278]. The perfusion fraction had a large and significant effect on MoCA variability in cortical GM and the hippocampus (Tables 7.4 and 7.5); f was shown to increase with decreasing MoCA (Figure 7.2).

Considering the hypoperfusion (reduced CBF) and capillary rarefaction measured in mild cognitive impairment and AD [20, 83], one might expect a decrease in f with MoCA or WML volume. However, several studies, including this work, show increasing f with WMH load in cSVD [279] and ageing [217], and with cognitive decline (MCI to AD) [154].

Wong et al. [279] suggest that increasing f may be a result of vasodilation as a compensatory mechanism for impaired blood flow (or a response to inflammation [280, 281]), or as an action of antihypertensive calcium antagonists. Although, when controlling for anti-hypertensives, a significant increase in f was still present. Bergamino et al. [154] suggest the glymphatic system may also contribute. For example, enlarged Virchow-Robin spaces due to plasma flow across an impaired blood-brain-barrier [17] could increase f. Wong et al. [279] show increased f is associated with higher perivascular space score, supporting this theory. The authors also suggest increased tortuosity could affect f since water molecules changing direction more contribute to the fast component. However, this would also affect D^*, which is not seen in our data. Østergaard et al. [55] discuss increases in CBF with mild capillary dysfunction in conditions that represent risk factors for cSVD. The authors argue that small reductions in oxygen extraction efficacy caused by capillary dysfunction can be compensated for by an increase in CBF. The review discusses an increase in CBF in animal models of disease. In rats with induced diabetes, total and cortical CBF were elevated compared to controls early after induction of disease. In early-stage hypertension in rats, elevated CBF responses to hypercapnia were reported compared to controls [22]. Increasing f with increasing QRISK might agree with this theory. Although, an increase in CBF does not necessarily mean an increase in CBV, which f is more commonly associated with.

Extravascular diffusion was positively correlated with QRISK and WML volume in cortical GM (Figure 7.1), but not the hippocampus. Changes in D are thought to be due to microstructural changes such as loss of structural barriers or increased extracellular space, which give more freedom to spins in the extravascular compartment, thus a higher D. One might expect to observe changes in D in the hippocampus, prior to, or at the same time as, changes in cortical GM, since the region is affected early in AD [282]. Although the relationships between hippocampal D and QRISK/WML follow the same trend as in cortical GM, the results are not significant and values appear to be more variable. This is likely due to the region being smaller than cortical GM resulting in lower SNR and noisier data. Results in cortical GM agree with a study by Wong et al. [279] showing an association

between D and white matter hyperintensity (WMH) load in cSVD. Literature investigating the links between the combined cardiovascular risk score (QRISK) and D could not be found, however increased D has been shown individually in obesity [283], hypertension [284] and diabetes [285]. The diffusion coefficient had no significant association with MoCA score in cortical GM or the hippocampus (Tables 7.4 and 7.5). These results agree with a study by Zhang et al. [286] who determine no association of D with cognitive function in cSVD. Conversely, Bergamino et al. [154] show D is able to identify changes in brain integrity in patients with MCI and AD at an earlier disease stage than other IVIM parameters in the hippocampus.

There were no associations between D^*, v or l, and QRISK or WML. Nielsen et al. describe elevated capillary transit time heterogeneity [20, 25, 83] in MCI and AD, which suggests changes in vessel structure or blood flow velocity, or perhaps by vessel size distribution which could be explained by chronic vasodilation and thus increased f. Buée et al. [5] document structural changes in the microvasculature in AD, including decreased vessel length. Conversely, Bouras et al. [287] find that mean capillary length per neuron did not correlate with cognitive status measured before death. Perhaps the stage of disease is too early to discern structural changes in the vasculature. The lack of precision in v and l, or inaccuracies introduced by the methods used may have reduced our sensitivity to structural microvascular changes. The pseudo-diffusion coefficient has been related to CBF [167], hence one might expect a change in the parameter.

Amyloid had no significant association with MoCA score. This suggests microvascular changes (detected by changing f) may occur before any pathological changes caused by amyloid. This result is surprising since amyloid deposition is considered a defining pathological feature of AD, and studies have demonstrated a link between amyloid accumulation and cognitive decline [288, 289]. Although, a recent meta-analysis by Ackley et al. [72] shows therapeutic reduction in amyloid-beta does not have a substantial effect on cognition. Additionally, Furst et al. [264] show global amyloid-beta burden does not correlate well with clinical status in probable AD patients, and Pike et al. [265] show amyloid-beta does not have a large effect on cognition in the healthy elderly. Increasing the number of subjects, particularly amyloid positive patients, would help clarify these results.

The absolute values of f are higher than expected (approximately double [217]) and values of D^* slightly lower than expected. This is likely due to the high b-value threshold of b=500 smm^{-2} (see Appendix A). Evidence shows IVIM parameters are dependent on the b-value threshold [139, 140], perhaps due to non-negligible intravascular contribution which would increase as the threshold is lowered. Studies show f increases with b-value threshold and D^* decreases [139, 140]. Values for D agree well with literature [166, 168, 217]. Estimates of v in human brain capillaries are scarce, however our estimates seem reasonable when compared to simulation work [218] and MR work [164]. Estimates of l agree with

the range presented in literature, but are generally smaller [36, 218–220], with some of the smallest values being on the order of capillary diameter [218]. The hippocampus had higher absolute values for f and D^* than cortical grey matter, possibly reflecting increased vascularity (i.e. possibly due to larger contribution from larger vessels). This is supported by measurements of l, which were also found to be higher in the hippocampus, although v is not significantly different. One might expect higher velocities in a region with larger vessels, hence there being no significant difference may be due to inaccuracies introduced via our methodology, as already discussed.

A limitation of our data is the non-constant δ value (Table 7.2); whilst effects are included in the VA model, they are not accounted for in the diffusive IVIM model or the extravascular model. In the two-step method used, the extravascular signal is subtracted from the intravascular signal for each diffusion-time. This method accounts for the effects of diffusion-time on the extravascular signal attenuation, but does not account for δ. Furthermore, for the three lowest diffusion-times, f and D could not be directly estimated and were inferred via linear extrapolation for f and averaging of results for D. f and D are required for each diffusion-time to allow for subtraction of the extravascular signal to fit the VA model. Extrapolating for f and averaging D could have affected the accuracy of v, and thus l. These errors may have masked any effects of v and l. Additionally, we were also unable to investigate IVIM parameters in cerebral white matter due to limitations on repeatability of parameters and the requirement for more complex modelling (Chapter 5). The use of two different T1 weighted MRI sequences may have introduced some variation into the ROI segmentation in our data. Last, we did not correct for multiple comparisons when investigating the relationship between DW-MRI metrics and, QRISK and WML (Figure 7.1). This could have led to false positives. Although, the significant correlations identified have much lower subject variability than other data, so are convincing. Additionally, the analysis is exploratory at this stage and is used to guide further regression analysis.

7.9 Conclusion

In this study, we used simultaneous DW-MRI and PET in an elderly cohort to characterise structural and functional properties of the cerebrovasculature, and related these to markers of cerebrovascular health and cognition. We demonstrate that the perfusion fraction, f, measured in cortical GM and the hippocampus is associated with QRISK and WML volume, and is predictive of cognitive function independent of the extravascular diffusion coefficient and amyloid-status. Our results emphasise the importance of vascular disease in early cognitive changes associated with both amyloid-positive (AD-type), and AD-negative patients. Future studies should investigate the factors underlying increased f

and its relationship with other vascular measures known to change in dementia, such as arterial arrival time, CBF, capillary transit time heterogeneity, and blood-brain barrier permeability.

7.10 Acknowledgements

The authors wish to acknowledge the study volunteers, University of Manchester radiographers and research nurses at Join Dementia Research (JDR)/Greater Manchester Mental Health (GMMH) for their contributions to the study.

Andrew Priest is financially supported by the Addenbrooke's Charitable Trust and the National Institute for Health Research [Cambridge Biomedical Research Centre at the Cambridge University Hospitals NHS Foundation Trust]. The views expressed are those of the authors and not necessarily those of the NHS, the NIHR or the Department of Health and Social Care.

7.11 Funding

The authors wish to thank the Medical Research Council (MRC) for PhD funding, and the Engineering and Physical Sciences Research Council (EPSRC; grant EP/M005909/1) for funding data acquisition.

7.12 Supplementary materials

7.12.1 Figures

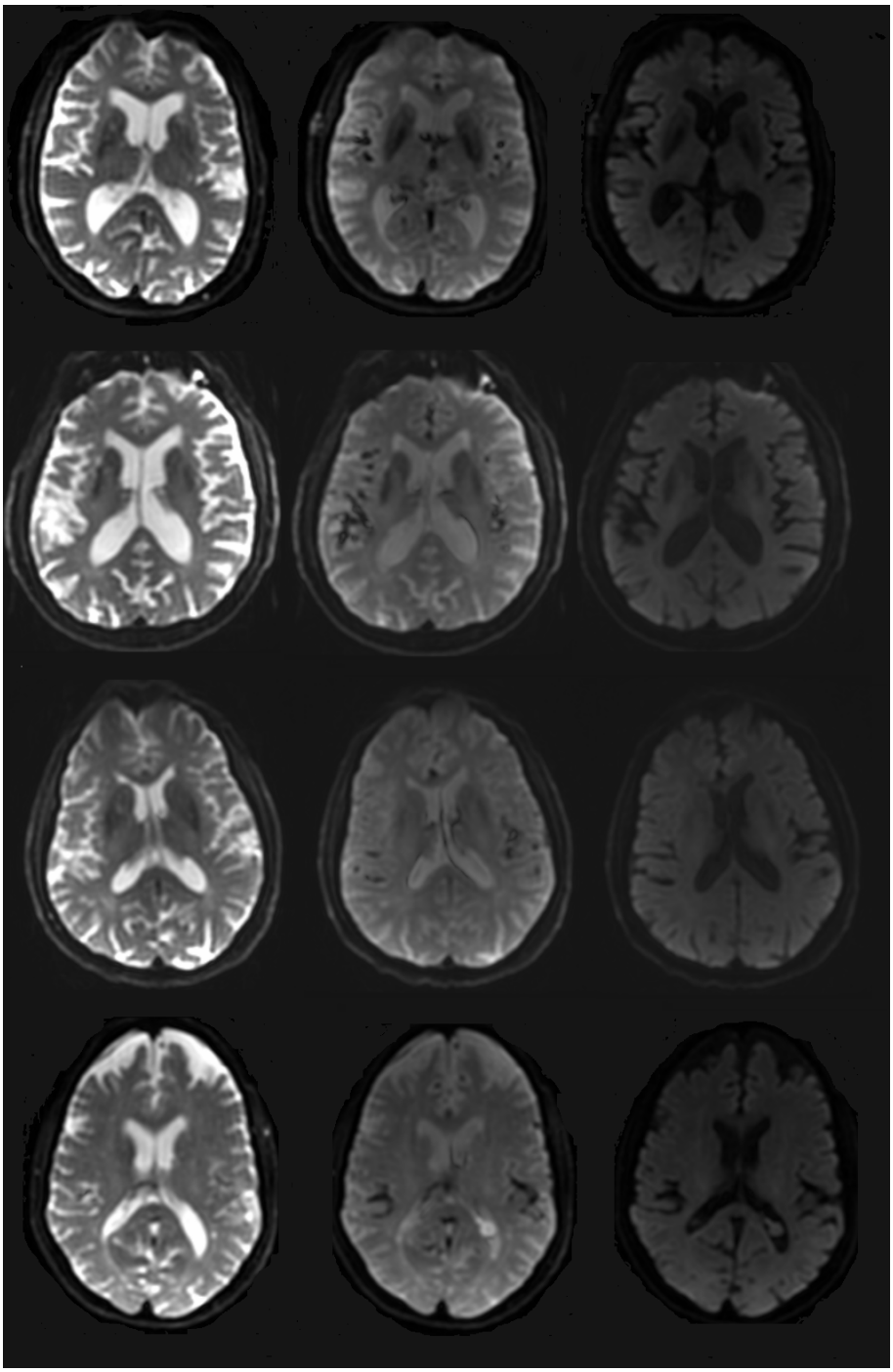

Figure 7.3: Mid-axial slices of diffusion-weighted (DW) MR images for four subjects for b= 10, 300 and 1000 smm^{-2} moving from left to right. Diffusion-time (Δ) is 49.89 ms. The top two rows show images for subjects diagnosed with mild cognitive impairment (005 and 006) and the bottom two rows for healthy subjects (009 and 010).

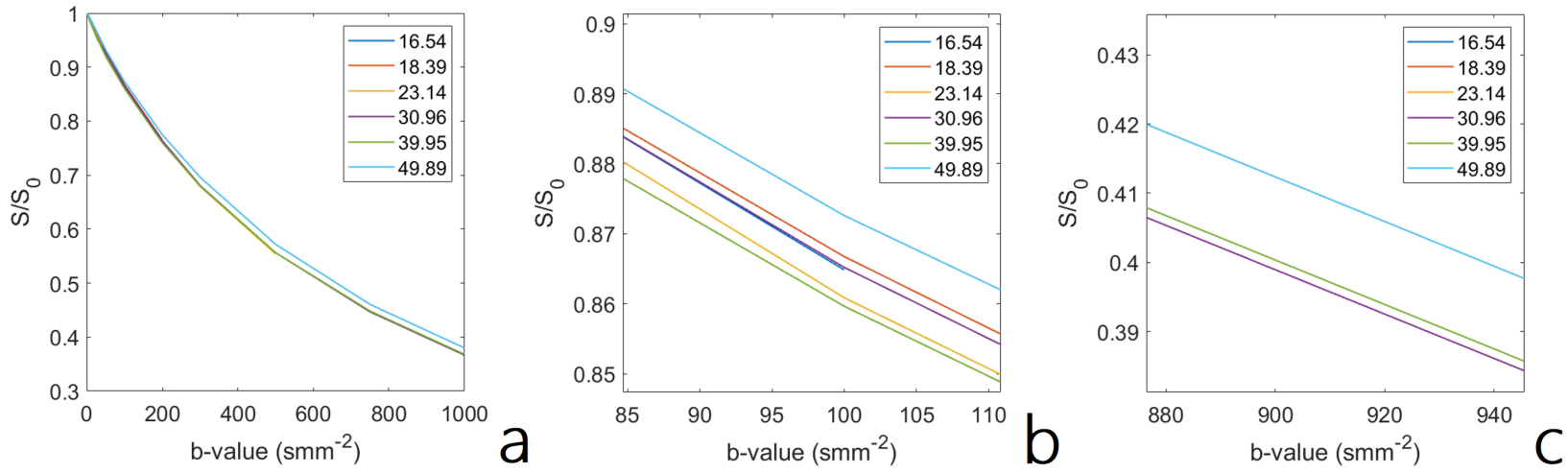

Figure 7.4: Subject average normalised diffusion-weighted MRI signal (S/S_0) for grey matter (GM) versus b-value for six values of diffusion-time (Δ in ms). (a) shows the full b-value range, (b) shows the signal at low b-values and (c) shows the signal at high b-values.

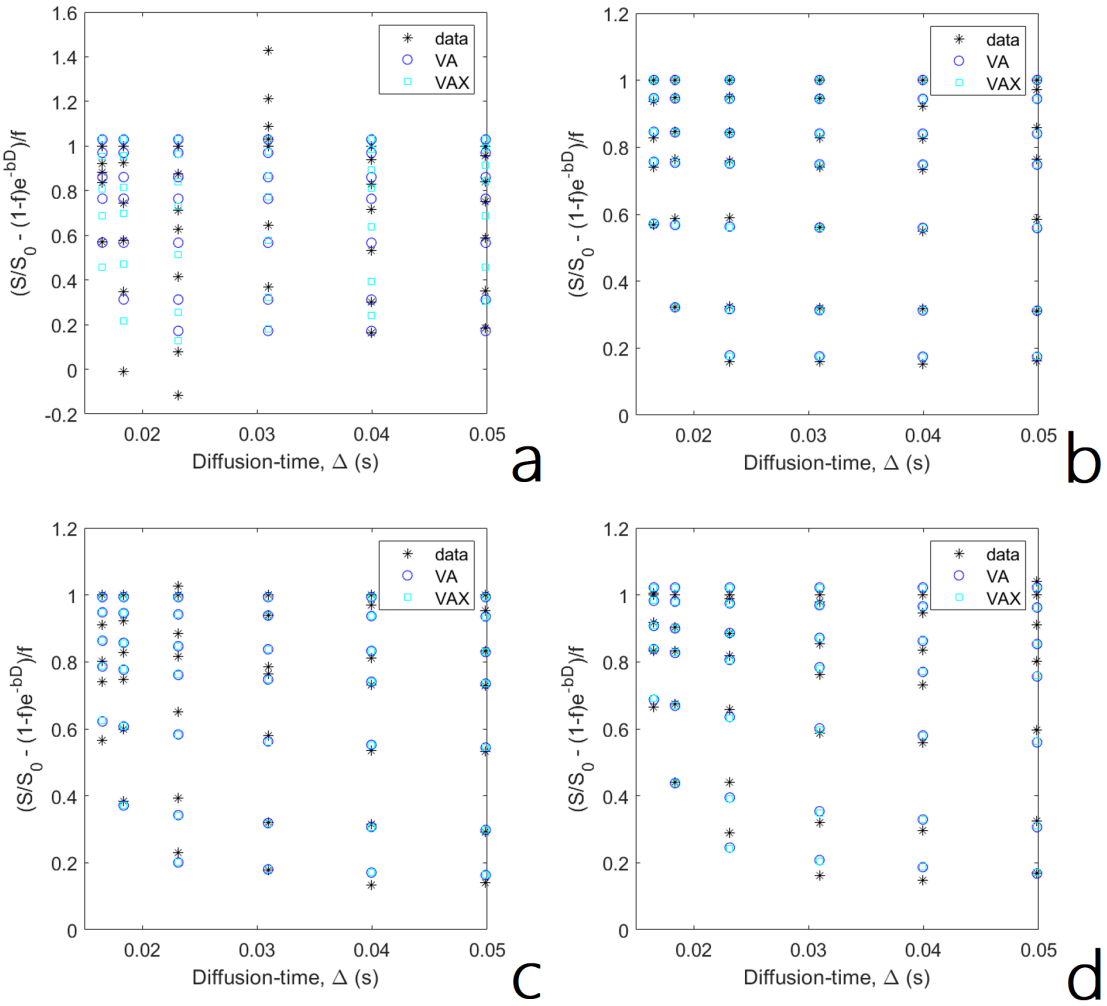

Figure 7.5: Isolated perfusion signal $(S/S_0–(1-f)e^{-bD})/f$ versus diffusion-time (Δ) (data) and, VA (blue) and VAX (cyan) model fits. Multiple points at each diffusion-time represent the changing b-value. (a) and (b) show grey matter (GM) data for subjects diagnosed with mild cognitive impairment (005 and 006) and, (c) and (d) show GM data for healthy subjects (009 and 010).

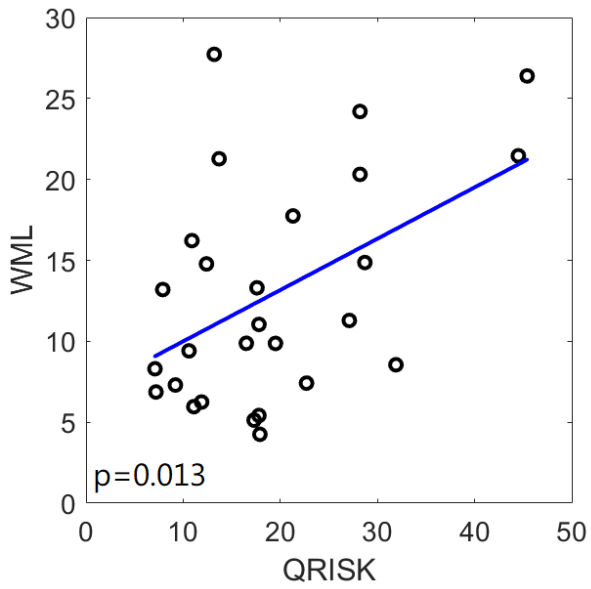

Figure 7.6: Regression plot of cardiovascular risk score (QRISK) with white matter lesion (WML) volume. p=0.013.

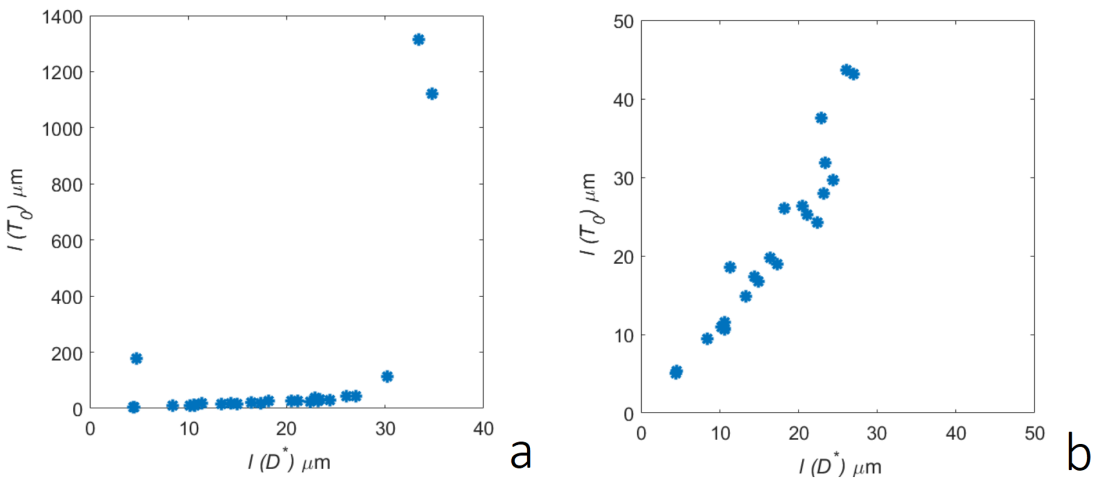

Figure 7.7: (a) average vessel segment length (l) for cortical grey matter estimated using $l = 6D^*/v$ and $l = 2vT_0$ ($l(T_0)$). (b) shows the point in (a) minus outliers (4 data points).

8 General discussion

8.1 Motivation and aims

The brain is an incredibly complex and dynamic organ; comprising around only 2% of our body mass, it consumes upwards of 20% of our glucose and oxygen intake [1]. Glucose, oxygen and other essential nutrients are transported to parenchyma via a vast network of blood vessels. Disruption to the vascular network resulting in ischaemia or hypoxia can cause cell damage and death within minutes [1]. Hence, it is unsurprising that a large body of evidence links vascular pathology and neurodegeneration (Chapter 2).

To examine vascular involvement in neurodegenerative disease in-vivo, magnetic resonance imaging (MRI) can be used. MRI techniques generally focus on measuring alterations to vascular function such as cerebral blood flow or blood-brain-barrier permeability [43]. Structural measures of the microvasculature have received less attention. This is likely due to there being no established methods of visualising the vascular network at the micron level in-vivo [290], whereas measures of estimating CBF and BBB permeability are very well established and widely used. As a result, most studies investigating the microvasculature use histological methods and generally focus on cellular changes, although some do briefly mention vessel architecture/morphology [4–6, 127, 287, 291–295]. Some studies have started to implement vessel size imaging (VSI)-MRI in human subjects [290, 296, 297], a method of measuring capillary diameter in-vivo.

Why the development of functional methods took precedence over structural methods is unclear. Perhaps because changes in function (without stimuli such as gas challenge) are more likely to be indicative of some pathological event whereas changes in morphology could be part of a physiological process. For example, string vessels are associated with disease but are also found in healthy brains from birth to old age [58]. Technological limitations could have been a factor. For example, IVIM imaging was introduced in 1988 using 0.5 T field strength [14] but remained largely unused due to spurious parameters that lacked repeatability [157]. The introduction of stronger static fields increased SNR. The use of echo planar imaging in DW-MRI and improved gradient hardware meant acquisition times decreased (number of b-values could increase) and data with higher b-values could be collected which were free of motion artifacts [134, 157].

Structural measures may have higher repeatability than functional measures. They are likely to be a stable parameter biologically, whereas functional measures are sensitive to temporal fluctuations in neural activity and thus could be more noisy. Although, depending on the models used to derive structural parameters (i.e. whether they incorporate functional parameters), the measure could be equally as variable. Microvascular structural changes might also precede functional changes and thus be an earlier marker of cerebrovascular

disease. Structural alterations such as vessel thinning due to loss of basement membrane components could occur before detectable changes in BBB permeability. Alterations in vessel tortuosity may alter the velocity distribution of blood, changing the extraction efficacy of nutrients including oxygen, which could lead to local ischaemia on a microscopic level [23–25] - this could lead to macroscopic evidence of vascular damage such as white matter lesions or subcortical infarcts, markers of cSVD (Chapter 2). Based on these ideas, the main aims of this thesis were to:

1. to develop a non-invasive method of measuring microvessel structure in-vivo using diffusion-weighted MRI (Chapters 4 and 5)

2. to comprehensively validate estimates of microvessel structure acquired in preclinical rat models against ground truth measures (i.e. corrosion cast) and to translate the method to measure microvessel structure in the human brain and further validate using noninvasive methods (i.e. gas challenge) (Chapters 4 and 6)

3. to investigate the link between microvascular structural measures and, vascular risk, amyloid and cognition, in the elderly population (Chapter 7).

We present four imaging studies which develop and validate a method of estimating microvascular structure using multi-diffusion-time DW-MRI data and IVIM modelling, and investigate microvascular changes in disease. Models used to determine microvascular structure also provide estimates of functional parameters, which are evaluated alongside structural estimates.

8.2 DW-MRI models

The first step was to identify which IVIM models allow for measurement of vascular structure (Chapter 3, summarised in Figure 8.1). The 'IVIM' model, as is used in almost all IVIM literature, describes extravascular diffusion and pseudo-diffusive flow in the vascular network at long diffusion-times, and is characterised by the pseudo-diffusion coefficient (D^*). Blood flow is assumed to mimic Brownian motion, and thus D^* can be described by: $D^* = vl/6$, where v is the average blood velocity and l is the average vessel segment length. This coefficient is more of a functional parameter and does not allow for estimation of vascular structure without additional information.

Kennan et al. [33] developed the velocity autocorrelation (VA) model that is valid across all diffusion-times (and thus flow regimes) and allows for estimation of the average blood velocity (v) and correlation time (T_0). The authors propose two methods of combining parameters to estimate vessel segment length, l. The first, using v, T_0, and the equation: $l = 2vT_0$. The second, using v from the VA model with D^* from the diffusive IVIM model

to estimate l with: $D^* = vl/6$. Estimates of l from both methods are expected to be consistent, since the VA model reduces to the diffusive IVIM model at long diffusion-times [33].

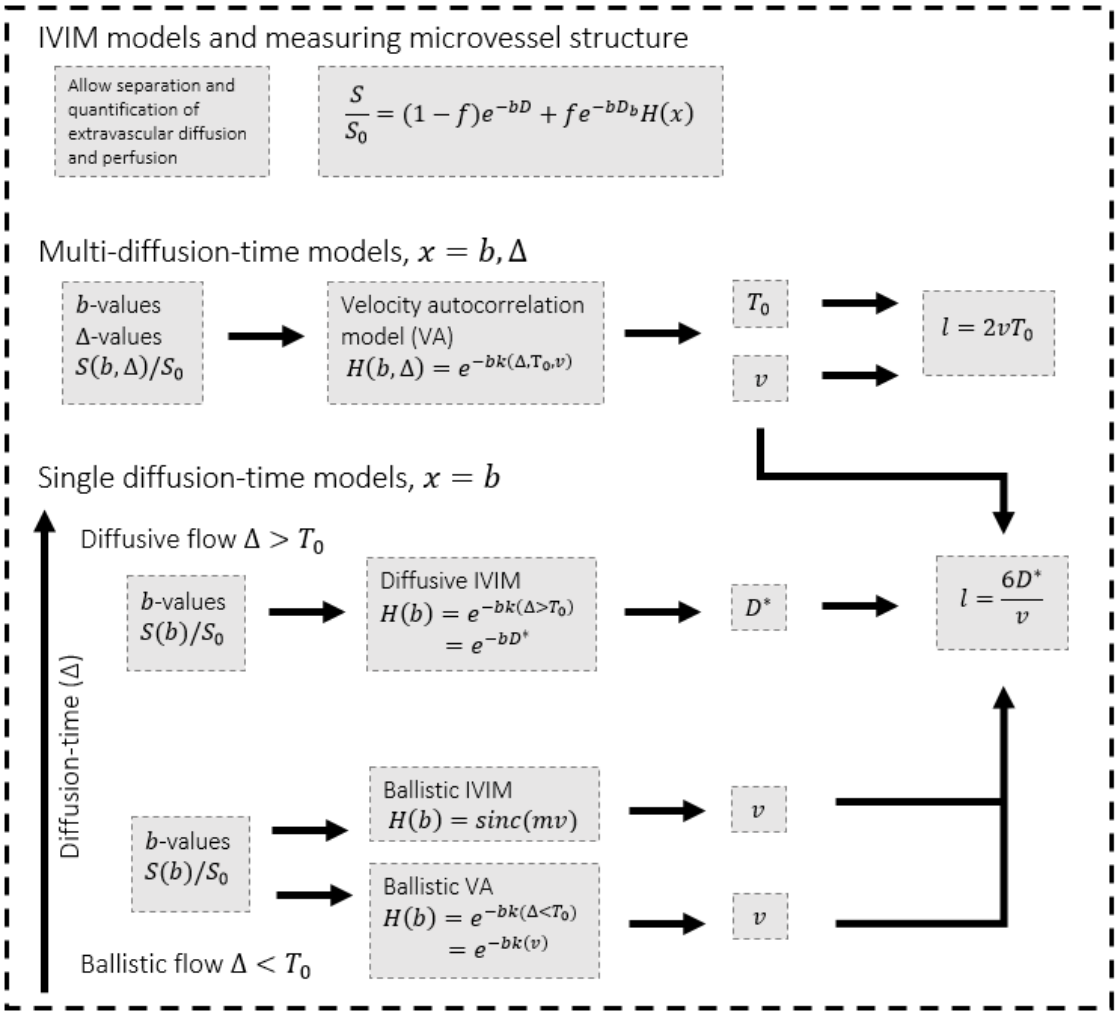

Figure 8.1: Estimating vessel segment length (l) using IVIM models. A biexponential model characterises extravascular diffusion (D, diffusion coefficient) and perfusion ($H(x)$). The perfusion fraction (f) quantifies the ratio of signal attenuation in each compartment. The diffusion-times (Δ) dictate which model is most appropriate. At short diffusion-times ($\Delta < T_0$), perfusion is characterised by ballistic flow, and ballistic models can be used to extract velocity (v). At long diffusion-times ($\Delta > T_0$), microvascular perfusion is characterised diffusive flow, and the diffusive IVIM model can be used to extract the pseudo-diffusion coefficient (D^*). The VA model can be fit across all diffusion-times to extract v and the correlation time (T_0). S is the DW-MRI signal, and S_0 is the signal with zero diffusion-weighting (b=0); b-value, describes diffusion sensitisation; k, perfusion attenuation coefficient.

The VA model has a ballistic approximation (VAB), valid at short diffusion-times, which assumes blood flow does not change direction during image acquisition and predicts that the signal is dependent on only v. Thus, v can be estimated and used with D^* to derive l, as with the VA model. Similarly, a ballistic IVIM model also allows for estimation of v, and thus l.

8.3 Imaging studies

In Chapter 4, the VA, VAB and ballistic IVIM models were fit to DW-MRI data acquired across eight b-values and four diffusion-times in the rat brain (F344 and WKY strains) to estimate v and l. The diffusive IVIM model was fit to the highest diffusion-time to extract D^*. Repeatability and accuracy of estimates from each model were compared. Scan-rescan repeatability was estimated from five F344 rats to investigate precision of measures. Parameter estimates (v and l) were compared between F344 and WKY rats to assess sensitivity to regional variation and precision. To investigate accuracy, estimates of l were compared to ground truth measures, obtained using micro-CT imaging of a vascular corrosion cast.

The VAB model produced estimates of l with lowest bias relative to corrosion cast estimates (Figure 4.4 - SSE=70), and the highest repeatability (Table 4.1 - CoV mean: v=22.4%, l=73.1%), although repeatability in l is low. The VA model also produced estimates of l with low bias (SSE=77) and reasonable repeatability for v (CoV mean: v=45.8%, l=109%). VA derived parameters had better agreement between rat strains than the VAB model (VA: $\rho_v = 0.92, \rho_l = 0.99$. VAB: $\rho_v = 0.44, \rho_l = 0.94$). The increased number of data points for VA model fitting might allow for more freedom in parameter values and better characterisation of regional variation. The IVIM ballistic model produced estimates with high bias (SSE=8800), which could be due to the its assumption of plug flow in the vasculature rather than laminar flow [33]. Using ballistic models to estimate l required use of equation: $D^* = vl/6$ (Figure 8.1). However, with the VA model we should have been able to use both $l = 6D^*/v$ and $l = 2vT_0$. Unfortunately, estimates of T_0 were spurious and lacked repeatability so $l = 2vT_0$ could not be used. We suspect this was due to the low number of diffusion-times used. We assessed the CoV with ten diffusion-times in the next study to compare.

This Chapter shows the potential of multi-diffusion-time DW-MRI and multi-diffusion-time IVIM modelling to estimate microvascular segment length (Aim 1). It is the first study to use the diffusive IVIM model and VA model to derive structural parameters, as well as to validate the methods against ground truth measures (Aim 2).

Due to limitations of gradient field strength in standard clinical imaging, it is challenging to acquire DW-MRI data at low enough diffusion-times where the ballistic regime is valid.

If we assume $l \approx 30$ μm and $v \approx 2$ mms^{-1} the time to travel one segment length would be approximately 15 ms. On the 3T PET/MR scanner, the shortest diffusion-time we could achieve whilst still collecting all b-values was 27 ms. Hence, the VAB model may not be appropriate in clinical imaging. Thus, the next step in the PhD was to investigate the VA model further. Specifically, to investigate the diffusion-time dependence of the intravascular compartment in detail and examine the VA model to determine if development was needed to improve characterisation of data. Increasing the number of diffusion-times might also allow us to estimate T_0 with higher accuracy and precision, allowing us to use it for estimation of l. Furthermore, trans-BBB water-exchange is considered to have a negligible effect on the signal attenuation in IVIM studies. However, as diffusion-time increases, water will have more opportunity to exchange across the BBB between diffusion encoding gradients, and this assumption might not hold. The assumption has not been investigated in IVIM studies to the best of our knowledge, and as diffusion-times start to be considered in intravascular DW-MRI methods, it is important to determine if there are any significant effects.

In Chapter 5, DW-MRI data was collected across ten b-values and ten diffusion-times in healthy volunteers. This was an increase of six additional diffusion-times and two additional b-values from the preclinical data. For seven volunteers, the protocol was repeated in the same scan session to assess intra-scan repeatability of DW-MRI derived parameters. The diffusion-time dependence of IVIM parameters (f, D and k, where $k = D^*$ at long diffusion-times) was examined in grey and white matter. The VA model describes the diffusion-time dependence of k, so this parameter was of particular interest. We developed the VA model to include effects of trans-BBB water-exchange (VAX) and assessed which model was most appropriate in the two regions using the Akaike information criterion.

We found that f decreased linearly with diffusion-time (Figure 5.2). We suspect that this may be due to decreasing contribution from larger vessels as diffusion-time increases, as discussed in Chapter 5. D did not have a significant relationship with diffusion-time. This was unexpected as a diffusion-time dependence in D has been measured [16]. This is discussed further in Section 8.4. $k(\Delta)$ followed the shape predicted by the VA model (Figure 5.1) in grey matter, increasing with diffusion-time and plateauing where the pseudo-diffusive limit was met ($k \equiv D^*$). However, in white matter, the behaviour of $k(\Delta)$ did not correspond to the VA model. The curve initially increased slightly with diffusion-time, following which there was a sharp decrease. We hypothesised that this decrease could be due to water from the extravascular compartment exchanging into the intravascular compartment during the diffusion-time, which is currently ignored. Indeed, the VAX model proved to be the most appropriate in white matter (Figure 5.3). This was further evidenced by VAX model parameters which agreed more favourably with literature. For example, the mean value for segment length for the VAX model was 46.4 μm versus 4.79 μm for

the VA model. Although, repeatability did suffer moving from the VA to VAX model with CoV of 61.1% for v, 47.5% for T_0, 40.5% for l and 47.1% for τ (CoV for VA fit for all parameters in WM <10%). Bias-variance trade off may explain these results. With increased accuracy comes higher variation and vice versa. For VA parameters in WM, we see poor accuracy but low variability (if we assume literature values are correct). Whereas the opposite seems to be true for VAX in WM, with higher accuracy when compared to literature, but more variation. Results of the Akaike analysis were inconclusive in grey matter, however parameters were generally more repeatable for the VA model. T_0 had CoV of 30.8% (vs 209% for VAX), v had CoV of 23.2% (vs 13.8% for VAX) and l had CoV of 18.7% (vs 200% for VAX). This could be due to fewer parameters meaning less freedom for the fit, or reduced risk of overfitting.

Chapter 5 demonstrates the diffusion-time dependence of the most commonly used IVIM parameters, often not considered in literature. Many studies only focus on the b-value when using the diffusive IVIM model. This could explain some of the variability across literature since not considering the diffusion-time may be introducing unknown and variable bias to D^* values. We show that water-exchange may affect the intravascular DW-MRI signal at long diffusion-times and that alternate modelling may be required. This is particularly important in white matter where estimates of D^* may be underestimated if diffusion-time is not considered. If investigating D^* in a patient cohort where water exchange across the blood-brain-barrier may be affected, the dependence in white matter should be accounted for otherwise false changes in D^* may be detected and attributed to changes in the vasculature. The finding may be useful in determining BBB permeability changes in disease, although the method requires validation as discussed in Section 8.5. Last, by increasing the number of diffusion-times compared to Chapter 4, we show the VA model can be fit to clinical data in grey matter and can be used alone to estimate l (due to improved repeatability of T_0). Thus, if the diffusive regime cannot be met (there have been doubts about the validity of the regime [35, 164]), this method would be useful in determining l.

Measures of vessel segment length, l, derived using $l = 6D^*/v$ were validated against ground truth measures in the rat brain. After which, using data collected in the human brain, we developed the VA model and used $l = 2vT_0$ to estimate vessel segment length. Limitations of the ground truth validation and the use of two different models to estimate l meant further work to validate the measure was needed. The two methods of estimation of l need to be compared and the biophysical origin of parameters investigated. The source of diffusive IVIM parameters, f and D^* has been attributed to numerous compartments in literature. Determining whether the parameters are indeed vascular in nature is key to using these parameters to investigate vascular pathology in disease. A hypercapnic gas challenge was used in human volunteers. An increase in CBF is expected with an

increase in CO_2 levels in the blood (partial pressure of CO_2, labelled $PaCO_2$ or PCO_2) [195, 230, 231, 238, 239]. This has been attributed to an increase in blood velocity and cerebral blood volume (CBV) [195, 231, 245]. We hypothesised that the vessel segment length (l) would remain unchanged from baseline to hypercapnia, whilst f, D^* and v would increase and T_0 would decrease, reflecting the increase in CBF and blood velocity [135, 195, 231, 244].

In Chapter 6, multi-diffusion-time DW-MRI data is collected in seven healthy subjects across ten b-values and nine diffusion-times whilst subjects breathed normal room air and CO_2 rich air. ASL data is collected to determine changes in CBF and arterial transit time (ATT). The Akaike information criterion is used to determine the most appropriate model (VA or VAX) in GM and WM. The diffusive IVIM model is fit to the longest diffusion-time data to extract f, D and D^*, and the VA model fit to all diffusion-time data to extract v and T_0. The segment length is calculated using $l = 2vT_0$ and $l = 6D^*/v$ to compare results. We predicted that functional parameters would alter and l would remain unchanged with gas challenge. Although, increasing literature shows smooth muscle cells and pericytes are involved in modulating capillary blood flow in the brain [298–301], so perhaps with capillary dilation in response to hypercapnia, there may be a small decrease in length as cellular architecture is altered (rather like a Chinese finger trap).

We found that ATT decreased (average in GM: 6.6% and WM: 5.0%) with hypercapnic gas challenge (p=2.1e-06 for effect of gas challenge as a binary variable). CBF, f, D, D^*, v, T_0 and l did not alter significantly with the gas challenge (Figure 6.2 and Table 6.4). Although, CBF increased in each subject (average in GM: 26% and WM: 31%) and trended towards significance (p=0.054). f also increased in most subjects (average in GM: 11% and WM: 10%) and trended towards significance (p=0.067). The variability across subjects in CBF, ATT and v was associated with end-tidal CO_2 levels which is consistent with literature. CBF and v were positively correlated, and ATT negatively correlated, with end-tidal CO_2 (Figure 6.11). We suspect the lack of significant results with gas challenge was due to the low number of subjects and the method of gas challenge used (which resulted in variable end-tidal CO_2 for each diffusion-time) as described in more detail in Section 8.4. Whilst the lack of significant change in l would validate our method, we cannot reject the null hypothesis of no change with increased CO_2 levels with our data.

Akaike analysis showed the VA model was most appropriate in baseline GM data, and results favour neither the VA nor VAX model for baseline WM data and hypercapnia data in the two regions. This differed from results presented in Chapter 5 where VAX was favoured in WM and results were inconclusive in GM. This is likely due to the different diffusion-time dependence measured in k compared to Chapter 5 (discussed in Chapter 6). It is not clear why diffusion-time dependence differed between Chapter 5 and 6 for baseline data, but we suspect low subjects numbers played a role, and possible differences caused

by the regional segmentation software used (Freesurfer versus SPM). Such a large variation between datasets is of concern as it suggests low reproducibility, meaning it would not be useful clinically. Although, we do show that the two methods of estimating l produce similar estimates in the two regions (GM: $l(D^*)$=22.2±3.0 μm and $l(T_0)$=24.6±4.0 μm. WM: $l(D^*)$=9.93±2.7 μm and $l(T_0)$=8.42±1.7 μm). It is reassuring that methods agree, indicating that they could be used interchangeably depending on the data and which method is more appropriate.

Following validation of measures preclinically and attempts to validate clinically, diffusive IVIM and VA model parameters were examined in data from a cohort of elderly individuals (ages 60 to 80), to investigate sensitivity of parameters to vascular health (cardiovascular risk and white matter lesion volume), cognitive performance and amyloid status. In Chapter 7, multi-diffusion-time DW-MRI data was collected in twenty-seven subjects across six diffusion-times with up to ten b-values. Diffusive IVIM model parameters (f, D and D^*) and VA model parameters (v and l) were estimated. White matter lesion (WML) volume was determined using T2-FLAIR MRI and amyloid-beta status determined using Flutemetamol [18F] PET. Cardiovascular health was assessed using the QRISK-2 measure and cognitive performance assessed using the Montreal cognitive assessment (MoCA). DW-MRI parameters were correlated against QRISK and WML in cortical grey matter (GM) and the hippocampus to determine sensitivity to vascular health. Following which, multivariate linear regression was used to determine whether f, D or amyloid status were associated with MoCA score.

The perfusion fraction was positively correlated with QRISK and WML (Figure 7.1), and negatively correlated with MoCA score (lower score = worse cognitive performance) (Figure 7.2). Variability in MoCA score was largely explained by the perfusion fraction, but not by amyloid status or D (Tables 7.4 and 7.5). The MoCA scores presented in the study (maximum score 30) reflect normal cognition (score 26-30) and mild cognitive impairment (score 18-25). Only one subject (score 17) could be classed as having moderate cognitive impairment according to guidelines presented on the MoCA test webpage (https://www.mocatest.org - although these scores are only guidelines and the range can vary). Hence, results suggest the perfusion fraction may be sensitive to vascular changes preceding major changes in cognition. Results may also evidence the 'two-hit' hypothesis of Zlokovic et al. [1], whereby vascular changes precede amyloid accumulation and neuronal degeneration, since f was associated with MoCA score (whereas amyloid was not), and correlated with WML volume and QRISK. The increase in f could represent vasodilation as a compensatory mechanism for other vascular changes, such as rarefaction or reduced oxygen extraction efficacy [55], thereby maintaining supply of essential nutrients to tissue and clearance of toxins. The vasodilation could also be an immune response as a result of toxins crossing an impaired BBB, or impaired NO signalling from malfunctioning en-

dothelial cells [119, 280]. This is discussed in more detail in Chapter 7. Since the perfusion fraction quantifies the ratio of intravascular/extravascular signal attenuation, increased f could reflect reduced contribution from the extravascular compartment due to neuronal atrophy. D increased in cortical GM with QRISK and WML, which may represent cell loss. This may confirm that atrophy is affecting the perfusion fraction. Although, D having no association with MoCA score suggests that no major changes in tissue have occurred, otherwise reduced cognitive performance may be expected. No changes in D^*, v or l were measured with vascular health or cognitive performance, which could be a result of limitations in the methodology as discussed in the Section 8.4.

We show that the two methods of estimating l produce similar estimates in cortical grey matter, which are highly correlated, with exception of a few outliers (Figure 7.7). This agrees with data presented in Chapter 6. In the hippocampus, estimates of l using T_0 are much more spurious and the two methods do not agree. We suspect the higher SNR in cortical grey matter improves accuracy of the measures. SNR was shown to scale directly with the square root of the number of voxels in a study by Parker et al. [302] and cortical grey matter is a much larger region than the hippocampus.

This study is the first to link changes in f with cerebro and cardio-vascular health, and cognitive performance. A previous study by Bergamino et al. [154] finds an increase in f in MCI patients compared to healthy volunteers, and other studies find increasing f in cSVD [279] and ageing [217]. This study links previous work on the parameter and may provide further evidence for vascular changes in neurodegenerative disease and effects of vascular risk factors on early cognitive changes. Although, it's not fully clear what the source(s) of f actually is. Whilst most literature on the topic suggests it is related to CBF and CBV (discussion of Chapter 6), others have suggested the glymphatic system [154, 279] may affect the parameter. The trend towards a significant increase in f with gas challenge (Chapter 6) suggests that the parameter is indeed vascular in nature, but hypercapnia data is limited and further investigation would be useful to really understand what the parameter quantifies and how this relates to neurodegenerative disease. The measurement of f can be done quickly with a single diffusion-time and low number of b-values, and is highly repeatable in clinical data (Chapter 7). The parameter could easily be added on to current clinical DW-MRI protocols, by including an additional one or two b-values. The parameter could eventually be useful as a diagnostic or prognostic biomarker, and help us to understand the pathophysiology of neurodegenerative disease.

Measures of blood flow velocity and vessel segment length were shown to be fairly repeatable in GM data with a high number of diffusion-times (CoV: v 23.2% and l 18.7% in Chapter 5). Although repeatability decreased substantially with decreasing number of diffusion-times used in data acquisition (CoV: v 73% and l 54% in Chapter 7). Whilst estimates of velocity compare well with what is available in literature, we're not able to

determine its accuracy using direct measures in humans (it would have been useful to measure v in the rat brain). Vessel segment length measures had low bias when compared to corrosion cast estimates, although limitations discussed in Section 8.4 might mean corrosion cast estimates aren't wholly accurate. Unfortunately, we were unable to validate the measure in human data due to low subject numbers. Comparing to literature values, l is on the low end of the range presented. Hence, the accuracy of measures is still not clear. The measure could still be useful in determining changes with disease rather than used to extract exact measures. Although, the requirement for a high number of diffusion-times limits the clinical use of the method. Imaging times for highest repeatability (Table 5.3) would be on the order of 25 minutes (without any other imaging). If the ballistic regime could be accessed clinically (e.g. could use the Connectome scanner which has approximately double the maximum gradient strength of a standard scanner (70-100 mT/m versus 40 mT/m), https://www.humanconnectome.org/study/hcp-young-adult/project-protocol/mr-hardware), this would reduce imaging time significantly as only two diffusion-times need collecting (approximately 6 minute sequence). Although, the low correlation between rat strains for v (but high repeatability) suggests the model isn't able to measure regional variability and is constrained. So perhaps the VA model would be more appropriate. Work should be done to assess the repeatability in smaller regions in the human brain, since investigating regional variation over smaller grey matter regions would be more interesting clinically. With more work to improve repeatability with a lower number of diffusion-times, v and l could still prove to be useful in investigating vascular changes in neurodegenerative disease.

8.4 Limitations

In Chapter 4, DW-MRI methods were validated using micro-CT imaging of a vascular corrosion cast. This validation was limited in several ways. Firstly, by the number of viable vascular corrosion casts. Unfortunately, difficulties such as high viscosity of the perfusing fluid, leaking fluid, or lack of stability in the solidified agent, meant the cerebrovasculature was not fully perfused, or the casts deformed or collapsed. The decision was made not to attempt any further corrosion casting due to the ethical implications of such a high rate of cast failure (approximately thirteen rats were used and one viable cast produced). It is unclear whether the vessel segment lengths obtained from the casts would have varied between rats. Visually, the small sections of vasculature that had successfully perfused in some of the failed casts looked highly similar to the successful cast when scanned using micro-CT imaging. Regardless, a larger number of corrosion casts would increase confidence in our results. Note that we did not process the failed casts which had small successful sections for analysis since it would have been highly challenging to determine which area of

the brain the perfused regions came from.

Secondly, although the regions of interest were chosen by comparing reconstructed large field of view micro-CT images to the Paxinos rat atlas [194], and by observing large vessel structures like the circle of Willis, the regions were inevitably chosen by eye. The use of two observers would have reduced the likelihood of error, however there may have been inaccuracies in the regions chosen. Thirdly, due to the long processing time of high resolution micro-CT images, only one subsection of each region was chosen. Again, it is difficult to tell how this would have affected results as visually, the entire subregion was highly similar when ignoring larger vessels. Last, we actively chose a subsection of each region which avoided larger vessels.

The choice to avoid large vessels was done so due to the assumptions of early IVIM papers that the parameters only described the microvasculture (papers have since argued against this theory and described the influence of slightly larger vessels [35]). This may explain why our values from micro-CT images are generally lower than average value presented in the literature - our values are on the lower end of the ranges presented (20-140 μm at capillary level [303], 30-300 μm vessel level unclear [304], 15-27 μm in microvessels [206], 12-302 μm capillaries [204], 10-200 μm microvessels [203]). A further explanation for the lower values are errors in the binarisation process required for skeletonisation and extraction of vessel lengths. In larger microvessels, the binarisation set the centre of the vessel to background. Thus, for the skeltonisation process, which should produce a line down the centre of the vessel and nodes at branches or at directional changes, nodes were placed around the vessel walls rather than through the centre. This meant very short lengths were recorded. To negate these errors, the automatic binarisation process was assessed and corrected for by hand. Whilst this removed most of the incorrect skeleton nodes, some undoubtedly would still exist.

Despite these errors, we believe the validation using the vascular corrosion casts was useful. Steps were taken to try to negate any errors. If errors did affect data, they may introduce similar bias to each region, meaning estimates of precision would still be useful. In any case, results agreed fairly well with MRI measures across the four regions, with correlation coefficients of 0.89 and 0.98, sum of squared errors of 77 and 70, and p-values of 0.11 and 0.017, for the VA and VAB models respectively. In general, VA estimates are lower than cast estimates, and VAB higher. The high correlations indicate that, even if not wholly accurate, the methods of estimating microvessel structure are still strongly related to segment length and could still be useful in investigating structural changes in disease. The slightly higher sum of squared errors and non-significant p-value for the VA model shows there is more variability in the derived segment lengths. Increased data collection (i.e. increasing number of b-values, diffusion-times or averages) may be useful in increasing reliability.

In Chapter 5, the lowest diffusion-time was limited to 27 ms due to need for high b-values to extract D and f. This meant we could not measure lower diffusion-times at which the VAB model would have been most valid (if we assume $l \approx 30$ μm and $v \approx 2$ mms^{-1} the time to travel one segment length would be approximately 15 ms). Hence, we could not compare parameter estimates from the VAB to those of the VA model in this dataset, which would have been useful for assessing relative differences in the estimate of v derived from the VA model in comparison to the VAB model with the increased number of diffusion-times. The lack of diffusion-time dependence in the extravascular diffusion coefficient (D) was of some concern, since this dependence has been recorded in literature [16]. Reynaud et al. [16] show an exponential relationship between D and the diffusion-time (in tumour tissue). At longer diffusion-times (>16 ms), this relationship becomes approximately linear where $D(\Delta) \propto 1/\Delta$. Using data from Reynaud et al. [16], we calculate the change in D from 27 ms to 60 ms to be approximately 0.25×10^{-4} mm^{2}s^{-1}, which is around 3% of our values in Chapter 5 (8×10^{-4} mm^{2}s^{-1}). Our repeatability in GM was estimated at 1.6% (Chapter 7). This CoV could explain why we do not see a 3% change in our data. Although, the use of data from Reynaud et al. [16] to determine the expected change may not be appropriate since the environments of the tumour and brain differ. Maier et al. [305] state that D is increased in the majority of tumours compared to healthy brain tissue suggesting different structure, so the relationship between D and diffusion-time may not be accurate in healthy brain tissue.

In Chapter 6, the low number of subjects scanned (n=7) reduced our ability to detect changes in IVIM parameters and reduced confidence in the results presented. Power calculations for v are presented in the Chapter which suggest 15 subjects are required to detect a 25% change in the parameter (using CoV=23.2% as presented in Chapter 5), and 16 subjects are required to detect a 25% reduction in T_0 (using CoV=30.8%). A change which is not unreasonable when compared to literature. For example, Hudetz et al. [195] measure a 46% increase in RBC velocity in rats with a 5% CO_2 gas mixture. With no significant change in CBF, it is perhaps unsurprising that we do not measure changes in IVIM parameters. Significant variation of parameters with end-tidal CO_2 but not gas challenge suggests CO_2 levels during the gas challenge were not high enough to produce a detectable change in cerebrovascular function (i.e levels need to be higher than intersubject variability). Thus increasing number of subjects and concentration of CO_2 supplied to subjects would be useful to clarify results.

We suspect the lower number of subjects (and possibly errors due to different regional segmentation software) may have impacted the diffusion-time dependence of IVIM diffusive parameters, which differed from results presented in Chapter 5. This meant results from Akaike analysis varied and as a result, models used were not consistent across Chapters 5 and 6. The VA model was fit to WM data (rather than the VAX model) in Chapter 6.

The parameters presented do not agree well with literature - vessel segment lengths are on the order of vessel diameter as seen when fitting the model in Chapter 5, likely due to the very low values of T_0 (<1 ms for many subjects). Some values for velocity tend to the upper limit of fitting bounds (5 mms^{-1}). Perhaps the VAX model should have been fit in WM. However with no support from Akaike analysis, it was difficult to justify fitting a more complex model to data. Perhaps data from white matter should be discarded.

Our decision to alter flow rate of gas to achieve a 1% increase in end-tidal CO_2, rather than supplying gas with a specific concentration of CO_2 (as described in a paper by Federau et al. [135]), may have limited the results. The method of gas challenge was chosen as the time to achieve a steady state after applying the CO_2 rich gas is low, meaning the time for imaging under hypercapnia can be extended. It was challenging to maintain a steady 1% increase in end-tidal CO_2 for the thirty minutes duration of the scan. This is particularly evident in subjects 002, 004, 005 and 006 in Figure 6.10. Table 6.2 also shows the target 1% rise was not achieved for any subject. For most subjects, the end-tidal level would decrease over time meaning the flow rate of gas had to be increased. Whilst controlling for this was not such an issue, the end-tidal levels for some subjects was quite sporadic (e.g. for subject 006, we see large increases and decreases in end-tidal CO_2) meaning it was difficult to gauge whether the flow-rate of gas needed altering. Furthermore, towards the end of the scan, when CO_2 flow rate was highest, large spurious peaks were present due to poor mixing of gases inside the set-up. This made the assessment of end-tidal CO_2 difficult and as such, the level was unlikely to be at 1% increase from baseline (as evidenced in Table 6.2). Variable end-tidal CO_2 across the 30 minutes scan introduces variable bias to data across diffusion-times, likely resulting in poor fitting of the VA model and, less accurate and precise measures of v and T_0. If the study was repeated, it may be preferable to use a supply of gas with a constant CO_2 concentration.

Methodological issues were encountered in Chapter 7 due to the reduced protocol needed to meet time constraints. These issues were briefly mentioned already, however they will be discussed in more detail here. First, D and f could not be estimated for the diffusion-times with maximum b-value $\leq$ 500 smm^{-2} (i.e. the three lowest diffusion-times out of six; 16.54, 18.39 and 23.14 ms). The values are of D and f are required for each diffusion-time to allow for isolation of the intravascular compartment by subtracting the extravascular compartment from the total signal. Since the values could not be estimated directly using high b-value data, the parameters were estimated using the relationships between f, D and Δ found in Chapter 5. Where f decreased linearly with diffusion-time, D has no relationship, and k increased with diffusion-time at lower values, following which it plateaued in grey matter and started to decrease in white matter. The perfusion fraction was estimated by linear extrapolation and the average diffusion coefficient was taken. Despite using the diffusion-time dependence found in previous data, some error will have

been introduced into parameters. These errors may have propagated through our analysis pipeline and affected accuracy of the intravascular parameters, v, T_0 and l.

Secondly, the repeatability of T_0 was reduced due to the low number of diffusion-times, so l was estimated using D^*, using the method established in Chapter 4. Although we determine the two methods can be used interchangeably with the view of maintaining accuracy in grey matter, when comparing the repeatability of the two methods between Chapters 4 and 5, l is more repeatable when T_0 is used. However, this could be due to higher SNR or larger regions used in Chapter 5 than in Chapter 4. It could also be due to increased repeatability in v due to the increased number of diffusion-times in Chapter 5.

A further effect of the limited data was low repeatability and spurious values of the exchange time (τ) when fitting to cerebral white matter. In Chapter 5, the VAX model provided a better model of signal attenuation in white matter. Hence, the pseudo-diffusion coefficient is affected by exchange more so than in grey matter. This meant any estimate of D^* would need to be corrected for using τ. Due to the spurious values of τ, we could not correct D^* and estimate l using the parameter. Hence, changes in IVIM parameters in white matter could not be investigated. Since most IVIM studies in literature do not consider diffusion-time, it is difficult to say to what extent the values of D^* estimated may be affected by exchange. This could explain some of the variability across values presented in literature; Huang et al. [166] measure a mean D^* across five subjects in WM to be $(5.80 \pm 0.75) \times 10^{-3}$ mm^{2}s^{-1}, Hara et al. [306] measure mean D^* as $(9.69 \pm 1.14) \times 10^{-3}$ mm^{2}s^{-1} across ten subjects, Wirestam et al. [167] measure $(21 \pm 60) \times 10^{-3}$ mm^{2}s^{-1} across 28 subjects. Hu et al. [307] measure $(4.93 - 6.24) \times 10^{-3}$ mm^{2}s^{-1} depending on b-value thresholds. Of course, the b-value threshold, fitting method and number of b-values could also affect this. Regardless, by not considering the diffusion-time dependence in estimating D^* in WM, there could be bias introduced.

In addition to the methodological issues, difficulties recruiting participants with mild cognitive impairment meant numbers were quite low. This was also the case with subjects with high cardiovascular risk scores. This means our data is slightly skewed towards healthier subjects. Increasing subjects with cognitive and vascular complaints would improve confidence in results and the significance of our findings.

Throughout the four chapters presented in this thesis, the diffusion-time is heavily featured and considered in every model or analysis method. This was not extended to the pulse gradient time. We aimed to keep this parameter constant in the studies, and achieved this in preclinical data. However the parameter was more challenging to control in clinical sequences. Only the diffusion-time and b-value could be specified. In the intravascular compartment, the parameter is explicitly considered in the VA, VAB and IVIM ballistic models. The diffusive IVIM model assumes $\delta << \Delta$, and this condition is generally met at long diffusion-times in our dataset. There was no dependence described in the extravascular

model. A small amount of literature exists describing the effect of the pulse gradient width on the extravascular DW-MRI signal. In the narrow pulse limit, the apparent diffusion coefficient (ADC) approaches the true diffusion coefficient [226], hence the smaller the pulse width, the more accurate the measure of ADC. Zielinski and Sen [227] find a maximum error in the ADC of 20%. However this is a 'worst-case scenario' where $\delta = \Delta$ and the space for diffusion was very largely restricted, although still in an open geometry (e.g. structure in rock). In reality, space for diffusion in the brain would not be restricted to this extent. The paper presents error for a random pack of mono-sized beads which may be a more appropriate model for the extravascular compartment in the brain. Thus, comparing our diffusion-times and pulsed gradient widths to error in ADC for mono-sized beads in the Zielinski and Sen paper [227], the maximum error is likely to be around 6%. This maximum error is likely to be at shorter diffusion-times where the ratio of δ/Δ was higher (e.g. the highest ratio at $\Delta = 27$ ms, with $\delta = 20$ ms, was 0.73).

The number of b-values used in imaging studies throughout this PhD was lower the majority of IVIM studies in literature (Table 8.1). This would likely result in lower precision in our estimates due to less accurate characterisation of the data. One might expect that this would impact the extravascular compartment in particular where the SNR is lower due to high diffusion-weighting and only two or three b-values were used to determine f and D. Although, D had excellent repeatability of 1.6% (Chapter 6) and f had good repeatability of 10% in GM. Increasing the number of b-values could improve repeatability in smaller regions which would allow more thorough investigation with disease. It may also allow for voxel-wise estimation of parameters, which would be more sensitive to changes with disease.

With the b-value limit set to b=500 smm^{-2} for the negligible decay of the intravascular compartment, this left five b-values in preclinical data in Chapter 4, six b-values in clinical data in Chapter 5, and six or less b-values in patient data in Chapter 7, for estimation of intravascular parameters. This meant more complex models could not be fit to data. An example includes Fournet's triexponential model (Equation 3.17) which is shown to provide a better fit to data at shorter diffusion-times than the monoexponential model, indicating multiple intravascular compartments. Work by Wetscherek et al. [35] agrees with the finding by identifying ballistic and diffusive flow between diffusion-times of approximately 20 and 50 ms. There is likely to be a distribution of different flow regimes within a voxel. Whilst the VA model includes diffusion-time dependence and thus can characterise different flow regimes through the diffusion-times, it will only characterise one regime at each diffusion-time. This would most likely be the regime which has the strongest influence on signal attenuation. With more than one flow regime or compartment present, it may be that the VA model is not fully characterising the data which could lead to inaccuracies in parameter estimates. With our reduced number of b-values, perhaps the best

Table 8.1: b-values used in each study presented and a selection of IVIM studies with their respective number of b-values and range of b-values.

Study	Number b-values	Range b-values	Threshold
Chapter 4	8	0, 10, 20, 50, 100, 200, 500, 1000	b>300
Chapter 5	10	0, 10, 30, 50, 100, 200, 300, 500, 750, 1000	b>300
Chapter 6	10	0, 10, 30, 50, 100, 200, 300, 500, 750, 1000	b>300
Chapter 7	5-10	0, 10, 30, 50, 100, 200, 300, 500, 750, 1000	b>300
Fournet et al. [131]	31	21 between 0 and 500, 10 between 500 and 2500	b>500
Federau et al. [135, 168, 169]	16	0, 10, 20, 40, 80, 110, 140, 170, 200, 300, 400, 500, 600, 700, 800, 900	b>200
Finkenstaedt et al. [172]	15	0, 5, 10, 20, 35, 55, 80, 110, 150, 200, 300, 500, 750, 1000, 1300	b>200
Keil et al. [170]	32	0-2000	-
Yao et al. [208]	15	0, 20, 40, 80, 110, 140, 170, 200, 300, 400, 500, 600, 700, 800, 900, 1000	b>200
Wu et al. [176]	17	25, 50, 75, 100, 125, 150, 200, 250, 300, 400, 500, 600, 700, 800, 900, 1000	b>250
Meeus et al. [174]	11	0, 20, 40, 80, 110, 140, 170, 200, 300, 500, 1000	b>300, b>500
Iima et al. [209]	19	0, 5, 10, 20, 30, 50, 70, 100, 200, 400, 600, 800, 1000, 1500, 2000, 2500, 3000, 3500, 4000	b>500
Chen et al. [139]	9	0, 50, 100, 150, 200, 300, 400, 800, 1000	b>200

characterisation of signal attenuation we can achieve is modelling only the dominant regime in the voxel. Biophysical models are unlikely to truly reflect the underlying physiology and thus will never provide full characterisation of the data. However, our estimates of l appear to correspond well to those of ground truth measures, which gives confidence in the use of the model.

A further limitation in each of the studies presented in this thesis is the use of the 'two-step' method for estimation of IVIM parameters. The two-step method is the process of first estimating either D, or D and f, using high b-value data where the intravascular signal is assumed to be negligible. These parameters are then substituted into the IVIM equation, after which the extravascular component can be subtracted from the total normalised signal (note that subtraction is not necessary) to isolate the intravascular component. The intravascular model is then fit to the data and vascular parameters extracted. This method was first introduced due to inherent difficulties of fitting a biexponential model, and the spurious values of D^* produced by fitting the model in one step [134]. The method is used in the majority of IVIM studies in literature [131, 135, 139, 140, 154, 156, 158, 168, 169, 176, 177, 208, 209, 307, 308]. However, it undoubtedly introduces bias into parameters due to the small amount of intravascular signal likely remaining at the high b-values (although Meeus et al. [158] and Wang et al. [309] do show similar accuracy between the one and two step fits). Any error would be propagated through from f and D to downstream parameters (D^*, v, T_0). Hence, any parameters that are estimated may include some bias, so perhaps the absolute values should not be considered as accurate and observing differences in parameters between diseased and healthy individuals may be more appropriate. Although this assumes bias is consistent across the two groups which may not be true in all circumstances (e.g. if bias is dependent on parameter magnitude).

The bias and variance of parameters estimated using the two-step and one-step fitting methods is investigated in Appendix A. Simulations show two-step parameters have bias even at high SNR (1000), whereas one-step fits have zero (or very little) bias at these SNR values. The one-step fit outperformed the two-step fit for every parameter, with exception of f and D at SNR<100. Although, f and D had very little bias at high SNR and were similar to those obtained by one-step fit which is consistent with literature [158, 309]. Simulations did not agree with in-vivo data for VA model fits however, which shows the two-step may perform well (see more detailed discussion in Appendix A).

The two-step method is further complicated by the choice of the b-value threshold at which one assumes the intravascular compartment is negligible, which varies largely across studies depending on the organ or pathology. In the brain, the b-value threshold is assumed to be lower than other organs due to lower blood volume and generally sits between b=200 and b=500 smm^{-2}. This range of b-value thresholds will introduce variability between studies and likely explains the wide range of values presented for IVIM parameters in

literature. Literature shows the parameters are dependent on the threshold used [139, 140] (as does simulated (Figures A1 and A2) and in-vivo (Figure A3) data presented in Appendix A), with f increasing, and D and D^* decreasing with increasing threshold. The threshold used in this thesis is consistent across all studies, although our high value of b=500 smm^{-2} gives higher values of f and lower estimates of D^* than one might expect.

We also found that the number of b-values used in estimating extravascular parameters affects estimates of f. If two b-values are used to estimate parameters, requiring a calculation, f is lower than if a higher number of values are used, requiring model fitting. Using the IVIM model requires many assumptions which could alter the magnitude of parameters, so care needs to be taken when comparing to literature in the field. With these issues, standardisation of IVIM imaging within organs or pathologies (e.g. tumours) would be a large help in translating the method to the clinic.

8.5 Further work

Despite being increasingly used throughout literature, the IVIM model has inherent problems related to its underlying assumptions, as discussed in Section 3.3.5.1 of Chapter 3. Additionally, although the source of the IVIM signal is assumed to be the microvasculature, it in unclear whether this is the case since the CSF or glymphatic system may affect the pseudo-diffusion coefficient. It is reasonable to assume that any fast moving protons within a voxel may contribute to the attenuation of the DW-MRI signal in the so called vascular compartment and lead to errors in the interpretation of estimated vascular parameters.

As discussed in the literature review, many models of IVIM have been proposed and have shown parameter estimates that are consistent with literature. The models are dependent on imaging parameters used. The number of b-values and diffusion-times determines the complexity of the model that can be used to describe the signal attenuation, and the amount of information which can be extracted. The diffusion-time can drive the number of compartments modelled in IVIM and allow us to probe compartment structure (e.g. by using the VA model). For example, Fournet et al. [131] show at low diffusion-times, a biexponential model provides a better fit than the mono-exponential IVIM model generally used in literature. This indicates increased sensitivity to more blood flow regimes with decreased diffusion-time (i.e. potentially increased sensitivity to type of vessel).

To elucidate the source of the IVIM signal and how many compartments contribute, simulations using the vascular corrosion cast presented in Chapter 4 could be used. Simulating the movement of spins in the vascular network, and signal decay with b-value and diffusion-time, would allow for comparison of models and validation of parameters. The ballistic and diffusive limits could be evaluated, and the effects of larger vessels on f and D^* assessed. To improve accuracy of simulations, the diffusion-time dependence of the

extravascular compartment could be modelled, as in the VERDICT [310] model. If the simulated signal does not fully characterise the DW-MRI signal as measured in-vivo, then this could indicate effects of other compartments. Note that a similar study was very recently presented by Van et al. who use two-photon microscopy to generate cortical vascular networks for simulations [311]. The study investigated the pseudo-diffusion coefficient of different vessel groups (i.e. arteries, veins, capillaries, whole network). However, the study did not consider diffusion-time and did not model the extravascular compartment.

The model of water exchange developed in Chapter 5 requires validation and may need further development. The model could be validated against other MR methods [211] in disease groups, to determine if the changes are consistent. The model could also be fit to DW-MRI data in animal models where the BBB is affected, for example, in aquaporin-4 knockout mice. The model produces estimates of exchange time which are lower than expected [211], further investigation would help us to understand this result.

Increasing the number of diffusion-times collected in the aged cohort, as in Chapter 5, might allow for more accurate and precise parameter estimates and improve our investigation of microvascular changes in disease. It is surprising that no changes in IVIM parameters were detected since studies evidence changes in velocity and vessel morphology in neurodegenerative disease. However, this could have been due to one of the many limitations discussed. Future data collection could include measures of inflammatory markers such as cytokines or C-reactive proteins which may be useful in determining whether the mechanisms behind the increase in f (which we suspect is due to vasodilation) are inflammatory in nature or if they could be compensatory in early disease [82]. During inflammatory responses, chemical mediators (e.g. histamine, nitric oxide) cause vasodilation and increased vascular permeability [280] to increase blood flow to infected or damaged areas. These responses may be caused by tissue damage and atrophy. Microglial cells are involved in removal of damaged neurons, however chronic activation of microglia has been related to increases in amyloid [312]. Amyloid itself has been identified as an activator of inflammation in the brain [313], as has oxidative stress [313]. A large amount of data was collected on each participant as part of the pre-scan cognitive testing and imaging examination. These measures are not put to use in this thesis. Further work could look in more detail at other measures of cSVD in participants; microbleeds, lacunes, PVS etc. Associations between the cognitive domains and vascular parameters could be investigated. IVIM derived parameters could be compared to parameters from other MRI techniques, such as CBF and CBV. Observing the oxygen extraction fraction from QSM in brain regions where f is affected may help clarify the mechanisms behind the increase in the parameter.

As discussed, a low number of b-values were collected to reduce imaging times, meaning more complex models couldn't be used. Whilst the mono-exponential model provides a good

fit to data at longer diffusion-times [131] and an appropriate fit to data lacking complexity, there may be multiple compartments to the IVIM signal, and these should be modelled to improve accuracy. Collecting a higher number of b-values, as well as diffusion-times, would allow us to fit more complex models. Although, use of more complex modelling could make parameter interpretation challenging. Separating different blood flow components using both flow and non-flow compensated sequences could reduce model complexity by nulling the ballistic signal.

IVIM has promising applications in oncology [134] (see review paper by Iima and Le Bihan [30]). Iima et al. [30] demonstrate correlations between the perfusion fraction and CBV from DSC-MRI in gliomas and DCE parameters in head and neck tumours. Detsky et al. [314] show IVIM may be useful in differentiating recurrent tumour from radiation necrosis for brain metastases treated with radiosurgery. Furthermore, tumour vessels are heterogeneous, tortuous, poorly or irregularly branched and often hyperpermeable [315]. Advanced IVIM measures of vessel structure could be useful in identifying these changes. Blood flow is chaotic and slow in abnormal tumour vasculature [315], meaning measures of velocity may be useful in determining tumour grade or subtle early changes before metastases are detectable. Tumour vascular morphology can vary according to the tumour cells, having distinct patterns of angiogenesis [315], hence structural microvascular measures could be useful in determining tumour type.

Recent simulation work (Appendix A) shows the one-step fit might outperform the two-step fit for VA model parameters. Although, in-vivo data and literature [158, 309] disagrees with this finding. Further work should be done to investigate the effects of different fitting methods in IVIM parameter estimation as described in more detail in Appendix A.

8.6 Concluding remarks

In this thesis, we show that multi-diffusion-time diffusion-weighted MRI and IVIM modelling can be used to extract parameters describing microvascular structure and function. Measures are validated using corrosion casting of the cerebrovasculature in rats. We demonstrate the diffusion-time dependence of diffusive IVIM parameters (f, D and D^*), which is not considered in most IVIM studies. We also show trans-BBB water-exchange may affect intravascular signal attenuation at long diffusion-times in white matter, and propose a model to describe the effects. The IVIM perfusion fraction was sensitive to vascular risk and cognitive health in aged individuals. We show no change in vascular structure in aged individuals with decreased cognitive performance or increased vascular risk. However, further work with a more extensive protocol in later stage disease may yet prove changes exist.

Appendix A

1 Determining bias and precision with simulation

IVIM parameters can be derived from DW-MRI data using two different model fitting methods. The first, a two-step method where extravascular parameters are derived using high b-value data, following which they are substituted into the biexponential equation (or the extravascular compartment is subtracted from the total normalised signal) and intravascular parameters are estimated. The second, a one-step fit where extravascular and intravascular parameters are estimated simultaneously using all b-value data. The two-step fit is used in the majority of IVIM literature since it is said to derive more repeatable and less spurious parameters [134, 135, 158] than the one-step fit. Whilst the precision and bias of diffusive IVIM parameter estimates have been investigated with the two fitting methods, no such investigation has been performed for the VA model.

Following the somewhat low levels of repeatability and poor response to hypercapnia (Chapter 6), we were interested in investigating the upper limits of precision and accuracy using simulations. In this Chapter, we consider the impact of SNR and model fitting options, namely the one-step and two-step fitting approaches. We also investigate the effect of b-value threshold on the two-step fit (i.e. the point above which the intravascular signal is considered negligible) and the use of an additional parameter (c) to improve fitting. Last, we determine whether the two-step fitting method introduces artificial diffusion-time dependence into f and D.

1.1 Methods

The normalised DW-MRI signal is generally modelled as a sum of two exponentials characterising the intravascular and extravascular compartments as described in Chapters 4-7:

$$\frac{S(b,\Delta)}{S_0} = fe^{-bD_b+c}H(b,\Delta) + (1-f)e^{-bD}, \tag{A1}$$

where $S(b,\Delta)$ is the DW-MRI signal as a function of b-value (diffusion-weighting) and diffusion-time (Δ). S_0 is the signal at $b = 0$. D is the extravascular diffusion coefficient, f is the perfusion fraction, D_b the diffusion coefficient of blood within a vessel and $H(b,\Delta)$ is the intravascular signal attenuation as function of b and Δ. c is a parameter introduced to improve fitting (see Chapter 4, Section 4.5.3.2).

The simulated diffusive IVIM signal was generated using Equation A1 where:

$$H(b,\Delta) = H(b) = e^{-bD^*} \tag{A2}$$

where D^* is the pseudo-diffusion coefficient, valid only where the diffusion-time is long enough for blood flow to mimic diffusion. The simulated VA signal was generated using Equation A1 where:

$$H(b, \Delta) = e^{-bk(\Delta)} \tag{A3}$$

where k, the perfusion attenuation coefficient, is equal to:

$$k = \frac{\Omega v^2 T_0}{3\delta^2(\Delta - \delta/3)} \tag{A4}$$

where v is the average blood velocity, T_0 is the average time that spins in the blood stay in a segment, and:

$$\Omega = \delta^2(\Delta - \delta/3) - 2T_0^2\delta - T_0^3 q \tag{A5}$$

$$q = 2\exp\Big(-\frac{\Delta}{T_0}\Big) + 2\exp\Big(-\frac{\delta}{T_0}\Big) - \exp\Big(-\frac{\Delta+\delta}{T_0}\Big) - \exp\Big(-\frac{\Delta-\delta}{T_0}\Big) \tag{A6}$$

Simulated data used the same b-value distribution as is collected in human data in Chapters 5-7 (b = 0, 10, 30, 50, 100, 200, 300, 500, 750, 1000 smm^{-2}). For VA signal generation, the same diffusion-time and pulse width distribution was used as in actual MRI data (Chapter 5, Table 5.1). The following parameter values were used to generate the model signals: f=0.114, D=8.04×10^{-4} mm^{2}s^{-1}, D^*=3.98×10^{-3} mm^{2}s^{-1}, D_b=1.75×10^{-3} mm^{2}s^{-1}, v=1.30 mms^{-1}, T_0=7.07 ms, c=0. Values for f, D and D^* were chosen from GM plots in Figure 5.2 (Chapter 5) at diffusion time 59.86 ms. v was chosen from Table 5.2 (Chapter 5) for the GM VA fit. T_0 was determined using: $T_0 = 3D^*/v^2$ for consistency with D^* (derived by rearranging $l = 2vT_0$ and $D^* = vl/6$). Note that a diffusion-time dependence in f or D was not modelled as we did not want to assume any particular dependence. However, fitting methods for the VA model estimate f and D at every diffusion-time. These values will be used to investigate whether the two-step fit introduces artificial diffusion-time dependence into f and D.

Random white Gaussian noise was added to the diffusive IVIM and VA simulated signal to mimic SNR levels of 20 to 1000 (steps of 20 to 500, and 50 to 1000) based on:

$$\text{SNR} = \frac{\mu}{\sigma} \tag{A7}$$

where μ is the maximum signal (which is equal to 1 for the normalised data) and σ is the standard deviation of the noise. The 'normrnd' function was used in Matlab (R2019b) with mean of the noise set to zero. The same level of noise was added to each b-value, this decreased SNR with increasing b-value, as is found in in-vivo DW-MRI data. The fitting simulations were performed using 100 random noise iterations for each model and SNR level. The mean and standard deviation of parameter estimates over the 100 iterations were calculated for each SNR for plots.

To estimate an approximate maximum SNR for simulations, actual MRI data was used. Voxel-wise signal to noise ratio (SNR) of normalised DW-MRI data was estimated at b=10 smm^{-2} using Equation A7 of Dietrich et al. [192] for GM and WM using repeat measurements from seven volunteers. To estimate regional SNR, voxel-wise estimates were multiplied by the square root of the number of voxels in the region. This method is likely to overestimate SNR due to correlations in noise between voxels. However, it gives a rough estimate of regional SNR.

Four fitting methods were investigated for the two models:

1. Two-step fit with c
2. Two-step fit without c
3. One-step fit with c
4. One-step fit without c.

The two-step fits were performed as with in-vivo MRI data, as described in Section 5.6.3 of Chapter 5. Three b-value thresholds were investigated for the two-step fit: b= 100, 200 and 300 smm^{-2}. The b=300 smm^{-2} threshold is used in all Chapters of this thesis. This value is the point above which the intravascular contribution to signal attenuation is considered negligible. For the diffusive IVIM model fit, only data at the longest diffusion-time (59.86 ms) was used, with $H(b, \Delta)$ equal to Equation A2. For one-step fits, Equation A1 was fit to data at the longest diffusion-time and all b-values simultaneously for the diffusive IVIM model, and all data, b-values, diffusion-times and pulse width values simultaneously for the VA model. All model fitting used the 'lsqcurvefit' function in Matlab (R2019b).

1.2 Results

1.2.1 Signal to noise ratio in grey and white matter

Voxel-wise and regional SNR is shown in Table A1. The voxel-wise SNR and regional SNR is higher in WM than GM.

Table A1: Voxel-wise SNR (± standard deviation), number of voxels per region (± standard deviation) and regional SNR averaged across subjects for diffusion-time 27 ms.

Region	Voxel-wise SNR	Number voxels	Regional SNR
GM	10.402 ± 4.25	202440 ± 18690	4680
WM	31.843 ± 8.904	171170 ± 17710	13175

1.2.2 Effect of b-value threshold on parameter estimates

Figure A1 shows mean parameter estimates (f, D, D^* and c) $\pm$ standard deviation derived from 100 random noise iterations of the simulated diffusive IVIM signal at SNR levels between 20 and 1000. As expected, the standard deviation of estimates decreases with increasing SNR (high precision). The precision is lowest for the b=300 smm^{-2} threshold. The pseudo-diffusion coefficient (D^*) is the least precise of all parameters, and the diffusion coefficient, the most. Conversely, the lowest bias for each parameter is achieved using the b=300 smm^{-2} threshold. However, none of the parameter estimates reach true values with increasing SNR, with f being underestimated ($\times$0.83 of true value), and D ($\times$1.03 of true value), D^* ($\times$1.3 of true value) and c (0.01 versus 0) being overestimated.

Figure A2 shows the same plots for VA model parameters (v, T_0 and c). Again, the standard deviation of estimates decreases with SNR. The precision is lower for the b=300 smm^{-2} threshold in T_0 and c, but comparable across all thresholds for v. The velocity maintains high bias ($\times$2 of true value) and low precision (standard deviation approximately equal to the magnitude of the true value) with increasing SNR. The lowest bias in v comes from the b=300 smm^{-2} threshold at higher SNR (>400). The correlation time (T_0) is approximately 0.7 times the true value at higher SNR (>400), with lowest bias from the b=300 smm^{-2} threshold. The bias in T_0 is very high and precision very low at lower SNR (<200), with up to 100 times the true value and standard deviation of $\pm$50 times the true value. c does run close to zero, with a value of 0.01 at high SNR (>400). Note that this value is consistent with in-vivo data (0.0194 $\pm$ 0.0201).

Figure A3 shows in-vivo parameter estimates from MRI data across ten subjects with b-value threshold (data from Chapter 5). f increases with b-value threshold, and D, D^*, v and T_0 decrease with b-value threshold. This is consistent with simulated data at higher SNR (approximately >200).

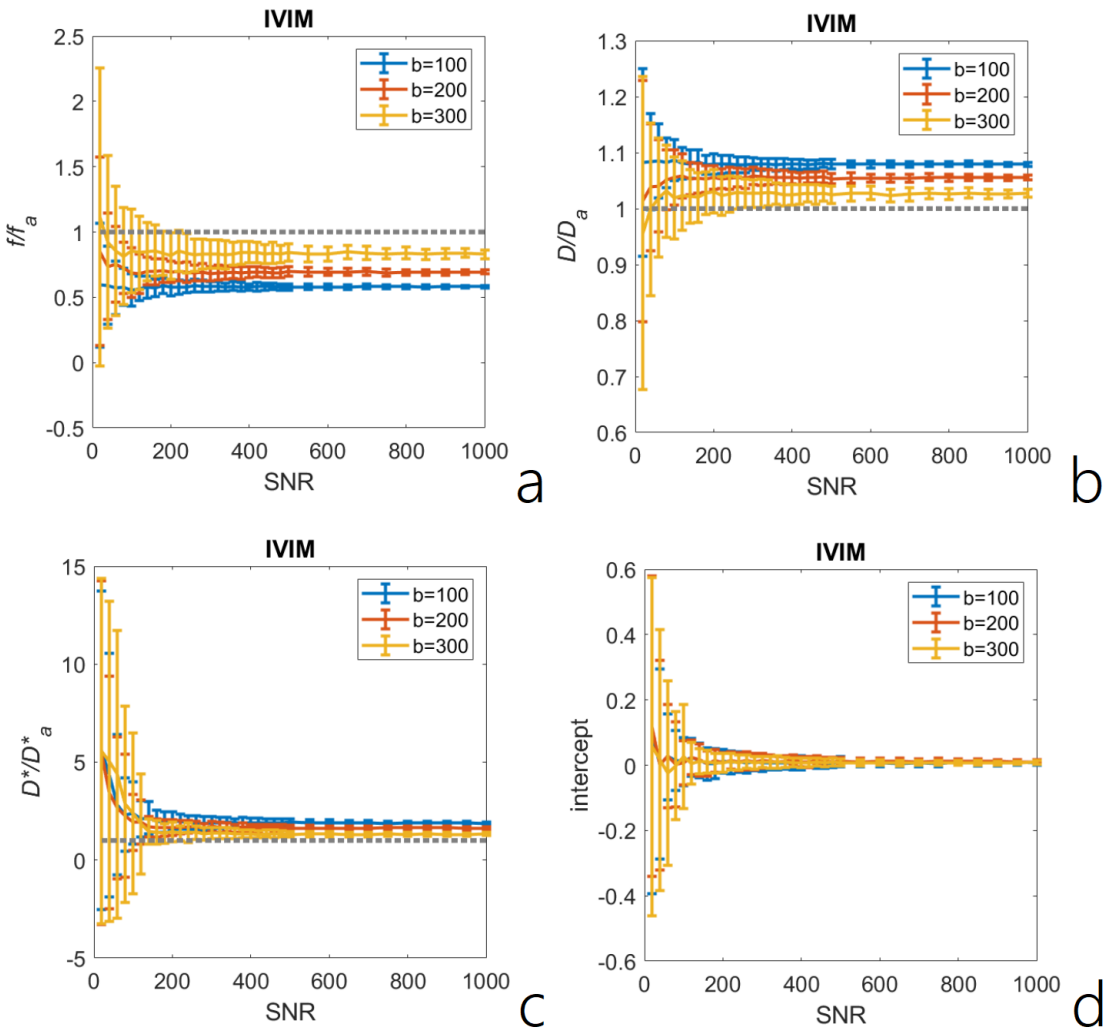

Figure A1: Mean parameter estimates ± standard deviation derived from 100 iterations of the diffusive IVIM signal with random noise at SNR levels between 20 and 1000. Parameter estimates are divided by true values, with exception of c which was set to zero in simulated signals. (a) shows the perfusion fraction (f), (b) the diffusion coefficient (D), (c) the pseudo-diffusion coefficient (D^*), (d) the parameter for improved fitting (c). Estimates for three b-value thresholds are shown: b=100 smm^{-2} (blue), b=200 smm^{-2} (orange) and b=300 smm^{-2} (yellow). Note that we use b=300 smm^{-2} in our data.

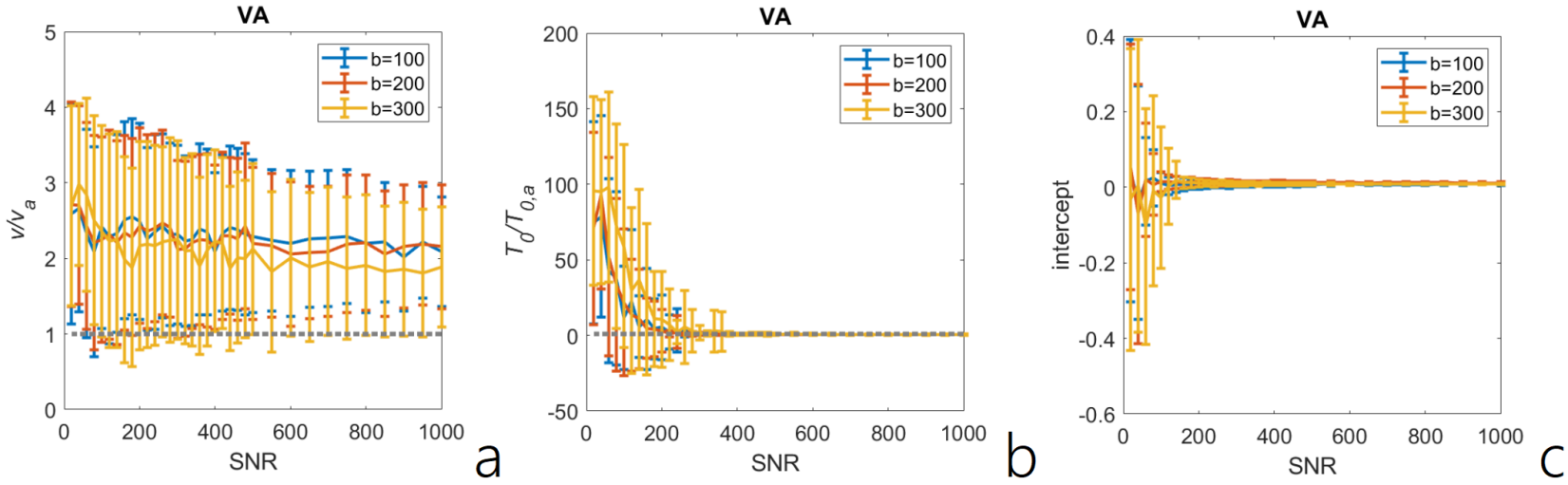

Figure A2: Mean parameter estimates ± standard deviation derived from 100 iterations of the VA model signal with random noise at SNR levels between 20 and 1000. Parameter estimates are divided by true values, with exception of c which was set to zero in simulated signals. (a) shows the average blood velocity (v), (b) the average correlation time (T_0), (c) the parameter for improved fitting (c). Estimates for three b-value thresholds are shown: b=100 smm^{-2} (blue), b=200 smm^{-2} (orange) and b=300 smm^{-2} (yellow). Note that we use b=300 smm^{-2} in our data.

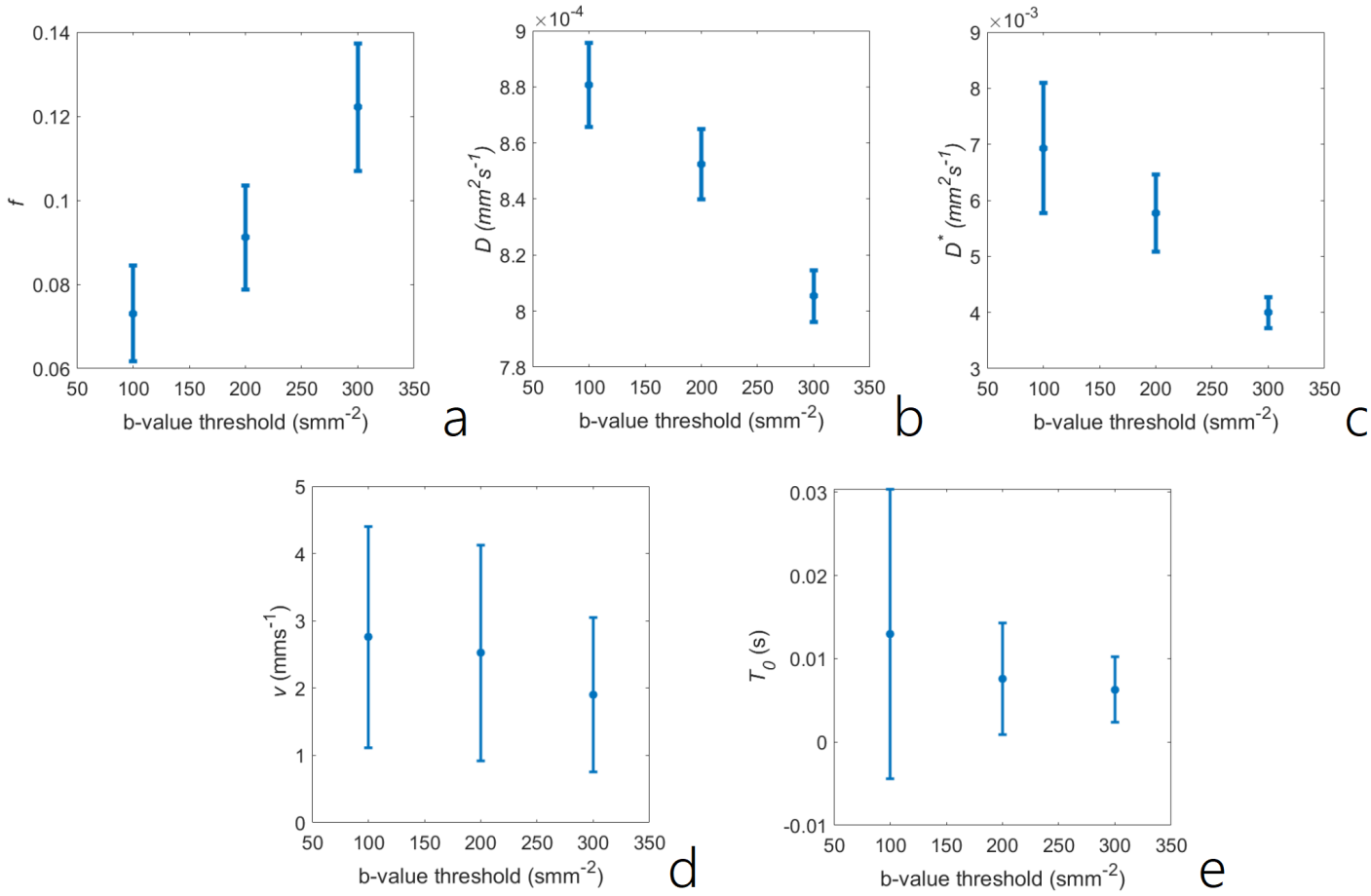

Figure A3: Mean parameter estimates ± standard deviation over subjects versus b-value threshold. (a) shows the perfusion fraction (f), (b) the diffusion coefficient (D), (c) the pseudo-diffusion coefficient (D^*), (d) the average blood velocity (v), and (e) the average correlation time (T_0).

1.2.3 Effect of two-step fitting method on diffusion-time dependence in f and D

Figure A4 shows estimates of f and D from simulated data with diffusion-time ($\pm$ standard deviation) for three SNR values: 500, 750 and 1000. f increases with diffusion-time with a maximum change of 3.4% between the lowest and highest diffusion-times. D decreases with diffusion-time with a maximum change of 0.7% between the lowest and highest diffusion-time. Standard deviation decreases with SNR, however bias does not appear to change with SNR.

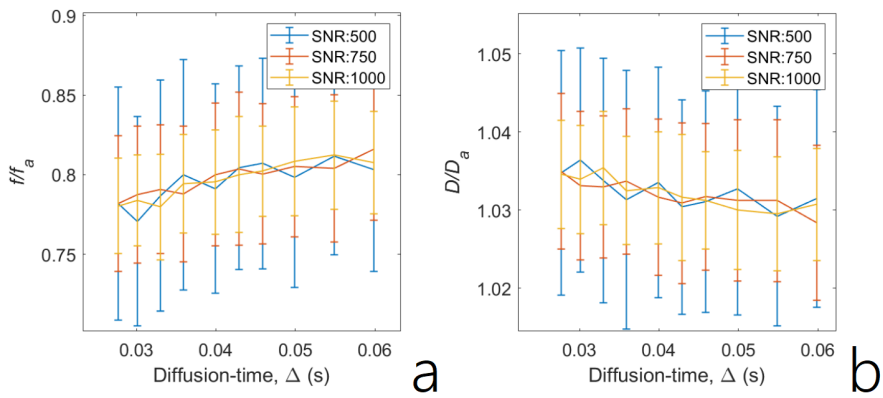

Figure A4: Mean parameter estimates ($\pm$ standard deviation) versus diffusion-time, derived from 100 random noise iterations, shown at SNR levels 500, 750 and 1000. Parameter estimates are divided by true values. (a) shows the perfusion fraction (f) and (b) the diffusion-coefficient (D). Estimates for the b=300 smm^{-2} threshold are shown.

1.2.4 Effects of fitting methods on parameter estimates (two-step versus one-step, and c)

Figure A5 shows diffusive IVIM parameters (f, D, D^*, c) for the four fitting methods previously mentioned. Two-step fits used the b=300 smm^{-2} threshold, as in in-vivo data (Chapters 4-7). Results for two-step fits with and without c are the same for f and D since c is in the intravascular term. The use of c does not largely affect parameter estimates; curves with and without c are very similar across all SNR, despite mean c of around 0.1 at low SNR (<200). For f and D, the two-step fit outperforms the one-step fit at SNR<200, with lower bias and standard deviation. However the one-step fits tend to the true value with higher SNR, whereas we see the small bias in two-step parameters. For D^*, one-step fits have lower bias than two-step fits for all SNR and slightly higher precision.

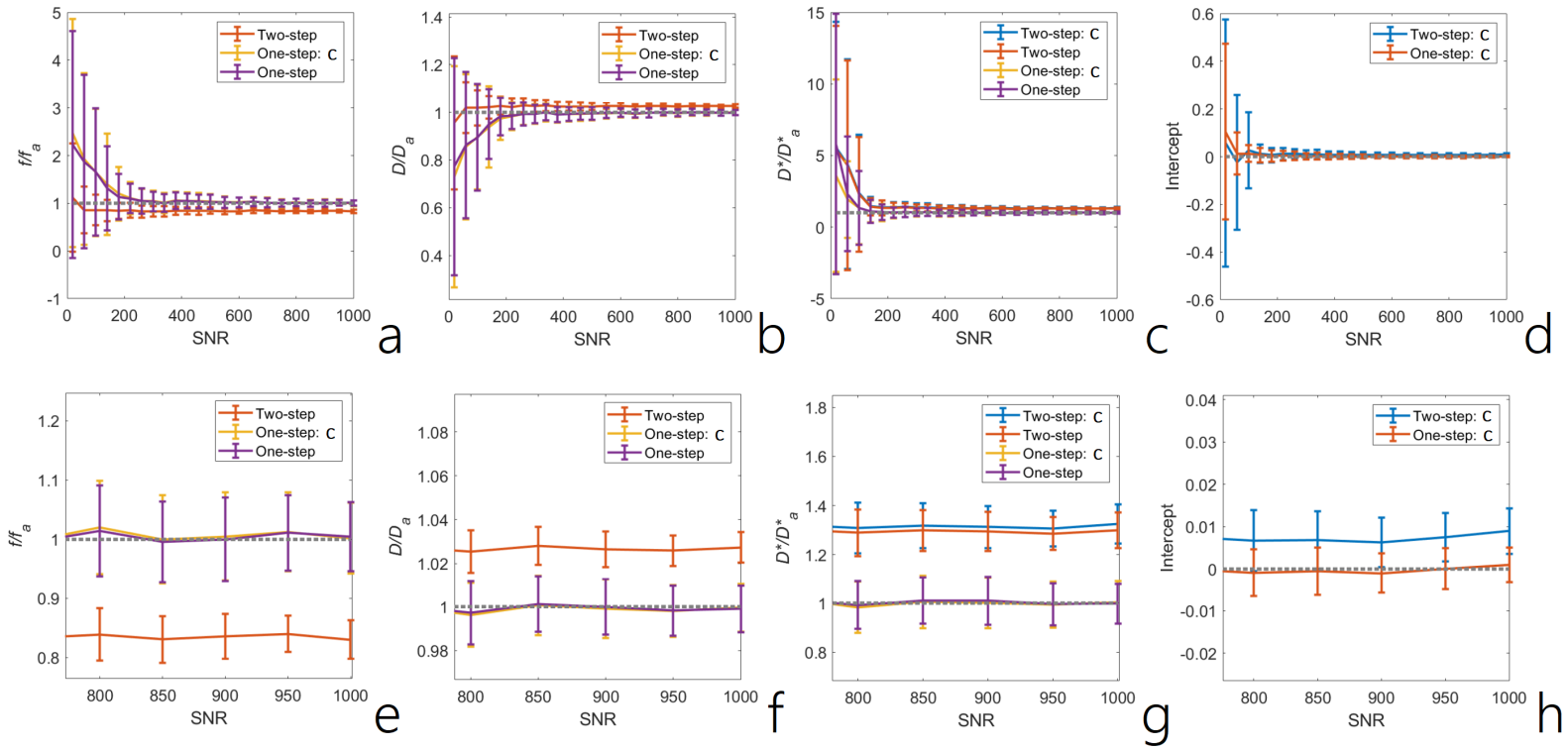

Figure A5: Mean parameter estimates ± standard deviation derived from 100 noise iterations of the diffusive IVIM model signal with random noise at SNR levels between 20 and 1000. Parameter estimates are divided by true values, with exception of c which was set to zero in simulated signals. (a) shows the perfusion fraction (f), (b) the diffusion coefficient (D), (c) the pseudo-diffusion coefficient (D^*), (d) the parameter for improved fitting (c). (e-h) are close-ups of parameter estimates at SNR 800-1000. Estimates for four methods of parameter estimation are shown: two-step fit with c (blue), two-step fit without c (orange), one-step fit with c (yellow) and one-step fit without c (purple). Plots for f and D for only show one two-step fit since c is in the intravascular term, thus does not affect these parameters. Note that we use the two-step fit with c in our data.

Figure A6 shows VA model parameters (v, T_0, c) for the four fitting methods. Again, the use of c does not largely affect parameter estimates; curves with and without c are very similar through all SNR despite values up to almost 0.6 in two-step fits. For v and T_0, the one-step fit outperforms the two-step fit for all SNR, with lower bias and standard deviation. For v, the two-step fits maintain high bias ($\times 2$ magnitude of true value) and standard deviation (equal to the value of v itself) at high SNR. One-step fits require SNR of approximately 600 to achieve highest accuracy in v. For T_0, one-step fits are close to true values around SNR 200, and two-step fits achieve highest accuracy around SNR 300. Precision is low in T_0 for the one-step and two-step fits until high accuracy is achieved, with standard deviation values of $\pm$ 50 times the parameter value or greater at SNR$<$100.

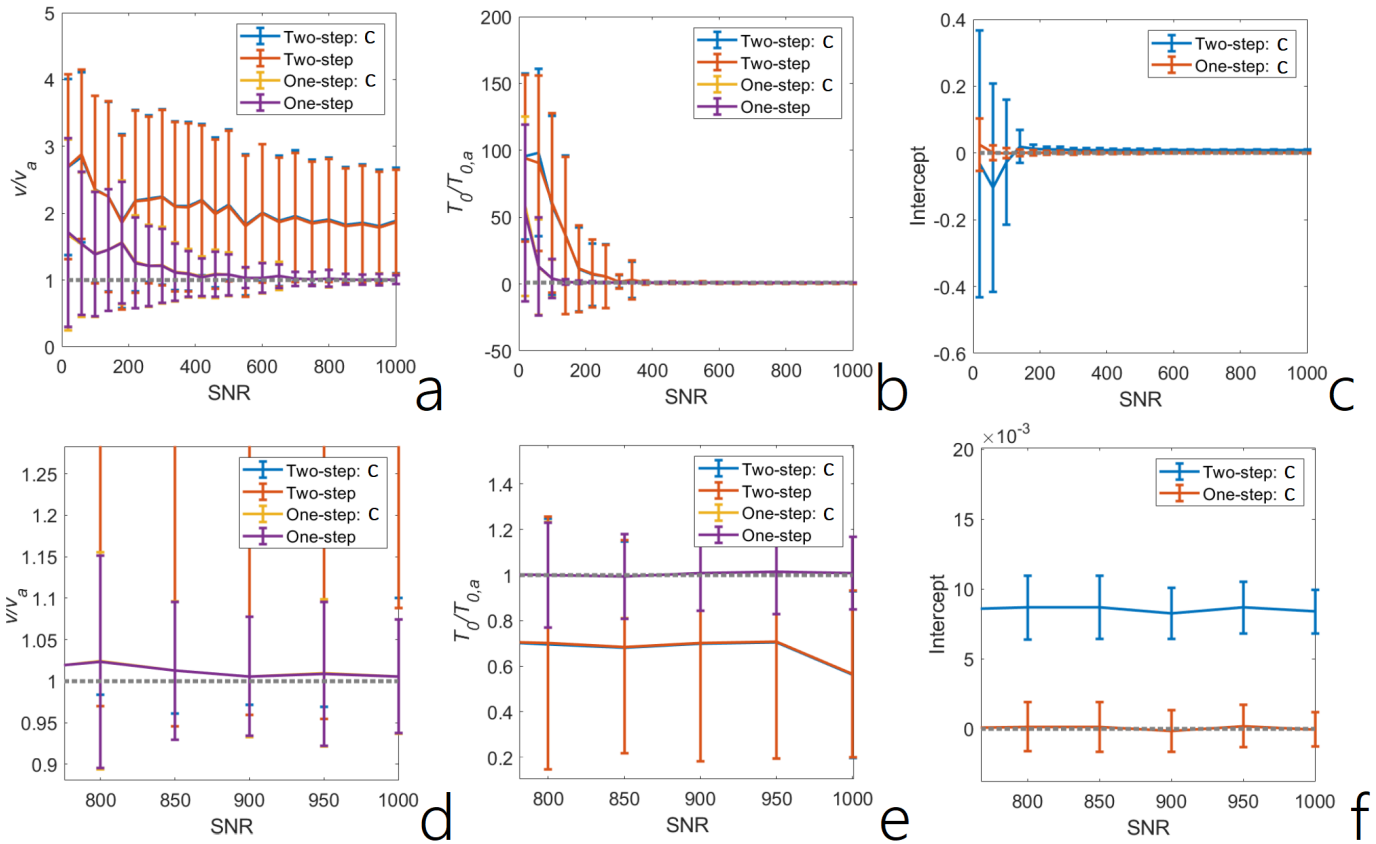

Figure A6: Mean parameter estimates ± standard deviation derived from 100 iterations of the diffusive IVIM model signal with random noise at SNR levels between 20 and 1000. Parameter estimates are divided by true values, with exception of c which was set to zero in simulated signals. (a) shows the average blood velocity (v), (b) the average correlation time (T_0), (c) the additional parameter for improved fitting (c). Estimates for four methods of parameter estimation are shown: two-step fit with c (blue), two-step fit without c (orange), one-step fit with c (yellow) and one-step fit without c (purple). Note that we use the two-step fit with c in our data.

1.2.5 Comparing in-vivo data for the one-step and two-step fits

Parameters from one-step and two-step fits of the VA model (with differing extravascular models) to data described in Chapter 5 are presented in Table A2. Three models of the extravascular compartment were used in one-step fitting in-vivo. Model 1 where no diffusion-time dependence is assumed in f and D. Model 2 where a linear diffusion-time dependence is assumed in f and no dependence in D. Model 3 where a linear diffusion-time dependence is assumed in f and the relationship $D{=}D_{inf} + A/\Delta$ assumed for D, where D_{inf} is the diffusion coefficient with infinite diffusion-time and A is a structural parameter [16]. Values are presented from the two-step fit as performed in Chapter 5 where f is presented from the longest diffusion-time.

f and D are fairly consistent across one-step Model 1 and 2 (f: 0.228 versus 0.216. D: $6.99{\times}10^{-4}$ versus $7.02{\times}10^{-4}$ mm^{2}s^{-1}). However, f and D approximately double with Model 3. Two-step f is smaller than all one-step methods (f=0.114), and D slightly larger than Model 1 and Model 2 for the one-step fit, but smaller than Model 3 D. v and T_0 vary across the one-step fit methods, with Model 1 showing higher v (3.03 versus 1.65 (2) and 1.20 (3) mms^{-1}) and lower T_0 (1.31 versus 8.66 (2) and 5.84 (3) ms). Model three values for v and T_0 are more consistent with two-step fit values (v=1.33 mmS^{-1} and T_0 = 6.29 ms), although slightly lower.

Table A2: One-step and two-step parameter estimates in grey matter (mean ± standard deviation) from in-vivo data collected in Chapter 5. f is the perfusion fraction, D is the diffusion coefficient, v is the average blood velocity and T_0 is the correlation time. Parameters are shown for three models for the one-step fit. Model 1 assumes no diffusion-time (Δ) dependence in the extravascular compartment. Model 2 assumes a linear diffusion-time dependence in f. Model 3 assumes a linear diffusion-time dependence in f, and $D{=}D_{inf} + A/\Delta$, where D_{inf} is the diffusion coefficient with infinite diffusion-time and A is a structural parameter [16]. Where a diffusion-time dependence is considered, presented values for f and D are from the longest diffusion-time. Two-step fitting is performed as desribed in chapter 5.

Parameter	One-step: Model 1	One-step: Model 2	One-step: Model 3	Two-step
f	0.228 ± 0.076	0.216 ± 0.073	0.397 ± 0.29	0.114 ± 0.19
D ($\times10^{-4}$ mm^{2}s^{-1})	6.99 ± 0.83	7.02 ± 0.80	16.5 ± 13	8.05 ± 0.020
v (mms^{-1})	3.03 ± 1.0	1.65 ± 1.15	1.20 ± 0.35	1.33 ± 0.17
T_0 (ms)	1.31 ± 2.0	8.66 ± 9.0	5.84 ± 2.5	6.29 ± 3.8

1.3 Discussion

Model data simulations were performed with varying SNR levels to determine the bias and precision of diffusive IVIM and VA model parameters estimated using the two-step fitting method with b=300 smm^{-2} threshold and intravascular fitting term (c) (methods used in Chapters 4-7 of this thesis). We investigate effects of choice of b-value threshold in two-step fitting and whether this method introduces artificial diffusion-time dependence into parameters. Additionally, we investigate the bias and precision of less complex fitting methods (i.e. one-step fitting versus two-step, removing c from the intravascular compartment model).

Simulations show the b-value threshold affects diffusive IVIM and VA model parameters (Figures A1 and A2) which is consistent with in-vivo data (Figure A3). f increases with increasing b-value threshold, and D decreases, which is consistent with literature [139, 140]. Vascular parameters (D^*, v and T_0) increase with threshold at low SNR and alter to decrease with threshold at high SNR (around 150 for D^*, 100 for v and 300 for T_0). The decrease in D^* is consistent with literature [139, 140] and likely drives the decrease in v and T_0 since the parameters are derived from D^* values with diffusion-time. Fitting using the b=300 smm^{-2} threshold gives estimates with lowest bias for all parameters for SNR values presented in this study (SNR>1000) (versus b=100 and 200 smm^{-2}). This is likely due to there being less intravascular signal with increasing b-value threshold, thus more accurate characterisation of f and D, which propagates through to intravascular parameters. The precision is lower for the b=300 smm^{-2} fit however, perhaps due to the bias-variance trade-off where reducing bias increases variance and vice-versa. The variance does seem to reduce exponentially with increasing SNR however, and SNR values presented here are very high (>1000), so variance is low regardless. These results demonstrate why our values of diffusive IVIM parameters differ from literature values, where a lower threshold (b=200 smm^{-2}) is often used in the brain [135, 172, 176, 208, 250]. It also suggests that the microvasculature is not the only source of f, since estimates with least bias are higher than what is generally considered to be representative of the microvascular network in literature (e.g. Le Bihan et al. [14] state the value is around 5% in GM and 2% in WM). Larger vessels could be contributing [311], or the glymphatic system [154], or perhaps segmentation errors or partial volume effects mean the CSF is contributing. Perhaps the use of multiple compartments as suggested by Fournet et al. [131], would be useful in measuring these additional effects.

In simulated data, we did not include diffusion-time dependence in f or D. However, fitting was run as described in Section 5.6.3: estimating f and D for each diffusion-time to subtract the extravascular signal from the total normalised DW-MRI signal to isolate the intravascular signal. We demonstrate that, using this method, the maximum variance

between diffusion-times in f is 3.4% at SNR values >500, and that bias in f decreases with increasing diffusion-time. The change between the two extremes of diffusion-time in in-vivo GM data (Figure 5.2) is approximately 8% and f decreases with diffusion-time. Thus, the diffusion-time dependence in f is likely to be a real effect. The maximum variance in D is 0.7% at SNR values >500, and bias reduced with increasing diffusion-time. The largest change in D in GM (Figure 5.2) is approximately 0.6%. Hence, effects of the two-step fit could explain the variance in D.

The addition of c does not seem to affect model fitting, particularly at high SNR where the curves with and without c are very similar, if not equivalent. For the one-step fit at low SNR (<100), the variability is increased slightly in f and D with the inclusion of c. However, variability and bias reduces in D^* indicating improved characterisation of the intravascular compartment at low SNR. For VA model parameters, the curves with and without c are almost completely aligned, despite intercept values of up to 0.6. This indicates that c can be used without any penalty to vascular parameters (no adverse effects on bias or variability). Although, perhaps c could be excluded since fitting appears similar. The use of c in simulations may not entirely reflect what occurs in-vivo where b-values are affected by imaging gradients, and thus are not the user input values, but effective values. These effective b-values mean data is incorrectly characterised when using input b-values to fit data. Bias could be introduced which propagates through each step of analysis. Thus simulated and true estimates may differ. However, in the case of no real intercept, there is no bias introduced by this term. If the two-step fitting method does introduce bias into model fitting, which does seem to be the case (Figure A5 and A6) particularly at low SNR, then correcting for the intercept does not appear to affect parameters largely.

The one-step fit outperforms the two-step fit for every parameter from the IVIM diffusive and VA models, with exception of f and D at low SNR (< 200). This is surprising considering most IVIM literature uses the two-step fit to negate errors in the one-step fit (erroneous values or low precision) [134, 135, 158]. Voxel-wise fitting of the IVIM signal would use SNR value at lower levels (< 200), so it perhaps not so surprising that some literature supports this. Meeus et al. [158] perform similar simulations and state the the accuracy of one-step and two-step diffusive IVIM parameters was similar, but the number of outliers was higher and reproducibility lower for the one-step fit. Wang et al. [309] also show no significant differences in one-step and two-step IVIM diffusive parameters. For diffusive IVIM parameters, the bias is quite small in f and D ($\times 0.83$ f, $\times 1.03$ D), so perhaps this would agree with the studies by Meeus et al. [158] and Wang et al. [309]. Although, bias in D^* is higher ($\times 1.3$ D^*) which might reflect our use of higher b-value thresholds and D_b in model fitting, which yields lower values of D^* that might be more susceptible to error. This bias in D^* may affect fitting of the VA model if not consistent across all diffusion-times. If bias is consistent, then one might expect an equal amount of

bias in the VA model parameters. The effect of diffusion-time on bias in D^* should be investigated.

Using the two-step fit in VA parameters results in overestimated v (by a factor of 2) and underestimated T_0 (by a factor of 0.7) at the highest SNR shown. The bias in v and T_0 means structural parameters derived using the measures will also be biased. Estimates of l derived using $l = 2vT_0$ would be overestimated by a factor of approximately 1.4 (at highest SNR). Using v with D^* to estimate l ($D^* = vl/6$) would produce values which were underestimated by a factor of approximately 0.65. However, we find the parameter estimates from in-vivo data using the two methods are consistent (Chapters 6 and 7) which disagrees with this simulation result. We also find that estimates of l in rat data, which use v from the VA model, have low bias when compared to cast data. Estimates of v also seem to compare reasonably well with literature (see Section 5.8). Halving the values presented in Table 5.2 would compare less favourably with literature.

At the highest SNR, simulated standard deviation (SD) disagrees with in-vivo CoV. The SD of v is 0.8 times the true value. CoV for v is 23.2% in grey matter (Table 5.3 in Chapter 5) . The SD of T_0 is 0.37 times the true value and CoV is 30.8%. This suggests the SNR in simulations isn't high enough, which would agree with calculated SNR levels and our cap of 1000. The CoV for f, D and D^* shown in Chapter 7 suggests that SNR levels for GM are between 350 and 600 (matching to standard deviation on plots). Lower SNR occurs at higher b-values since diffusion-weighting, and thus signal attenuation, is increased.

Interestingly, parameters estimated using the one-step fit in in-vivo data follow a different pattern to simulated data. Using a one-step fit without assuming a diffusion-time dependence in f and D (Model 1) gives higher estimates of v than the two-step fit in GM (v=3.03± 1.0 versus v=1.33± 0.17 mms^{-1}) and lower estimates of T_0 (T_0=1.31 ± 2.0 versus T_0=6.29 ± 3.8 ms) in contrast to the simulated data which showed higher estimates with the two-step fit. Using a one-step fit that assumes some diffusion-time dependence in f (and D) produces estimates of v and T_0 which are in line with two-step estimates (v=1.65± 1.15 (2) and v=1.20 ± 0.35 (3) versus v=1.33± 0.17 mms^{-1}; T_0=8.66 ± 9.0 (2) and T_0=5.84 ± 2.5 (3) versus T_0=6.29 ± 3.8 ms). Model 3 results agree best with simulations for v, but the difference is much lower than simulations predict at 11%. In any case, results for T_0 disagree with simulations. f and D from Model 3 do not agree well with literature. These values drove our decision to chose the two-step fit in human data, along with the desire to be consistent with previous work (Chapter 4).

In in-vivo data, outliers were removed which were outside of three median absolute deviations of the median. For two-step data presented in Table A2, 30% of data were classed as outliers for v in GM, and none for T_0. These outliers would have increased the mean value since all were greater than the mean. If outliers are removed in two-step

simulation data presented (approximately 20% of data points were classed as outliers), then at SNR 1000, the value becomes 1.4 times the true value. With the pseudo-diffusion coefficient being approximately 1.3 times the true value at this high SNR, this might explain most of the bias in v. Additional variability could be explained by varying D^* with diffusion-time.

The work presented in this Chapter largely suggests that the choices made with regards to deriving parameter estimates are appropriate. However, it is clear from the data presented that further work is needed to clarify the effects of the one-step and two-step fitting methods in IVIM parameter estimation. Bias and precision with different diffusion-time dependencies in f and D should be assessed with simulations. The sensitivity of bias and precision to parameter magnitude should also be assessed.

Bibliography

[1] Berislav V. Zlokovic. Neurovascular pathways to neurodegeneration in Alzheimer's disease and other disorders. *Nature Reviews Neuroscience*, 12(12), dec 2011.

[2] Berislav V. Zlokovic. The Blood-Brain Barrier in Health and Chronic Neurodegenerative Disorders. *Neuron*, 57(2):178–201, jan 2008.

[3] Melanie D. Sweeney, Kassandra Kisler, Axel Montagne, Arthur W. Toga, and Berislav V. Zlokovic. The role of brain vasculature in neurodegenerative disorders. *Nature Neuroscience*, 21(10):1318–1331, oct 2018.

[4] Eszter Farkas and Paul G.M. Luiten. Cerebral microvascular pathology in aging and Alzheimer's disease. *Progress in Neurobiology*, 64(6):575–611, 2001.

[5] Luc Buée, Patrick R. Hof, and André Delacourte. Brain microvascular changes in Alzheimer's disease and other dementias. *Annals of the New York Academy of Sciences*, 826:7–24, 1997.

[6] Stavros J. Baloyannis and Ioannis S. Baloyannis. The vascular factor in Alzheimer's disease: A study in Golgi technique and electron microscopy. *Journal of the Neurological Sciences*, 322(1-2):117–121, nov 2012.

[7] Joanna M. Wardlaw, Colin Smith, and Martin Dichgans. Small vessel disease: mechanisms and clinical implications. *The Lancet Neurology*, 18(7):684–696, 2019.

[8] Donald W. McRobbie, Elizabeth A. Moore, and Martin J. Graves. *MRI from picture to proton*. Cambridge University Press, 2nd edition, 2006.

[9] Paul Suetens. *Fundamentals of medical imaging*. Cambridge University Press, 2nd edition, 2009.

[10] Peter J. Basser and Evren Özarslan. Introduction to diffusion MR. In *Diffusion MRI*, pages 2–10. Elsevier Inc., 2009.

[11] Lei Tang and Xiaohong Joe Zhou. Diffusion MRI of cancer: From low to high b-values. *Journal of Magnetic Resonance Imaging*, 49(1):23–40, jan 2019.

[12] Marta Drake-Pérez, Jose Boto, Aikaterini Fitsiori, Karl Lovblad, and Maria Isabel Vargas. Clinical applications of diffusion weighted imaging in neuroradiology. *Insights into Imaging*, 9(4):535–547, aug 2018.

[13] Christian Federau. Intravoxel incoherent motion MRI as a means to measure in vivo perfusion: A review of the evidence. *NMR in Biomedicine*, 30(11):e3780, nov 2017.

[14] D. Le Bihan, E. Breton, D. Lallemand, M. L. Aubin, J. Vignaud, and M. Laval-Jeantet. Separation of diffusion and perfusion in intravoxel incoherent motion MR imaging. *Radiology*, 168(2):497–505, 1988.

[15] Adam J. Schwarz, Anne Danckaert, Torsten Reese, Alessandro Gozzi, George Paxinos, Charles Watson, Emilio V. Merlo-Pich, and Angelo Bifone. A stereotaxic MRI template set for the rat brain with tissue class distribution maps and co-registered anatomical atlas: Application to pharmacological MRI. *NeuroImage*, 32(2):538–550, aug 2006.

[16] Olivier Reynaud, Kerryanne Veronica Winters, Dung Minh Hoang, Youssef Zaim Wadghiri, Dmitry S. Novikov, and Sungheon Gene Kim. Pulsed and oscillating gradient MRI for assessment of cell size and extracellular space (POMACE) in mouse gliomas. *NMR in Biomedicine*, 29(10):1350–1363, oct 2016.

[17] Joanna M Wardlaw, Eric E Smith, Geert J Biessels, Charlotte Cordonnier, Franz Fazekas, Richard Frayne, Richard I Lindley, John T O'Brien, Frederik Barkhof, Oscar R Benavente, Sandra E Black, Carol Brayne, Monique Breteler, Hugues Chabriat, Charles DeCarli, Frank-Erik de Leeuw, Fergus Doubal, Marco Duering, Nick C Fox, Steven Greenberg, Vladimir Hachinski, Ingo Kilimann, Vincent Mok, Robert van Oostenbrugge, Leonardo Pantoni, Oliver Speck, Blossom C M Stephan, Stefan Teipel, Anand Viswanathan, David Werring, Christopher Chen, Colin Smith, Mark van Buchem, Bo Norrving, Philip B Gorelick, and Martin Dichgans. Neuroimaging standards for research into small vessel disease and its contribution to ageing and neurodegeneration. *The Lancet Neurology*, 12(8):822–838, aug 2013.

[18] Costantino Iadecola. The overlap between neurodegenerative and vascular factors in the pathogenesis of dementia. *Acta Neuropathologica*, 120(3):287–296, sep 2010.

[19] Robert D. Bell and Berislav V. Zlokovic. Neurovascular mechanisms and blood-brain barrier disorder in Alzheimer's disease. *Acta Neuropathologica*, 118(1):103–113, 2009.

[20] Rune B. Nielsen, Peter Parbo, Rola Ismail, Rikke Dalby, Anna Tietze, Hans Brændgaard, Hanne Gottrup, David J. Brooks, Leif Østergaard, and Simon F. Eskildsen. Impaired perfusion and capillary dysfunction in prodromal Alzheimer's disease. *Alzheimer's & Dementia: Diagnosis, Assessment & Disease Monitoring*, 12(1), jan 2020.

[21] Amy R. Nelson, Melanie D. Sweeney, Abhay P. Sagare, and Berislav V. Zlokovic. Neurovascular dysfunction and neurodegeneration in dementia and Alzheimer's disease. *Biochimica et Biophysica Acta (BBA) - Molecular Basis of Disease*, 1862(5):887–900, may 2016.

[22] Leif Østergaard, Rasmus Aamand, Eugenio Gutiérrez-Jiménez, Yi Ching L. Ho, Jakob U. Blicher, Søren M. Madsen, Kartheeban Nagenthiraja, Rikke B. Dalby, Kim R. Drasbek, Arne Møller, Hans Brændgaard, Kim Mouridsen, Sune N. Jespersen, Morten S. Jensen, and Mark J. West. The capillary dysfunction hypothesis of Alzheimer's disease. *Neurobiology of Aging*, 34(4):1018–1031, apr 2013.

[23] Sune N. Jespersen and Leif Østergaard. The roles of cerebral blood flow, capillary transit time heterogeneity, and oxygen tension in brain oxygenation and metabolism. *Journal of Cerebral Blood Flow and Metabolism*, 32(2):264–277, feb 2012.

[24] Leif Østergaard, A. Gregory Sorensen, David A. Chesler, Robert M. Weisskoff, Walter J. Koroshetz, Ona Wu, Carsten Gyldensted, and Bruce R. Rosen. Combined Diffusion-Weighted and Perfusion-Weighted Flow Heterogeneity Magnetic Resonance Imaging in Acute Stroke. *Stroke*, 31(5):1097–1103, may 2000.

[25] Leif Østergaard, Thorbjørn S. Engedal, Rasmus Aamand, Ronni Mikkelsen, Nina K. Iversen, Maryam Anzabi, Erhard T. Næss-Schmidt, Kim R. Drasbek, Vibeke Bay, Jakob U. Blicher, Anna Tietze, Irene K. Mikkelsen, Brian Hansen, Sune N. Jespersen, Niels Juul, Jens C.H. Sørensen, and Mads Rasmussen. Capillary transit time heterogeneity and flow-metabolism coupling after traumatic brain injury. *Journal of Cerebral Blood Flow and Metabolism*, 34(10):1585–1598, oct 2014.

[26] Tetsuo Hashimura, Takemi Kimura, and Taihei Miyakawa. Morphological Changes of Blood Vessels in the Brain with Alzheimer's Disease. Technical Report 3, 1991.

[27] Merideth A. Addicott, Lucie L. Yang, Ann M. Peiffer, Luke R. Burnett, Jonathan H. Burdette, Michael Y. Chen, Satoru Hayasaka, Robert A. Kraft, Joseph A. Maldjian, and Paul J. Laurienti. The effect of daily caffeine use on cerebral blood flow: How much caffeine can we tolerate? *Human Brain Mapping*, 30(10):3102–3114, oct 2009.

[28] Otto M Henriksen, Christina Kruuse, Jes Olesen, Lars T Jensen, Henrik BW Larsson, Steffen Birk, Jakob M Hansen, Troels Wienecke, and Egill Rostrup. Sources of Variability of Resting Cerebral Blood Flow in Healthy Subjects: A Study Using 133 Xe SPECT Measurements. *Journal of Cerebral Blood Flow & Metabolism*, 33(5):787–792, may 2013.

[29] Jin Woo Choi and Won-Jin Moon. Gadolinium Deposition in the Brain: Current Updates. *Korean Journal of Radiology*, 20(1):134, 2019.

[30] Mami Iima and Denis Le Bihan. Clinical intravoxel incoherent motion and diffusion MR imaging: Past, present, and future. *Radiology*, 278(1):13–32, jan 2016.

[31] Denis Le Bihan and Mami Iima. Diffusion Magnetic Resonance Imaging: What Water Tells Us about Biological Tissues. *PLOS Biology*, 13(7):e1002203, jul 2015.

[32] Denis Le Bihan. Apparent diffusion coefficient and beyond : What diffusion mr imaging can tell us about tissue structure. *Radiology*, 268(2):318–322, aug 2013.

[33] Richard P. Kennan, Jia Hong Gao, Jianhui Zhong, and John C. Gore. A General Model of Microcirculatory Blood Flow Effects in Gradient Sensitized MRI. *Medical Physics*, 21(4):539–545, 1994.

[34] Hui Zhang, Torben Schneider, Claudia A. Wheeler-Kingshott, and Daniel C. Alexander. NODDI: Practical in vivo neurite orientation dispersion and density imaging of the human brain. *NeuroImage*, 61(4):1000–1016, jul 2012.

[35] Andreas Wetscherek, Bram Stieltjes, and Frederik Bernd Laun. Flow-compensated intravoxel incoherent motion diffusion imaging. *Magnetic Resonance in Medicine*, 74(2):410–419, aug 2015.

[36] Asamoah Bosomtwi, Michael Chopp, Li Zhang, Zheng Gang Zhang, Mei Lu, and Quan Jiang. Mean microvessel segment length and radius after embolic stroke: Comparison of magnetic resonance imaging (MRI) and laser scanning confocal microscopy (LSCM). *Brain Research*, 1381:217–227, mar 2011.

[37] Helene Girouard and Costantino Iadecola. Neurovascular coupling in the normal brain and in hypertension, stroke, and Alzheimer disease. *Journal of Applied Physiology*, 100(1):328–335, jan 2006.

[38] Richard Daneman and Alexandre Prat. The Blood–Brain Barrier. *Cold Spring Harbor Perspectives in Biology*, 7(1):a020412, jan 2015.

[39] Erin D. Ozturk and Can Ozan Tan. Human cerebrovascular function in health and disease: insights from integrative approaches. *Journal of Physiological Anthropology*, 37(1):4, dec 2018.

[40] Michael A. Moskowitz, Eng H. Lo, and Costantino Iadecola. The Science of Stroke: Mechanisms in Search of Treatments. *Neuron*, 67(2):181–198, jul 2010.

[41] Gordon W. Blair, Maria Valdez Hernandez, Michael J. Thrippleton, Fergus N. Doubal, and Joanna M. Wardlaw. Advanced Neuroimaging of Cerebral Small Vessel Disease. *Current Treatment Options in Cardiovascular Medicine*, 19(7), 2017.

[42] Viviana Frantellizzi, Arianna Pani, Maria Ricci, Nicoletta Locuratolo, Francesco Fattapposta, and Giuseppe De Vincentis. Neuroimaging in Vascular Cognitive Impairment and Dementia: A Systematic Review. *Journal of Alzheimer's Disease*, 73(4):1279–1294, feb 2020.

[43] Axel Montagne, Daniel A. Nation, Judy Pa, Melanie D. Sweeney, Arthur W. Toga, and Berislav V. Zlokovic. Brain imaging of neurovascular dysfunction in Alzheimer's disease. *Acta Neuropathologica*, 131(5):687–707, may 2016.

[44] Michael J. Thrippleton, Walter H. Backes, Steven Sourbron, Michael Ingrisch, Matthias J.P. van Osch, Martin Dichgans, Franz Fazekas, Stefan Ropele, Richard Frayne, Robert J. van Oostenbrugge, Eric E. Smith, and Joanna M. Wardlaw. Quantifying blood-brain barrier leakage in small vessel disease: Review and consensus recommendations. *Alzheimer's & Dementia*, 15(6):840–858, jun 2019.

[45] Leonardo Pantoni. Cerebral small vessel disease: from pathogenesis and clinical characteristics to therapeutic challenges. *The Lancet Neurology*, 9(7):689–701, jul 2010.

[46] Sven Haller, Enikö Kövari, François R Herrmann, Victor Cuvinciuc, Ann-Marie Tomm, Gilbert B Zulian, Karl-Olof Lovblad, Panteleimon Giannakopoulos, and Constantin Bouras. Do brain T2/FLAIR white matter hyperintensities correspond to myelin loss in normal aging? A radiologic-neuropathologic correlation study. *Acta Neuropathologica Communications*, 1(1):14, dec 2013.

[47] Joanna M. Wardlaw, Maria C. Valdés Hernández, and Susana Muñoz-Maniega. What are White Matter Hyperintensities Made of? *Journal of the American Heart Association*, 4(6), jun 2015.

[48] Dixon M. Moody, William R. Brown, Venkata R. Challa, Hani S. Ghazi-Birry, and David M. Reboussin. Cerebral microvascular alterations in aging, leukoaraiosis, and Alzheimer's disease. *Annals of the New York Academy of Sciences*, 826:103–116, 1997.

[49] Michelle R. Caunca, Andres De Leon-Benedetti, Lawrence Latour, Richard Leigh, and Clinton B. Wright. Neuroimaging of Cerebral Small Vessel Disease and Age-Related Cognitive Changes. *Frontiers in Aging Neuroscience*, 11(145), jun 2019.

[50] Yulu Shi and Joanna M. Wardlaw. Update on cerebral small vessel disease: A dynamic whole-brain disease. *Stroke and Vascular Neurology*, 1(3):83–92, 2016.

[51] K Matsushita, Y Kuriyama, K Nagatsuka, M Nakamura, T Sawada, and T Omae. Periventricular white matter lucency and cerebral blood flow autoregulation in hypertensive patients. *Hypertension*, 23(5):565–568, may 1994.

[52] C L Franke, J C van Swieten, and J van Gijn. Residual lesions on computed tomography after intracerebral hemorrhage. *Stroke*, 22(12):1530–1533, dec 1991.

[53] Samuel Groeschel, Wui Khean Chong, Robert Surtees, and Folker Hanefeld. Virchow-Robin spaces on magnetic resonance images: normative data, their dilatation, and a review of the literature. *Neuroradiology*, 48(10):745–754, oct 2006.

[54] A. Shoamanesh, C.S. Kwok, and O. Benavente. Cerebral Microbleeds: Histopathological Correlation of Neuroimaging. *Cerebrovascular Diseases*, 32(6):528–534, 2011.

[55] Leif Østergaard, Thorbjørn S. Engedal, Fiona Moreton, Mikkel B. Hansen, Joanna M. Wardlaw, Turgay Dalkara, Hugh S. Markus, and Keith W. Muir. Cerebral small vessel disease: Capillary pathways to stroke and cognitive decline. *Journal of Cerebral Blood Flow and Metabolism*, 36(2):302–325, feb 2016.

[56] Tiemei Li, Yinong Huang, Wei Cai, Xiaodong Chen, Xuejiao Men, Tingting Lu, Aiming Wu, and Zhengqi Lu. Age-related cerebral small vessel disease and inflammaging. *Cell Death & Disease*, 11(10):932, oct 2020.

[57] Steven M. Greenberg, Brian J. Bacskai, Mar Hernandez-Guillamon, Jeremy Pruzin, Reisa Sperling, and Susanne J. van Veluw. Cerebral amyloid angiopathy and Alzheimer disease — one peptide, two pathways. *Nature Reviews Neurology*, 16(1):30–42, jan 2020.

[58] W. R. Brown and C. R. Thore. Review: Cerebral microvascular pathology in ageing and neurodegeneration. *Neuropathology and Applied Neurobiology*, 37(1):56–74, feb 2011.

[59] J. Jean Chen, H. Diana Rosas, and David H. Salat. Age-associated reductions in cerebral blood flow are independent from regional atrophy. *NeuroImage*, 55(2):468–478, mar 2011.

[60] Francesco Amenta, Daniela Cavallotti, Miguel Del Valle, Maurizio Mancini, Francisco Javier Naves, JoséAntonio Vega, and Yong Chun Zeng. Age-related changes

in brain microanatomy: Sensitivity to treatment with the dihydropyridine calcium channel blocker darodipine (PY 108-068). *Brain Research Bulletin*, 36(5):453–460, 1995.

[61] William A. Banks, May J. Reed, Aric F. Logsdon, Elizabeth M. Rhea, and Michelle A. Erickson. Healthy aging and the blood–brain barrier. *Nature Aging*, 1(3):243–254, mar 2021.

[62] Axel Montagne, Samuel R. Barnes, Melanie D. Sweeney, Matthew R. Halliday, Abhay P. Sagare, Zhen Zhao, Arthur W. Toga, Russell E. Jacobs, Collin Y. Liu, Lilyana Amezcua, Michael G. Harrington, Helena C. Chui, Meng Law, and Berislav V. Zlokovic. Blood-Brain Barrier Breakdown in the Aging Human Hippocampus. *Neuron*, 85(2):296–302, jan 2015.

[63] Inge C. M. Verheggen, Joost J. A. de Jong, Martin P. J. van Boxtel, Ed H. B. M. Gronenschild, Walter M. Palm, Alida A. Postma, Jacobus F. A. Jansen, Frans R. J. Verhey, and Walter H. Backes. Increase in blood–brain barrier leakage in healthy, older adults. *GeroScience*, 42(4):1183–1193, aug 2020.

[64] Yolanda Ohene, Ian F. Harrison, Phoebe G. Evans, David L. Thomas, Mark F. Lythgoe, and Jack A. Wells. Increased blood–brain barrier permeability to water in the aging brain detected using noninvasive multi-TE ASL MRI. *Magnetic Resonance in Medicine*, 85(1):326–333, jan 2021.

[65] William E. Sonntag, Delrae M. Eckman, Jeremy Ingraham, and David R. Riddle. Regulation of Cerebrovascular Aging. In David R. Riddle, editor, *Brain Aging: Models, Methods and Mechanisms*, chapter 12, pages 279–304. CRC Press, oct 2019.

[66] Qiang Liu, Wei-Jye Lin, and Yamei Tang. New Insights into the Dysfunctions of Pericytes and Neurovascular Units in Neurodegenerative Diseases. *Neuroscience Bulletin*, 36(12):1570–1572, dec 2020.

[67] Raj N. Kalaria. Vascular basis for brain degeneration: Faltering controls and risk factors for dementia. *Nutrition Reviews*, 68(SUPPL. 2):S74–S87, 2010.

[68] Andrew C. Yang, Marc Y. Stevens, Michelle B. Chen, Davis P. Lee, Daniel Stähli, David Gate, Kévin Contrepois, Winnie Chen, Tal Iram, Lichao Zhang, Ryan T. Vest, Aisling Chaney, Benoit Lehallier, Niclas Olsson, Haley du Bois, Ryan Hsieh, Haley C. Cropper, Daniela Berdnik, Lulin Li, Elizabeth Y. Wang, Gavin M. Traber, Carolyn R. Bertozzi, Jian Luo, Michael P. Snyder, Joshua E. Elias, Stephen R. Quake, Michelle L. James, and Tony Wyss-Coray. Physiological blood–brain transport is impaired with age by a shift in transcytosis. *Nature*, 583(7816):425–430, jul 2020.

[69] Şefik Evren Erdener and Turgay Dalkara. Small vessels are a big problem in neurodegeneration and neuroprotection. *Frontiers in Neurology*, 10(AUG), 2019.

[70] A. Kapasi and J. A. Schneider. Vascular contributions to cognitive impairment, clinical Alzheimer's disease, and dementia in older persons. *Biochimica et Biophysica Acta - Molecular Basis of Disease*, 1862(5):878–886, may 2016.

[71] Sandrine Andrieu, Nicola Coley, Simon Lovestone, Paul S. Aisen, and Bruno Vellas. Prevention of sporadic Alzheimer's disease: Lessons learned from clinical trials and future directions. *The Lancet Neurology*, 14(9):926–944, sep 2015.

[72] Sarah F Ackley, Scott C Zimmerman, Willa D Brenowitz, Eric J Tchetgen Tchetgen, Audra L Gold, Jennifer J Manly, Elizabeth Rose Mayeda, Teresa J Filshtein, Melinda C Power, Fanny M Elahi, Adam M Brickman, and M Maria Glymour. Effect of reductions in amyloid levels on cognitive change in randomized trials: instrumental variable meta-analysis. *BMJ*, page n156, feb 2021.

[73] Malee S. Fernando and Paul G. Ince. Vascular pathologies and cognition in a population-based cohort of elderly people. *Journal of the Neurological Sciences*, 226(1-2):13–17, nov 2004.

[74] Jon B. Toledo, Steven E. Arnold, Kevin Raible, Johannes Brettschneider, Sharon X. Xie, Murray Grossman, Sarah E. Monsell, Walter A. Kukull, and John Q. Trojanowski. Contribution of cerebrovascular disease in autopsy confirmed neurodegenerative disease cases in the National Alzheimer's Coordinating Centre. *Brain*, 136(9):2697–2706, 2013.

[75] Zoe Arvanitakis, Ana W Capuano, Sue E Leurgans, David A Bennett, and Julie A Schneider. Relation of cerebral vessel disease to Alzheimer's disease dementia and cognitive function in elderly people: a cross-sectional study. *The Lancet Neurology*, 15(9):934–943, aug 2016.

[76] Leif Østergaard, Sune Nørhøj Jespersen, Thorbjørn Engedahl, Eugenio Gutiérrez Jiménez, Mahmoud Ashkanian, Mikkel Bo Hansen, Simon Eskildsen, and Kim Mouridsen. Capillary Dysfunction: Its Detection and Causative Role in Dementias and Stroke. *Current Neurology and Neuroscience Reports*, 15(6), jun 2015.

[77] Costantino Iadecola. Neurovascular regulation in the normal brain and in Alzheimer's disease. *Nature Reviews Neuroscience*, 5(5):347–360, 2004.

[78] Ruiqing Ni, Markus Rudin, and Jan Klohs. Cortical hypoperfusion and reduced cerebral metabolic rate of oxygen in the arcAβ mouse model of Alzheimer's disease. *Photoacoustics*, 10:38–47, jun 2018.

[79] Dengrong Jiang, Zixuan Lin, Peiying Liu, Sandeepa Sur, Cuimei Xu, Kaisha Hazel, George Pottanat, Jacqueline Darrow, Jay J. Pillai, Sevil Yasar, Paul Rosenberg, Abhay Moghekar, Marilyn Albert, and Hanzhang Lu. Brain Oxygen Extraction Is Differentially Altered by Alzheimer's and Vascular Diseases. *Journal of Magnetic Resonance Imaging*, 52(6):1829–1837, dec 2020.

[80] Christina E Wierenga, Chelsea C Hays, and Zvinka Z Zlatar. Cerebral blood flow measured by arterial spin labeling MRI as a preclinical marker of alzheimer's disease. *Journal of Alzheimer's Disease*, 42:S411—-S419, 2014.

[81] Harm J. van de Haar, Jacobus F.A. Jansen, Matthias J.P. van Osch, Mark A. van Buchem, Majon Muller, Sau May Wong, Paul A.M. Hofman, Saartje Burgmans,

Frans R.J. Verhey, and Walter H. Backes. Neurovascular unit impairment in early Alzheimer's disease measured with magnetic resonance imaging. *Neurobiology of Aging*, 45:190–196, sep 2016.

[82] Weiying Dai, Oscar L. Lopez, Owen T. Carmichael, James T. Becker, Lewis H. Kuller, and H. Michael Gach. Mild Cognitive Impairment and Alzheimer Disease: Patterns of Altered Cerebral Blood Flow at MR Imaging. *Radiology*, 250(3):856–866, mar 2009.

[83] Rune B. Nielsen, Lærke Egefjord, Hugo Angleys, Kim Mouridsen, Michael Gejl, Arne Møller, Birgitte Brock, Hans Brændgaard, Hanne Gottrup, Jørgen Rungby, Simon F. Eskildsen, and Leif Østergaard. Capillary dysfunction is associated with symptom severity and neurodegeneration in Alzheimer's disease. *Alzheimer's and Dementia*, 13(10):1143–1153, oct 2017.

[84] Eric E. Smith and Steven M. Greenberg. β-Amyloid, blood vessels, and brain function. *Stroke*, 40(7):2601–2606, jul 2009.

[85] Y. Iturria-Medina, R. C. Sotero, P. J. Toussaint, J. M. Mateos-Pérez, and A. C. Evans. Early role of vascular dysregulation on late-onset Alzheimer's disease based on multifactorial data-driven analysis. *Nature Communications*, 7(1):11934, sep 2016.

[86] Anna E. Leeuwis, Marije R. Benedictus, Joost P.A. Kuijer, Maja A.A. Binnewijzend, Astrid M. Hooghiemstra, Sander C.J. Verfaillie, Teddy Koene, Philip Scheltens, Frederik Barkhof, Niels D. Prins, and Wiesje M. van der Flier. Lower cerebral blood flow is associated with impairment in multiple cognitive domains in Alzheimer's disease. *Alzheimer's & Dementia*, 13(5):531–540, may 2017.

[87] Ross Nortley, Nils Korte, Pablo Izquierdo, Chanawee Hirunpattarasilp, Anusha Mishra, Zane Jaunmuktane, Vasiliki Kyrargyri, Thomas Pfeiffer, Lila Khennouf, Christian Madry, Hui Gong, Angela Richard-Loendt, Wenhui Huang, Takashi Saito, Takaomi C. Saido, Sebastian Brandner, Huma Sethi, and David Attwell. Amyloid b oligomers constrict human capillaries in Alzheimer's disease via signaling to pericytes. *Science*, 365(6450), jul 2019.

[88] Aisha Abeelen, Joep Lagro, Arenda Beek, and Jurgen Claassen. Impaired Cerebral Autoregulation and Vasomotor Reactivity in Sporadic Alzheimer's Disease. *Current Alzheimer Research*, 11(1):11–17, jan 2014.

[89] S A Rombouts, F Barkhof, D J Veltman, W C Machielsen, M P Witter, M A Bierlaagh, R H Lazeron, J Valk, and P Scheltens. Functional MR imaging in Alzheimer's disease during memory encoding. *AJNR. American journal of neuroradiology*, 21(10):1869–75, 2000.

[90] Daniel A. Nation, Melanie D. Sweeney, Axel Montagne, Abhay P. Sagare, Lina M. D'Orazio, Maricarmen Pachicano, Farshid Sepehrband, Amy R. Nelson, David P. Buennagel, Michael G. Harrington, Tammie L. S. Benzinger, Anne M. Fagan, John M. Ringman, Lon S. Schneider, John C. Morris, Helena C. Chui, Meng Law, Arthur W. Toga, and Berislav V. Zlokovic. Blood–brain barrier breakdown is an early biomarker of human cognitive dysfunction. *Nature Medicine*, 25(2):270–276, feb 2019.

[91] Ben R. Dickie, Matthias Vandesquille, José Ulloa, Hervé Boutin, Laura M. Parkes, and Geoff J.M. Parker. Water-exchange MRI detects subtle blood-brain barrier breakdown in Alzheimer's disease rats. *NeuroImage*, 184(May 2018):349–358, 2019.

[92] Sara Shams and Lars-Olof Wahlund. Cerebral microbleeds as a biomarker in Alzheimer's disease? A review in the field. *Biomarkers in Medicine*, 10(1):9–18, jan 2016.

[93] Sophie M. Heringa, Yael D. Reijmer, Alexander Leemans, Huiberdina L. Koek, L. Jaap Kappelle, and Geert Jan Biessels. Multiple Microbleeds are Related to Cerebral Network Disruptions in Patients with Early Alzheimer's Disease. *Journal of Alzheimer's Disease*, 38(1):211–221, oct 2013.

[94] J C de la Torre and G B Stefano. Full-length review Evidence that Alzheimer's disease is a microvascular disorder: the role of constitutive nitric oxide. *Brain Research Reviews*, 34:119–136, 2000.

[95] Trevor Hardigan, Rebecca Ward, and Adviye Ergul. Cerebrovascular complications of diabetes: focus on cognitive dysfunction. *Clinical Science*, 130(20):1807–1822, oct 2016.

[96] Dariusz Gąsecki, Mariusz Kwarciany, Walenty Nyka, and Krzysztof Narkiewicz. Hypertension, brain damage and cognitive decline. *Current Hypertension Reports*, 15(6):547–558, 2013.

[97] Costantino Iadecola and Robin L. Davisson. Hypertension and Cerebrovascular Dysfunction. *Cell Metabolism*, 7(6):476–484, jun 2008.

[98] Costantino Iadecola. Hypertension and dementia. *Hypertension*, 64(1):3–5, 2014.

[99] Costantino Iadecola and Rebecca F. Gottesman. Neurovascular and Cognitive Dysfunction in Hypertension. *Circulation Research*, 124(7):1025–1044, mar 2019.

[100] Paulo W. Pires, Carla M. Dams Ramos, Nusrat Matin, and Anne M. Dorrance. The effects of hypertension on the cerebral circulation. *American Journal of Physiology-Heart and Circulatory Physiology*, 304(12):H1598–H1614, jun 2013.

[101] J. Mayet and A. Hughes. Cardiac and vascular pathophysiology in hypertension. *Heart*, 89(9):1104–1109, sep 2003.

[102] Leila Buttler, Maria T. Jordão, Matheus G. Fragas, Adriana Ruggeri, Alexandre Ceroni, and Lisete C. Michelini. Maintenance of Blood-Brain Barrier Integrity in Hypertension: A Novel Benefit of Exercise Training for Autonomic Control. *Frontiers in Physiology*, 8, dec 2017.

[103] J. R. Jennings, M. F. Muldoon, C. Ryan, J. C. Price, P. Greer, K. Sutton-Tyrrell, F. M. van der Veen, and C. C. Meltzer. Reduced cerebral blood flow response and compensation among patients with untreated hypertension. *Neurology*, 64(8):1358–1365, apr 2005.

[104] Hai Chao Han. Twisted blood vessels: Symptoms, etiology and biomechanical mechanisms. *Journal of Vascular Research*, 49(3):185–197, may 2012.

[105] R. Humar, L. Zimmerli, and E. Battegay. Angiogenesis and hypertension: An update. *Journal of Human Hypertension*, 23(12):773–782, 2009.

[106] W Todd Cade. Diabetes-Related Microvascular and Macrovascular Diseases in the Physical Therapy Setting. *Physical Therapy*, 88(11):1322–1335, nov 2008.

[107] Annika Armulik, Guillem Genové, Maarja Mäe, Maya H. Nisancioglu, Elisabet Wallgard, Colin Niaudet, Liqun He, Jenny Norlin, Per Lindblom, Karin Strittmatter, Bengt R. Johansson, and Christer Betsholtz. Pericytes regulate the blood–brain barrier. *Nature*, 468(7323):557–561, nov 2010.

[108] B. van Harten, F.-E. de Leeuw, H. C. Weinstein, P. Scheltens, and G. J. Biessels. Brain Imaging in Patients With Diabetes: A systematic review. *Diabetes Care*, 29(11):2539–2548, nov 2006.

[109] B. Fulesdi, M. Limburg, D. Bereczki, R. P. J. Michels, G. Neuwirth, D. Legemate, A. Valikovics, and L. Csiba. Impairment of Cerebrovascular Reactivity in Long-Term Type 1 Diabetes. *Diabetes*, 46(11):1840–1845, nov 1997.

[110] B Keymeulen, A Jacobs, K de Metz, C de Sadeleer, A Bossuyt, and G Somers. Regional cerebral hypoperfusion in long-term type 1 (insulin-dependent) diabetic patients: relation to hypoglycaemic events. *Nuclear Medicine Communications*, 16(1):10–16, 1995.

[111] D. Last, D. C. Alsop, A. M. Abduljalil, R. P. Marquis, C. de Bazelaire, K. Hu, J. Cavallerano, and V. Novak. Global and Regional Effects of Type 2 Diabetes on Brain Tissue Volumes and Cerebral Vasoreactivity. *Diabetes Care*, 30(5):1193–1199, may 2007.

[112] Aruni Bhatnagar. Environmental Determinants of Cardiovascular Disease. *Circulation Research*, 121(2):162–180, jul 2017.

[113] Peter Kraft, Michael K. Schuhmann, Cornelia Garz, Solveig Jandke, Daniela Urlaub, Stine Mencl, Alma Zernecke, Hans-Jochen Heinze, Roxana O. Carare, Christoph Kleinschnitz, and Stefanie Schreiber. Hypercholesterolemia induced cerebral small vessel disease. *PLOS ONE*, 12(8):e0182822, aug 2017.

[114] Grillo, Salvi, Coruzzi, Salvi, and Parati. Sodium Intake and Hypertension. *Nutrients*, 11(9):1970, aug 2019.

[115] Yian Gu and Nikolaos Scarmeas. Diet and Neuroimaging Markers of Cerebrovascular Disease. *Current Nutrition Reports*, 2(2):81–89, jun 2013.

[116] Vivek Srinivasan, Nady Braidy, Eunice K. W. Chan, Ying-Hua Xu, and Daniel K. Y. Chan. Genetic and environmental factors in vascular dementia: an update of blood brain barrier dysfunction. *Clinical and Experimental Pharmacology and Physiology*, 43(5):515–521, may 2016.

[117] Lauren Howitt, Shaun L. Sandow, T. Hilton Grayson, Zoe E. Ellis, Margaret J. Morris, and Timothy V. Murphy. Differential effects of diet-induced obesity on BK Ca β 1 -subunit expression and function in rat skeletal muscle arterioles and small cerebral arteries. *American Journal of Physiology-Heart and Circulatory Physiology*, 301(1):H29–H40, jul 2011.

[118] Anne Dorrance, Nusrat Matin, and Paulo Pires. The Effects of Obesity on the Cerebral Vasculature. *Current Vascular Pharmacology*, 12(3):462–472, may 2014.

[119] Aurelio Leone and Linda Landini. Vascular Pathology from Smoking: Look at the Microcirculation! *Current Vascular Pharmacology*, 11(4):524–530, jul 2013.

[120] Aruni Bhatnagar. Environmental Cardiology. *Circulation Research*, 99(7):692–705, sep 2006.

[121] Kristen E. Cosselman, Ana Navas-Acien, and Joel D. Kaufman. Environmental factors in cardiovascular disease. *Nature Reviews Cardiology*, 12(11):627–642, nov 2015.

[122] Johannes Attems and Kurt A Jellinger. The overlap between vascular disease and Alzheimer's disease - lessons from pathology. *BMC Medicine*, 12(1):206, dec 2014.

[123] Plamena R. Angelova and Andrey Y. Abramov. Role of mitochondrial ROS in the brain: from physiology to neurodegeneration. *FEBS Letters*, 592(5):692–702, mar 2018.

[124] Simon G. Patching. Glucose Transporters at the Blood-Brain Barrier: Function, Regulation and Gateways for Drug Delivery. *Molecular Neurobiology*, 54(2):1046–1077, mar 2017.

[125] Gabriele Pizzino, Natasha Irrera, Mariapaola Cucinotta, Giovanni Pallio, Federica Mannino, Vincenzo Arcoraci, Francesco Squadrito, Domenica Altavilla, and Alessandra Bitto. Oxidative Stress: Harms and Benefits for Human Health. *Oxidative Medicine and Cellular Longevity*, 2017:1–13, 2017.

[126] Thiago Fernando Beckhauser, José Francis-Oliveira, and Roberto De Pasquale. Reactive Oxygen Species: Physiological and Physiopathological Effects on Synaptic Plasticity. *Journal of Experimental Neuroscience*, 10s1:JEN.S39887, jan 2016.

[127] Yaroslav Kolinko, Kristyna Krakorova, Jan Cendelin, Zbynek Tonar, and Milena Kralickova. Microcirculation of the brain: morphological assessment in degenerative diseases and restoration processes. *Reviews in the Neurosciences*, 26(1), jan 2015.

[128] Chung S. Lim, Serafim Kiriakidis, Ann Sandison, Ewa M. Paleolog, and Alun H. Davies. Hypoxia-inducible factor pathway and diseases of the vascular wall. *Journal of Vascular Surgery*, 58(1):219–230, jul 2013.

[129] Richard B. Buxton. *Introduction to functional magnetic resonance imaging: Principles and techniques*, volume 9780521899. Cambridge University Press, 2nd edition, 2009.

[130] E. O. Stejskal and J. E. Tanner. Spin diffusion measurements: Spin echoes in the presence of a time-dependent field gradient. *The Journal of Chemical Physics*, 42(1):288–292, 1965.

[131] Gabrielle Fournet, Jing Rebecca Li, Alex M. Cerjanic, Bradley P. Sutton, Luisa Ciobanu, and Denis Le Bihan. A two-pool model to describe the IVIM cerebral perfusion. *Journal of Cerebral Blood Flow and Metabolism*, 37(8):2987–3000, aug 2017.

[132] Ileana O. Jelescu and Matthew D. Budde. Design and Validation of Diffusion MRI Models of White Matter. *Frontiers in Physics*, 28(61), nov 2017.

[133] Jens H. Jensen, Joseph A. Helpern, Anita Ramani, Hanzhang Lu, and Kyle Kaczynski. Diffusional kurtosis imaging: The quantification of non-gaussian water diffusion by means of magnetic resonance imaging. *Magnetic Resonance in Medicine*, 53(6):1432–1440, jun 2005.

[134] Denis Le Bihan. What can we see with IVIM MRI? *NeuroImage*, 187:56–67, feb 2019.

[135] Christian Federau, Philippe Maeder, Kieran O'Brien, Patrick Browaeys, Reto Meuli, and Patric Hagmann. Quantitative measurement of brain perfusion with intravoxel incoherent motion MR imaging. *Radiology*, 265(3):874–881, 2012.

[136] Chris A. Clark and Denis Le Bihan. Water diffusion compartmentation and anisotropy at high b values in the human brain. *Magnetic Resonance in Medicine*, 44(6):852–859, dec 2000.

[137] Thoralf Niendorf, Rick M. Dijkhuizen, David G. Norris, Menno van Lookeren Campagne, and Klaas Nicolay. Biexponential diffusion attenuation in various states of brain tissue: Implications for diffusion-weighted imaging. *Magnetic Resonance in Medicine*, 36(6):847–857, dec 1996.

[138] Jonathan V. Sehy, Joseph J.H. Ackerman, and Jeffrey J. Neil. Evidence that both fast and slow water ADC components arise from intracellular space. *Magnetic Resonance in Medicine*, 48(5):765–770, nov 2002.

[139] Wenjing Chen, Juan Zhang, Dan Long, Zhenchang Wang, and Jian Ming Zhu. Optimization of intra-voxel incoherent motion measurement in diffusion-weighted imaging of breast cancer. *Journal of Applied Clinical Medical Physics*, 18(3):191–199, 2017.

[140] Moritz C. Wurnig, Olivio F. Donati, Erika Ulbrich, Lukas Filli, David Kenkel, Harriet C. Thoeny, and Andreas Boss. Systematic analysis of the intravoxel incoherent motion threshold separating perfusion and diffusion effects: Proposal of a standardized algorithm. *Magnetic Resonance in Medicine*, 74(5):1414–1422, nov 2015.

[141] Yaniv Assaf and Yoram Cohen. Non-Mono-Exponential Attenuation of Water and N-Acetyl Aspartate Signals Due to Diffusion in Brain Tissue. *Journal of Magnetic Resonance*, 131(1):69–85, mar 1998.

[142] Kevin D. Harkins, Jean Philippe Galons, Timothy W. Secomb, and Theodore P. Trouard. Assessment of the effects of cellular tissue properties on ADC measurements by numerical simulation of water diffusion. *Magnetic Resonance in Medicine*, 62(6):1414–1422, dec 2009.

[143] Robert V Mulkern, Hakon Gudbjartsson, Carl-Fredrik Westin, Hale Pinar Zengingonul, Werner Gartner, Charles R G Guttmann, Richard L Robertson, Walid Kyriakos, Richard Schwartz, David Holtzman, Ferenc A Jolesz, and Stephan E Maier. Multicomponent apparent diffusion coefficients in human brain. *NMR Biomed*, 12:51–62, 1999.

[144] Roy Steier, József Pál, Gabor Perlaki, Gergely Orsi, Mihály Aradi, Gábor Perlaki, Péter Bogner, Ferenc Galyas, Péter Bukovics, József Janszky, Tamás Dóczi, and Attila Schwarcz. A biexponential DWI study in rat brain intracellular oedema. *European Journal of Radiology*, 81:1758–1765, 2011.

[145] Jens H. Jensen and Joseph A. Helpern. MRI quantification of non-Gaussian water diffusion by kurtosis analysis, aug 2010.

[146] Kevin M. Bennett, Kathleen M. Schmainda, Raoqiong Bennett (Tong), Daniel B. Rowe, Hanbing Lu, and James S. Hyde. Characterization of continuously distributed cortical water diffusion rates with a stretched-exponential model. *Magnetic Resonance in Medicine*, 50(4):727–734, oct 2003.

[147] Xiaohong Joe Zhou, Qing Gao, Osama Abdullah, and Richard L. Magin. Studies of anomalous diffusion in the human brain using fractional order calculus. *Magnetic Resonance in Medicine*, 63(3):562–569, mar 2010.

[148] M. Muge Karaman, Yi Sui, He Wang, Richard L. Magin, Yuhua Li, and Xiaohong Joe Zhou. Differentiating low- and high-grade pediatric brain tumors using a continuous-time random-walk diffusion model at high b -values. *Magnetic Resonance in Medicine*, 76(4):1149–1157, oct 2016.

[149] M. Muge Karaman, He Wang, Yi Sui, Herbert H. Engelhard, Yuhua Li, and Xiaohong Joe Zhou. A fractional motion diffusion model for grading pediatric brain tumors. *NeuroImage: Clinical*, 12:707–714, feb 2016.

[150] Yaniv Assaf, Tamar Blumenfeld-Katzir, Yossi Yovel, and Peter J. Basser. AxCaliber: A method for measuring axon diameter distribution from diffusion MRI. *Magnetic Resonance in Medicine*, 59(6):1347–1354, 2008.

[151] Eletheria Panagiotaki, Simon Walker-Samuel, Bernard Siow, S. Peter Johnson, Vineeth Rajkumar, R. Barbara Pedley, Mark F. Lythgoe, and Daniel C. Alexander. Noninvasive quantification of solid tumor microstructure using VERDICT MRI. *Cancer Research*, 74(7):1902–1912, 2014.

[152] Yaniv Assaf and Peter J. Basser. Composite hindered and restricted model of diffusion (CHARMED) MR imaging of the human brain. *NeuroImage*, 27(1):48–58, aug 2005.

[153] Nathan S. White, Trygve B. Leergaard, Helen D'Arceuil, Jan G. Bjaalie, and Anders M. Dale. Probing tissue microstructure with restriction spectrum imaging: Histological and theoretical validation. *Human Brain Mapping*, 34(2):327–346, feb 2013.

[154] Maurizio Bergamino, Ashley Nespodzany, Leslie C. Baxter, Anna Burke, Richard J. Caselli, Marwan N. Sabbagh, Ryan R. Walsh, and Ashley M. Stokes. Preliminary Assessment of Intravoxel Incoherent Motion Diffusion-Weighted MRI (IVIM-DWI) Metrics in Alzheimer's Disease. *Journal of Magnetic Resonance Imaging*, 52(6):1811–1826, dec 2020.

[155] M D King, N Van Bruggen, A L Busza, J Houseman, S R Williams, and D G Gadian. Perfusion and Diffusion MR Imaging. *Magnetic Resonance in Medicine*, 24:288–301, 1992.

[156] Oliver J. Gurney-Champion, Susanne S. Rauh, Kevin Harrington, Uwe Oelfke, Frederik B. Laun, and Andreas Wetscherek. Optimal acquisition scheme for flow-compensated intravoxel incoherent motion diffusion-weighted imaging in the abdomen: An accurate and precise clinically feasible protocol. *Magnetic Resonance in Medicine*, 83(3):1003–1015, mar 2020.

[157] Denis Le Bihan. Intravoxel incoherent motion perfusion MR imaging: A wake-up call. *Radiology*, 249(3):748–752, dec 2008.

[158] Emma M. Meeus, Jan Novak, Stephanie B. Withey, Niloufar Zarinabad, Hamid Dehghani, and Andrew C. Peet. Evaluation of intravoxel incoherent motion fitting methods in low-perfused tissue. *Journal of Magnetic Resonance Imaging*, 45(5):1325–1334, may 2017.

[159] Oscar Jalnefjord, Mats Andersson, Mikael Montelius, Göran Starck, Anna-Karin Elf, Viktor Johanson, Johanna Svensson, and Maria Ljungberg. Comparison of methods for estimation of the intravoxel incoherent motion (IVIM) diffusion coefficient (D) and perfusion fraction (f). *Magnetic Resonance Materials in Physics, Biology and Medicine*, 31(6):715–723, dec 2018.

[160] Oscar Jalnefjord, Mikael Montelius, Göran Starck, and Maria Ljungberg. Optimization of b-value schemes for estimation of the diffusion coefficient and the perfusion fraction with segmented intravoxel incoherent motion model fitting. *Magnetic Resonance in Medicine*, 82(4):1541–1552, oct 2019.

[161] N. Bessonov, A. Sequeira, S. Simakov, Yu. Vassilevskii, and V. Volpert. Methods of Blood Flow Modelling. *Mathematical Modelling of Natural Phenomena*, 11(1):1–25, dec 2016.

[162] Martin Kehrer and Martin Schöning. A Longitudinal Study of Cerebral Blood Flow Over the First 30 Months. *Pediatric Research*, 66(5):560–564, nov 2009.

[163] W. H. Bouvy, L. J. Geurts, H. J. Kuijf, P. R. Luijten, L. J. Kappelle, G. J. Biessels, and J. J. M. Zwanenburg. Assessment of blood flow velocity and pulsatility in

cerebral perforating arteries with 7-T quantitative flow MRI. *NMR in Biomedicine*, 29(9):1295–1304, sep 2016.

[164] André Ahlgren, Linda Knutsson, Ronnie Wirestam, Markus Nilsson, Freddy Ståhlberg, Daniel Topgaard, and Samo Lasič. Quantification of microcirculatory parameters by joint analysis of flow-compensated and non-flow-compensated intravoxel incoherent motion (IVIM) data. *NMR in Biomedicine*, 29(5):640–649, may 2016.

[165] Wen-Chau Wu, Ya-Fang Chen, Han-Min Tseng, Shun-Chung Yang, and Pei-Chi My. Caveat of measuring perfusion indexes using intravoxel incoherent motion magnetic resonance imaging in the human brain. *European Radiology*, 25(8):2485–2492, aug 2015.

[166] Hsuan-Ming Huang. Reliable estimation of brain intravoxel incoherent motion parameters using denoised diffusion-weighted MRI. *NMR in Biomedicine*, 33(4), apr 2020.

[167] Ronnie Wirestam, M. Borg, S. Brockstedt, A. Lindgren, S. Holtås, and F. Ståhlberg. Perfusion-related parameters in intravoxel incoherent motion MR imaging compared with CBV and CBF measured by dynamic susceptibility-contrast MR technique. *Acta Radiologica*, 42(2):123–128, 2001.

[168] Christian Federau, Kieran O'Brien, Reto Meuli, Patric Hagmann, and Philippe Maeder. Measuring brain perfusion with intravoxel incoherent motion (IVIM): Initial clinical experience. *Journal of Magnetic Resonance Imaging*, 39(3):624–632, mar 2014.

[169] Christian Federau, Patric Hagmann, Philippe Maeder, Markus Müller, Reto Meuli, Matthias Stuber, and Kieran O'Brien. Dependence of Brain Intravoxel Incoherent Motion Perfusion Parameters on the Cardiac Cycle. *PLoS ONE*, 8(8), aug 2013.

[170] Vera C. Keil, Burkhard Mädler, Gerrit H. Gielen, Bogdan Pintea, Kanishka Hiththetiya, Alisa R. Gaspranova, Jürgen Gieseke, Matthias Simon, Hans H. Schild, and Dariusch R. Hadizadeh. Intravoxel incoherent motion MRI in the brain: Impact of the fitting model on perfusion fraction and lesion differentiability. *Journal of Magnetic Resonance Imaging*, 46(4):1187–1199, oct 2017.

[171] Tan Guo, Juan Chen, Bing Wu, Dandan Zheng, Sheng Jiao, Yan Song, and Min Chen. Use of intravoxel incoherent motion diffusion-weighted imaging in identifying the vascular and avascular zones of human meniscus. *Journal of Magnetic Resonance Imaging*, 45(4):1090–1096, apr 2017.

[172] Tim Finkenstaedt, Markus Klarhoefer, Christian Eberhardt, Anton S. Becker, Gustav Andreisek, Andreas Boss, and Cristina Rossi. The IVIM signal in the healthy cerebral gray matter: A play of spherical and non-spherical components. *NeuroImage*, 152:340–347, may 2017.

[173] Georg R. Spinner, Johannes F.M. Schmidt, Constantin von Deuster, Christian Federau, Christian T. Stoeck, and Sebastian Kozerke. Enhancing intravoxel incoherent

motion parameter mapping in the brain using k-b PCA. *NMR in Biomedicine*, 31(12):e4008, dec 2018.

[174] Emma M. Meeus, Jan Novak, Hamid Dehghani, and Andrew C. Peet. Rapid measurement of intravoxel incoherent motion (IVIM) derived perfusion fraction for clinical magnetic resonance imaging. *Magnetic Resonance Materials in Physics, Biology and Medicine*, 31(2):269–283, apr 2018.

[175] Jeffrey J. Neil and Joseph J.H. Ackerman. Detection of pseudodiffusion in rat brain following blood substitution with perfluorocarbon. *Journal of Magnetic Resonance (1969)*, 97(1):194–201, 1992.

[176] Dan Wu and Jiangyang Zhang. Evidence of the diffusion time dependence of intravoxel incoherent motion in the brain. *Magnetic Resonance in Medicine*, 82(6):2225–2235, dec 2019.

[177] Olivier Chevallier, Nan Zhou, Jean-Pierre Cercueil, Jian He, Romaric Loffroy, and Yì Xiáng Wáng. Comparison of tri-exponential decay vs. bi-exponential decay and full fitting vs. segmented fitting for modeling liver intravoxel incoherent motion diffusion MRI. *bioRxiv*, page 429977, sep 2018.

[178] Jean-Pierre Cercueil, Jean-Michel Petit, Stéphanie Nougaret, Philippe Soyer, Audrey Fohlen, Marie-Ange Pierredon-Foulongne, Valentina Schembri, Elisabeth Delhom, Sabine Schmidt, Alban Denys, Serge Aho, and Boris Guiu. Intravoxel incoherent motion diffusion-weighted imaging in the liver: comparison of mono-, bi- and tri-exponential modelling at 3.0-T. *European Radiology*, 25(6):1541–1550, jun 2015.

[179] Andreas Julian Riexinger, Jan Martin, Susanne Rauh, Andreas Wetscherek, Mona Pistel, Tristan Anselm Kuder, Armin Michael Nagel, Michael Uder, Bernhard Hensel, Lars Müller, and Frederik Bernd Laun. On the Field Strength Dependence of Bi- and Triexponential Intravoxel Incoherent Motion (IVIM) Parameters in the Liver. *Journal of Magnetic Resonance Imaging*, 50(6):1883–1892, dec 2019.

[180] Sophie van Baalen, Alexander Leemans, Pieter Dik, Marc R. Lilien, Bennie ten Haken, and Martijn Froeling. Intravoxel incoherent motion modeling in the kidneys: Comparison of mono-, bi-, and triexponential fit. *Journal of Magnetic Resonance Imaging*, 46(1):228–239, jul 2017.

[181] René van der Bel, Oliver J. Gurney-Champion, Martijn Froeling, Erik S.G. Stroes, Aart J. Nederveen, and C.T. Paul Krediet. A tri-exponential model for intravoxel incoherent motion analysis of the human kidney: In silico and during pharmacological renal perfusion modulation. *European Journal of Radiology*, 91:168–174, jun 2017.

[182] Jeffrey H. Maki, James R. Macfall, and G. Allan Johnson. The use of gradient flow compensation to separate diffusion and microcirculatory flow in MRI. *Magnetic Resonance in Medicine*, 17(1):95–107, jan 1991.

[183] Zi Xiang Kuai, Wan Yu Liu, Yan Li Zhang, and Yue Min Zhu. Generalization of intravoxel incoherent motion model by introducing the notion of continuous

pseudodiffusion variable. *Magnetic Resonance in Medicine*, 76(5):1594–1603, nov 2016.

[184] Ling Jiang, Taotao Sun, Yuhao Liao, Yi Sun, Zhaoxia Qian, Yi Zhang, and Dan Wu. Probing the ballistic microcirculation in placenta using flow-compensated and non-compensated intravoxel incoherent motion imaging. *Magnetic Resonance in Medicine*, 85(1):404–412, jan 2020.

[185] Moritz Jörg Schneider, Thomas Gaass, Jens Ricke, Julien Dinkel, and Olaf Dietrich. Assessment of intravoxel incoherent motion MRI with an artificial capillary network: analysis of biexponential and phase-distribution models. *Magnetic Resonance in Medicine*, 82(4):1373–1384, oct 2019.

[186] R. Mark Henkelman, Jeffrey J. Neil, and Qing-San -S Xiang. A quantitative interpretation of IVIM measurements of vascular perfusion in the rat brain. *Magnetic Resonance in Medicine*, 32(4):464–469, 1994.

[187] Irène Troprès, Stephan Grimault, Albert Vaeth, Emmanuelle Grillon, Cécile Julien, Jean François Payen, Laurent Lamalle, and Michel Décorps. Vessel size imaging. *Magnetic Resonance in Medicine*, 45(3):397–408, 2001.

[188] Sarah Al-Bachari, Laura M. Parkes, Rishma Vidyasagar, Martha F. Hanby, Vivek Tharaken, Iracema Leroi, and Hedley C.A. Emsley. Arterial spin labelling reveals prolonged arterial arrival time in idiopathic Parkinson's disease. *NeuroImage: Clinical*, 6:1–8, 2014.

[189] Denis Le Bihan and Robert Turner. The capillary network: a link between ivim and classical perfusion. *Magnetic Resonance in Medicine*, 27(1):171–178, 1992.

[190] Carol Kilkenny, William J. Browne, Innes C. Cuthill, Michael Emerson, and Douglas G. Altman. Improving Bioscience Research Reporting: The ARRIVE Guidelines for Reporting Animal Research. *PLoS Biology*, 8(6):e1000412, jun 2010.

[191] Brian B. Avants, Nicholas J. Tustison, Michael Stauffer, Gang Song, Baohua Wu, and James C. Gee. The Insight ToolKit image registration framework. *Frontiers in Neuroinformatics*, 8, apr 2014.

[192] Olaf Dietrich, José G. Raya, Scott B. Reeder, Maximilian F. Reiser, and Stefan O. Schoenberg. Measurement of signal-to-noise ratios in MR images: Influence of multichannel coils, parallel imaging, and reconstruction filters. *Journal of Magnetic Resonance Imaging*, 26(2):375–385, aug 2007.

[193] Miyuki Unekawa, Minoru Tomita, Yutaka Tomita, Haruki Toriumi, Koichi Miyaki, and Norihiro Suzuki. RBC velocities in single capillaries of mouse and rat brains are the same, despite 10-fold difference in body size. *Brain Research*, 1320:69–73, mar 2010.

[194] George Paxinos and Charles Watson. *The Rat Brain in Stereotaxic Coordinates*. Elsevier Inc., 6th edition, 2007.

[195] Antal G Hudetz, Bharat B Biswal, Gabriella Fehér, and John P Kampine. Effects of Hypoxia and Hypercapnia on Capillary Flow Velocity in the Rat Cerebral Cortex. *Microvascular Research*, 54:35–42, 1997.

[196] Joonas Autio, Hiroshi Kawaguchi, Shigeyoshi Saito, Ichio Aoki, Takayuki Obata, Kazuto Masamoto, and Iwao Kanno. Spatial frequency-based analysis of mean red blood cell speed in single microvessels: Investigation of microvascular perfusion in rat cerebral cortex. *PLoS ONE*, 6(8), aug 2011.

[197] Kazuto Masamoto, Takayuki Obata, and Iwao Kanno. Intracortical Microcirculatory Change Induced by Anesthesia in Rat Somatosensory Cortex. *Advances in Experimental Medicine and Biology*, 662:57–61, 2010.

[198] Miyuki Unekawa, Minoru Tomita, Takashi Osada, Yutaka Tomita, Haruki Toriumi, Jemal Tatarishvili, and Norihiro Suzuki. Frequency distribution function of red blood cell velocities in single capillaries of the rat cerebral cortex using intravital laser-scanning confocal microscopy with high-speed camera. *Asian Biomedicine*, 2(3):203–218, 2008.

[199] Christophe Leys, Christophe Ley, Olivier Klein, Philippe Bernard, and Laurent Licata. Detecting outliers: Do not use standard deviation around the mean, use absolute deviation around the median. *Journal of Experimental Social Psychology*, 49(4):764–766, jul 2013.

[200] J M. Bland and D. G Altman. Statistics notes: Measurement error. *BMJ*, 312(7047):1654–1654, jun 1996.

[201] Arno Villringer, Andreas Them, Ute Lindauer, Karl Einhäupl, and Ulrich Dirnagl. Capillary perfusion of the rat brain cortex: An in vivo confocal microscopy study. *Circulation Research*, 75(1):55–62, 1994.

[202] Albertina Cortés-Sol, Miguel Lara-Garcia, Mayvi Alvarado, Robyn Hudson, Pere Berbel, and Pablo Pacheco. Inner capillary diameter of hypothalamic paraventricular nucleus of female rat increases during lactation. *BMC Neuroscience*, 14(1):7, dec 2013.

[203] Vladimir Mironov, Martin A. Hritz, Joseph C. LaManna, Antal G. Hudetz, and Sami I. Harik. Architectural alterations in rat cerebral microvessels after hypobaric hypoxia. *Brain Research*, 660(1):73–80, 1994.

[204] Gunter Pawlik, Angelika Rackl, and Richard J Bing. Quantitative capillary topography and blood flow in the cerebral cortex of cats: an in vivo microscopic study. *Brain Research*, 208(1):35–58, 1981.

[205] Zheng Gang Zhang, Li Zhang, Wayne Tsang, Hamid Soltanian-Zadeh, Daniel Morris, Ruilan Zhang, Anton Goussev, Cecylia Powers, Thomas Yeich, and Michael Chopp. Correlation of VEGF and angiopoietin expression with disruption of blood-brain barrier and angiogenesis after focal cerebral ischemia. *Journal of Cerebral Blood Flow and Metabolism*, 22(4):379–392, 2002.

[206] Daniel C. Morris, Thomas Yeich, Mohammad Mehdi Khalighi, Hamid Soltanian-Zadeh, Zheng G. Zhang, and Michael Chopp. Microvascular structure after embolic focal cerebral ischemia in the rat. *Brain Research*, 972(1-2):31–37, may 2003.

[207] D Le Bihan, E Breton, D Lallemand, P Grenier, E Cabanis, and M Laval-Jeantet. MR imaging of intravoxel incoherent motions: application to diffusion and perfusion in neurologic disorders. *Radiology*, 161(2):401–407, nov 1986.

[208] Y. Yao, S. Zhang, X. Tang, S. Zhang, J. Shi, W. Zhu, and W. Zhu. Intravoxel incoherent motion diffusion-weighted imaging in stroke patients: initial clinical experience. *Clinical Radiology*, 71(9):938.e11–938.e16, sep 2016.

[209] Mami Iima, Tomomi Nobashi, Hirohiko Imai, Sho Koyasu, Tsuneo Saga, Yuji Nakamoto, Masako Kataoka, Akira Yamamoto, Tetsuya Matsuda, and Kaori Togashi. Effects of diffusion time on non-Gaussian diffusion and intravoxel incoherent motion (IVIM) MRI parameters in breast cancer and hepatocellular carcinoma xenograft models. *Acta Radiologica Open*, 7(1):205846011775156, jan 2018.

[210] Yuxi Pang, Baris Turkbey, Marcelino Bernardo, Jochen Kruecker, Samuel Kadoury, Maria J. Merino, Bradford J. Wood, Peter A. Pinto, and Peter L. Choyke. Intravoxel incoherent motion MR imaging for prostate cancer: An evaluation of perfusion fraction and diffusion coefficient derived from different b-value combinations. *Magnetic Resonance in Medicine*, 69(2):553–562, feb 2013.

[211] Ben R. Dickie, Geoff J.M. Parker, and Laura M. Parkes. Measuring water exchange across the blood-brain barrier using MRI. *Progress in Nuclear Magnetic Resonance Spectroscopy*, 116:19–39, 2020.

[212] Mark Jenkinson, Christian F Beckmann, Timothy E J Behrens, Mark W Woolrich, and Stephen M Smith. FSL. *NeuroImage*, 62:782–790, 2012.

[213] Bruce Fischl. FreeSurfer. *NeuroImage*, 62(2):774–781, 2012.

[214] Christophe Destrieux, Bruce Fischl, Anders Dale, and Eric Halgren. Automatic parcellation of human cortical gyri and sulci using standard anatomical nomenclature. *NeuroImage*, 53(1):1–15, 2010.

[215] Hirotugu Akaike. A New Look at the Statistical Model Identification. *IEEE Transactions on Automatic Control*, 19(6):716–723, 1974.

[216] K. L. Leenders, D. Perani, A. A. Lammertsma, J. D. Heather, P. Buckingham, T. Jones, M. J.R. Healy, J. M. Gibbs, R. J.S. Wise, J. Hatazawa, S. Herold, R. P. Beaney, D. J. Brooks, T. Spinks, C. Rhodes, and R. S.J. Frackowiak. Cerebral blood flow, blood volume and oxygen utilization: Normal values and effect of age. *Brain*, 113(1):27–47, 1990.

[217] Casey Vieni, Benjamin Ades-Aron, Bettina Conti, Eric E. Sigmund, Peter Riviello, Timothy M. Shepherd, Yvonne W. Lui, Dmitry S. Novikov, and Els Fieremans. Effect of intravoxel incoherent motion on diffusion parameters in normal brain. *NeuroImage*, 204(1):116228, jan 2020.

[218] Amy F. Smith, Vincent Doyeux, Maxime Berg, Myriam Peyrounette, Mohammad Haft-Javaherian, Anne Edith Larue, John H. Slater, Frédéric Lauwers, Pablo Blinder, Philbert Tsai, David Kleinfeld, Chris B. Schaffer, Nozomi Nishimura, Yohan Davit, and Sylvie Lorthois. Brain capillary networks across species: A few simple organizational requirements are sufficient to reproduce both structure and function. *Frontiers in Physiology*, 10:10:233, 2019.

[219] Francis Cassot, Frederic Lauwers, Céline Fouard, Steffen Prohaska, and Valerie Lauwers-Cances. A novel three-dimensional computer-assisted method for a quantitative study of microvascular networks of the human cerebral cortex. *Microcirculation*, 13(1):1–18, 2006.

[220] Frederic Lauwers, Francis Cassot, Valerie Lauwers-Cances, Prasanna Puwanarajah, and Henri Duvernoy. Morphometry of the human cerebral cortex microcirculation: General characteristics and space-related profiles. *NeuroImage*, 39(3):936–948, 2008.

[221] Miguel Marín-Padilla. The human brain intracerebral microvascular system: Development and structure. *Frontiers in Neuroanatomy*, 13:6–38, 2012.

[222] Sebastian Wolf, Oliver Arend, Karin Schulte, Thomas H. Ittel, and Martin Reim. Quantification of retinal capillary density and flow velocity in patients with essential hypertension. *Hypertension*, 23(4):464–467, 1994.

[223] Fei Ye, Songchao Yin, Meirong Li, Yujie Li, and Jingang Zhong. In-vivo full-field measurement of microcirculatory blood flow velocity based on intelligent object identification. *Journal of Biomedical Optics*, 25(1):1, 2020.

[224] Martin Hahn, Thomas Klyscz, and Michael Jünger. Synchronous measurements of blood pressure and red blood cell velocity in capillaries of human skin. *Journal of Investigative Dermatology*, 106(6):1256–1259, 1996.

[225] D. A. Tata and B. J. Anderson. A new method for the investigation of capillary structure. *Journal of Neuroscience Methods*, 113(2):199–206, 2002.

[226] Jens H. Jensen and Joseph A. Helpern. Effect of gradient pulse duration on MRI estimation of the diffusional kurtosis for a two-compartment exchange model. *Journal of Magnetic Resonance*, 210(2):233–237, jun 2011.

[227] Lukasz J. Zielinski and Pabitra N. Sen. Effects of finite-width pulses in the pulsed-field gradient measurement of the diffusion coefficient in connected porous media. *Journal of Magnetic Resonance*, 165(1):153–161, nov 2003.

[228] Swati Rane, Elaine Peskind, Rebecca Hendrickson, Murray Raskind, and Jalal Andre. Intra-Voxel Incoherent Motion imaging as a potential marker of parenchymal glymphatic flow. *Proceedings of the International Society for Magnetic Resonance in Medicine*, 27, 2019.

[229] Reuben Howden, J. Timothy Lightfoot, Stephen J. Brown, and Ian L. Swaine. The effects of breathing 5% CO 2 on human cardiovascular responses and tolerance to orthostatic stress. *Experimental Physiology*, 89(4):465–471, jul 2004.

[230] Frank Grüne, Stephan Kazmaier, Robert J. Stolker, Gerhard H. Visser, and Andreas Weyland. Carbon dioxide induced changes in cerebral blood flow and flow velocity: Role of cerebrovascular resistance and effective cerebral perfusion pressure. *Journal of Cerebral Blood Flow and Metabolism*, 35(9):1470–1477, 2015.

[231] Hiroshi Ito, Iwao Kanno, Masanobu Ibaraki, Jun Hatazawa, and Shuichi Miura. Changes in Human Cerebral Blood Flow and Cerebral Blood Volume during Hypercapnia and Hypocapnia Measured by Positron Emission Tomography. *Journal of Cerebral Blood Flow & Metabolism*, 23(6):665–670, jun 2003.

[232] David C. Alsop, John A. Detre, Xavier Golay, Matthias Günther, Jeroen Hendrikse, Luis Hernandez-Garcia, Hanzhang Lu, Bradley J. MacIntosh, Laura M. Parkes, Marion Smits, Matthias J. P. van Osch, Danny J. J. Wang, Eric C. Wong, and Greg Zaharchuk. Recommended implementation of arterial spin-labeled perfusion MRI for clinical applications: A consensus of the ISMRM perfusion study group and the European consortium for ASL in dementia. *Magnetic Resonance in Medicine*, 73(1):102–116, jan 2015.

[233] Rishma Vidyasagar, Arno Greyling, Richard Draijer, Douglas R. Corfield, and Laura M. Parkes. The effect of black tea and caffeine on regional cerebral blood flow measured with arterial spin labeling. *Journal of Cerebral Blood Flow and Metabolism*, 33(6):963–968, 2013.

[234] Wallace O. Fenn and Albert B. Craig. Effect of CO2 on respiration using a new method of administering CO2. *Journal of Applied Physiology*, 18(5):1023–1024, sep 1963.

[235] L. Palumbo, P. Bosco, M.E. Fantacci, E. Ferrari, P. Oliva, G. Spera, and A. Retico. Evaluation of the intra- and inter-method agreement of brain MRI segmentation software packages: A comparison between SPM12 and FreeSurfer v6.0. *Physica Medica*, 64:261–272, aug 2019.

[236] Mahsa Dadar and Simon Duchesne. Reliability assessment of tissue classification algorithms for multi-center and multi-scanner data. *NeuroImage*, 217:116928, aug 2020.

[237] Erhard Næss-Schmidt, Anna Tietze, Jakob Udby Blicher, Mikkel Petersen, Irene K. Mikkelsen, Pierrick Coupé, José V. Manjón, and Simon Fristed Eskildsen. Automatic thalamus and hippocampus segmentation from MP2RAGE: comparison of publicly available methods and implications for DTI quantification. *International Journal of Computer Assisted Radiology and Surgery*, 11(11):1979–1991, nov 2016.

[238] Yongxia Zhou, Zachary B. Rodgers, and Anderson H. Kuo. Cerebrovascular reactivity measured with arterial spin labeling and blood oxygen level dependent techniques. *Magnetic Resonance Imaging*, 33(5):566–576, jun 2015.

[239] Manus J Donahue, Carlos C Faraco, Megan K Strother, Michael A Chappell, Swati Rane, Lindsey M Dethrage, Jeroen Hendrikse, and Jeroen CW Siero. Bolus Arrival Time and Cerebral Blood Flow Responses to Hypercarbia. *Journal of Cerebral Blood Flow & Metabolism*, 34(7):1243–1252, jul 2014.

[240] Susanne Wegener, Wen-Chau Wu, Joanna E. Perthen, and Eric C. Wong. Quantification of rodent cerebral blood flow (CBF) in normal and high flow states using pulsed arterial spin labeling magnetic resonance imaging. *Journal of Magnetic Resonance Imaging*, 26(4):855–862, oct 2007.

[241] Daniel M. Mandell, Jay S. Han, Julien Poublanc, Adrian P. Crawley, Jeff A. Stainsby, Joseph A. Fisher, and David J. Mikulis. Mapping Cerebrovascular Reactivity Using Blood Oxygen Level-Dependent MRI in Patients With Arterial Steno-occlusive Disease. *Stroke*, 39(7):2021–2028, jul 2008.

[242] Hiroshi Ito, Iwao Kanno, and Hiroshi Fukuda. Human cerebral circulation: positron emission tomography studies. *Annals of Nuclear Medicine*, 19(2):65–74, apr 2005.

[243] Stefan K. Piechnik, Peter A. Chiarelli, and Peter Jezzard. Modelling vascular reactivity to investigate the basis of the relationship between cerebral blood volume and flow under CO2 manipulation. *NeuroImage*, 39(1):107–118, jan 2008.

[244] Elizabeth B. Hutchinson, Bojana Stefanovic, Alan P. Koretsky, and Afonso C. Silva. Spatial flow-volume dissociation of the cerebral microcirculatory response to mild hypercapnia. *NeuroImage*, 32(2):520–530, aug 2006.

[245] Yi-Ching Lynn Ho, Esben Thade Petersen, Ivan Zimine, and Xavier Golay. Similarities and Differences in Arterial Responses to Hypercapnia and Visual Stimulation. *Journal of Cerebral Blood Flow & Metabolism*, 31(2):560–571, feb 2011.

[246] Varsha Jain, Jeffrey Duda, Brian Avants, Mariel Giannetta, Sharon X. Xie, Timothy Roberts, John A. Detre, Hallam Hurt, Felix W. Wehrli, and Danny J. J. Wang. Longitudinal Reproducibility and Accuracy of Pseudo-Continuous Arterial Spin–labeled Perfusion MR Imaging in Typically Developing Children. *Radiology*, 263(2):527–536, may 2012.

[247] Alexander D. Cohen, Mohit Agarwal, Amritpal S. Jagra, Andrew S. Nencka, Timothy B. Meier, R. Marc Lebel, Michael A. McCrea, and Yang Wang. Longitudinal Reproducibility of MR Perfusion Using 3D Pseudocontinuous Arterial Spin Labeling With Hadamard-Encoded Multiple Postlabeling Delays. *Journal of Magnetic Resonance Imaging*, 51(6):1846–1853, jun 2020.

[248] André M. Paschoal, Renata F. Leoni, Antonio C. dos Santos, and Fernando F. Paiva. Intravoxel incoherent motion MRI in neurological and cerebrovascular diseases. *NeuroImage: Clinical*, 20:705–714, 2018.

[249] Guangming Zhu, Christian Federau, Max Wintermark, Hui Chen, David G Marcellus, Blake W Martin, and Jeremy J Heit. Comparison of MRI IVIM and MR perfusion imaging in acute ischemic stroke due to large vessel occlusion. *International Journal of Stroke*, 15(3):332–342, apr 2020.

[250] C. Federau, R. Meuli, K. O'Brien, P. Maeder, and P. Hagmann. Perfusion Measurement in Brain Gliomas with Intravoxel Incoherent Motion MRI. *American Journal of Neuroradiology*, 35(2):256–262, feb 2014.

[251] Osamu Togao, Akio Hiwatashi, Koji Yamashita, Kazufumi Kikuchi, Daichi Momosaka, Koji Yoshimoto, Daisuke Kuga, Masahiro Mizoguchi, Satoshi O Suzuki, Toru Iwaki, Marc Van Cauteren, Koji Iihara, and Hiroshi Honda. Measurement of the perfusion fraction in brain tumors with intravoxel incoherent motion MR imaging: validation with histopathological vascular density in meningiomas. *The British Journal of Radiology*, 91(1085):20170912, may 2018.

[252] Fiona C. Moreton, Krishna A. Dani, Colin Goutcher, Kevin O'Hare, and Keith W. Muir. Respiratory challenge MRI: Practical aspects. *NeuroImage: Clinical*, 11:667–677, 2016.

[253] Matthew Grech-Sollars, Patrick W. Hales, Keiko Miyazaki, Felix Raschke, Daniel Rodriguez, Martin Wilson, Simrandip K. Gill, Tina Banks, Dawn E. Saunders, Jonathan D. Clayden, Matt N. Gwilliam, Thomas R. Barrick, Paul S. Morgan, Nigel P. Davies, James Rossiter, Dorothee P. Auer, Richard Grundy, Martin O. Leach, Franklyn A. Howe, Andrew C. Peet, and Chris A. Clark. Multi-centre reproducibility of diffusion MRI parameters for clinical sequences in the brain. *NMR in Biomedicine*, 28(4):468–485, apr 2015.

[254] Xiufeng Li, Subhendra N. Sarkar, David E. Purdy, and Richard W. Briggs. Quantifying Cerebellum Grey Matter and White Matter Perfusion Using Pulsed Arterial Spin Labeling. *BioMed Research International*, 2014:1–12, 2014.

[255] Laura M. Parkes, Waqar Rashid, Declan T. Chard, and Paul S. Tofts. Normal cerebral perfusion measurements using arterial spin labeling: Reproducibility, stability, and age and gender effects. *Magnetic Resonance in Medicine*, 51(4):736–743, apr 2004.

[256] J. Helenius, J. Perkiö, L. Soinne, L. Østergaard, R. A. D. Carano, O. Salonen, S. Savolainen, M. Kaste, H. J. Aronen, and T. Tatlisumak. Cerebral hemodynamics in a healthy population measured by dynamic susceptibility contrast MR imaging. *Acta Radiologica*, 44(5):538–546, sep 2003.

[257] Maolin Qiu, R. Paul Maguire, Jagriti Arora, Beata Planeta-Wilson, David Weinzimmer, Jinghua Wang, Yuenan Wang, Hyeonjin Kim, Nallakkandi Rajeevan, Yiyun Huang, Richard E. Carson, and R. Todd Constable. Arterial transit time effects in pulsed arterial spin labeling CBF mapping: Insight from a PET and MR study in normal human subjects. *Magnetic Resonance in Medicine*, 63(2):374–384, feb 2010.

[258] Jan Karbowski. Global and regional brain metabolic scaling and its functional consequences. *BMC Biology*, 5(1):18, dec 2007.

[259] H S Markus, D J Lythgoe, L Ostergaard, M O'Sullivan, and S C Williams. Reduced cerebral blood flow in white matter in ischaemic leukoaraiosis demonstrated using quantitative exogenous contrast based perfusion MRI. *Journal of Neurology, Neurosurgery & Psychiatry*, 69(1):48–53, jul 2000.

[260] Laura M. Parkes and Paul S. Tofts. Improved accuracy of human cerebral blood perfusion measurements using arterial spin labeling: Accounting for capillary water permeability. *Magnetic Resonance in Medicine*, 48(1):27–41, jul 2002.

[261] Tetsuya Tsujikawa, Hirohiko Kimura, Tsuyoshi Matsuda, Yasuhiro Fujiwara, Makoto Isozaki, Ken-ichiro Kikuta, and Hidehiko Okazawa. Arterial Transit Time Mapping Obtained by Pulsed Continuous 3D ASL Imaging with Multiple Post-Label Delay Acquisitions: Comparative Study with PET-CBF in Patients with Chronic Occlusive Cerebrovascular Disease. *PLOS ONE*, 11(6):e0156005, jun 2016.

[262] Unknown. 2020 Alzheimer's disease facts and figures. *Alzheimer's & Dementia*, 16(3):391–460, mar 2020.

[263] Raj N. Kalaria. Neuropathological diagnosis of vascular cognitive impairment and vascular dementia with implications for Alzheimer's disease. *Acta Neuropathologica*, 131(5):659–685, may 2016.

[264] Ansgar J. Furst, Gil D. Rabinovici, Ara H. Rostomian, Tyler Steed, Adi Alkalay, Caroline Racine, Bruce L. Miller, and William J. Jagust. Cognition, glucose metabolism and amyloid burden in Alzheimer's disease. *Neurobiology of Aging*, 33(2):215–225, feb 2012.

[265] Kerryn E. Pike, Kathryn A. Ellis, Victor L. Villemagne, Norm Good, Gael Chételat, David Ames, Cassandra Szoeke, Simon M. Laws, Giuseppe Verdile, Ralph N. Martins, Colin L. Masters, and Christopher C. Rowe. Cognition and beta-amyloid in preclinical Alzheimer's disease: Data from the AIBL study. *Neuropsychologia*, 49(9):2384–2390, jul 2011.

[266] Harm J. van de Haar, Saartje Burgmans, Jacobus F. A. Jansen, Matthias J. P. van Osch, Mark A. van Buchem, Majon Muller, Paul A. M. Hofman, Frans R. J. Verhey, and Walter H. Backes. Blood-Brain Barrier Leakage in Patients with Early Alzheimer Disease. *Radiology*, 281(2):527–535, nov 2016.

[267] Gene L. Bowman, Loïc Dayon, Richard Kirkland, Jérôme Wojcik, Gwendoline Peyratout, India C. Severin, Hugues Henry, Aikaterini Oikonomidi, Eugenia Migliavacca, Michael Bacher, and Julius Popp. Blood-brain barrier breakdown, neuroinflammation, and cognitive decline in older adults. *Alzheimer's & Dementia*, 14(12):1640–1650, dec 2018.

[268] Philip S.J. Weston, Ivor J.A. Simpson, Natalie S. Ryan, Sebastien Ourselin, and Nick C. Fox. Diffusion imaging changes in grey matter in Alzheimer's disease: A potential marker of early neurodegeneration. *Alzheimer's Research and Therapy*, 7(1):1–8, 2015.

[269] Kejal Kantarci, Clifford R. Jack, Yue Cheng Xu, Norberg G. Campeau, Peter C. O'Brien, Glenn E. Smith, Robert J. Ivnik, Bradley F. Boeve, Emre Kokmen, Eric G. Tangalos, and Ronald C. Petersen. Mild Cognitive Impairment and Alzheimer Disease: Regional Diffusivity of Water. *Radiology*, 219(1):101–107, apr 2001.

[270] K. Kantarci, R. C. Petersen, B. F. Boeve, D. S. Knopman, S. D. Weigand, P. C. O'Brien, M. M. Shiung, G. E. Smith, R. J. Ivnik, E. G. Tangalos, and C. R. Jack. DWI predicts future progression to Alzheimer disease in amnestic mild cognitive impairment. *Neurology*, 64(5):902–904, 2005.

[271] T A Sandson, O Felician, R R Edelman, and S Warach. Diffusion-Weighted Magnetic Resonance Imaging in Alzheimer's. 10(2):166–171, 1999.

[272] M. Bozzali, A. Falini, M. Franceschi, M. Cercignani, M. Zuffi, G. Scotti, G. Comi, and M. Filippi. White matter damage in Alzheimer's disease assessed in vivo using diffusion tensor magnetic resonance imaging. *Journal of Neurology Neurosurgery and Psychiatry*, 72(6):742–746, 2002.

[273] Paul Schmidt, Christian Gaser, Milan Arsic, Dorothea Buck, Annette Förschler, Achim Berthele, Muna Hoshi, Rüdiger Ilg, Volker J. Schmid, Claus Zimmer, Bernhard Hemmer, and Mark Mühlau. An automated tool for detection of FLAIR-hyperintense white-matter lesions in Multiple Sclerosis. *NeuroImage*, 59(4):3774–3783, feb 2012.

[274] Roger Bakeman. Recommended effect size statistics for repeated measures designs. *Behavior Research Methods*, 37(3):379–384, aug 2005.

[275] Hyo Jung Park, Yu Sub Sung, Seung Soo Lee, Yedaun Lee, Hyunhee Cheong, Yeong Jae Kim, and Moon-gyu Lee. Intravoxel incoherent motion diffusion-weighted MRI of the abdomen: The effect of fitting algorithms on the accuracy and reliability of the parameters. *Journal of Magnetic Resonance Imaging*, 45(6):1637–1647, jun 2017.

[276] Augustin Lecler, Julien Savatovsky, Daniel Balvay, Mathieu Zmuda, Jean-Claude Sadik, Olivier Galatoire, Frédérique Charbonneau, Olivier Bergès, Hervé Picard, and Laure Fournier. Repeatability of apparent diffusion coefficient and intravoxel incoherent motion parameters at 3.0 Tesla in orbital lesions. *European Radiology*, 27(12):5094–5103, dec 2017.

[277] Yedaun Lee, Seung Soo Lee, Namkug Kim, Eunki Kim, Yeong Jae Kim, Sung-Cheol Yun, Bernd Kühn, In Seong Kim, Seong Ho Park, So Yeon Kim, and Moon-Gyu Lee. Intravoxel Incoherent Motion Diffusion-weighted MR Imaging of the Liver: Effect of Triggering Methods on Regional Variability and Measurement Repeatability of Quantitative Parameters. *Radiology*, 274(2):405–415, feb 2015.

[278] K. Shaw, L. Bell, K. Boyd, D. M. Grijseels, D. Clarke, O. Bonnar, H. S. Crombag, and C. N. Hall. Neurovascular coupling and oxygenation are decreased in hippocampus compared to neocortex because of microvascular differences. *Nature Communications*, 12(1):3190, dec 2021.

[279] Sau May Wong, C. Eleana Zhang, Frank C.G. van Bussel, Julie Staals, Cécile R.L.P.N. Jeukens, Paul A.M. Hofman, Robert J. van Oostenbrugge, Walter H. Backes, and Jacobus F.A. Jansen. Simultaneous investigation of microvasculature and parenchyma in cerebral small vessel disease using intravoxel incoherent motion imaging. *NeuroImage: Clinical*, 14:216–221, 2017.

[280] Jordan S. Pober and William C. Sessa. Inflammation and the Blood Microvascular System. *Cold Spring Harbor Perspectives in Biology*, 7(1):a016345, jan 2015.

[281] Krystyna Solarana, Meijun Ye, Yu-Rong Gao, Harmain Rafi, and Daniel X. Hammer. Longitudinal multimodal assessment of neurodegeneration and vascular remodeling correlated with signal degradation in chronic cortical silicon microelectrodes. *Neurophotonics*, 7(1):1, jan 2020.

[282] Aleksandra Maruszak and Sandrine Thuret. Why looking at the whole hippocampus is not enough- a critical role for anteroposterior axis, subfield and activation analyses to enhance predictive value of hippocampal changes for Alzheimer's disease diagnosis. *Frontiers in Cellular Neuroscience*, 8, mar 2014.

[283] Alpay Alkan, Ibrahim Sahin, Lezan Keskin, Ayse Sertkaya Cikim, Hakki Muammer Karakas, Ahmet Sigirci, and Gulnur Erdem. Diffusion-weighted imaging features of brain in obesity. *Magnetic Resonance Imaging*, 26(4):446–450, may 2008.

[284] Yanwei Zhao, Gang Wu, Haiming Shi, Zhijie Xia, and Tao Sun. Relationship between cognitive impairment and apparent diffusion coefficient values from magnetic resonance-diffusion weighted imaging in elderly hypertensive patients. *Clinical Interventions in Aging*, 28(9):1223–31, jul 2014.

[285] Tieli Liu, Yunpeng Han, Lemei Tang, Jianlin Wu, Yanwei Miao, Bingbing Gao, and Jin Shang. Detection of chronic brain damage by diffusion-weighted imaging with multiple b values in patients with type 2 diabetes. *Medicine*, 95(35):e4726, aug 2016.

[286] C. Eleana Zhang, Sau May Wong, Renske Uiterwijk, Julie Staals, Walter H. Backes, Erik I. Hoff, Tobien Schreuder, Cécile R.L.P.N. Jeukens, Jacobus F.A. Jansen, and Robert J. van Oostenbrugge. Intravoxel Incoherent Motion Imaging in Small Vessel Disease. *Stroke*, 48(3):658–663, mar 2017.

[287] Constantin Bouras, Enikö Kövari, François R. Herrmann, Claire-Bénédicte Rivara, Thomasina L. Bailey, Armin von Gunten, Patrick R. Hof, and Panteleimon Giannakopoulos. Stereologic Analysis of Microvascular Morphology in the Elderly. *Journal of Neuropathology and Experimental Neurology*, 65(3):235–244, mar 2006.

[288] Karra D. Harrington, Yen Ying Lim, David Ames, Jason Hassenstab, Simon M. Laws, Ralph N. Martins, Stephanie Rainey-Smith, Joanne Robertson, Christopher C. Rowe, Olivier Salvado, Vincent Doré, Victor L. Villemagne, Peter J. Snyder, Colin L. Masters, and Paul Maruff. Amyloid β–associated cognitive decline in the absence of clinical disease progression and systemic illness. *Alzheimer's & Dementia: Diagnosis, Assessment & Disease Monitoring*, 8(1):156–164, jan 2017.

[289] Michelle E. Farrell, Xi Chen, Melissa M. Rundle, Micaela Y. Chan, Gagan S. Wig, and Denise C. Park. Regional amyloid accumulation and cognitive decline in initially amyloid-negative adults. *Neurology*, 91(19):e1809–e1821, nov 2018.

[290] Hyeon-Il Choi, Chang-Woo Ryu, Songvin Kim, Hak Young Rhee, and Geon-Ho Jahng. Changes in Microvascular Morphology in Subcortical Vascular Dementia: A Study of Vessel Size Magnetic Resonance Imaging. *Frontiers in Neurology*, 11, oct 2020.

[291] Yoshiki Hase, Ren Ding, Gina Harrison, Emily Hawthorne, Amilia King, Sean Gettings, Charlotte Platten, William Stevenson, Lucinda J. L. Craggs, and Raj N.

Kalaria. White matter capillaries in vascular and neurodegenerative dementias. *Acta Neuropathologica Communications*, 7(1):16, dec 2019.

[292] Matthew R Halliday, Sanket V Rege, Qingyi Ma, Zhen Zhao, Carol A Miller, Ethan A Winkler, and Berislav V Zlokovic. Accelerated pericyte degeneration and blood–brain barrier breakdown in apolipoprotein E4 carriers with Alzheimer's disease. *Journal of Cerebral Blood Flow & Metabolism*, 36(1):216–227, jan 2016.

[293] Jesse M. Hunter, Jason Kwan, Michael Malek-Ahmadi, Chera L. Maarouf, Tyler A. Kokjohn, Christine Belden, Marwan N. Sabbagh, Thomas G. Beach, and Alex E. Roher. Morphological and Pathological Evolution of the Brain Microcirculation in Aging and Alzheimer's Disease. *PLoS ONE*, 7(5):e36893, may 2012.

[294] V. W. Fischer, A. Siddiqi, and Y. Yusufaly. Altered angioarchitecture in selected areas of brains with Alzheimer's disease. *Acta Neuropathologica*, 79(6):672–679, apr 1990.

[295] Jesse D. Sengillo, Ethan A. Winkler, Corey T. Walker, John S. Sullivan, Mahlon Johnson, and Berislav V. Zlokovic. Deficiency in Mural Vascular Cells Coincides with Blood-Brain Barrier Disruption in Alzheimer's Disease. *Brain Pathology*, 23(3):303–310, may 2013.

[296] Kyrre E. Emblem, Christian T. Farrar, Elizabeth R. Gerstner, Tracy T. Batchelor, Ronald J. H. Borra, Bruce R. Rosen, A. Gregory Sorensen, and Rakesh K. Jain. Vessel calibre—a potential MRI biomarker of tumour response in clinical trials. *Nature Reviews Clinical Oncology*, 11(10):566–584, oct 2014.

[297] H.-Y. Kang, H.-L. Xiao, J.-H. Chen, Y. Tan, X. Chen, T. Xie, J.-Q. Fang, S. Wang, Y. Yang, and W.-G. Zhang. Comparison of the Effect of Vessel Size Imaging and Cerebral Blood Volume Derived from Perfusion MR Imaging on Glioma Grading. *American Journal of Neuroradiology*, 37(1):51–57, jan 2016.

[298] Yoshiaki Itoh and Norihiro Suzuki. Control of Brain Capillary Blood Flow. *Journal of Cerebral Blood Flow & Metabolism*, 32(7):1167–1176, jul 2012.

[299] F. Fernandez-Klett, N. Offenhauser, U. Dirnagl, J. Priller, and U. Lindauer. Pericytes in capillaries are contractile in vivo, but arterioles mediate functional hyperemia in the mouse brain. *Proceedings of the National Academy of Sciences*, 107(51):22290–22295, dec 2010.

[300] Changsi Cai, Jonas C. Fordsmann, Sofie H. Jensen, Bodil Gesslein, Micael Lønstrup, Bjørn O. Hald, Stefan A. Zambach, Birger Brodin, and Martin J. Lauritzen. Stimulation-induced increases in cerebral blood flow and local capillary vasoconstriction depend on conducted vascular responses. *Proceedings of the National Academy of Sciences*, 115(25):E5796–E5804, jun 2018.

[301] Lila Khennouf, Bodil Gesslein, Alexey Brazhe, J Christopher Octeau, Nikolay Kutuzov, Baljit S Khakh, and Martin Lauritzen. Active role of capillary pericytes during stimulation-induced activity and spreading depolarization. *Brain*, 141(7):2032–2046, jul 2018.

[302] Dennis L. Parker and Grant T. Gullberg. Signal-to-noise efficiency in magnetic resonance imaging. *Medical Physics*, 17(2):250–257, mar 1990.

[303] Antonino Paolo Di Giovanna, Alessandro Tibo, Ludovico Silvestri, Marie Caroline Müllenbroich, Irene Costantini, Anna Letizia Allegra Mascaro, Leonardo Sacconi, Paolo Frasconi, and Francesco Saverio Pavone. Whole-Brain Vasculature Reconstruction at the Single Capillary Level. *Scientific Reports*, 8(1):12573, dec 2018.

[304] Bernd Minnich and Alois Lametschwandtner. Lengths measurements in microvascular corrosion castings: Two-dimensional versus three-dimensional morphometry. *Scanning*, 22(3):173–177, dec 2006.

[305] Stephan E. Maier, Yanping Sun, and Robert V. Mulkern. Diffusion imaging of brain tumors. *NMR in Biomedicine*, 23(7):849–864, sep 2010.

[306] Shoko Hara, Masaaki Hori, Ryo Ueda, Akifumi Hagiwara, Shihori Hayashi, Motoki Inaji, Yoji Tanaka, Taketoshi Maehara, Kenji Ishii, Shigeki Aoki, and Tadashi Nariai. Intravoxel incoherent motion perfusion in patients with Moyamoya disease: comparison with 15 O-gas positron emission tomography. *Acta Radiologica Open*, 8(5):205846011984658, may 2019.

[307] Yu-Chuan Hu, Lin-Feng Yan, Yu Han, Shi-Jun Duan, Qian Sun, Gang-Feng Li, Wen Wang, Xiao-Cheng Wei, Dan-Dan Zheng, and Guang-Bin Cui. Can the low and high b-value distribution influence the pseudodiffusion parameter derived from IVIM DWI in normal brain? *BMC Medical Imaging*, 20(1):14, dec 2020.

[308] Misa Sumi, Marc Van Cauteren, Tadateru Sumi, Makoto Obara, Yoko Ichikawa, and Takashi Nakamura. Salivary gland tumors: Use of intravoxel incoherent motion MR imaging for assessment of diffusion and perfusion for the differentiation of benign from malignant tumors. *Radiology*, 263(3):770–777, 2012.

[309] Xue Wang, Jiao Song, Shengfa Zhou, Yi Lu, Wenxiao Lin, Tong San Koh, Zujun Hou, and Zhihan Yan. A comparative study of methods for determining Intravoxel incoherent motion parameters in cervix cancer. *Cancer Imaging*, 21(1):12, dec 2021.

[310] Eleftheria Panagiotaki, Torben Schneider, Bernard Siow, Matt G. Hall, Mark F. Lythgoe, and Daniel C. Alexander. Compartment models of the diffusion MR signal in brain white matter: A taxonomy and comparison. *NeuroImage*, 59(3):2241–2254, 2012.

[311] Valerie Phi Van, Franca Schmid, Georg Spinner, Sebastian Kozerke, and Christian Federau. Simulation of intravoxel incoherent perfusion signal using a realistic capillary network of a mouse brain. *NMR in Biomedicine*, apr 2021.

[312] Marco A. Meraz-Rios, Danira Toral-Rios, Diana Franco-Bocanegra, Juana Villeda-Hernández, and Victoria Campos-Peña. Inflammatory process in Alzheimer's Disease. *Frontiers in Integrative Neuroscience*, 13:7:59, 2013.

[313] Karan Govindpani, Laura G McNamara, Nicholas R Smith, Chitra Vinnakota, Henry J Waldvogel, Richard LM Faull, and Andrea Kwakowsky. Vascular Dysfunction

in Alzheimer's Disease: A Prelude to the Pathological Process or a Consequence of It? *Journal of Clinical Medicine*, 8(5):651, may 2019.

[314] Jay S. Detsky, Julia Keith, John Conklin, Sean Symons, Sten Myrehaug, Arjun Sahgal, Chinthaka C. Heyn, and Hany Soliman. Differentiating radiation necrosis from tumor progression in brain metastases treated with stereotactic radiotherapy: utility of intravoxel incoherent motion perfusion MRI and correlation with histopathology. *Journal of Neuro-Oncology*, 134(2):433–441, sep 2017.

[315] R H Farnsworth, M Lackmann, M G Achen, and S A Stacker. Vascular remodeling in cancer. *Oncogene*, 33(27):3496–3505, jul 2014.